



HAL
open science

Synthesis and Development New 8-Hydroxyquinoline Derivatives for the Treatment of Chlamydia trachomatis Infection

Thi Huyen Vu

► **To cite this version:**

Thi Huyen Vu. Synthesis and Development New 8-Hydroxyquinoline Derivatives for the Treatment of Chlamydia trachomatis Infection. Other. Université Paris Cité, 2020. English. NNT : 2020UNIP7030 . tel-03275323

HAL Id: tel-03275323

<https://theses.hal.science/tel-03275323>

Submitted on 1 Jul 2021

HAL is a multi-disciplinary open access archive for the deposit and dissemination of scientific research documents, whether they are published or not. The documents may come from teaching and research institutions in France or abroad, or from public or private research centers.

L'archive ouverte pluridisciplinaire **HAL**, est destinée au dépôt et à la diffusion de documents scientifiques de niveau recherche, publiés ou non, émanant des établissements d'enseignement et de recherche français ou étrangers, des laboratoires publics ou privés.

Université de Paris

Chimie Physique et Chimie Analytique Paris Centre – ED 388

Laboratoire ITODYS UMR CNRS 7086

Synthesis and Development New 8-Hydroxyquinoline Derivatives for the Treatment of *Chlamydia trachomatis* Infection

Par Thi Huyen VU

Thèse de doctorat de [[Chimie/Chimie Energie Nanosciences Surfaces](#)]

Dirigée par Nawal SERRADJI

Présentée et soutenue le 30 Juin 2020

Devant un jury composé de :

Isabelle LERAY	Directrice de recherches, ENS Paris Saclay	Rapportrice
Benjamin CARBONNIER	Professeur, Université Paris Est	Rapporteur
Thierry LE GALL	Président du jury - Chercheur HDR, CEA Saclay	Examineur
Catherine GOMEZ	Maître de conférences, CNAM	Examinatrice
Nguyet-Thanh HA DUONG	Maître de conférences HDR, Université de Paris	Examinatrice
Nawal SERRADJI	Maître de conférences HDR, Université de Paris	Directrice de thèse



Except where otherwise noted, this is work licensed under
<https://creativecommons.org/licenses/by-nc-nd/3.0/fr/>

Université de Paris

Chimie Physique et Chimie Analytique Paris Centre – ED 388

Laboratoire ITODYS UMR CNRS 7086

Synthesis and Development New 8-Hydroxyquinoline Derivatives for the Treatment of *Chlamydia trachomatis* Infection

Par Thi Huyen VU

Thèse de doctorat de **[Chimie/Chimie Energie Nanosciences Surfaces]**

Dirigée par Nawal SERRADJI

Présentée et soutenue le 30 Juin 2020

Devant un jury composé de :

Isabelle LERAY	Directrice de recherches, ENS Paris Saclay	Rapportrice
Benjamin CARBONNIER	Professeur, Université Paris Est	Rapporteur
Thierry LE GALL	Président du jury - Chercheur HDR, CEA Saclay	Examineur
Catherine GOMEZ	Maître de conférences, CNAM	Examinatrice
Nguyet-Thanh HA DUONG	Maître de conférences HDR, Université de Paris	Examinatrice
Nawal SERRADJI	Maître de conférences HDR, Université de Paris	Directrice de thèse



Except where otherwise noted, this is work licensed under
<https://creativecommons.org/licenses/by-nc-nd/3.0/fr/>

TITRE :

Synthèse et développement de nouveaux dérivés de la 8-hydroxyquinoléine pour le traitement de l'infection par *Chlamydia trachomatis*.

RESUME :

Chlamydia trachomatis, une bactérie à Gram négatif, est responsable, à la fois, de l'infection bactérienne sexuellement transmissible la plus diagnostiquée dans le monde et du trachome, une cause importante de cécité. Aucun vaccin n'est disponible mais deux antibiotiques (Azithromycine, Doxycycline) sont recommandés par l'Organisation Mondiale de la Santé. Toutefois, un échec du traitement est signalé chez 10 à 20% des patients et résulte probablement d'un manque de sensibilité des formes persistantes de la bactérie et des modestes concentrations intracellulaires des médicaments conventionnellement prescrits. Pour ces raisons, l'objectif de ma thèse était de proposer de nouveaux outils de lutte l'infection à *C. trachomatis* tels que de nouveaux dérivés de la 8-hydroxyquinoléine actifs contre cette bactérie. J'ai, tout d'abord, synthétisé de nouvelles molécules et évalué leur activité anti-chlamydiale ainsi que leurs propriétés chélatantes du fer. Le composé **1** résulte du couplage de l'acide 8-hydroxyquinoléine-2-carboxylique et de la Ciprofloxacine (Cip), un antibiotique actif contre *C. trachomatis*. Nous voulions obtenir des dérivés plus actifs que l'antibiotique-parent par ses propriétés chélatantes de métaux et son effet antibiotique. Le composé **1** présente effectivement une activité anti-chlamydiale plus élevée que la Cip mais cet effet ne semble pas lié à ses propriétés chélatantes du métal. En modifiant certains paramètres physicochimiques tels que la lipophilie, nous avons synthétisé plusieurs dérivés du composé **1**. Nous avons également préparé un conjugué d'acide folique pour permettre sa délivrance aux cellules infectées via le récepteur de ce dernier. Tous les composés obtenus sont plus actifs que la Ciprofloxacine, l'un d'entre eux atteignant une activité au nanomolaire contre la bactérie.

Dans la deuxième partie, nous avons étudié l'influence de la position du carbonyle sur les propriétés chélatantes du fer de la 8-hydroxyquinoléine. Pour cela, nous avons effectué une étude mixte expérimentale (synthèse organique, spectrophotométrie et calorimétrie de titrage isotherme) et théorique (théorie de la densité fonctionnelle). Deux dérivés esters de 8-hydroxyquinoléine, en position 2 et position 7, ont été synthétisés et les complexes de fer correspondants ont été étudiés. Nous avons démontré que selon la position du groupe attracteur d'électrons sur le squelette hétérocyclique, l'encombrement stérique peut déstabiliser le complexe de

fer (III) en le forçant à adopter une structure déformée, éloignée de l'environnement octaédrique idéal.

Dans la dernière partie, j'ai synthétisé et caractérisé des Carbone dots (CDs) d'acide folique et de Ciprofloxacine, comme nouveaux nano-objets pour cibler les cellules infectées et inhiber la croissance bactérienne. Les deux populations de CDs ont une taille de 4 à 5 nm, émettent en lumière bleue et présentent un comportement fluorescent indépendant de l'excitation. L'efficacité antibactérienne de ces nanoparticules est actuellement en cours d'étude.

MOTS CLEFS :

8-hydroxyquinoléine, Ciprofloxacine, *Chlamydia trachomatis*, chélateurs de fer, acide folique, nanoparticules, Carbon dots, spectrophotométrie.

TITLE :

Synthesis and development new 8-hydroxyquinoline derivatives for the treatment of *Chlamydia trachomatis* infection.

ABSTRACT :

Chlamydia trachomatis, a Gram-negative bacterium, is responsible for both the most common sexually transmitted bacterial infection in the world and trachoma, an important cause of blindness worldwide. No vaccine is available but antibiotics (azithromycine, doxycycline) are recommended by the World Health Organization. However, treatment failure is reported 10-20% of patients and probably results from a lack of sensitivity of persistent forms of bacteria and modest intracellular concentrations of the conventionally prescribed drugs. For this reasons, the aim of my thesis was to propose new tools to fight *C. trachomatis* infection such as novel 8-hydroxyquinoline derivatives active against this bacterium.

In the first part, I synthesised new compounds and evaluated their anti-chlamydia activity as well as their iron-chelating properties. Compound 1 results from the coupling of 8-hydroxyquinoline-2-carboxylic acid and Ciprofloxacin (Cip), a commercially available antibiotic. We wanted to obtain more active derivatives than the parent antibiotic through its metal-chelating properties and its antibiotic effect. Compound 1 presents a higher antichlamydia activity than Cip but this antibacterial effect seems not be linked to its iron-chelating properties. Modifying physicochemical parameters such as lipophilicity, we synthesized several derivatives. We also prepared a folic acid conjugate to enable its delivery to the infected cells through folic acid receptor. All compounds are more potent than Ciprofloxacin, one of them reaching nanomolar potency against *C. trachomatis*.

In the second part, I studied the influence of the carbonyl position on the iron-chelating properties of the 8-hydroxyquinoline heterocycle. For this purpose, we performed a mixed experimental (organic synthesis, spectrophotometry and isothermal titration calorimetry) and theoretical (density-functional theory) study. Two 8-hydroxyquinoline ester-derivatives, at 2-position and 7-position, were synthesized and the corresponding iron-complexes were investigated. We demonstrated that according to the position of the withdrawing group on the heterocyclic skeleton, the steric hindrance can destabilize the iron(III) complex by forcing it to adopt a distorted structure far from the ideal octahedral environment.

In the last part, I synthesized and characterized Carbon dots (CDs) from folic acid and Ciprofloxacin as new nano-tools to target the infected cells

and inhibit the bacterial growth. Both populations of CDs have a 4-5 nm size, emit in blue light and present an excitation-independent fluorescent behaviour. These nanoparticles are actually under biological investigation.

KEYWORDS:

8-hydroxyquinoline, Ciprofloxacin, *Chlamydia trachomatis*, Iron chelation, folic acid, carbon dots, spectrophotometry.

CONTENTS

	Page
RESUME	i
ABSTRACT	iii
ACKNOWLEDGEMENTS	ix
ABBREVIATIONS	xi
LIST OF FIGURES	xiii
LIST OF SCHEMES	xviii
LIST OF TABLES	xix
CHAP I: <i>CHLAMYDIA TRACHOMATIS</i> INFECTION	1
1. Introduction	1
2. <i>Chlamydia trachomatis</i> life cycle	2
3. Treatment and treatment failures	3
4. Inhibitors of <i>C. trachomatis</i> growth	5
4.1. The bacterial targets	6
4.1.1. The chlamydial lipooligosaccharide biosynthesis pathway	6
4.1.2. The Na ⁺ -translocating NADH: ubiquinone oxidoreductase	6
4.1.3. The chlamydial virulence factors	6
4.1.4. Disruption of the glucose 6-phosphate metabolic pathway	11
4.1.5. Bacterial DNA synthesis	11
4.1.6. The serine protease CPAF (Chlamydia protease-like activity factor)	12
4.1.7. The bacterial peptide deformylase (PDF)	13
4.1.8. The bacterial ribosome	14
4.1.9. The type II fatty acid synthesis (FASII) pathway	14
4.2. The host cell targets	15
4.2.1. Long-chain Acyl-CoA synthetases (ACSLs)	15
4.2.2. Sphingolipid trafficking from the host cell Golgi apparatus into the bacterial	15

inclusions	
4.2.3. Indolamine-2,3 dioxygenase (IDO1)	16
4.3. The unknown targets	16
5. Iron chelators as bacterial growth inhibitor	19
5.1. Iron chelators	19
5.2. Bacterial iron homeostasis disruption	20
5.2.1. Iron depletion	22
5.2.2. The “Trojan Horse” strategy	24
5.2.3. Inhibition of the siderophores synthesis	25
5.2.4. Iron chelators as <i>C. trachomatis</i> bacterial growth inhibitors	26
6. Previous work done in the laboratory and objectives of my PhD	26
CHAPTER II: NEW FLUOROQUINOLONE DERIVATIVES HIGHLY ACTIVE AGAINST <i>CHLAMYDIA TRACHOMATIS</i>	30
1. Introduction	30
2. Compound 1	34
2.1. Chemistry	34
2.2. Biological evaluation	35
2.2.1. The anti-Chlamydia activity	35
2.2.2. Other antimicrobial activities	37
2.3. Iron-chelating properties	40
3. Compound 1’s derivatives	44
3.1. Organic synthesis	44
3.1.1. Increasing compound 1’s lipophilicity	44
3.1.2. Compound 6 – An isomer of compound 1	46
3.1.3. Coupling between folic acid and ciprofloxacin	47
3.2. Iron chelating properties of compound 1’s derivatives	47
3.3. Antibacterial activity of compound 1’s derivatives 5a-d, 6 and 7	52
4. Conclusions & Perspectives	54

5. Experimental part	55
5.1. Organic synthesis	55
5.2. Biology	62
5.2.1. Compound 1	62
5.2.2. Compound 1's derivatives (5a, 5b, 5d, 6, 7)	63
5.3. Metal chelation	65
5.3.1. <i>Stock solutions.</i>	65
5.3.2. <i>Spectrophotometric measurements</i>	65
CHAPTER III: INFLUENCE OF THE CARBONYL GROUP OF THE 8-HYDROXYQUINOLINE MOIETY ON ITS METAL CHELATING PROPERTIES	66
1. Introduction	66
2. Results and discussions	69
2.1. Organic synthesis	69
2.2. Free ligands	69
2.2.1. UV-vis absorbance spectra of the ligands	69
2.2.2. Determination of the thermodynamic constant	74
2.3. Formation of the iron (III) complexes	76
2.3.1. Stoichiometry of the iron(III) complexes	76
2.3.2. Structure of the iron(III) complexes	80
2.3.3. UV/vis spectra of the iron(III) complexes	83
2.3.4. Determination of the thermodynamic constants	89
3. Conclusions & Perspectives	91
4. Experiments	92
4.1. Materials and methods	92
4.2. Methyl 8-hydroxyquinoline-2-carboxylate (NHQ) synthesis	92
4.3. Methyl 8-hydroxyquinoline-7-carboxylate (OHQ) synthesis	93
4.4. Stock solutions	93
4.5. pH Measurements	93

4.6. Spectrophotometric measurements	94
4.7. Microcalorimetry	94
4.8. Computational details	94
CHAPTER IV: THE USE OF NANOPARTICLES TO OVERCOME <i>C. TRACHOMATIS</i> INFECTION	96
1. The use of nanoparticles to overcome <i>C. trachomatis</i> infection – state of art	96
1.1. Metallic nanoparticles	96
1.2. Polymeric nanoparticles	97
1.3. From Folate-based polymeric NPs to Folate-based carbon dots	98
2. Pioneer study on CDs as antibacterial agents against <i>C. trachomatis</i> infection	100
3. Results and discussion	101
3.1. Synthesis and characterizations of FA-CDs	101
3.2. Synthesis and characterizations of Cip-CDs	108
4. Conclusions and Perspectives	112
5. Experimental section	113
5.1. Chemicals	113
5.2. Apparatus and characterization	113
5.3. FA-CDs hydrothermal synthesis	113
5.4. Cip-CDs hydrothermal synthesis	113
5.5. Quantum yield (QY) measurement	114
CHAP V: GENERAL CONCLUSIONS	115
REFERENCES	118

ACKNOWLEDGEMENTS

My doctoral research was carried out for three years in the ITODYS laboratory (Interfaces, Traitements, Organisation et Dynamique des Systèmes) at Paris Diderot University, University of Paris. During these years, I learned many new things and, therefore, I obtained and accumulated different results thanks to the help of many people and organizations that I wish to highlight.

I would like to express my great gratitude to my supervisor, Dr Nawal SERRADJI. I am indebted to her for having given me the PhD position and for her guidance, advices, support, encouragement and inspiration during these three years of doctorate. In addition to working in the laboratory, she also encouraged me to participate to conferences, online courses and English lessons. I am also grateful for her help in my life. She is one of the most patient and enthusiastic teachers I have ever known. It was a great honor to be one of her students.

I would like to offer my special thanks to Dr Thanh HA-DUONG for her precious guidance and supports in my work as well as joyful parties she organized.

I am particularly grateful to the director of the laboratory, Pr François MAUREL, for his acceptance so that I can carry out my doctorate in ITODYS, and also for his help during my thesis process. I would also like to thank Mr Pierre-François QUENIN, administrator of ITODYS, and Mr Frédérick GUICHEN, at the UFR de chimie, for their help in the financial management of my scholarship.

I would like to thank Dr Philippe VERBEKE (Inserm U1149, Paris Diderot, Paris), Dr Eric BREMOND and Dr Mahamadou SEYDOU (ITODYS, Université de Paris), Pr Alexandra AUBRY (CIMI, Paris), Pr Patrick PLESIAT (Hôpital Jean Minjoz, Besançon,), and Dr Åsa GYLFE (Umeå university, Umeå, Sweden) for their supports.

I am sincerely thankful to Pr Souad AMMAR, Mr Alexandre CHEVILLOT, Dr Delphine SCHAMING, Dr Mercé MARTIN-SABI and Mr Antonino MADONIA for technical supports and helps.

I would like to thank Dr Ha Anh NGUYEN, Dr Thi Thuy Khue NGUYEN, and Dr Thuan Nguyen PHAM TRUONG for supports and sharing about life in France.

I acknowledge the Vietnam International Education Development (VIED)-Ministry of Education and Training of Vietnam for offering me a PhD grant through the University of Science and Technology of Hanoi (USTH) program.

I also thank all the members of my thesis committee for agreeing to evaluate this work.

I take this opportunity to express my sincerest love and thanks to my family and my close friends for the love and understanding.

Paris, May 2020

VU Thi Huyen

ABBREVIATIONS

AB	Aberrant Body
ACSLs	Long-chain Acyl-CoA Synthetases
<i>C. trachomatis</i>	<i>Chlamydia trachomatis</i>
CDs	Carbon Dots
Cip	Ciprofloxacin
Cip-CDs	CDs from Cip
CorA	Corallopyronin A
CPAF	Chlamydial Protease/proteasome-like Activity Factor
CtHtrA	<i>C. trachomatis</i> High Temperature Requirement A
DFRA	Deferasirox
DIEA	<i>N,N</i> -diisopropylethylamine
EBs	Elementary Bodies
EC ₅₀	Half-maximal Effective Concentration
FA-CDs	Folate-based CDs
FA-Rs	Folate Receptors
FBS	Fetal Bovine Serum
Fe-NTA	Fe-nitrilotriacetic Acid
FT-IR	Fourier transform infrared spectroscopy
HBSS	Hank Balanced Salt Solution
HIV	Human Immunodeficiency Virus
HPV	Human Papilloma Virus
HQ	8-hydroxyquinoline
HRMS	High-resolution Mass Spectra
IC ₅₀	Half-maximal Inhibitory Concentration
IDO1	Indolamine-2,3 Dioxygenase
IFU	Inclusion Forming Unit
LGV	Lymphogranuloma Venereum
LMCT	Ligand to Metal Charge Transfer

LOS	Lipo-oligosaccharide
MBC	Minimal Bactericidal Concentration
MCC	Minimal Chlamydicidal Concentrations
MEP	MEalonate Pathway
MIC	Minimum Inhibitory Concentration
MIC ₅₀	Half-minimal Inhibitory Concentration
MIP	Macrophage Infectivity Potentiator
MOI	Multiplicity of Infection
MOMP	Major Outer Membrane Protein
NHQ	Methyl 8-hydroxyquinoline-2-carboxylate
NPs	Nanoparticles
NRPS	Non-ribosomal Peptides Synthetase
OHQ	Methyl 8-hydroxyquinoline-7-carboxylate
PAMAM	Poly(amidoamine)
PDF	Peptide Deformylase
PLGA	Poly(lactide-co-glycolide)
PPIase	Peptidyl-Prolyl cis/trans Isomerase
QDs	Quantum Dots
RBs	Reticulate Bodies
RNR	Ribonucleotide Reductase
SPGG	Sulfated Pentagalloyl Glucoside
STIs	Sexually Transmitted Infections
T3SS	Type III Secretion System
TARP	Translocated Actin Recruiting Phosphoprotein
TBE	Tris-Borate-EDTA
TBTU	2-(1 <i>H</i> -benzotriazole-1-yl)-1,1,3,3-tetramethyluronium tetrafluoroborate

LIST OF FIGURES

	Page
Figure 1.1. <i>C. trachomatis</i> life cycle	3
Figure 1.2. Traditional targets of antimicrobial compounds at various stages of the chlamydial developmental cycle	4
Figure 1.3. LPC-011 (left) and PEG-2S (right)	6
Figure 1.4. The pipecolic acid derivatives	7
Figure 1.5. CF001 (left), CF002 (centre) and SF3 (right)	8
Figure 1.6. CL-55 (left) and INP0341 (right)	9
Figure 1.7. (-)-Hopeaphenol (left) and INP derivatives (right)	9
Figure 1.8. Salicylidene acylhydrazides synthesized by Sunduru <i>et al.</i>	10
Figure 1.9. W1227933 (left) and W1774182 (right)	10
Figure 1.10. JO146	11
Figure 1.11. KSK 120, the corresponding optimized compound KSK213 and the triazolo-derivative 20	11
Figure 1.12. AZD0914	12
Figure 1.13. Nafamostat mesylate	13
Figure 1.14. GM6001 (left) and TAPI-0 (right)	14
Figure 1.15. Compound 18	14
Figure 1.16. Rottlerin	15
Figure 1.17. Biochanin A	16
Figure 1.18. Some recently published <i>C. trachomatis</i> inhibitors	19
Figure 1.19. Examples of responses of <i>Staphylococci</i> to deferoxamine	23
Figure 1.20. Structures of sideromycins	25
Figure 1.21. Structure of <i>p</i> -aminosalisylates (left) and SAL-AMS analogues (right)	26
Figure 1.22. An acylhydrazone	26
Figure 1.23. Structure of the previously obtained inhibitors by Abdelsayed <i>et al.</i>	27

Figure 1.24.	Compound 19	27
Figure 1.25.	Hypothetical structures of iron complexes proposed by V. Corcé <i>et al.</i>	28
Figure 1.26.	Structures of <i>O</i> - and <i>N</i> -TRENTOX and their iron chelating capacities	29
Figure 2.1.	8-hydroxyquinoline	30
Figure 2.2.	Schematic HQ metal coordination (left) for divalent metal, (right) for trivalent metal.	31
Figure 2.3.	INP derivatives	32
Figure 2.4.	Ciprofloxacin	32
Figure 2.5.	Main coordination modes of ciprofloxacin	33
Figure 2.6.	Compound 2	35
Figure 2.7.	Inhibitory effects on <i>C. trachomatis</i> infectious capacity of compounds tested <i>in cellulo</i> (grey bars: compound 1; black bars: ciprofloxacin. Statistically significant differences are noted as follows: ** p<0.01, *** p<0.001)	36
Figure 2.8.	Compound 1 inhibitory effect in the presence of excess iron citrate (200 μM). Statistically significant differences are noted as follows: * p<0.05, ** p<0.01, *** p<0.001	37
Figure 2.9.	Absorption spectra in the presence of increasing concentrations of FeCl ₃ at pH 2 and 25±0.5 °C (A) of compound 1 (10 ⁻⁴ M) (FeCl ₃ : 0–10 ⁻³ M; solvent: DMSO/water pH 2, 1:1, v/v) with absorbance at 450 nm plotted against [Fe(III)]/[1] in inset, and (B) of Methyl 8-hydroxyquinoline-2-carboxylate (10 ⁻⁴ M), (FeCl ₃ : 0–10 ⁻⁵ M; solvent: EtOH/water pH 2, 1:4, v/v)	42
Figure 2.10.	Methyl 8-hydroxyquinoline-2-carboxylate	42
Figure 2.11.	Absorption spectra in the presence of Fe-NTA (A) of compound 1 (5.10 ⁻⁵ M) (buffer: 50 mM HEPES - 150 mM KCl, pH 7.0, solvent: DMSO; buffer/solvent, 1:1, v/v) (B) of Methyl 8-hydroxyquinoline-2-carboxylate (5.10 ⁻⁴ M) (buffer: 50 mM HEPES - 150 mM KCl, pH 7.0, solvent: EtOH; buffer/solvent, 4:1, v/v)	43
Figure 2.12.	Structures of compounds 1 and 6	47
Figure 2.13.	Absorption spectra in the presence of increasing concentrations of FeCl ₃ (0 - 672 μM) at pH 2 and 25±0.5 °C (A) of compound 5a	48

	(10^{-4} M) (solvent: DMSO/water pH 2, 1:1, v/v); (B) Absorbance at 450 nm plotted against [Fe(III)]/[5a].	
Figure 2.14.	Absorption spectra in the presence of increasing concentrations of FeCl ₃ (0 – 384 μM) at pH 2 and 25±0.5 °C of compound 6 (10^{-4} M) (solvent: DMSO/water pH 2, 1:1 v/v); Absorbance at 450 nm and 600 nm plotted against [Fe(III)]/[6]	50
Figure 2.15.	Absorption spectra in the presence of increasing concentrations of Fe-NTA (0 - 136 μM) at pH 7 and 25±0.5 °C of compound 6 ($5 \cdot 10^{-5}$ M) (buffer: 50 mM HEPES - 150 mM KCl, solvent: DMSO; buffer/solvent, 1:1, v/v). Absorbance at 435 nm and 570 nm plotted against [Fe(III)]/[6]	51
Figure 2.16.	Immunofluorescence images of different concentrations of compound 6 against <i>C. trachomatis</i> L2-454/Bu infected Hela cells at 46 hours post infection (the bacterial inclusions appear in red).	54
Figure 3.1.	Structures of <i>O</i> - and <i>N</i> -TRENTOX and their iron chelating capacities	67
Figure 3.2.	Previously 8-hydroxyquinoline derivatives obtained in the group.	68
Figure 3.3.	Representation of the free ligands investigated.	68
Figure 3.4.	Experimental absorption spectra of HQ ($5 \cdot 10^{-4}$ M) acquired at different pH values in (left) sodium acetate 50 mM, KCl 140 mM, 20% EtOH, pH 2.35–6.10; in (right) carbonate 50 mM, KCl 150 mM, 20% EtOH, pH 7.35–12.45. All the experiments are performed at 25 ± 0.5°C. Arrows indicate the direction of spectral changes when pH value decreases.	70
Figure 3.5.	Absorption spectra of (A) NHQ ($5 \cdot 10^{-4}$ M) in sodium acetate 50 mM, KCl 140 mM, 20 % DMSO, pH 3.82–6.12 (B) NHQ ($5 \cdot 10^{-4}$ M) in carbonate 50 mM, KCl 150 mM, 20 % DMSO, pH 7.34–12.08 (C) OHQ ($5 \cdot 10^{-4}$ M) in sodium acetate 50 mM, KCl 140 mM, 20 % DMSO, pH 1.81–6.46 (D) OHQ ($5 \cdot 10^{-4}$ M) in carbonate 50 mM, KCl 150 mM, 20 % DMSO, pH 10.92–13.02 at 25 ± 0.5 °C. Arrows indicate the direction of spectral changes when pH value decreases.	73
Figure 3.6.	Absorption spectra in the presence of iron of (A) HQ ($5 \cdot 10^{-4}$ M) in sodium formiate 50 mM, KCl 140 mM, 20 % DMSO, pH 2.11–3.95 (B) HQ ($5 \cdot 10^{-4}$ M) in sodium acetate 50 mM, KCl 150 mM, 20 % DMSO, pH 4.52–6.34 (C) NHQ ($5 \cdot 10^{-4}$ M) in sodium formiate 50 mM, KCl 140 mM, 20 % DMSO, pH 2.09–4.00 (D) NHQ	77

(5.10^{-4} M) in sodium acetate 50 mM, KCl 150 mM, 20 % DMSO, pH 4.20–6.41 at 25 ± 0.5 °C. (E) OHQ (5.10^{-4} M) in sodium formiate 50 mM, KCl 140 mM, 20 % DMSO, pH 2.09–4.00 (F) OHQ (5.10^{-4} M) in sodium acetate 50 mM, KCl 150 mM, 20 % DMSO, pH 3.32–6.25 at 25 ± 0.5 °C. Arrows indicate the direction of spectral changes when pH value decreases.

- Figure 3.7. Isothermal titration data for the titration at 25°C of: (A) HQ (5 mM) with Fe^{3+} (15 mM) at pH 2.0, (B) Fe^{3+} (0.5 mM) with HQ (10 mM) at pH 2.0, (C) HQ (2 mM) with Fe(citrate) (10 mM) at pH 7.0. The first two data points were deleted before curve fitting. 79
- Figure 3.8. Low energy computational model of (A) $\text{Fe}(\text{HQ})_3$, (B) $\text{Fe}(\text{NHQ})_3$, (C) $\text{Fe}(\text{OHQ})_3$ and (D) $\text{Fe}_{\text{OO}}(\text{OHQ})_3$ 82
- Figure 3.9. Experimental absorption spectra function of the pH (2.0 and 7.4) and the corresponding vertical electronic transitions function of the acid (LH_2^+) and neutral (LH) form of HQ in case of the (left) free ligand and (right) iron(III) complex. Vertical excitations are computed with the 6-31+G* basis set at PCM-TD-PBE0 and PCM-TD-CAM-B3LYP levels of theory for the free ligand and iron(III) complex, respectively. Both insets depict the absorption spectra Gaussian convolution of the vertical excitations. 83
- Figure 3.10. Computed electronic density variations ($\Delta\rho$, isovalue 0.0004 a.u.) for the main vertical electronic transitions of the neutral form of the $[\text{Fe}(\text{HQ})_3]$ complex. The blue and red surfaces represent a density increase and depletion upon excitation, respectively. 85
- Figure 3.11. Experimental absorption spectra of (A) HQ (5.10^{-4} M), (B) NHQ (5.10^{-4} M), and (C) OHQ (1.10^{-4} M) in presence of an increasing concentration of FeCl_3 at pH 2.0. Same experiments for (D) HQ (5.10^{-4} M), (E) NHQ (1.10^{-4} M), and (F) OHQ (5.10^{-4} M) in presence of an increasing concentration of Fe(III)-NTA at pH 7.4. All the experiments are performed at 25 ± 0.5 °C. Arrows indicate the direction of spectral changes when the concentration in iron(III) increases. 87
- Figure 4.1. Fluorescence emission intensity as a function of the cell type incubated with the FA-CDs. 99
- Figure 4.2. Solution of free FA and FA-CDs in water under white light and under UV irradiation at 365 nm. 102
- Figure 4.3. Size distribution histogram of FA-CDs, extracted from the DLS 102

experiments in water

Figure 4.4.	Ultraviolet-visible (UV/Vis) absorption spectra of FA-CDs (50 $\mu\text{g}/\text{mL}$ in water, black line) and free FA (25 $\mu\text{g}/\text{mL}$ in water, red line) in aqueous solution.	103
Figure 4.5.	Photoluminescence spectra of FA-CDs (1 $\mu\text{g}/\text{mL}$ in water) for various excitation wavelengths.	104
Figure 4.6.	Slope method for the calculation of fluorescence quantum yield.	105
Figure 4.7.	Photoluminescence spectra of free FA (1 $\mu\text{g}/\text{mL}$ in water) and FA-CDs (1 $\mu\text{g}/\text{mL}$ in water), $\lambda_{\text{exc}}=355$ nm.	105
Figure 4.8.	FT-IR spectra of free FA (upper spectrum) and FA-CDs (lower spectrum).	106
Figure 4.9.	Aqueous FA-CDs suspension zeta potential distribution at pH 4.	107
Figure 4.10.	Variation of the measured Zeta potential of an aqueous FA-CDs suspension at different pH values.	108
Figure 4.11.	Size distribution histogram of Cip-CDs, extracted from the DLS experiments in water.	109
Figure 4.12.	UV-visible absorption spectra of free Cip (25 $\mu\text{g}/\text{mL}$ in 0.1N HCl, red line) and Cip-CDs (50 $\mu\text{g}/\text{mL}$ in H_2O , black line).	110
Figure 4.13.	Photoluminescence spectra of free Cip (10 $\mu\text{g}/\text{mL}$ in 1N HCl) and Cip-CDs (1 $\mu\text{g}/\text{mL}$ in water) for various excitation wavelengths.	110
Figure 4.14.	FT-IR spectra of Cip (blue spectrum) and Cip-CDs (red spectrum).	111
Figure 4.15.	Aqueous Cip-CD suspension zeta potential distribution at pH 4.	112

LIST OF SCHEMES

	Page
Scheme 2.1. Compound 1 synthesis	34
Scheme 2.2. Synthesis of compound 1 's derivatives	45
Scheme 2.3. Synthesis of compound 7	47
Scheme 3.1. Synthesis of NHQ and OHQ	69
Scheme 4.1. Schematic FA-CDs synthesis from folic acid	101
Scheme 4.2. Cip-CDs synthesis from Ciprofloxacin	108

:

LIST OF TABLES

		Page
Table 1.1.	Type, name, chemical structure, and main sources of siderophores.	20
Table 1.2.	MICs of iron chelators (deferoxamine and deferiprone ApoL1) against ATCC type strains grown.	24
Table 2.1.	Formation constants of metal complexes of HQ.	31
Table 2.2.	Minimal bactericidal concentrations of the studied compounds 1-2 versus their lipophilicity (log P).	36
Table 2.3.	<i>In vitro</i> antibacterial activities (IC ₅₀ or MIC) of compounds 1-2 , ciprofloxacin and acid 3 .	39
Table 2.4.	Characterization of absorption spectra of compound 5a and 1 at pH 2.0.	49
Table 2.5.	The clog and EC ₅₀ values of compound 1 's derivatives.	53
Table 3.1.	Energies (<i>e</i> , in eV), wavelengths (λ , in nm), oscillator strengths (<i>f</i> , in a.u.) and charge-transfer distance (DCT in Å) of the main vertical electronic transitions computed for the acid (LH ₂ ⁺), neutral (LH) and basic (L ⁻) forms of the HQ molecule at PCM-TD-PBE0 and PCM-TD-CAM-B3LYP level of theory with the 6-31+G* basis set. Only transitions with sufficiently large enough oscillator strength are retained. Experimental energies and wavelengths of the main absorption bands are provided as a matter of comparison.	72
Table 3.2.	Energies (<i>e</i> , in eV), wavelengths (λ , in nm) and oscillator strengths (<i>f</i> , in a.u.) of the main vertical electronic transitions computed for the acid (LH ₂ ⁺), neutral (LH) and basic (L ⁻) forms of the NHQ and OHQ molecules at PCM-TD-PBE0 and PCM-TD-CAM-B3LYP level of theory with the 6-31+G* basis set. Only transitions with sufficiently large enough oscillator strength are retained. Experimental energies and wavelengths of the main absorption bands are provided as a matter of comparison.	74
Table 3.3.	Acid-base dissociation constants of the HQ ligand and its NHQ and OHQ ester derivatives in absence or presence of iron(III).	75
Table 3.4.	Energy gaps (kcal mol ⁻¹) between the low- and high-spin states (Δ_{LS-HS}) and intermediate- and high-spin states (Δ_{IS-HS}) for a series of	80

iron(III) complexes computed at the PCM-DFT level of theory with different density functionals and the 6-31+G* basis set. For all iron(III) complexes, the high-spin state is found as the most stable electronic state.

Table 3.5.	Coordination bond distance (\AA) between iron(III) and the different chelating sites for a selection of HQ-based complexes. Bond distances are optimized at PCM-PBE0 level of theory with (+D3(bj)) or without (noCor) empirical dispersion corrections with the 6-31+G* basis set. Crystallographic structure parameters of the O-TRENTOX-based complex are reported as a matter of comparison.	81
Table 3.6.	Energies (e , in eV), wavelengths (λ , in nm), oscillator strengths (f , in a.u.) and charge-transfer distance (DCT in \AA) of the main vertical electronic transitions computed for the acid ($[\text{Fe}(\text{HQ})_3]^{3+}$, pH 2.0) and neutral ($[\text{Fe}(\text{HQ})_3]$, pH 7.4) forms of the iron(III) complex chelated by 3 HQ ligands at PCM-TD-PBE0 and PCM-TD-CAMB3LYP level of theory with the 6-31+G* basis set. Only transitions with sufficiently large enough oscillator strengths and one among the quasi-generated states are retained. Experimental energies and wavelengths of the main absorption bands are provided as a matter of comparison.	84
Table 3.7.	Energies (e , in eV), wavelengths (λ , in nm), oscillator strengths (f , in a.u.) and charge-transfer distance (D_{CT} in \AA) of the main vertical electronic transitions computed for the neutral $[\text{Fe}(\text{NHQ})_3]$, $[\text{Fe}(\text{OHQ})_3]$ and $[\text{Fe}_{\text{oo}}(\text{OHQ})_3]$ forms of the iron(III) complex (pH 7.4) at PCM-TD-PBE0 and PCM-TD-CAM-B3LYP level of theory with the 6-31+G* basis set. Only transitions with sufficiently large enough oscillator strengths and one among the quasi-generated states are retained. Experimental energies and wavelengths of the main absorption bands are provided as a matter of comparison.	88
Table 3.8.	Formation constants of the $[\text{Fe}(\text{L})_3]$ complex for a selection of ligands L.	89
Table 4.1.	Slope method for the calculation of fluorescence quantum yield of FA-CDs and Cip-CDs.	114

CHAPTER I:

CHLAMYDIA TRACHOMATIS INFECTION

1. Introduction

Worldwide, sexually transmitted infections (STIs) are a major public health problem. Infection consequences include infertility [Schuchardt 2018], cancers [Caini 2014] and pregnancy complications [Xia 2020] leading to serious morbidity and mortality. They also facilitate human immunodeficiency virus (HIV) [Peterman 2015] [Buckner 2016] or human papilloma virus (HPV) [Naldini 2019] transmission. In 2012, about 360 million new cases of curable STIs (gonorrhea, chlamydia, syphilis and trichomoniasis) occurred among 15-49 year-olds worldwide, including 131 million cases of chlamydial infection [WHO 2016]. Chlamydiosis is a STI disease caused by the bacterium *Chlamydia trachomatis* (*C. trachomatis*). Genital infections due to *C. trachomatis* are asymptomatic in 70% of women and 50% of men. This bacterium is also responsible for trachoma, an ocular infection and the world's leading infectious cause of blindness [Evans 2019]. It is responsible for the blindness or visual impairment of about 1.9 million people and causes about 1.4% of all blindness worldwide [WHO 2011] [Mariotti 2009].

C. trachomatis is part of the *Chlamydophila* genus. These bacteria are gram-negative, anaerobic, intracellular obligates that replicate within eukaryotic cells. In 1907, Halberstaedter and von Prowazek first described *C. trachomatis* in intracytoplasmic inclusions in conjunctival scrapings taken from monkey inoculated with ocular material from children with trachoma [Halberstaedter 1907]. In the 1930s, *C. trachomatis* was first grown in mouse brain and in eggs from a patient with lymphogranuloma venereum (LGV) [Mabey 2012]. Until 1957, the more meticulous trachoma biovar was isolated from humans with trachoma by inoculating conjunctival material into the chick-embryo yolk-sac [Tang 1957a] [Tang 1957b]. The trachoma biovar was first grown in tissue culture in 1965, making it possible for the first time to study the epidemiology and clinical features of *C. trachomatis* infection [Gordon 1965]. *C. trachomatis* differentiates into 18 serovars (serologically variant strains) based on monoclonal antibody-based typing assays against the Major Outer Membrane Protein (MOMP) of *C. trachomatis* [Dean 2000] [Wang 1991]. These serovars correlate with multiple medical conditions:

-Serovars A, B, Ba, and C are responsible for trachoma.

-Serovars D-K lead to genital tract and neonatal infections.

-Serovars L1-L3 are responsible for Lymphogranuloma venereum (LGV), which correlates with genital ulcer disease frequent in tropical countries.

2. *Chlamydia trachomatis* life cycle

C. trachomatis is characterized by its unique life cycle and exists mainly in two morphological forms: the elementary bodies (EBs) and the reticulate bodies (RBs). EBs (0.25 to 0.3 μm in diameter) are extracellular, metabolically inert forms and are responsible for infection of host cells. Upon attachment to the host cell, which is mediated by several unknown bacterial ligands and receptors, the type III secretion system (T3SS) gets through the plasma membrane of the host cell and injects virulence factors, such as TARP, into the cytosol. Those virulence factors activate Rho GTPase and the rearrangement of actin cytoskeleton near the bacteria attachment site. Those cytoskeleton remodelings lead to the internalization of the EBs. After few hours, EBs differentiate into metabolically active forms, termed reticulate body (RBs; 0.5 to 0.6 μm in diameter). After 24 to 74 hours of infection, and repeated cycles of binary fission, RBs differentiate back in EBs. The host cells are then lysed, releasing EBs that infect surrounding cells (Figure 1.1).

élément sous droit, diffusion non autorisée

Figure 1.1. *C. trachomatis* life cycle [Abdelrahman 2005]. TARP (Translocated Actin Recruiting Phosphoprotein, CT456), MEP (non-MEalonate Pathway), CPAF (Chlamydial Protease/proteasome-like Activity Factor).

Several stressful growth conditions, including immunological responses (mainly IFN- γ and TNF- α production), antibiotics or nutrient (iron, tryptophane) deprivation, stop chlamydial cell division and cause development of a morphologically enlarged but viable form termed aberrant body (AB). This phenotype constitutes the chlamydial developmental state known as persistence. This state is reversible as removal of the stressor allows the AB to differentiate back into RBs and complete the normal developmental cycle [Hogan 2004].

3. Treatment and treatment failures

No vaccine is available [Phillips 2019]. Fortunately, when detected, chlamydial infection can be treated with antibiotics. Control of chlamydial infections relies mainly on the use of macrolides and tetracyclines. Indeed, *C. trachomatis* is not sensitive to aminoglycosides, antibiotics conventionally used against gram negative bacteria, and to other antibiotics that do not penetrate cells efficiently. WHO recommended two antibiotics to treat *C. trachomatis*:

Azithromycin (1g orally x 1 dose) and Doxycycline (100 mg twice daily x 7 days) [WHO 2016]. These antibiotics inhibit the growth of *C. trachomatis* by preventing the protein synthesis. Both Azithromycin and Doxycycline are lipophilic antibiotics and reach high intracellular concentrations, explaining their good activity against *C. trachomatis*. Other drugs can be used, as described in the figure below (Figure 1.2). There are some antibiotics with traditional targets such as other tetracyclines or macrolides, phenicols (protein synthesis inhibitors), quinolones, rifampins (nucleic acid synthesis inhibitors) and β -lactams (peptidoglycan synthesis inhibitors).



Figure 1.2. Traditional targets of antimicrobial compounds at various stages of the chlamydial developmental cycle [Bommana 2019].

Although *Chlamydiae* are sensitive to many antibiotics, treatment failures rates range from 5 to 23% [Horner 2012]. Majority of cases can be explained by post-treatment reinfection or lack of treatment compliance but some of them are linked to therapeutic failures, such as resistance and persistence in the case of *C. trachomatis*.

In an era of increasing bacterial resistance to antibiotics, resistance is a rare phenomenon in *C. trachomatis*. However, clinical treatment failures attributed to multidrug-resistant *C. trachomatis* strains have however been described [Mestrovic 2018] [Forslund 2017]. *C. trachomatis* is often present as a co-infection (e.g. with *Neisseria gonorrhoeae* or *Mycoplasma genitalium*) and in these pathogens, resistance to the commonly used

anti-chlamydial therapies (macrolides, tetracyclines) is increasingly common [Forslund 2017] [Unemo 2014]. Hence, a drug targeted to *Chlamydia* may reduce the selection of antibiotic resistance in the other pathogens.

Moreover, during treatment, bacteria can "persist" in a form less sensitive to antibiotics, the aberrant body [Witkin 2017]. Once the treatment is completed, persistent bacteria could then resume its development cycle explaining treatment failure in some patients. This persistent form could remain for several years in infected tissues causing recurrent infections, chronic inflammation and tissue fibrosis. For instance, Jackie Sherrard *et al* recently described "a case of a 22 years-old woman with genital *C. trachomatis* infection, which persisted for 8 months despite treatment with four 1g doses of azithromycin and both a 7-day and 14-day course of doxycycline [Sherrard 2019]. She denied any sexual contact during this time. Tests for other infections including extragenital sites were negative".

As illustrated with this example, treatment failures are the consequence of several parameters including a lack of antibiotic sensitivity of persistent forms of *Chlamydiaceae* but also to too low intracellular concentrations of the conventionally prescribed drugs. Resistance, reinfection, too early post-infection antibiotic treatment, poor compliance with treatment can also explain clinical failures in *C. trachomatis*-infected patients.

Any strategy improving antibiotic penetration in bacterial inclusions and targeting persistent form would increase treatment efficacy. All these elements highlight the importance of seeking new antibiotics and / or new drug delivery strategies against *Chlamydiaceae*.

4. Inhibitors of *C. trachomatis* growth

In 2015, Kohlhoff *et al.* published an update of available treatments to fight this infection [Kohlhoff 2015]. Beside, reviews have been proposed to focus on certain kinds of inhibitors of *C. trachomatis*, such as inhibitors of its T3S system [Dumoux 2015] [Dai 2014] while Potroz *et al.* reviewed efficient natural compounds [Potroz 2015]. Many strategies have been proposed to try to inhibit the growth of this pathogen. We reviewed the literature to give a global and comprehensive overview in the field of inhibitors of *C. trachomatis* published in the last decade:

4.1. The bacterial targets

4.1.1. The chlamydial lipooligosaccharide biosynthesis pathway

The lipo-oligosaccharide (LOS) is a highly conserved molecule between chlamydial species and one of the main lipid components of bacterial outer membranes, making it essential for cell viability in most Gram-negative bacteria. LOS has been described as essential for the production of EBs in *C. trachomatis* [Nguyen 2011]. Recently, Cram *et al.* evaluated the sensitivity of other bacterial species to LPC-011 (Figure 1.3), a potent inhibitor of LpxC, an enzyme implicated in the LOS biosynthesis pathway [Cram 2017]. The authors demonstrated that LOS biosynthesis is an important step in the development cycle of members of the genus *Chlamydia* (*C. abortus*, *C. caviae*, *C. muridarum*, *C. suis* and *C. trachomatis*), with however differences between the various species of *Chlamydia* tested: the minimum effective concentration of the drug, for instance.

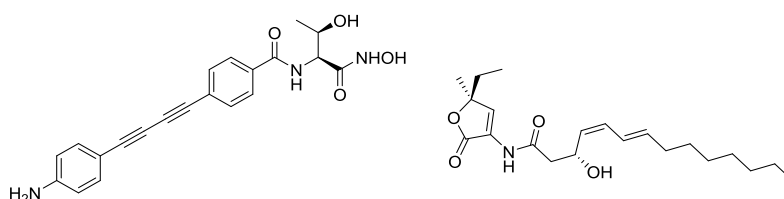


Figure 1.3. LPC-011 (left) and PEG-2S (right)

4.1.2. The Na⁺-translocating NADH: ubiquinone oxidoreductase

A major primary Na⁺ pump, the Na⁺-translocating NADH: ubiquinone oxidoreductase (Na⁺-NQR), is encoded by *Chlamydiae* and generates a gradient of Na⁺ as a direct source of energy for several pathogenic bacteria such as *C. trachomatis*, making this protein a putative interesting pharmacological target. PEG-2S (Figure 1.3), an analogue of korormimicin, a well-known Na⁺-NQR inhibitor, was used to validate this hypothesis. This compound presents an half-minimal inhibitory concentration (MIC₅₀) of 1.76 nM in an enzymatic assay and a chlamydicidal activity of 0.7 μM in infected HeLa cells [Dibrov 2017].

4.1.3. The chlamydial virulence factors

Approaches consisting in targeting bacterial virulence instead of growth would preserve the integrity of the host cells while decreasing the bacterial pathogenicity.

- ***The macrophage infectivity potentiator (MIP)***

MIP, a protein associated to the virulence of several bacterial pathogens, was first characterized in *Legionella pneumophila* and exhibits peptidyl-prolyl *cis/trans* isomerase (PPIase) activity. A homologous MIP-like protein (Ctr-MIP) has also been identified in *C. trachomatis* and considered as an interesting target to decrease the bacterial virulence. Reimer *et al.* synthesized pipercolic acid derivatives, without immunosuppressive properties, as efficient inhibitors against various MIPs, including Ctr-MIP, and affecting both the bacteria developmental cycle and the infectious progeny [Reimer 2016]. PipN3 and PipN4 (Figure 1.4), the most powerful compounds, inhibit the PPIase activity with an half-maximal inhibitory concentration (IC₅₀) values of 241 nM and 64.6 nM, respectively, in correlation with their ability to inhibit the bacterial growth.

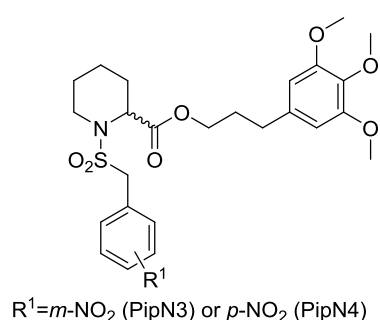


Figure 1.4. The pipercolic acid derivatives

- ***The type III secretion system (T3SS)***

T3SS is highly conserved in many Gram-negative pathogenic bacteria, such as *C. trachomatis*. This system translocates pathogenicity factors from the bacteria directly into the cytoplasm of the infected cells, as a molecular syringe. Inhibitors of this system have been fully reviewed. The article proposed by McShan *et al.* in 2015 is an exemple [McShan 2015]. Slepkin and *al.* proposed, in 2007, T3SS inhibitors belonging to the salicylidene acylhydrazide family with anti-chlamydial activity. Compounds were screened for their ability to inhibit the bacterial developmental cycle of *C. trachomatis* serovar D at 20 and 50 μM in McCoy and HeLa cells [Slepkin 2007]. They also demonstrated that this antibacterial activity was reversed by addition of exogenous iron supplied as both Fe²⁺ (ferrous sulfate) or Fe³⁺ (FeCl₃ or holotransferrin), with an effect on the T3SS gene expression during the *Chlamydia* biological cycle. However, a mechanism of action through a direct inhibition of T3S system was not clear as effect of those compounds was reversed by iron. These compounds were then considered as putative vaginal microbicides and were tested

against a lymphogranuloma venereum strain of *C. trachomatis* serovar L2, *Neisseria gonorrhoeae*, hydrogen peroxide-producing *Lactobacillus crispatus* and *Lactobacillus jensenii* [Chu 2010]. Among them, INP0341 (Figure 1.6), an inhibitor of both *C. trachomatis* with a minimal bactericidal concentration (MBC) of 25 μM and *N. gonorrhoeae* (MBC of 6.3 μM), not cytotoxic in HeLa cells and without action on the normal vaginal flora, was found to be active *in vivo*. INP0341 was then selected for formulation and further investigations in mice, as a potential vaginal microbicide [Slepenkin 2011] [Pedersen 2014]. The formulation proposed (1 mM INP0341, 1.6 wt% Cremophor ELP and 1.5 wt% poly(acrylic acid)) attenuated the vaginal challenge performed with *C. trachomatis* serovar D.

Bao *et al.*, in 2014, designed new benzylidene acylhydrazides without any iron-chelating properties, to separate iron chelation effect from inhibition of T3SS [Bao 2014]. Among them, CF001 did not inhibit T3S system in *Yersinia pseudotuberculosis* but demonstrated an antichlamydial effect against *C. muridarum* and *C. trachomatis* L2 insensitive to the addition of iron. These benzylidene acylhydrazides also failed to inhibit lactobacilli at concentrations effective against *Chlamydiae* and can therefore be considered as a novel class of antichlamydia molecules. Recently, Zhang *et al.* reported SF1 to SF3 as analogues of CF001 and CF002 (Figure 1.5) with increased antichlamydial effects at minimal chlamydicidal concentrations (MCC=50 μM) and no toxicity to lactobacilli. Among them, SF3 was well tolerated by mammalian cells and generates a lower rate of mutation than the parent molecules, CF001 and CF002 [Zhang 2017].

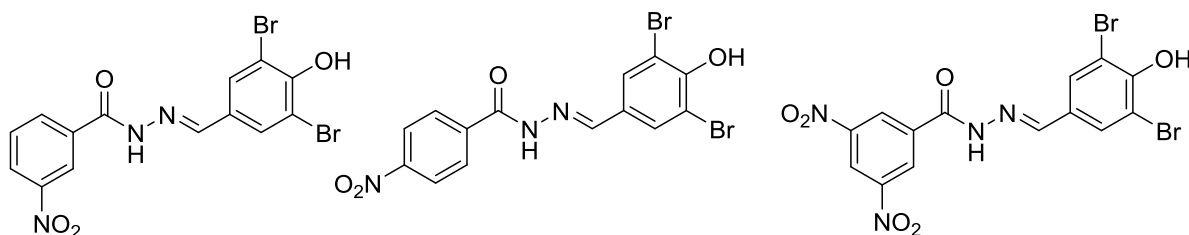


Figure 1.5. CF001 (left), CF002 (centre) and SF3 (right).

Later, Zigangirova *et al.* described several T3SS inhibitors, with aromatic hydrazide moieties. CL-55 (Figure 1.6) was selected as the most potent compound on the basis of its low toxicity on eukaryotic cells and high activity against *Chlamydiae*. Indeed, no *Chlamydia*-inclusion was observed when infected-cells were treated with 50 μM of CL-55 [Zigangirova 2012]. Moreover, in an *in vitro* penicillin-induced persistence model, the addition of CL-55 to the growth medium led to the lysis of the aberrant bacterial cells and prevented them from back differentiation into RBs [Zigangirova 2016]. This compound also suppressed both acute and

chronic infection in DBA/2 mice intravaginally infected with *C. trachomatis* serovar D [Koroleva 2015].

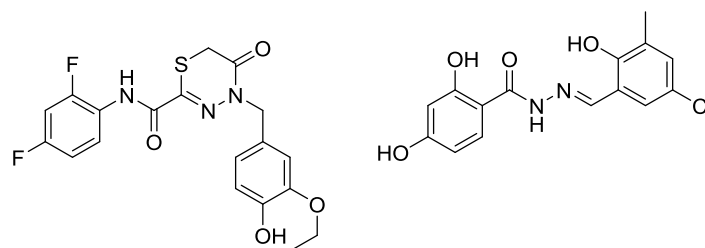


Figure 1.6. CL-55 (left) and INP0341 (right).

In 2012 also, INP1750 (Figure 1.7), an 8-hydroxyquinoline derivative, was identified by Enquist *et al.* after screening 17,500 compounds with the aim of finding new T3SS inhibitors structurally different from those already described [Enquist 2012]. The activity of this inhibitor against *C. trachomatis* was also investigated and a minimal inhibitory concentration (MIC) of 25 μM in HeLa cells was measured. A structure-activity relationship led to the synthesis of INP1855 with a MIC of 3.13 μM (Figure 1.7).

In 2013, in an attempt to find antichlamydia natural products, Zetterström *et al.* explored the effect of (-)-hopeaphenol (Figure 1.7), a polyphenolic compound isolated from Papua New Guinean rainforest plants, *Anisoptera thurifera* and *A. polyandra*, on the T3SS in *Y. pseudotuberculosis*, *P. aeruginosa* and *C. trachomatis* [Zetterström 2013]. They found that (-)-hopeaphenol presents an IC_{50} of 6.6 μM . This T3SS inhibitor is also active against *C. trachomatis* but the inhibition requires the pre-treatment of the EBs with (-)-hopeaphenol before infection of HeLa cells, otherwise no inhibition is observed, suggesting that this compound targets EBs entry into the host cells.

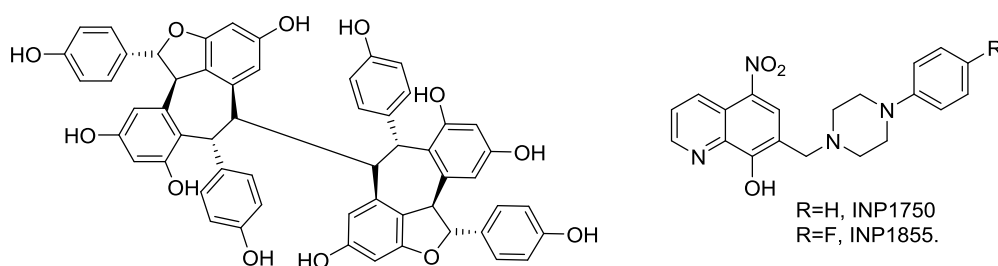


Figure 1.7. (-)-Hopeaphenol (left) and INP derivatives (right).

In 2015, Sunduru *et al.* proposed salicylidene acylhydrazides (Figure 1.8) with a multi-activity profile:

- T3SS inhibitors in *Yersinia pseudotuberculosis*, another Gram-negative pathogen, with iron-chelating properties,
- Antichlamydial activity through an unclear mechanism [Sunduru 2015].

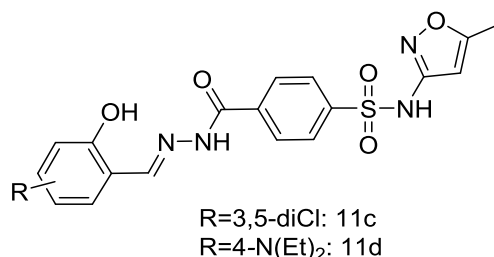


Figure 1.8. Salicylidene acylhydrazides synthesized by Sunduru *et al.*

In 2017, Grishin *et al.* aimed to discover T3SS inhibitors using a virtual screening. They particularly focused on T3SS ATPase, a target validated by several previous studies to obtain this kind of inhibitors [Grishin 2017]. A series of *N*-arylbenzylamines was synthesized and the most potent compounds W1227933 and W1774182 were able to decrease the number of chlamydial inclusions by 70% and 90% respectively, when added at 50 μ M and to block Chlamydia protein translocation through T3SS (Figure 1.9).

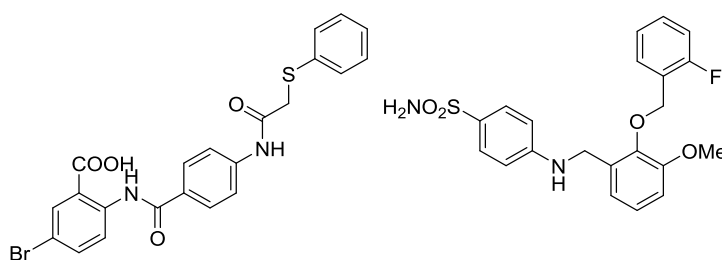


Figure 1.9. W1227933 (left) and W1774182 (right).

- ***The highly conserved protease HtrA***

This protease has been described in several pathogens, including *C. trachomatis* (CtHtrA), in which it plays a role as a bacterial cell-associated protease and a secreted virulence factor [Marsh 2017]. Gloeck *et al.* screened *in vitro* 1090 serine inhibitors against CtHtrA protease activity and discovered JO146 (Figure 1.10), a selective inhibitor with an IC₅₀ of 12.5 μ M. At the cellular level, the treatment of infected cells led to the complete death of *C. trachomatis* through a loss of cell morphology and a decrease in the inclusion size, demonstrating the important role of this protein in the bacterial developmental cycle [Gloeck 2013]. Moreover, when added to infected-cells during either reversion from penicillin persistence and recovery from heat stress, JO146 is bactericidal as well [Ong 2013]. This compound also demonstrated

an *in vivo* activity against *C. muridarum* in mice, after vaginal administration. Later, Ong *et al.* established its ability to also inhibit *C. trachomatis* clinical isolates from women, demonstrating its pharmacological relevance [Ong 2015].

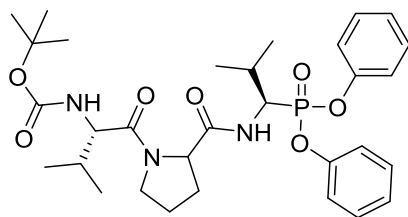


Figure 1.10. JO146.

4.1.4. Disruption of the glucose 6-phosphate metabolic pathway

Engström *et al.* identified KSK 120 (Figure 1.11) which inhibits of *C. trachomatis* infectivity by preventing the bacteria from acquiring glucose 6-phosphate, its principal source of carbon [Engström 2014]. This deficiency relies on several point mutations in genes involved in the metabolic pathway generated after *C. trachomatis* is serially passed with the drug. Later, Good *et al.* proposed an optimization of this inhibitor by the synthesis of KSK213 (Figure 1.11) with an half-maximal effective concentration (EC_{50}) ≤ 100 nM and no observed toxicity on the human commensal flora at 50 μ M [Good 2016].

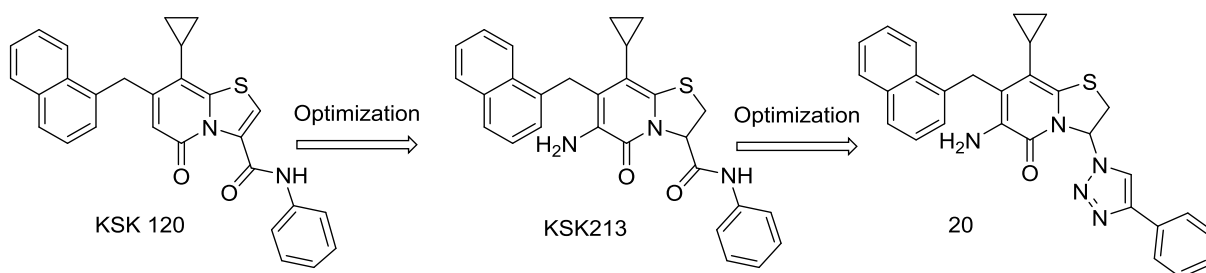


Figure 1.11. KSK 120, the corresponding optimized compound KSK213 and the triazolo-derivative 20.

At the end of 2017 and to complete their study on KSK213, Good *et al.* first proposed amide isosteres and finally discovered compound 20, a potent C-3 1,2,3-triazolo inhibitor with an $EC_{50} \leq 20$ nM (Figure 1.11) [Good 2017].

4.1.5. Bacterial DNA synthesis

Like a wide range of bacteria, *C. trachomatis* is sensitive to quinolones whose antibacterial activity relies on the inhibition of bacterial DNA synthesis. The *in vitro* activity of AZD0914

(Figure 1.12), a DNA gyrase inhibitor, has been measured in Hep-2 cells infected with ten isolates of *C. trachomatis* and compared to the activity of commercially available antibiotics [Kohlhoff 2014]. Its MBC, the lowest antimicrobial concentration that results in absence of inclusion in host cells, is 0.125-1 $\mu\text{g/mL}$ which is comparable to the Chlamydia MBC of levofloxacin and doxycycline but lower than MBC of azithromycin.

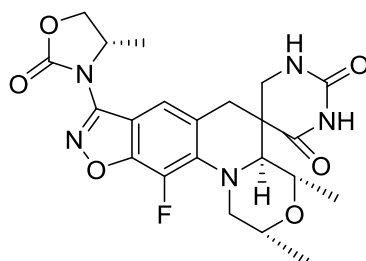


Figure 1.12. AZD0914.

C. trachomatis class Ic ribonucleotide reductase (RNR) belongs to a class of enzymes that catalyse conversion of ribonucleotides to deoxyribonucleotides for *de novo* DNA synthesis and repair. In 2011, Öhrström *et al.* investigated the putative inhibitory effect of six short peptides derived from the C-terminus of *C. trachomatis* R2, a protein closely related to *C. trachomatis* class Ic RNR [Öhrström 2011]. Only four oligopeptides corresponding to the full C-terminus of R2 were able to inhibit RNR activity in an enzymatic assay, with IC_{50} of 190-600 μM . These results indicate that the Chlamydial RNR can indeed be considered as a pharmaceutical target.

4.1.6. The serine protease CPAF (Chlamydia protease-like activity factor)

When secreted by *C. trachomatis* in the host cell through T3SS, CPAF is involved in the cleavage of several host proteins involved in cell regulation especially host cell apoptosis. This protease is also involved in inclusion development and can therefore be considered as an interesting target for drug synthesis. In 2011, Bednar *et al.* developed peptide 4 [H-SLFYSPMVPHFVAELRNHYATSGLKRRRRRRRRR6-NH₂], a CPAF inhibitor derived from its zymogene, having nanomolar affinity in an *in vitro* assay for CPAF hydrolytic activity [Bednar 2011]. This inhibitory effect was also observed when infected HeLa cells were treated with the peptide, demonstrating its ability to penetrate the plasma cell membrane but also to target CPAF *in cellulo*.

In 2011 as well, Christian *et al.* also proposed to target CPAF using WEHD-fmk, another caspase-1-inhibitor. Indeed, this peptide is able to block the lysis of all CPAF substrates and was used to prevent the Golgi apparatus from fragmentation, a required step for chlamydia inclusion development during infection [Christian 2011].

In 2012, in order to limit reactive arthritis induced by *C. trachomatis* infection, Inman *et al.* studied the antimicrobial activity of nafamostat mesylate (Figure 1.13), a serine protease inhibitor clinically used in Asia as an anti-inflammatory agent [Chang 2009]. When it was incubated with infected fibroblast monolayers at a dose of 50 µg/mL, no inclusions were observed. In rats, swelling of infected knee joints was significantly reduced in animals daily-treated with this molecule. This observation was associated with a decrease in the Chlamydia load in the joints [Inman 2012].

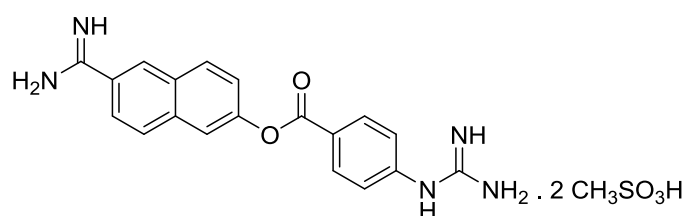


Figure 1.13. Nafamostat mesylate.

4.1.7. The bacterial peptide deformylase (PDF)

Identifying host factors essential for the bacterial development led Balakrishnan *et al.* to evaluate the putative inhibitory effect of metalloprotease inhibitors on *C. trachomatis* serovar L2 growth in HeLa cells [Balakrishnan 2006]. They identified two hydroxamic acids, GM6001 and TAPI-0 (Figure 1.14), without any action on the growth of other common bacteria (*E. coli*, *L. delbrueckii* and *S. enterica*) and investigated their biological target. After several passages, GR10, a L2 mutant, was selected and gene sequencing enabled the discovery of the bacterial target of these compounds: PDF, a chlamydial metalloprotease essential for protein maturation that catalyses the removal of the *N*-formyl group from newly synthesized proteins in bacteria [Bao 2011]. GM6001 was then selected for *in vivo* studies in the murine genital *C. muridarum* infection model where its topical application greatly decreases *C. muridarum* loading, without affecting both the vaginal mucosal cell and the vaginal *Lactobacillus plantarum* viability [Balakrishnan 2009].

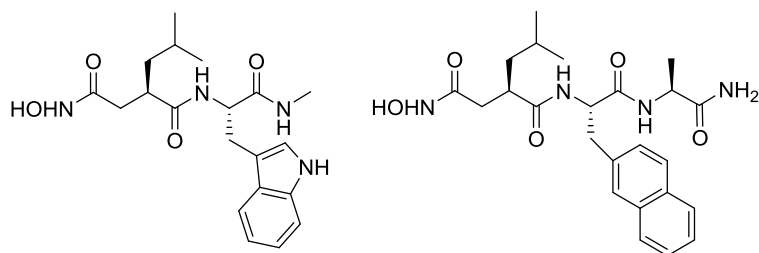


Figure 1.14. GM6001 (left) and TAPI-0 (right).

4.1.8. The bacterial ribosome

Bitespiramycin, a genetically engineered macrolide produced by *Streptomyces spiramyceticus* F21, was evaluated for its ability to inhibit *C. trachomatis in cellulo* [He 2017]. According to the study proposed by He et al., this compound presents similar MIC (0.064 $\mu\text{g/mL}$) to those of Azithromycin (0.032-0.5 $\mu\text{g/mL}$) but with the advantage to be easy to produce.

4.1.9. The type II fatty acid synthesis (FASII) pathway

Marwaha *et al.* described sulfamethoxazole and sulfafurazole derivatives, as compound 18 (Figure 1.15), with activity against *C. trachomatis* L2 (MIC=6 μM) [Marwaha 2014]. This antibacterial effect seems to be selective to *C. trachomatis* since no inhibition of *C. pneumoniae* was observed with this molecule. This family of compounds does not affect folate synthesis, in contrast to sulfonamide antibiotics and represent an interesting starting point, as they also follow Lipinski's rules of five. In 2017, Mojica *et al.* discovered that these acylated sulphonamides act as inhibitors of *Chlamydia* FASII pathway, which is responsible for the synthesis of the fatty acids required for bacterial membranes. They also demonstrated that these compounds directly interact with the 3-oxoacyl-acyl carrier protein synthase II (FabF) enzyme, *in vitro*, thus specifying its mode of action [Mojica 2017].

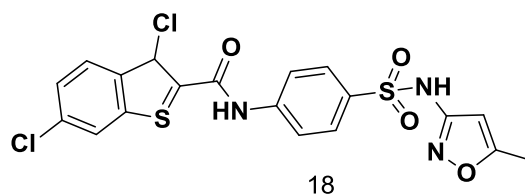


Figure 1.15. Compound 18.

4.2. The host cell targets

C. trachomatis must acquire nutrients and energy from the host cell to develop. Targeting host components essential for bacterial replication has also been proposed. Several examples are presented below.

4.2.1. Long-chain Acyl-CoA synthetases (ACSLs)

ACSLs, a family of isoenzymes, are directly responsible for host lipid biosynthesis through the activation of host fatty acids into acyl-CoA, an essential metabolite in lipid synthesis. Recuero-Checa *et al.* demonstrated that *C. trachomatis* recruits ACSLs into the bacterial inclusion early in infection, making this family of enzymes important for the development of the pathogen [Recuero-Checa 2016]. Indeed, inhibitors of ACSLs, such as triacsin C or 2-fluoropalmitic acid, block *C. trachomatis* growth in a dose-dependent manner.

4.2.2. Sphingolipid trafficking from the host cell Golgi apparatus into the bacterial inclusions

In 2008 Shivshankar *et al.* studied a plant-derived compound, Rottlerin (Figure 1.16), already described for its anticancer activity and ability to inhibit various protein kinases. Rottlerin also completely inhibits *C. trachomatis* growth at a concentration of 1 μM in HeLa 229 cells [Shivshankar 2008]. Host cell reactions essential for chlamydia development are blocked by this compound without host cell toxicity at this concentration. This molecule negatively affects sphingolipid trafficking from the Golgi apparatus to chlamydial inclusions. Its inhibitory effect is not specific to *C. trachomatis* as all *Chlamydia* species are also sensitive to Rottlerin. In 2012 Lei *et al.* demonstrated that the inhibition mediated by Rottlerin is independent of p38-regulated/activated protein kinase, a known target of this molecule [Lei 2012].

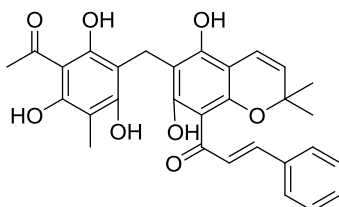


Figure 1.16. Rottlerin.

4.2.3. Indolamine-2,3 dioxygenase (IDO1)

Under particular conditions, i.e. in the presence of interferon- γ (IFN- γ), some antibiotics or nutrient deprivation, *C. trachomatis* enters into a reversible persistence form characterized by the formation of large and morphologically aberrant RBs (Abberant Bodies) into non-growing inclusions. This state would provide a bacterial reservoir and lead to immune evasion. The back differentiation into normal EBs is generally allowed by the withdrawal of persistence inducer. In human epithelial cells, IFN- γ induces the expression of indolamine-2,3 dioxygenase (IDO1), an enzyme catabolizing tryptophan, an essential amino-acid for the auxotrophic bacteria that does not express Tryptophan synthase. Indeed, tryptophan depletion induced by this enzyme is responsible for the limitation of the growth of *C. trachomatis* ocular strains in the presence of IFN- γ . In 2011, Ibane *et al.* proposed a strategy to eradicate persistent forms of *C. trachomatis* using a specific inhibitor of IDO1, levo-methyl-tryptophan (L-1MT) [Ibane 2011]. While this inhibitor does not alter the normal development of *C. trachomatis*, it decreases IDO1 activity in IFN- γ -exposed cells, delaying tryptophan depletion during the bacterial cycle and limiting the production of aberrant bodies. Additional studies suggested that this amino-acid depletion inhibits IFN- γ -induced *C. trachomatis* persistence. The authors also demonstrated that L-1MT increases the sensitivity of persistent forms of *C. trachomatis* to doxycycline, an antibiotic currently used to treat chlamydial infections.

4.3. The unknown targets

Other compounds present an antichlamydial activity *in cellulo* without any mechanisms of action being described. For instance, isoflavones, produced by plants, are preconized to limit postmenopausal syndromes in women. In 2014 Hanski *et al.* established the antichlamydial activity of biochanin A (Figure 1.17) against both *C. trachomatis* and *C. pneumoniae*, illustrating that this compound can decrease the *C. trachomatis* serovar L2 inclusion size and the infectivity with an IC₅₀ of 62 μ M, without showing any host cell toxicity [Hanski 2014].

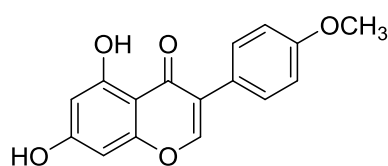


Figure 1.17. Biochanin A.

In 2018, we published this global overview of the prospective drug targets and the related inhibitors of this human pathogen proposed between 2007 and 2017 [Serradji 2018].

Since then, new molecules have been proposed to limit the growth of *Chlamydia*. Several examples, published in the last two years, are presented below, illustrating the diversity of biological targets exploited (Figure 1.18).

Gallegos *et al.* hypothesized that a heparin sulfate-like cell surface receptor is involved in *Chlamydia* entrance into host cells. They synthesized sulfated pentagalloyl glucoside (SPGG) as sulfated and sulfonated mimics of heparin sulfate and tested their ability to block *Chlamydia* (*C. muridarum* and *C. trachomatis* serovar LGV) endocytosis [Gallegos 2019]. Indeed, sulfated polyanion SPGG has multiple sulfate groups mimicking the sulfated glycosaminoglycan chains present on host cell surfaces. Their results show that SPGG had inhibitory activity against *C. trachomatis* LGV strain with a significantly reduction of infection down to 20% at 218 µg/mL of SPGG.

Corallopyronin A (CorA), isolated from *Coralloccoccus corralloides* [Irschik 1985], is a polyketide-derived α -pyrone antibiotic that inhibits the bacterial DNA dependent RNA polymerase, leading to inhibit bacterial growth. CorA has a broad-spectrum antibacterial activity, including Gram-positive [Irschik 1985] and Gram-negative [Schiefer 2012] [Kock 2018]. Shima *et al.*, in 2018, shown that CorA is not only effective against *C. trachomatis* (MIC 0.5 µg/mL) but also eradicates rifampicin-resistance *C. trachomatis* serovar L2 *in vitro* [Shima 2018]. In 2019, Loeper *et al.* reported high activity of CorA against *C. trachomatis* in an *ex vivo* human fallopian tube model with MIC 1 – 2 µg/mL.

In support of the important role of selenium in bacteria, Mosolygó *et al.* evaluated the effects of selenocompounds on growth of a panel of bacteria. At 0.25 µM, some of them inhibited more than 50% of the growth of *C. trachomatis* D [Mosolygó 2019].

Agbowuro *et al.* designed analogues of JO146, a previously described selective and irreversible *C. trachomatis* high temperature requirement A (CtHtrA) inhibitor. They identified a potent compound bearing a diphenylphosphonate moiety however less active than JO146 which remains the most active inhibitor (IC₅₀=12.5 µM) in terms of cellular performance [Agbowuro 2019].

Sadhasivam *et al.* proposed new inhibitors of *C. trachomatis* L,L-diaminopimelate aminotransferase (CtDAP-AT), a potential drug target due its essential role in cell survival and host nonspecificity. They identified NSC_5485

(1,3-bis((7-chloro-4-quinoliny)amino)-2-propanol) as a compound bactericidal against a broad spectrum of *C. trachomatis* strains [Sadhasivam 2018].

Prusty *et al.* identified human serine peptidase inhibitor, PI15, as a potential host factor involved in the regulation of CPAF, a chlamydial protease expressed during the replicative phase of the chlamydial developmental cycle. They also demonstrated that bacterial proteases like CPAF are important for the normal development of *Chlamydia* [Prusty 2018].

Grishin *et al.* proposed inhibitors against a Chlamydial-protein never targeted before, *C. trachomatis* ATPase SctN, an important T3SS (type III secretion system) component involved in bacterial virulence. They identified two compounds that can block protein translocation through T3SS and inhibit chlamydial survival at 50 to 100 μM [Grishin 2018].

Through its actin remodelling and anti-inflammatory properties, capsaicin, an active component of chili pepper, was proposed by Yamakawa *et al.* to control chlamydial growth in a dose-dependent manner but without the requirement of host cell protein synthesis [Yamakawa 2018].

Saleeb *et al.* synthesized a library of bio-inspired compounds with dihydrobenzofuran scaffolds. Some of them have an activity of lower than 3 μM and can therefore serve as a starting point for obtaining even more active molecules [Saleeb 2018].

Finally, Slade *et al.* focused on the isoprenoid synthesis during the chlamydial development using fosmidomycin, an antibiotic targeting Dxr (1-deoxy-D-xylulose 5-phosphate reductoisomerase), an essential enzyme for intracellular bacteria. *Chlamydia*-infected cultures exposition to fosmidomycin led to a significantly reduced EBs production. However, this inhibition of isoprenoid synthesis is not lethal to *C. trachomatis*, but instead induces persistence [Slade 2019].

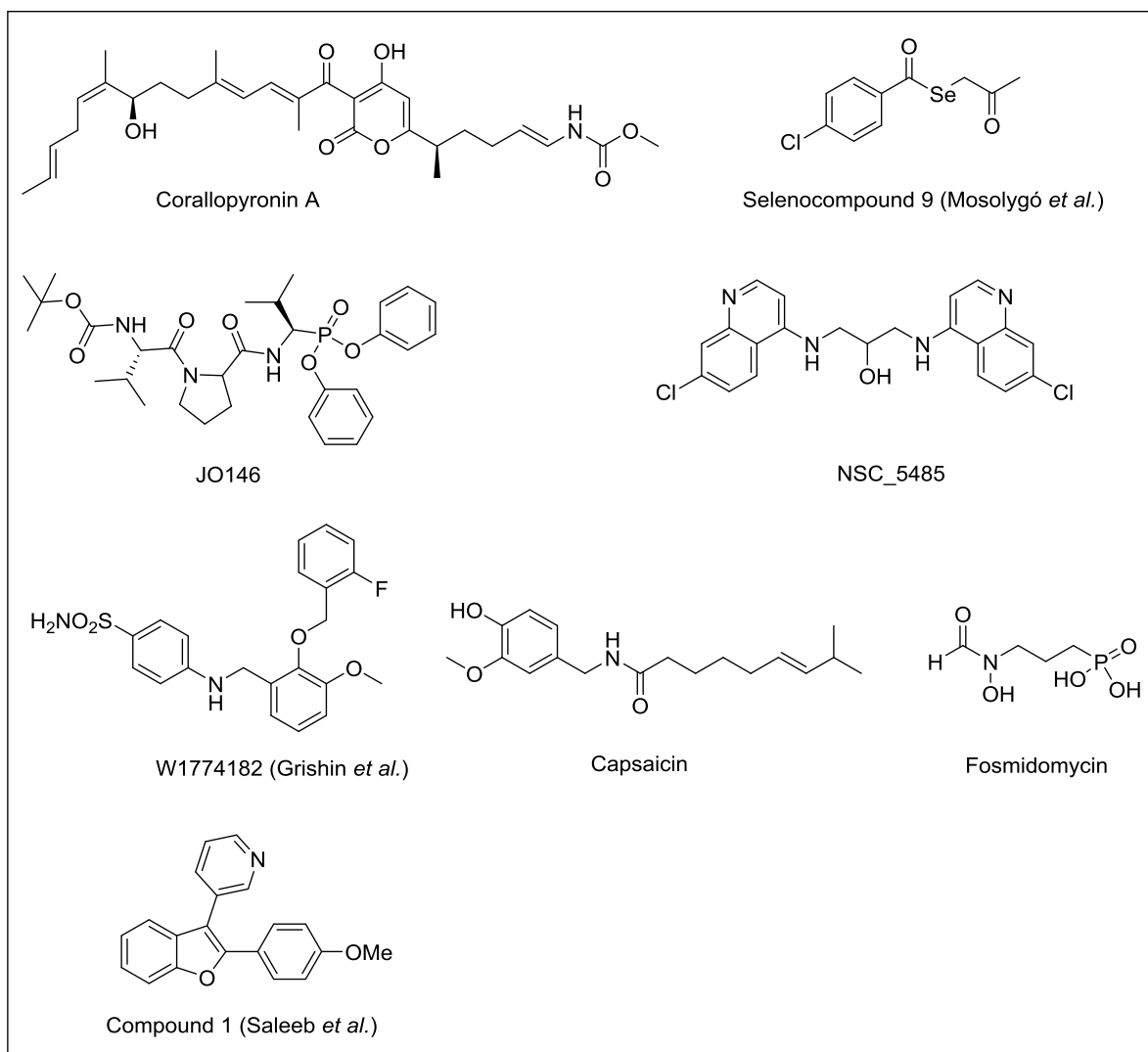


Figure 1.18. Some recently published *C. trachomatis* inhibitors.

The search for compounds raised against *C. trachomatis* therefore remains very active, in particular because of the huge public health and therefore economic challenges.

Inhibitors blocking the iron supply of *Chlamydia* have also been proposed.

5. Iron chelators as bacterial growth inhibitors

5.1. Iron chelators

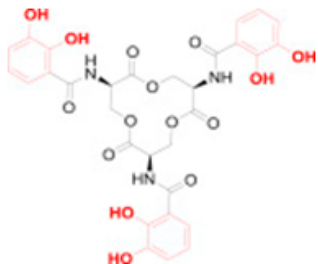
Iron chelators are ligands that have a capacity to bind iron ions through at least two coordinate bonds. Different coordinate spheres can be formed by different types of atoms as oxygen, nitrogen, sulphur. Different number of coordinate bonds (2, 3, 4, 6, etc) were classified into different denticity (bidentate, tridentate, tetradentate, hexadentate, etc). The affinity of an iron chelator is defined by its stability constant, $\log \beta$. In physiological conditions, the

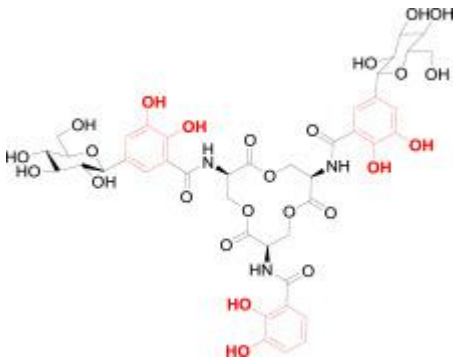
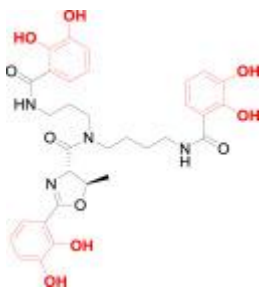

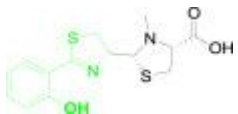
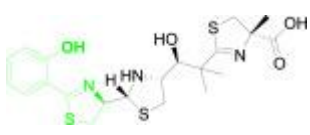
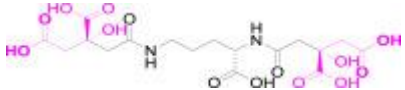
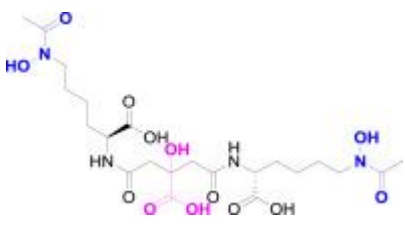
effectiveness of a chelator to withdraw Fe(III) from the environment is better achieved by comparison of the respective $p\text{Fe(III)} = -(\log[\text{Fe(III)}])$ values, which are calculated considering pH 7.4, a total ligand concentration of 10^{-5} M and a total Fe(III) concentration of 10^{-6} M [Raymond 1984] in opposition to the standard thermodynamic conditions considered for the determination of the stability constant ($\log \beta$) [Dhungana 2007].

5.2. Bacterial iron homeostasis disruption

Iron is critical for bacterial cell growth and survival. Microorganisms acquire iron by capturing the metal with ligands chelating it called siderophores (Table 1.1). Siderophores (from the Greek sideros = iron and pherien = transport) are produced by bacteria, fungi and certain plants in order to scavenge iron from the environment. These low molecular weight compounds (500–1500 Daltons) have high affinity and selectivity for Fe(III) ($\log \beta > 10^{30}$). The cell production of one or more siderophores takes place in response to iron deficiency conditions, i.e. when the intracellular metal concentration falls below 10^{-6} M, the concentration critical for bacterial growth [Miethke 2007]. They are either excreted to internalize extracellular iron, or are produced intracellularly to store iron in the cell [Piña-Vázquez 2013]. Their role therefore intervenes in the iron acquisition system by dissolving the latter on the one hand, and by transporting it in cell, on the other hand. In general, most siderophoric transport systems are highly specific [Glasauer 2013]. However, many bacteria can use exogenous siderophores (or xenosiderophores) as a source of iron [Miethke 2013]. These molecules have affine functions for the metal, mainly catechol or hydroxamic acid. Examples are provided in Table 1.1.

Table 1.1. Type, name, chemical structure, and main sources of siderophore [Kong 2019].

Siderophore type	Name	Structure	Source
Catecholate	Enterobactin		<i>P. aeruginosa</i> , <i>K. pneumoniae</i> , <i>E. coli</i> .

Siderophore type	Name	Structure	Source
	Salmochelin		<i>Salmonella</i> , <i>E. coli</i> .
	Agrobactin		<i>Agrobacterium tumefaciens</i>
Hydroxamate	Ferrichrome		<i>Shigella flexneri</i> , <i>P. aeruginosa</i>
Phenolate	Pyochelin		<i>P. aeruginosa</i>
	Yersiniabactin		<i>K. pneumoniae</i>
Carboxylate	Staphyloferrin A		<i>S. aureus</i>
Mixed	Aerobactin		<i>Salmonella</i> , <i>Yersinia</i> , <i>Shigella</i> , <i>K. pneumoniae</i> ,

Siderophore type	Name	Structure	Source
			<i>E. coli.</i>
	Carboxymycobactins		<i>M. tuberculosis</i>
	Pyoverdine		<i>P. aeruginosa</i>

In support of the iron requirements of microorganisms, several strategies have been developed to inhibit their growth by blocking iron supply.

5.2.1. Iron depletion

This first strategy consists in reducing the iron concentration in the environment of the pathogen using chelators, in particular artificial compounds, which will not be used as a source of iron by the microorganism. It is therefore a competition with pre-existing siderophores. In order to be competitive, the iron chelators must have a sufficiently different structure from the bacteria's natural siderophores. Indeed, an important similarity would lead to recognition of chelators by siderophoric receptors of the microorganism and would promote its growth. Several reviews describe that siderophores possess antimicrobial properties which can be used against number of microbes [Khan 2017] [Negash 2019].

Beside, iron chelators, traditionnaly used to cure iron overload in humans, were also proposed to inhibit bacterial growth of various pathogens. For instance, Kim *et al.* showed antibacterial activity of deferoxamine in 2008 [Kim 2009]. Deferoxamine was incubated with *S. epidermidis* KCTC1917 and *S. saprophyticus* KCTC3345 strain at 37°C for 48 hours in presence of iron. Then, they observed that the growth of both bacterial strains was inhibited (Figure 1.19).

élément sous droit, diffusion non autorisée

Figure 1.19. Examples of responses of *Staphylococci* to deferoxamine [Kim 2009].

Mitchell *et al.* evaluated antibacterial activity of deferoxamine and deferiprone ApoL1 in cation-adjusted Mueller-Hinton broth (a rich mixture with excess iron, carbon sources and other cofactors far exceeding the concentration existing in Human), against different bacterial strains (Table 1.2) [Mitchell 2012]. They observed that deferiprone inhibited the growth of some strains of *P. aeruginosa* and *K. pneumoniae* as well as *E. coli* and *A. baumannii*, while no effect was observed on *S. aureus*. In contrast, deferoxamine did not affect bacterial growth (MIC > 512 µg/mL for all bacteria tested).

Deferasirox (DFRA), a tridentate ligand which binds iron in a 2:1 ratio [Steinhauser 2004], presents an antibacterial activity against *Prevotella intermedia*, a black-pigmented anaerobic Gram-negative bacterium. The colony formation of this bacterium was completely inhibited on Brucella blood agar by DFRA with MIC and MBC values of 0.16 mg/mL [Moon 2013].

Other examples of therapeutic applications of siderophores have been explored and have recently been reviewed [Khan 2018] [Saha 2016] [Wilson 2016].

Table 1.2. MICs of iron chelators (deferoxamine and deferiprone ApoL1) against ATCC type strains grown [Mitchell 2012].

Bacterial species	Strain no.	MIC of iron chelator (µg/ml)	
		DFO	ApoL1
<i>A. baumannii</i>	17978	>512	128
<i>A. baumannii</i>	19606	>512	128
<i>S. aureus</i>	25923	>512	>512
<i>S. aureus</i>	43300	>512	>512
<i>P. aeruginosa</i>	PAO1	>512	256
<i>P. aeruginosa</i>	27853	>512	>512
<i>K. pneumoniae</i>	BAA-2146	>512	256
<i>K. pneumoniae</i>	700603	>512	512
<i>E. coli</i>	35718	>512	512
<i>E. coli</i>	43888	>512	512

5.2.2. The "Trojan Horse" strategy [Kong 2019]

Some bacteria express receptors that specifically recognize the iron complexes of their own siderophores. To ensure competitive growth, bacteria generally have machinery to recognize and transport iron-iron complexes also produced by other organisms. Over the course of evolution, some bacteria have learned to exploit this "usurpation" path to eliminate competing bacteria with which they compete in their biotope. To do this, they deliver antibiotics by attaching a toxic substance to siderophores. These compounds are siderophore-antibiotic conjugates called sideromycins (Figure 1.20). The siderophore part of the compound can capture iron and is recognized by a siderophore-iron complex acquisition system, while the other part carries an antibiotic activity which uses the siderophore as a "Trojan horse" and exploits the iron acquisition system as a gateway into the cell. There are several natural siderophore-antibiotic conjugates such as albomycin, ferrimycin, danomycin and salmycin, isolated mainly from *Streptomyces* or *Actinomyces* (Figure 1.20). Ferrimycin, for example, is a hybrid of ferrioxamine B and an antibiotic group active against gram-positive bacteria such as *S. aureus* and *Bacillus spp.*

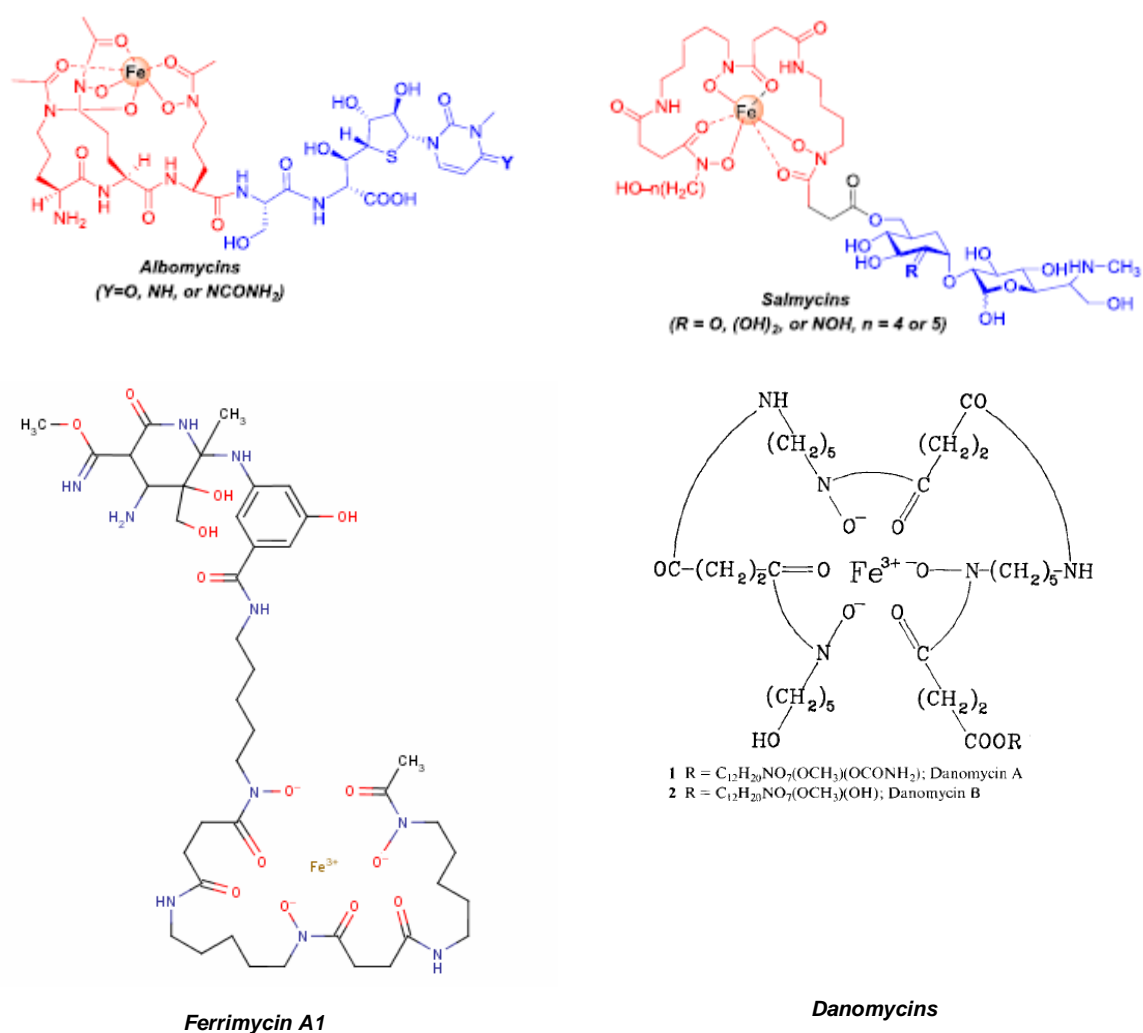


Figure 1.20. Structures of sideromycins

5.2.3. Inhibition of the siderophores synthesis

[Miethke 2007]

Another way to control the multiplication of the pathogen is the use of chemical compounds that block the synthesis of siderophores by inhibiting the enzymes involved in this process. Most studies have targeted enzymes for the synthesis of non-ribosomal peptides, also called NRPS (non-ribosomal peptides synthetase). They are involved in the synthesis of all siderophores made up of aryl groups and use salicylic acid or 2,3-dihydroxybenzoic acid as initial substrate. Thus, the inhibitors designed prevent the growth of the pathogen in an iron-depleted medium. Examples of such inhibitors include p-aminosalicylates in *M. smegmatis* and *M. bovis* [Brown 1975], of the SAL-AMS analogues (salicyl sulfamoyl adenosine) in *M. tuberculosis* and *Y. pestis* (Figure 1.21) [Ferrerias 2005].

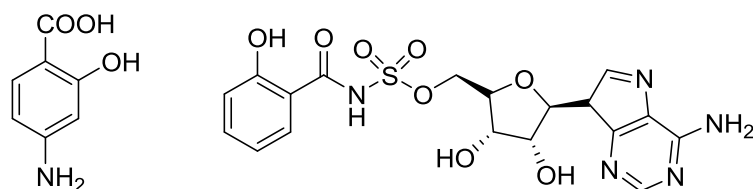


Figure 1.21. Structure of *p*-aminosalicylates (left) and SAL-AMS analogues (right).

5.2.4. Iron chelators as *C. trachomatis* bacterial growth inhibitors

Iron acquisition is a fundamental step during the development of *C. trachomatis* in the host cell [Raulston 1997] [Al-Younes 2001]. Controlling the sources of iron available to this pathogen is one of the possible strategies that can be successfully used by novel antibacterial drugs. For instance, Sessa and colleagues proposed the protective effect of Lactoferrine, a pleiotropic iron binding glycoprotein, against *C. trachomatis* infection [Sessa 2017]. Pradkar *et al.* demonstrated that the incubation of macrophages with the oral iron chelators deferriprone or desferasirox reduced intracellular bacterial growth [Pradkar 2008]. *In cellulo* and *in vivo* studies have shown that iron chelators such as the acylsalicylidene hydrazone type (Figure 1.22) have an effect against *C. trachomatis* with a minimum bactericidal concentration (MBC) of 25-50 μ M [Slepenkin 2007]. These results therefore suggest that these compounds can limit the growth of *C. trachomatis* by reducing iron availability in the host cell.

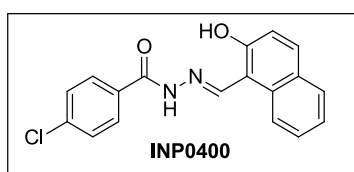


Figure 1.22. An acylhydrazone.

6. Previous work done in the laboratory and objectives of my PhD

In collaboration with Dr P. Verbeke (Inserm U1149, Paris), N. Serradji and co-workers were first interested in compounds made up of a central 4-amino-3-isoxazolidinone nucleus (Figure 25). Indeed, D-cycloserine or (*R*)-4-amino-3-isoxazolidinone (Figure 1.23) inhibits the growth

of *C. trachomatis* with a MIC of 30 $\mu\text{g/mL}$ [Gordon 1972]. They also noticed that this heterocycle was present in the structure of Pseudomonine, a natural iron chelator without any anti-chlamydial activity described [Mercado-Blanco 2001]. They then proposed to graft iron-chelating groups (catechol, 8-hydroxyquinoline etc...) on the 4-amino-3-isoxazolidinone heterocycle to provide putative new iron chelators with antibacterial properties (Figure 1.23) [Abdelsayed 2014].

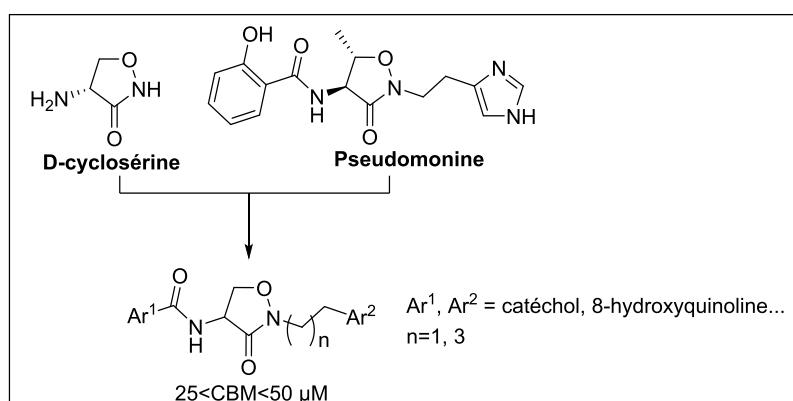


Figure 1.23. Structure of the previously obtained inhibitors by Abdelsayed *et al.*

They also investigated the behaviour of these new compounds in infected-HeLa cells with or without exogenously added iron to evaluate the metal ability to reverse the antibacterial effect observed. Compound 19 (Figure 1.24), an 8-hydroxyquinoline derivative, presented a bactericidal activity which was not suppressed by iron at high inhibitor concentrations (100-200 μM). They then assumed that iron chelation was not the only mechanism involved in the inhibition of *C. trachomatis*. Moreover, despite the presence of the metal chelating pattern, the 8-hydroxyquinoline moiety, this molecule does not have metal-chelating properties (iron, copper and zinc).

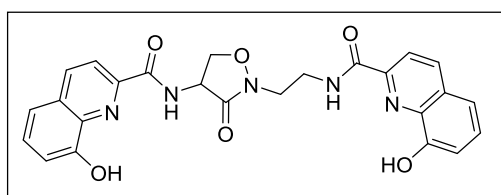


Figure 1.24. Compound 19

At the same time, Corcé *et al.* also described 8-hydroxyquinoline iron chelators linked to polyamines and studied their chelating properties and anticancer activity [Corcé 2014]. The proposed complexes are shown in Figure 1.25 below.

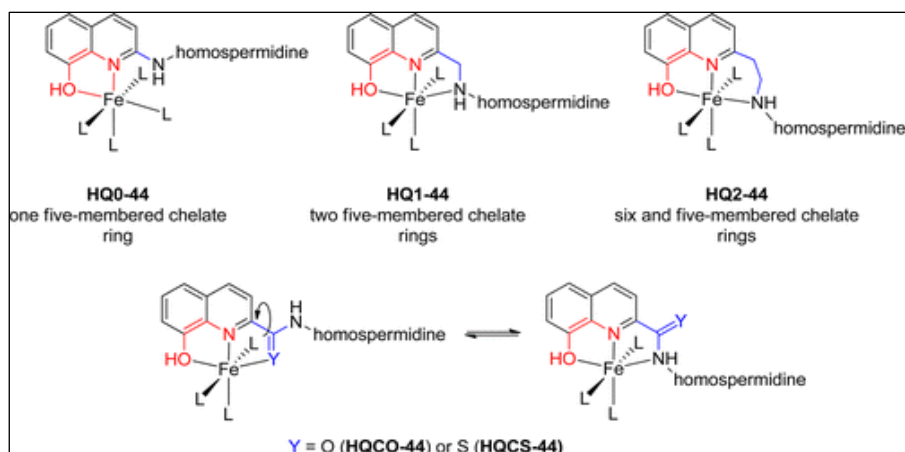


Figure 1.25. Hypothetical structures of iron complexes proposed by V. Corcé *et al.*

Their results showed that several molecules (HQ0-44, HQ1-44 and HQ2-44) have very good chelating capacities, especially when the latter have a secondary amine function spaced by 0 to 2 carbons of the quinoline nucleus. On the other hand, molecules presenting a carbonyl in the 2-position of heterocyclic nitrogen are weak iron chelators (HQCO-44 and HQCS-44; F. Gaboriau's personal data). This therefore illustrates that the introduction of a carbonyl function at this position seems unfavourable to iron chelation. This observation is consistent with what we have obtained with compound **19**. However, the reasons for this low chelation have not been described to date.

Finally, the significant difference in chelation efficiency between *O*-Trensox and *N*-Trensox, its isomer, which differ only in the position of the carbonyl on the 8-hydroxyquinolin moiety, is remarkable and could be attributed to the deleterious effect of carbonyl in *N*-trensox (Figure 1.26) [Serratrice 1997].

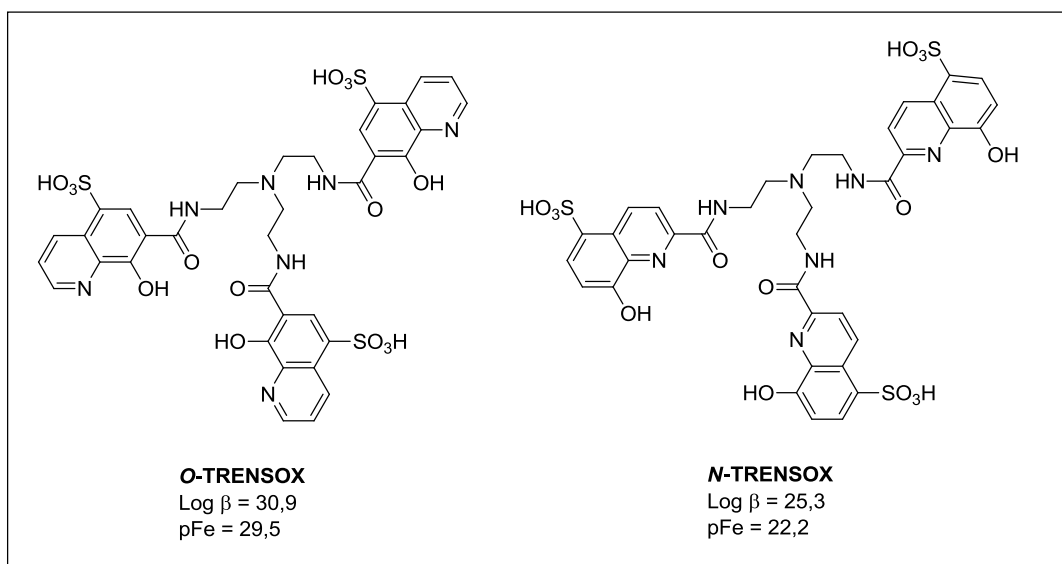


Figure 1.26. Structures of O- and N-TRENTOX and their iron chelating capacities.

In support of all of this information, the objectives of my thesis work were as follows.

We first wanted to obtain new *C. trachomatis* growth inhibitors. For this, we coupled an 8-hydroxyquinoline moiety with ciprofloxacin, a broad-spectrum antibiotic active against this bacterium, with the idea of improving the antibacterial activity of this drug against *Chlamydia*.

We also tried to understand the absence of chelation observed in the 8-hydroxyquinoline derivatives previously synthesized in the laboratory. For this, we combined experimental and theoretical studies using "model" molecules that I synthesized. We questioned the deleterious effect of the positioning of carbonyl on the heterocyclic motif.

Furthermore, we wanted to provide new tools to reach and image *C. trachomatis*-infected cells using vectors such as nanoparticles never described before to fight *C. trachomatis* infection.

All of these points will be developed in the following chapters.

CHAPTER II:

NEW FLUOROQUINOLONE DERIVATIVES HIGHLY ACTIVE AGAINST *CHLAMYDIA TRACHOMATIS*

In this chapter, we describe the rationale for obtaining 8-hydroxyquinoline derivatives active against *C. trachomatis*. The antibacterial activity of the obtained compounds was evaluated together with their ability to complex iron.

1. Introduction

In the last two decades, the metal-chelating properties of 8-hydroxyquinoline, a heterocyclic compound (HQ, Figure 2.1), has given it a particular interest, especially in drug design strategies [Oliveri 2016] [Savić-Gajić 2020]. It was explored widely thanks to two behaviours: (1) metal chelating ability and (2) a lipophilic character.

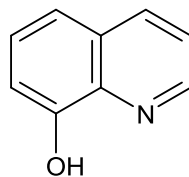
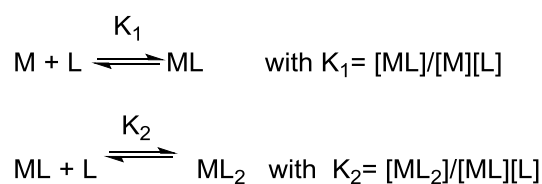


Figure 2.1. 8-hydroxyquinoline.

HQ is a metal chelator. HQ possesses two potential protonation sites, a pyridinyl nitrogen atom and a phenolate oxygen atom with acid dissociation constants of $pK_{NH} = 3.97$ and $pK_{OH} = 11.54$, respectively [Johnston 1952]. HQ is a bidentate chelator that binds metal ions through the oxygen and nitrogen atoms. It reacts with metal ions, losing the proton and forming HQ-metal complexes. Indeed, HQ has affinity for divalent metals (Figure 2.2, left) with a trend $Mg^{2+} < Mn^{2+} < Co^{2+} \sim Zn^{2+} < Ni^{2+} < Cu^{2+}$ (Table 2.1) [Stevenson 1967] [Burger 1973]. Besides, HQ has also affinity for trivalent metals (Figure 2.2, right) like Al^{3+} [Khaorapapong 2002], Fe^{3+} [Turnquist 1968], etc. It can form stable complexes with iron with a stoichiometry of 3 ligands and 1 metal at pH 7.0 (Figure 2.2) [Turnquist 1968].

Table 2.1. Formation constants of metal complexes of HQ. L is 8-hydroxyquinoline, M is metal, K_1 and K_2 are formation constants that refer to the formation of the complexes one step at a time [Stevenson 1967] [Burger 1973].



	Mg^{2+}	Mn^{2+}	Co^{2+}	Zn^{2+}	Ni^{2+}	Cu^{2+}
log K_1	5.04	7.30	9.65	9.45	10.50	13.29
log K_2	4.29	6.19	8.40	8.70	9.77	12.61

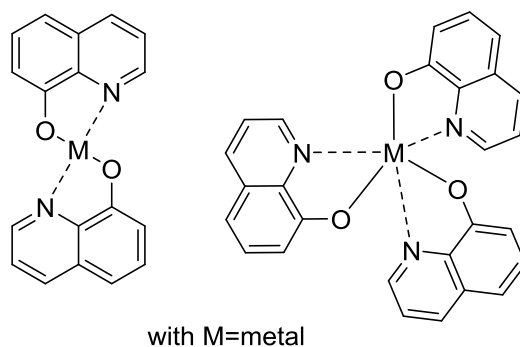


Figure 2.2. Schematic HQ metal coordination (left) for divalent metal, (right) for trivalent metal.

Lipophilicity of a compound was characterized by the octanol-water partition coefficient, usually expressed as $\log P$. HQ is a lipophilic ligand with $\log P = 2.02$ [Hansch 1995]. This property is needed for developing new antibiotic drug against intracellular bacteria like *C. trachomatis* because it is one of elements that increasing drug's ability to penetrate a membrane leading high intracellular concentration [Bongers 2019] [Shah 2015] [Nau 2010].

Thanks to its characteristics, HQ and derivatives were widely explored with a very large spectrum of various biological activities such as neuroprotection [Knez 2019] [Yang 2018] [Ghosh 2010] [Kanizsai 2018], anticancer agents [Tremlett 2019] [Xie 2018], anti-HIV agents [Velthuisen 2016], antifungal agents [Pippi 2017], antibacterial activity [Rbaa 2019] [Kos 2015], cytotoxicity [Tardito 2012]. Enquist *et al.* published the antibacterial activity of a HQ derivative (Figure 2.3) against *C. trachomatis* with a MIC of $3.13 \mu\text{M}$ [Enquist 2012].

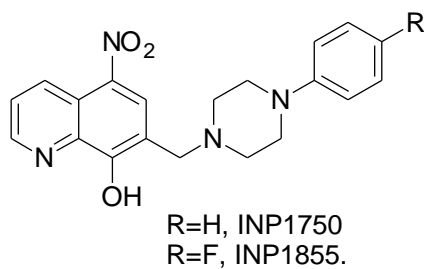


Figure 2.3. INP derivatives [Enquist 2012].

Ciprofloxacin (Cip, Figure 2.4) or 1-cyclopropyl-6-fluoro-4-oxo-7-(piperazin-1-yl)-1,4-dihydroquinoline-3-carboxylic acid, is a broad spectrum fluoroquinolone antibiotic. Cip molecule contains three substituents contributed to the drug's high antibacterial activity: (1) a 6-fluoro substituent; (2) 7-piperazino group, which is found in cefoperazone and piperacillin (two broad-spectrum antibiotics); (3) a cyclopropyl chain, which is found in other fluoroquinolones [Lebel 1988].

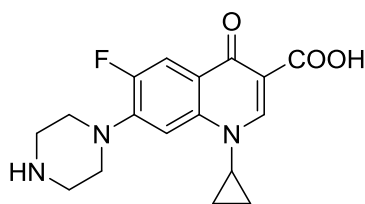


Figure 2.4. Ciprofloxacin.

Cip is a hydrophilic compound ($\log P = -0.13$) [Volgyi 2012] with two ionisable functional groups: the carboxylic group at the 3-position ($pK_{a1} = 6.0$) and the piperazinyl group at the 7-position ($pK_{a2} = 8.8$) with an isoelectric point of 7.4 [Jack 1986]. In addition, Cip has also the capacity to form stable complexes with metal ions [Uivarosi 2013]. Usually, Cip is coordinated in a bidentate manner via one of oxygen atoms of deprotonated carboxylic function and the ring carbonyl oxygen atom (Figure 2.5). Cip can also form complexes as unidentate coordinated to the metal ion through terminal nitrogen of piperazinyl group. Cip can bind divalent metal (Mg^{2+} , Ca^{2+} , Cu^{2+} , Zn^{2+} , Fe^{2+} , Co^{2+} , etc) with a stoichiometry between metal and ligand of 1:1 or 1:2, or trivalent metal (Al^{3+} , Fe^{3+}) with a stoichiometry of 1:1, 1:2 or 1:3. The affinities for metal decrease in the following order: $Al^{3+} > Fe^{3+} > Cu^{2+} > Zn^{2+} > Mn^{2+} > Mg^{2+}$ [Ma 1997].

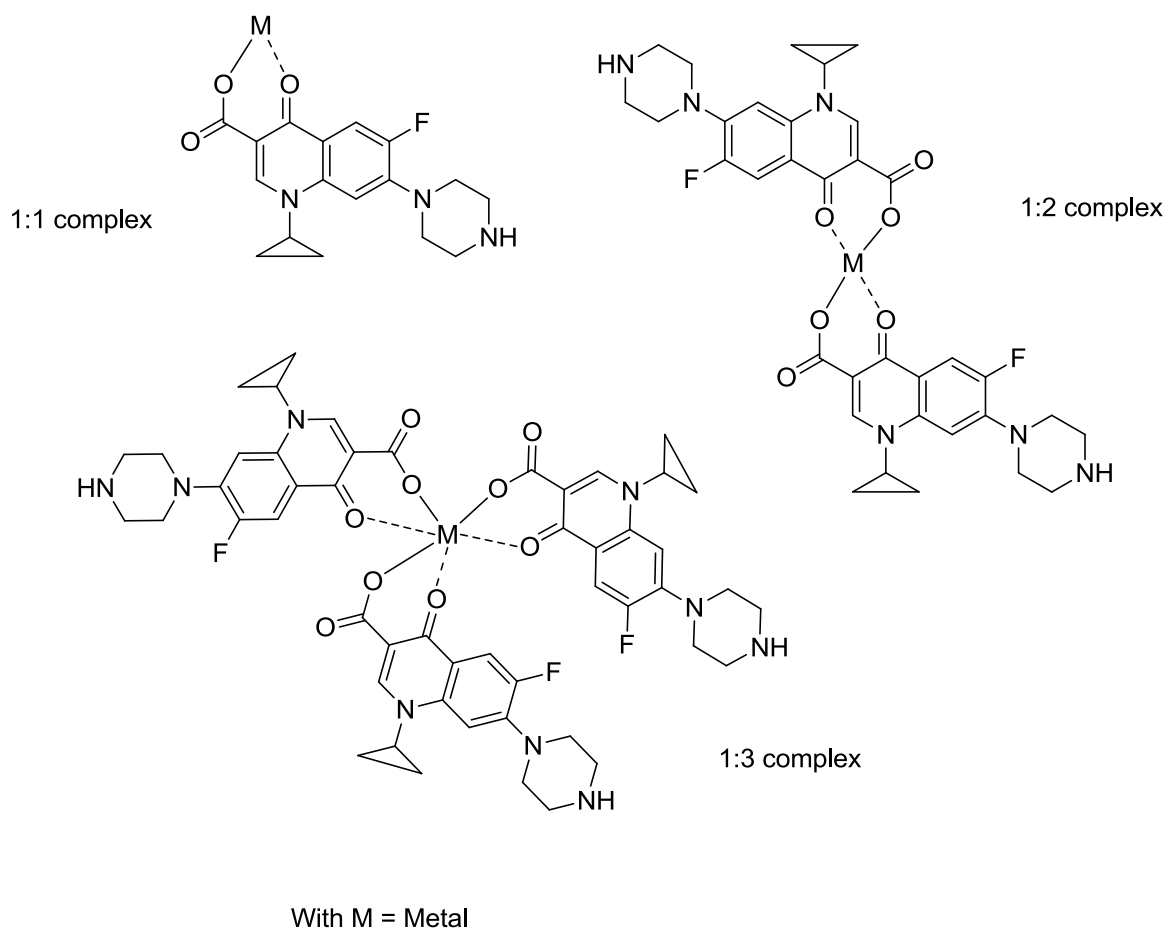


Figure 2.5. Main coordination modes of ciprofloxacin.

Cip, a synthetic broad-spectrum antibiotic, is potent against Gram-negative bacteria, but also has effectiveness against some Gram-positive bacteria [Campoli-Richards 1988]. It prevents DNA from replication by inhibiting bacterial DNA topoisomerase and DNA gyrase. The Cip *in vitro* activity against *C. trachomatis* was investigated in 1984 by Rumpianesi *et al.* who proposed MIC of 1 $\mu\text{g}/\text{mL}$ and a minimum bactericidal concentration (MBC) of 10 $\mu\text{g}/\text{mL}$ [Rumpianesi 1984]. At the same time, in 1984, Ridgway *et al.* confirmed Cip antibacterial activity against *C. trachomatis* with MIC and MBC of 1 $\mu\text{g}/\text{mL}$ [Ridgway 1984]. In 2000, Dreses-Werringloer *et al.* showed persistence of *C. trachomatis* during Cip treatment *in vitro* [Dreses-Werringloer 2000].

Besides, iron is perhaps the most important nutrient for bacteria, including *C. trachomatis*, and it is implicated in their proliferation and their ability to cause diseases. Therefore, iron depletion severely affects their development (detailed in chapter 1) and could be a relevant strategy to inhibit bacterial growth [Wooldridge 1993].

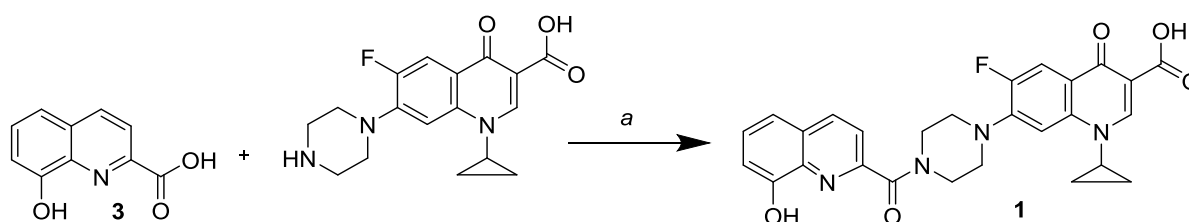
In medicinal chemistry, the search for dual therapeutic activity is commonly encountered in the literature, to try to counter the phenomenon of bacterial resistance, for instance. Indeed, despite the growing need for antibiotics to fight infectious diseases, few new molecules are available on the market. The modification or combination of pre-existing drugs is therefore an interesting strategy, making it possible to increase the therapeutic potential of the parent molecules. The search for hybrids with polypharmacological modes of action has, for instance, been used successfully by Sunduru *et al.* to obtain inhibitory compounds against both *C. trachomatis* and the T3SS of gram-negative bacteria [Sunduru 2015].

Hence, in this chapter, we first present results obtained with compound **1**, a new inhibitor of *C. trachomatis* growth, synthesized based on some prerequisites: (i) the iron dependency of the bacterium, (ii) Cip, a commercially available broad-spectrum antibiotic and (iii) a short synthetic pathway. The idea was to obtain a new compound presenting inhibitory potency through its metal chelating-properties and its antibiotic effect. Conjugation of HQ derivatives and ciprofloxacin was realized, with the objective to obtain more active derivatives than the parent antibiotic and, therefore, potentially useful for the treatment of *C. trachomatis* infection. The corresponding catechol derivative was used as control. The ability to complex Fe^{3+} as well as the anti-chlamydial activities of the resulting compounds were studied.

2. Compound 1

2.1. Chemistry

The coupling of ciprofloxacin and 8-hydroxyquinoline-2-carboxylic acid (**3**) using TBTU (2-(1*H*-benzotriazole-1-yl)-1,1,3,3-tetramethyluronium tetrafluoroborate) and DIEA (*N,N*-diisopropylethylamine) led to compound **1** (Scheme 2.1).



Reagents: (a) TBTU, DIEA, DMF.

Scheme 2.1. Compound **1** synthesis.

To compare with HQ, we synthesized the catechol analog (Figure 2.6). Indeed, catechol is a conventionally described metal-chelating entity which forms extremely stable complexes with

iron(III) [Karpishin 1991]. This explains why the catechol group is present in many siderophores, molecules which are synthesized by microorganisms to trap iron in the external environment in order to facilitate its intracellular transport [Wilson 2016] [Fardeau 2014] [Miethke 2007]. The catechol-ciprofloxacin conjugate **2** was prepared as previously described using the 2,3-dihydroxybenzoic acid as starting material [Fardeau 2014].

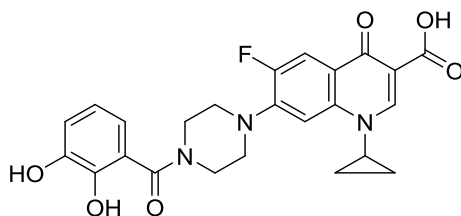


Figure 2.6. Compound **2**.

Both compounds were evaluated for their putative antibacterial activities.

2.2. Biological evaluation

2.2.1. The anti-*Chlamydia* activity

This study was carried out in collaboration with Dr Philippe Verbeke (Inserm U1149, Paris Diderot, Paris). The compounds were first screened for cell toxicity. Host cell viability was monitored by Trypan Blue exclusion in the presence of the compounds at different concentrations. No cell toxicity was observed at the concentrations tested (0–200 μM) on either HeLa cells, a tumour cell line, or primary cell cultures of mouse fibroblasts, a non-cancerous mammalian cell line. Compounds were then screened for their capacity to inhibit *C. trachomatis* growth in HeLa cells (Figure 2.7). The cells were infected by *C. trachomatis* serovar L2 strain as previously described [Dumoux 2013]. Infection was performed with or without the test molecules (0–50 μM) and with or without iron citrate (200 μM). 72 h post-infection, cell lysates were processed and used to infect new HeLa cells. The reinfection capacity was scored by calculating the Inclusion Forming Unit (IFU) of each cellular lysate. Ciprofloxacin (black bars) was used as external control. The results presented in Figure 2.7 show that the MBC is higher than 16.5 $\mu\text{g/mL}$ (or > 50 μM) is similar to that described in the literature (> 10 $\mu\text{g/mL}$) [Rumpianesi 1984] while compound **1** (grey bars) presents a MBC of 2–5 $\mu\text{g/mL}$ (5–10 μM). Therefore, functionalization of the fluoroquinolone nitrogen by an 8-hydroxyquinoline entity does not inhibit its antibacterial activity. The resulting compound is even more active than the parent molecule, probably due to a gain in lipophilicity. Indeed, its

calculated octanol-water partition coefficient (clog from Chemdrawbio Ultra version 13.0.03015) is higher than that of Cip (clogP(Cip) = 1.32 vs clog P(**1**) = 3.09).

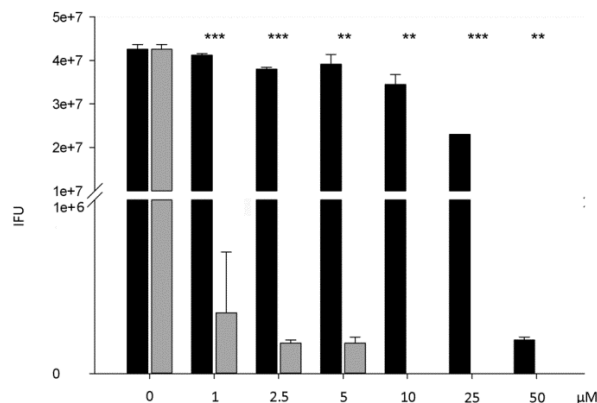


Figure 2.7. Inhibitory effects on *C. trachomatis* infectious capacity of compounds tested *in cellulo* (grey bars: compound **1**; black bars: ciprofloxacin. Statistically significant differences are noted as follows: ** $p < 0.01$, *** $p < 0.001$).

Under the same conditions, the catechol analogue **2** is inactive despite the strong catechol iron-chelating ability and its certain lipophilicity (Table 2.2). This suggests that other parameters should be considered to understand this phenomenon, as illustrated by the weak Doxycycline log P which is however active against this bacterium (Table 2.2).

Table 2.2. Minimal bactericidal concentrations of the studied compounds **1-2** versus their lipophilicity (log P):

Compound/Antibiotic	log P	MBC (μg/mL)
Cip	-0.13 ^a	> 16.5
1	2.99 ^b	2-5
2	2.16 ^b	Inactive
Azithromycine	3.03 ^c	10-50 ^d
Doxycycline	0.63 ^c	2.5-5 ^d

^a From [Volgyi 2012]; ^b Computed with Chemdrawbio Ultra version 13.0.03015;

^c From PubChem; ^d From [Reveneau 2005].

Iron is an essential element for *C. trachomatis*. However, to date, no siderophores or siderophore receptors have been described in *Chlamydiaceae* [Stephens 1999]. Since catechol is one of the most powerful iron-chelating agents, the inactivity of compound **2** against

C. trachomatis suggests that the inhibition induced by compound **1** is not mainly due to iron chelation.

Taking into account the iron-chelating properties of both entities, 8-hydroxyquinoline and the fluoroquinolone, we evaluated the ability of iron(III) to reverse compound **1** inhibitory effect by adding exogenous iron citrate (200 μM). The results in Figure 2.8 show that the inhibitory effect of compound **1** is only partially reversed by excess Fe^{3+} (20%, 35% and 60% decrease at 1, 2.5 and 5 μM , respectively), confirming that iron chelation is not its main antibacterial mechanism.

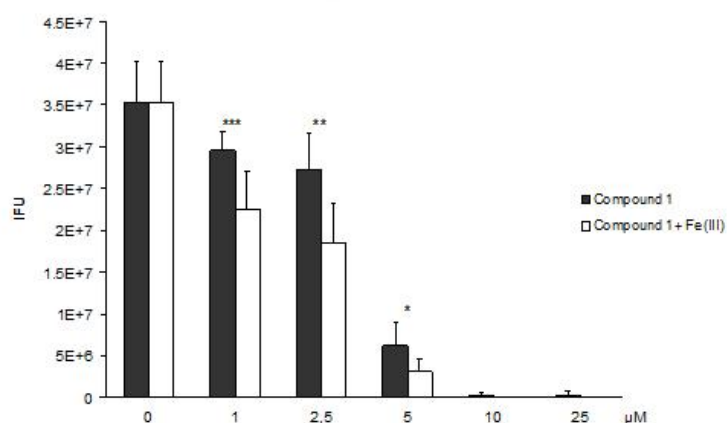


Figure 2.8. Compound **1** inhibitory effect in the presence of excess iron citrate (200 μM). Statistically significant differences are noted as follows:

* $p < 0.05$, ** $p < 0.01$, *** $p < 0.001$.

The World Health Organization Sexually Transmitted Infections guidelines suggest treatment of *C. trachomatis* infection with one of the following drugs: azithromycin (1 g orally as a single dose) or doxycycline (100 mg twice a day for 7 days). The *in cellulo* anti-chlamydia bactericidal activities of both compounds have been published: doxycycline and azithromycin have MBCs of 2.5–5.0 $\mu\text{g}/\text{mL}$ and 10–50 $\mu\text{g}/\text{mL}$, respectively [Reveneau 2005]. Compound **1** is therefore at least as effective *in cellulo* as these two molecules.

2.2.2. Other antimicrobial activities

This study was performed in collaboration with Pr Alexandra Aubry (*E. coli* and *M. tuberculosis*; CIMI, Paris) and Pr Patrick Plesiat (bacteria from the ESKAPE group; Hôpital Jean Minjot, Besançon).

Ciprofloxacin is a broad-spectrum antibiotic. We therefore looked at the ability of compound **1** to inhibit other human pathogens, including Gram-negative and Gram-positive bacteria

from the ESKAPE group, an acronym including pathogenic bacteria present in the hospital environment and difficult to treat (*Enterococcus faecium*, *Staphylococcus aureus*, *Klebsiella pneumoniae*, *Acinetobacter baumannii*, *Pseudomonas aeruginosa* and *Enterobacter species*). *Staphylococcus aureus* is the most common staphylococcus strain responsible for human diseases, particularly nosocomial infections, along with *Escherichia coli*. The minimal inhibitory concentrations (MIC) of the derivatives were then determined (Table 2.3). Many microbes, including *P. aeruginosa* strains, are well known to synthesize siderophores to scavenge iron from their environment. In order to facilitate the transport of antibiotics into bacteria, siderophore-conjugates have been described and used in a Trojan-horse strategy [Cézard 2015]. Compound **2** was previously described as a new antibiotic following this strategy [Fardeau 2014]. Indeed, in iron-deficient culture conditions only, compound **2** is active against the *P. aeruginosa* DSM 1117 susceptible strain with a MIC of 32 µg/mL, suggesting effective transport of the corresponding iron(III) complex by bacterial iron-uptake pathways. We found that compound **2** is inactive against *P. aeruginosa* ATCC-27853, a reference strain (MIC > 128 µg/mL, Table 2.3), unlike compound **1** (MIC = 4 µg/mL).

While inactive against *M. tuberculosis*, compound **1** exhibits inhibitory activity against all the other Gram-negative and Gram-positive bacteria tested. For instance, it stops the growth of *E. coli* (MIC ≤ 0.06 µg/mL), perhaps by inhibiting its DNA gyrase, one of the bacterial targets of quinolones (IC₅₀ = 8–16 µg/mL; Table 2.3) but to a lesser extent compared to the Cip. In addition, this inhibition is not observed in *M. tuberculosis*. In fact, this compound has a panel of interesting antibacterial activities, in that the MICs obtained are in the µg/mL range and can be considered as a starting point to try to obtain more potent compounds, against *S. aureus*, especially against laboratory and clinical isolates (Table 2.3).

As already observed for *C. trachomatis*, the catechol analogue **2** is less potent than the 8-hydroxyquinoline derivative **1** on the panel of bacteria tested.

The starting acid was tested in order to evaluate its contribution to the antibacterial activity of compound **1**. The results (Table 2.3) show that whatever the pathogen, this acid is inactive, which suggests that the fluoroquinolone part of **1** is responsible for its efficacy.

Table 2.3. *In vitro* antibacterial activities (IC₅₀ or MIC) of compounds **1–2**, ciprofloxacin and acid **3**:

Organism	Gram ^a	Cip	1	2	3
<i>M. tuberculosis</i>	-	12–17 ^{b,c}	>128 ^b	>128 ^b	>128 ^b
<i>E. coli</i>	N	1–2.9 ^b	8–16 ^b	4–15 ^b	>128 ^b
<i>E. coli</i> ATCC-25922	N	≤ 0.06 ^d	≤ 0.06 ^d	nd	>8 ^d
<i>K. pneumoniae</i> ATCC-700603	N	0.25 ^d	4 ^d	nd	>8 ^d
<i>P. aeruginosa</i> ATCC-27853 ^e	N	0.25 ^d	4 ^d	>128 ^f	>8 ^d
<i>A. baumannii</i> CIP-7010	N	0.125 ^d	2 ^d	nd	>8 ^d
<i>S. aureus</i> HG001 (laboratory strain)	P	0.125 ^d	0.0625 ^d	5 ^d	nd
<i>S. aureus</i> ATCC-25923 (clinical isolate)	P	0.25 ^d	0.125 ^d	nd	>8 ^d
<i>S. aureus</i> ATCC-700699 (resistant isolate)	P	>8 ^d	>8 ^d	nd	>8 ^d
<i>S. epidermis</i> ATCC-14990	P	0.125 ^d	0.25 ^d	nd	>8 ^d
ATCC-35984	P	≤ 0.06 ^c	≤ 0.06 ^d		>8 ^d
<i>E. faecalis</i> JH2-2	P	2 ^d	8 ^c	nd	>8 ^d
UCN41	P	1 ^d	8 ^d	nd	>8 ^d
<i>E. faecium</i> ATCC-19434T	P	1 ^d	8 ^d	nd	>8 ^d
BM-4147	P	4 ^d	>8 ^d	nd	>8 ^d

^aP/N : positive/negative.

^bIC₅₀ (μg/mL) against wild-type DNA gyrases of *M. tuberculosis* and *E. coli*.

^cIC₅₀s slightly higher than those previously determined [Aubry 2004].

^dMIC (μg/mL).

^e Similar MIC were obtained against *P. aeruginosa* PAO1, a laboratory strain (data not shown).

^f*P. aeruginosa* DSM 1117 [Fardeau 2014]

nd: not determined.

2.3. Iron-chelating properties

To further characterize compound **1**, its ability to complex Fe^{3+} was studied. This study was carried out under the supervision of Dr Thanh Ha Duong (ITODYS, Université de Paris).

We usually determined thermodynamic constants of iron-binding molecules by UV-visible absorption spectrophotometry.

Chelators binding sites for iron(III) are for the most part negatively charged and therefore, in aqueous solution, there is a competition between H^+ and Fe^{3+} binding. Consequently, the equilibrium expression for the formation of the iron–siderophore complex must take into account proton participation in the reaction.



$$K_{aff} = \frac{[\text{FeL}^{3-n}][\text{H}^+]^x}{[\text{Fe}^{3+}][\text{LH}]}$$

This means that the sequestration equilibrium reaction will be pH-dependent. The constant K_{aff} is known as the “affinity” equilibrium constant. However, to compare the ability of different molecules to complex iron, it may be more convenient to compare the affinity constant at the same pH value or the equilibrium constant for the proton independent reaction between iron and ligand (or siderophore). This can also be useful in a theoretical sense, as it allows comparison of complex stability where siderophores have different protonation constants. Therefore, two thermodynamic constants are usually calculated to describe the chelation tendency of molecules:

- The overall affinity constant β , which corresponds to the iron-affinity constant when the ligand is in its deprotonated form:

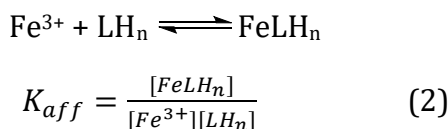


$$\beta = \frac{[\text{FeL}^{3-n}]}{[\text{Fe}^{3+}][\text{L}^{n-}]}$$

- The pFe value, which is the negative logarithm of the free aqueous iron(III) concentration at arbitrary fixed $[\text{Fe}^{3+}]$, [ligand], and $[\text{H}^+]$ concentrations. The concentrations for pFe calculations usually found in the literature are $[\text{Fe}^{3+}]_{\text{tot}} = 1 \mu\text{M}$, $[\text{L}]_{\text{tot}} = 10 \mu\text{M}$, and $\text{pH} = 7.4$. This constant allows the comparison of chelators at physiological pH.

Experimentally, the overall affinity constant β cannot be measured directly, because the ligand is deprotonated in basic medium, and at those high pH values, Fe^{3+} precipitate

(pKs = 37). Therefore, we measure an apparent affinity constant K_{aff} at pH = 2, where Fe^{3+} is soluble and the ligand is totally protonated.



The determination of pFe and β takes into account the acid-base constants of free ligand (K_{an} , Eq 4) and those of iron-complex (K'_{an} , Eq 6). The β value is then calculated from the apparent affinity constant K_{aff} (Eq. 7). For clarity, the charges of the ligand and the complex are omitted.



$$K_{an} = \frac{[LH_{n-1}][H^+]}{[LH_n]} \quad (4)$$



$$K'_{an} = \frac{[FeLH_{n-1}][H^+]}{[FeLH_n]} \quad (6)$$

$$\log \beta = \log K_{aff} + \sum pK_{an} - \sum pK'_{an} \quad (7)$$

Each acid-base species presents a typical absorption spectrum which allows determination of their proton-dissociation constants by spectrophotometric titration and analysis by the SPECFIT software. Similarly, the addition of iron to a solution of ligand leads to spectral modifications and the appearance of Ligand to Metal Charge Transfer (LMCT) band. The SPECFIT analysis of the spectra allows the determination of K_{aff} .

To evaluate the iron chelation at physiological pH, some titration experiments can be performed at pH 7, by adding to a solution of ligand, an iron-complex soluble at this pH, usually FeNTA (Fe(III)-nitrilotriacetic acid).

In our study, only the constant K_{aff} was evaluated.

In the case of compound **1**, complexation experiments were performed in a H₂O/DMSO (1:1; v/v) mixture to avoid precipitation of any ligand and/or complex. The pH values mentioned are those of aqueous solutions before mixing with DMSO. Compound **1** has two potential sites for metal complexation: the ciprofloxacin carboxylate and keto groups and the 8-hydroxyquinoline part.

At pH 2, the addition of FeCl₃ to a solution of **1** leads to a bathochromic shift (red shift) of the π - π^* band from 284 to 290 nm and the appearance of a ligand-to-metal charge-transfer (LMCT) band at 450 nm (Figure 2.9 A). The latter is identical to the LMCT of a complex

between iron(III) and ciprofloxacin described by Fardeau *et al.* [Fardeau 2014], whereas those of the complex between Fe^{3+} and methyl 8-hydroxyquinoline-2-carboxylate, a surrogate of the 8-hydroxyquinoline moiety (Figure 2.10), are observed at 481 and 632 nm (Figure 2.9 B). This result suggests that only the fluoroquinolone part of compound **1** complexes Fe^{3+} at this pH.

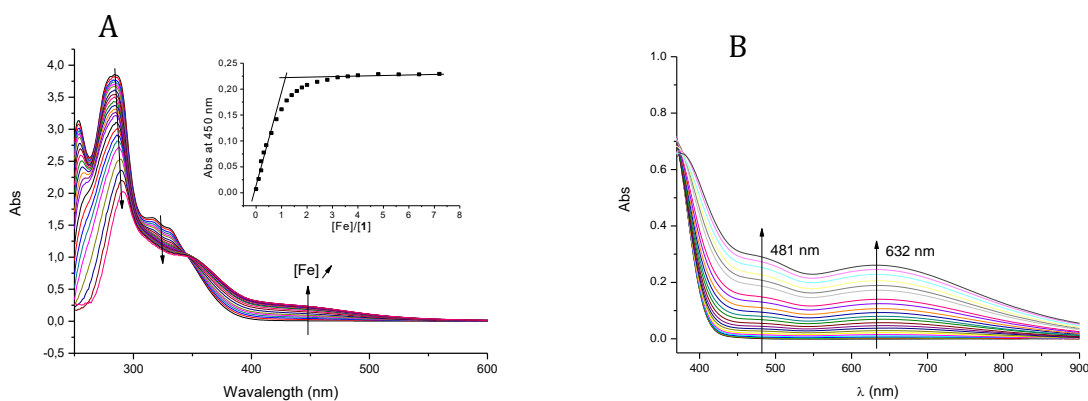


Figure 2.9. Absorption spectra in the presence of increasing concentrations of FeCl_3 at pH 2 and 25 ± 0.5 °C (A) of compound **1** (10^{-4} M) (FeCl_3 : 0 – 10^{-3} M; solvent: DMSO/water pH 2, 1:1, v/v) with absorbance at 450 nm plotted against $[\text{Fe(III)}]/[\mathbf{1}]$ in inset, and (B) of Methyl 8-hydroxyquinoline-2-carboxylate (10^{-4} M), (FeCl_3 : 0 – 10^{-5} M; solvent: EtOH/water pH 2, 1:4, v/v)

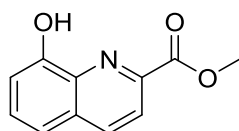


Figure 2.10. Methyl 8-hydroxyquinoline-2-carboxylate.

In order to transpose our work to the physiological conditions and pH values measured by Grieshaber *et al.* (pH of 7.28 and 7.25 for eukaryotic cell cytoplasm and bacterial inclusion respectively) [Grieshaber 2002], we conducted a study at pH 7. Iron-exchange experiments between Fe-nitrilotriacetic acid (Fe-NTA), a chelating agent, and **1** in one hand or Methyl 8-hydroxyquinoline-2-carboxylate, in the other hand show also differences in the LMCT bands (Figure 2.11). Indeed, the addition of Fe-NTA to a solution of compound **1** leads to a decrease in absorbance at 282 and 319 nm. A red shift from 319 to 350 nm for the second band is also observed (Fig 2.11 A). In the case of Methyl 8-hydroxyquinoline-2-carboxylate (Fig 2.11 B), there is an isosbestic point at 390 nm, and two LMCT appear at 465 and 605 nm. These LMCT bands are not observed for compound **1**, which implies that even at pH 7.0 iron is

coordinated differently in these two molecules. The fluoroquinolone part of compound **1** probably chelates iron at pH 7.0.

Hence, the 8-hydroxyquinoline part of compound **1** does not complex Fe^{3+} while in free form, 8HQ has a strong affinity with iron(III). This issue will be investigated in Chap III.

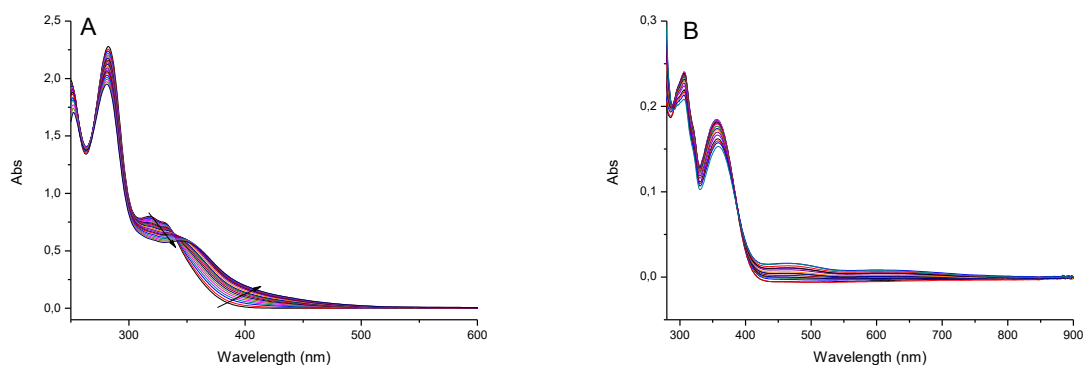


Figure 2.11. Absorption spectra in the presence of Fe-NTA (A) of compound **1** (5.10^{-5} M) (buffer: 50 mM HEPES - 150 mM KCl, pH 7.0, solvent: DMSO; buffer/solvent, 1:1, v/v) (B) of Methyl 8-hydroxyquinoline-2-carboxylate (5.10^{-4} M) (buffer: 50 mM HEPES - 150 mM KCl, pH 7.0, solvent: EtOH; buffer/solvent, 4:1, v/v)

In Figure 2.9, an isosbestic point at 340 nm indicates the formation of a single iron complex between **1** and Fe^{3+} , at pH 2. The inset in this figure presents the plot of the absorbance at 450 nm against the ratio $[\text{Fe(III)}]/[\mathbf{1}]$: an increase in the absorbance is followed by a plateau. The two asymptotes intersect at a ratio of 1, implying a 1:1 stoichiometry (metal-ligand) for the complex. We then determined the affinity constant of the complex at this pH, using Specfit analysis of the spectra. The low value obtained ($\log K_{11} = 2.5 \pm 0.3$) confirms that iron chelation might be not the main antibacterial mechanism of action of this compound.

We reported here the synthesis of a novel ciprofloxacin derivative by a single-step coupling of the parent antibiotic. This compound has notable antibacterial activity against Gram-negative and Gram-positive bacteria, in particular the obligate intracellular bacterium *C. trachomatis*. This antibacterial effect is only partially reversed by the addition of iron(III), which is complexed by the fluoroquinolone part of the molecule. This work was published in *Bioorganic Chemistry*, in 2019.

Compound **1** was then considered as a starting point to obtain new derivatives potentially more active. They are described below.

3. Compound 1's derivatives

Previously we showed that compound **1** has a higher anti-*Chlamydia trachomatis* activity than ciprofloxacin, the parent antibiotic. To increase this antibacterial effect, we followed three approaches: (1) we increased compound **1**'s lipophilicity with the introduction of an alkyl chain on the hydroxyl function of the quinoline heterocycle; (2) we changed the coupling position of the antibiotic from C-2 to C-7; and (3) we prepared a folic acid-ciprofloxacin conjugate to use folic acid as a vector to target infected Hela cells.

3.1. Organic synthesis

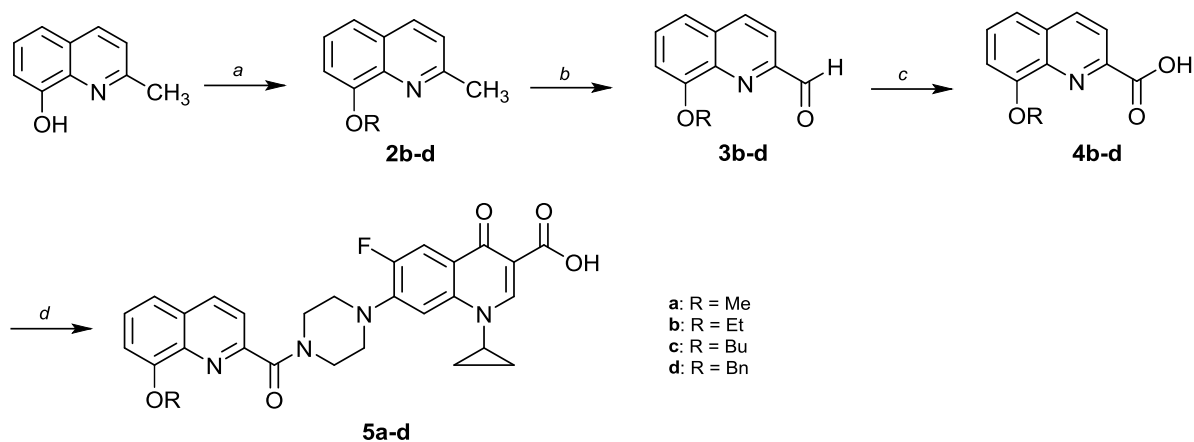
3.1.1. Increasing compound 1's lipophilicity

In drug design and discovery, drug lipophilicity is a critical element. This property plays a crucial role in determining a compound's absorption, distribution in the body, metabolism, excretion and toxicity (ADMET) properties and the overall suitability of drug candidates [Arnott 2012]. Lipophilicity is determined experimentally as partition coefficients ($\log P$, valid only for a single chemical species). The partition coefficient ($\log P$) measures how much of solute dissolves in the water portion versus an organic portion. In our case, $\text{clog } P$, calculated with ChemDraw Ultra 13.0.0.3015 software, was used to establish the possible link between this parameter and the antibacterial activity of the synthesized molecules. In 2014, Mallavadhani *et al* followed the same strategy: an increase of the lipophilicity of pentacyclic triterpenes by the extension of their alkyl chain length was associated to higher antimicrobial activity against a series of Gram positive and Gram negative bacteria, probably due to an improved permeation of compounds through the bacterial lipid layer [Mallavadhani 2014]. Hence, we substituted compound **1** using alkyl halides to increase its carbon chain length as well as lipophilicity.

Procedure to obtain four ciprofloxacin derivatives (R = Me, Et, Bu, Bn) is presented in Scheme 2.2 and includes four steps (except for the methyl derivative):

- (1) Alkylation of the 2-methylquinolin-8-ol;
- (2) Oxidation of the methyl group into an aldehyde function;
- (3) Oxidation of the aldehyde function into the corresponding carboxylic acid;
- (4) Carboxylic acid coupling with ciprofloxacin.

These obtained compounds were fully characterized by infrared spectroscopy, ^1H and ^{13}C NMR and HRMS and their anti-*Chlamydia trachomatis* activity was evaluated through collaboration with Dr Åsa Gylfe (Umeå university, Umeå, Sweden).



Reagents : (a) RBr, K_2CO_3 , DMF, Ar (for **2b-c**) or RBr, KI, K_2CO_3 , acetone, Ar (for **2d**); (b) SeO_2 , 1,4-dioxane, Δ ; (c) Oxone, DMF, Ar (for **4b-c**) or NH_2SO_3 , NaClO_2 , $\text{H}_2\text{O}/\text{THF}$ (for **4d**); (d) Cip, TBTU, DIEA, DMF, Ar.

Scheme 2.2. Synthesis of compound **1**'s derivatives.

Alkylation of 2-methylquinolin-8-ol

Following the procedure described by Qu *et al.* [Qu 2017], 2-methylquinolin-8-ol was reacted with alkyl halides using K_2CO_3 as base in DMF to afford the alkyl derivatives **2b-c** with good yields (89-99%) while Terazzi *et al* [Terazzi 2009]. described the synthesis of compound **2d** in acetone in presence of potassium iodide.

The butyl derivative **2c** was however formed with 50% yield and was very difficult to purify as the starting material was co-eluted during TLC and column chromatography despite very distinct frontal ratios, explaining the poor yield obtained. In order to remove the starting material, a basic washing prior to the chromatography on silica gel was carried out. Finally, the addition of potassium iodide, as catalyst, to the reaction mixture enables the important conversion of the starting material (95% yield).

Oxidation of the methyl group to the aldehyde

Compound **3b-d** were formed using selenium dioxide in 1,4-dioxane [Qu 2017] [Terazzi 2009], under an inert atmosphere. Especially, compound **3c** was engaged in the next step without purification.

Oxidation of the aldehyde function to the corresponding carboxylic acid

For compounds **4b-c**, and in support of the work carried out by de Qu *et al* [Qu 2017], we first used potassium permanganate to oxidize aldehydes **3b-c** into the corresponding carboxylic acids. However, the two experiments realized did not allow the compounds to be isolated, the NMR analysis revealing no relevant peak.

We therefore opted for another strategy described by Jisha *et al* and using potassium hydrogen sulfate (Oxone®) [Jisha 2013]. The acids formed were obtained with a yield of 52% and 63% for compound **4b** and **4c**, respectively.

These moderate yields prompted us to modify the procedure to get compound **4d**. The use of a mixture of H₂NSO₃H (sulfamic acid) and NaClO₂ (sodium chlorite) in THF and water afforded the desired compound with a yield of 91%.

Coupling of acids 4b-d with ciprofloxacin

The last step to obtain compound **5a-d** was the coupling between the acid derivatives (commercially available 8-methoxyquinoline-2-carboxylic acid and compounds **4b-d**) and ciprofloxacin in a single step, under argon. This reaction was carried out using TBTU and DIEA, as previously described for compound **1**. The coupling products **5a-d** were obtained with good yields (71-92%).

3.1.2. Compound 6 - An isomer of compound 1

The study we published in 2020 proposes an effect of the position of the carbonyl group of the 8-hydroxyquinoline moiety on its iron-chelating properties [Vu 2020]. Briefly, comparing the isomers we synthesized, we observed, as the literature also did, that higher iron-chelating capacity was obtained when the carbonyl function was at position C7. This point will be presented in the next chapter. Compound **6**, an isomer of **1** (Figure 2.12), was then obtained from Cip and 8-hydroxyquinoline-7-carboxylic acid, using TBTU and DIEA, but this coupling required heating of the mixture (80°C) and longer reaction time compared to compound **1**. Iron-chelating and anti-chlamydial properties of **6** were then investigated, as previously described.

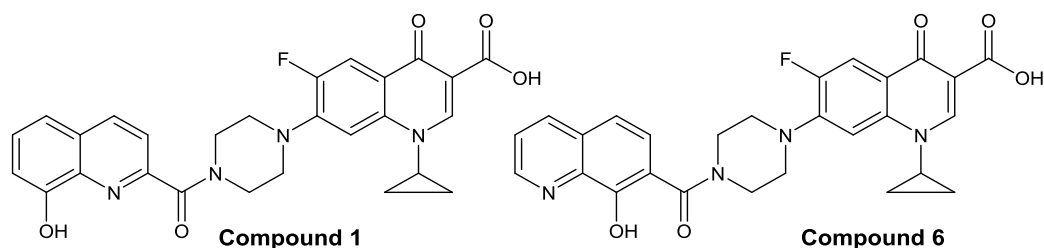
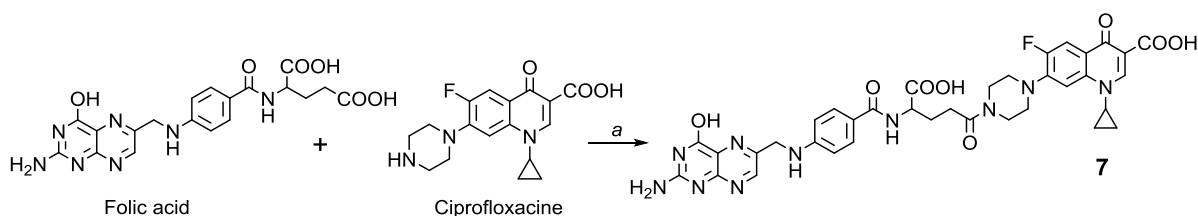


Figure 2.12. Structures of compounds **1** and **6**.

3.1.3. Coupling between folic acid and ciprofloxacin

Folic acid (Scheme 2.3) is a member of the vitamin B family that stimulates the hematopoietic system. It is present in the liver and kidney and is found in mushrooms, spinach, yeast, green leaves, and grasses. The folic acid congeners are transported across cells by receptor-mediated endocytosis [Merrell 2020]. The overexpression of its receptor in several pathological conditions enabled the use of this vitamin as delivery system, mostly in cancer field, for instance [Guo 2017] [Zhao 2008]. Folic acid-receptor is also overexpressed in *C. trachomatis* infected cells [Benchala 2014]. Hence, we synthesized the folic acid-ciprofloxacin conjugate **7** (Scheme 2.3) to address this molecule to the infected cells and increase the antibacterial activity of the parent antibiotic. Compound **7** was obtained following the procedure described for the synthesis of compound **1**.



Reagents: (a) TBTU, DIEA, DMF, Ar.

Scheme 2.3. Synthesis compound **7**

3.2. The iron chelating properties of compound 1's derivatives

Compounds **5a-d** do not bear a free hydroxyl function in the quinoline moiety. Thus, they probably only present the previously described fluoroquinolones chelating properties, i.e. through Cip carboxylate and keto groups [Vu 2019]. Compound **5a** (R=Me) was selected as a

model in this family of compounds and its ability to complex iron(III) was evaluated to verify this idea. We used UV-visible spectrophotometry, as already performed for compound **1**.

Figure 2.13 shows absorbance spectra of compound **5a** in presence of iron (III) at pH 2. The addition of FeCl_3 to a solution of **5a** leads to a red shift of the π - π^* band from 284 to 296 nm and the appearance of a LMCT band at 450 nm as observed for compound **1**, suggesting iron-chelation through its fluoroquinolone part only. Besides, the spectrum also shows one isosbestic point at 344 nm, indicating the formation of a single iron complex. In addition, when the absorbance at 450 nm was plotted against the ratio $[\text{Fe(III)}]/[\mathbf{5a}]$, we observed an increase in the absorbance, followed by a plateau. The two asymptotes intersect at a ratio of 1, implying a 1:1 stoichiometry (metal-ligand) for the complex. The affinity constant of the complex at pH 2 was determined using Specfit analysis of the spectra. The low value obtained ($\log K_{11} = 2.6 \pm 0.2$) is close to that of compound **1** ($\log K_{11} = 2.5 \pm 0.3$). These results show that iron-chelating ability at pH 2.0 of compounds **1** and **5a** are similar (Table 2.4), and as expected confirm that the iron chelation occurs through by the fluoroquinolone part of **5a**.

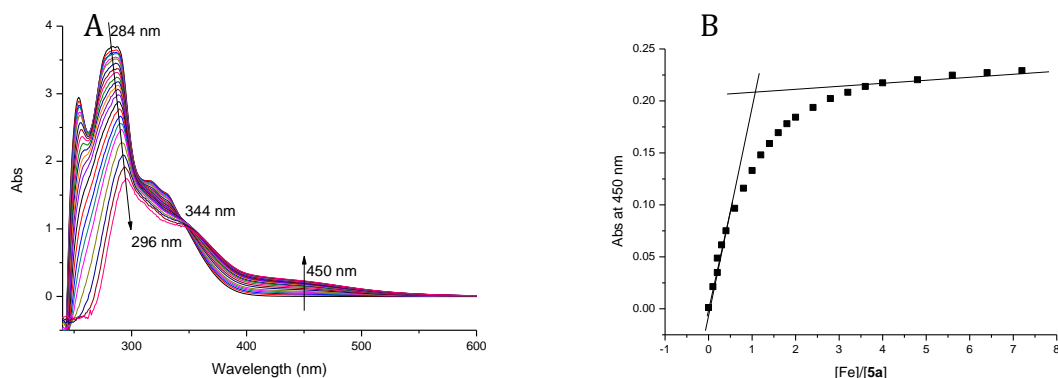


Figure 2.13. Absorption spectra in the presence of increasing concentrations of FeCl_3 (0 - 672 μM) at pH 2 and 25 ± 0.5 °C (A) of compound **5a** (10^{-4} M) (solvent: DMSO/water pH 2, 1:1, v/v); (B) Absorbance at 450 nm plotted against $[\text{Fe(III)}]/[\mathbf{5a}]$.

Table 2.4. Characterization of absorption spectra of compound **5a** and **1** at pH 2.0

Compound	π - π^* (nm)	isosbestic point (nm)	LMCT (nm)	log K_{11}
5a	284 - 296	344	450	2.6 ± 0.2
1	284 - 290	340	450	2.5 ± 0.3

Compound **6**, compound **1**'s isomer, was also studied to compare its ability to complex iron (III). Complexation experiments were performed in the same conditions, i.e. in a H₂O/DMSO (1:1; v/v) mixture.

Compound **6** has three potential sites for metal complexation: the carboxylate and the keto groups on the ciprofloxacin moiety but also the hydroxyl and the carbonyl groups or the nitrogen and hydroxyl groups on the 8-hydroxyquiniline part.

At pH 2, the addition of FeCl₃ to a solution of **6** leads to a hypsochromic shift of the π - π^* band from 284 to 280 nm (concentration of Fe³⁺, from 0 to 196 μ M) and then a bathochromic shift (red shift) of the π - π^* band from 280 to 285 nm (from 196 μ M to 385 μ M), as well as the appearance of two ligand-to-metal charge-transfer (LMCT) bands at 450 nm and 600 nm (Figure 2.14). Furthermore, an isosbestic point is observed at 352 nm and is corresponding to the formation of a single iron complex. The plots of the absorbance at 450 and 600 nm against the [Fe³⁺]/[**6**] ratio show increases in the absorbance, followed by a plateau (Figure 2.14). For each plot, the asymptotes intersect at a ratio of 1, implying the formation of iron complex with the stoichiometry of one metal for one ligand. The Specfit analysis of the spectra allows the determination of log K_{11} value of 2.8 ± 0.2 .

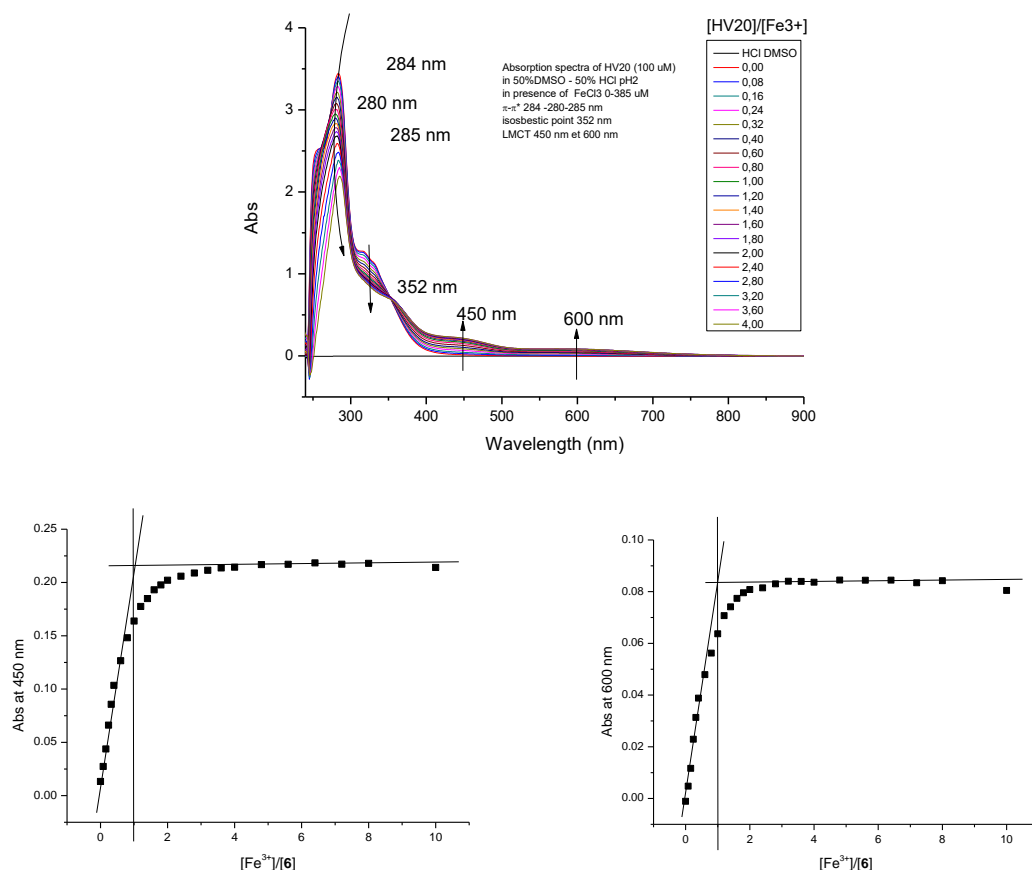


Figure 2.14. Absorption spectra in the presence of increasing concentrations of FeCl₃ (0 – 384 μ M) at pH 2 and 25 \pm 0.5 $^{\circ}$ C of compound **6** (10^{-4} M) (solvent: DMSO/ water pH 2, 1:1 v/v); Absorbance at 450 nm and 600 nm plotted against [Fe(III)]/[**6**].

In addition, at pH 7, iron-exchange experiments between Fe-nitrilotriacetic acid (Fe-NTA) and compound **6** leads to the appearance of two isosbestic points at 256 and 342 nm and two LMCT bands at 435 nm and 570 nm (Fig 2.15). The plots of absorbance at these wavelengths allow predicting the formation of a single iron complex with the same stoichiometry than at pH 2. Unlike what we observed for compound **1**, two LMCT are present in the presence of iron, and these bands are red-shifted when pH value increases. These spectral modifications are also observed in the case of HQ derivatives (see chapter III), we then supposed that iron chelation by **6** occurs through its quinoline part.

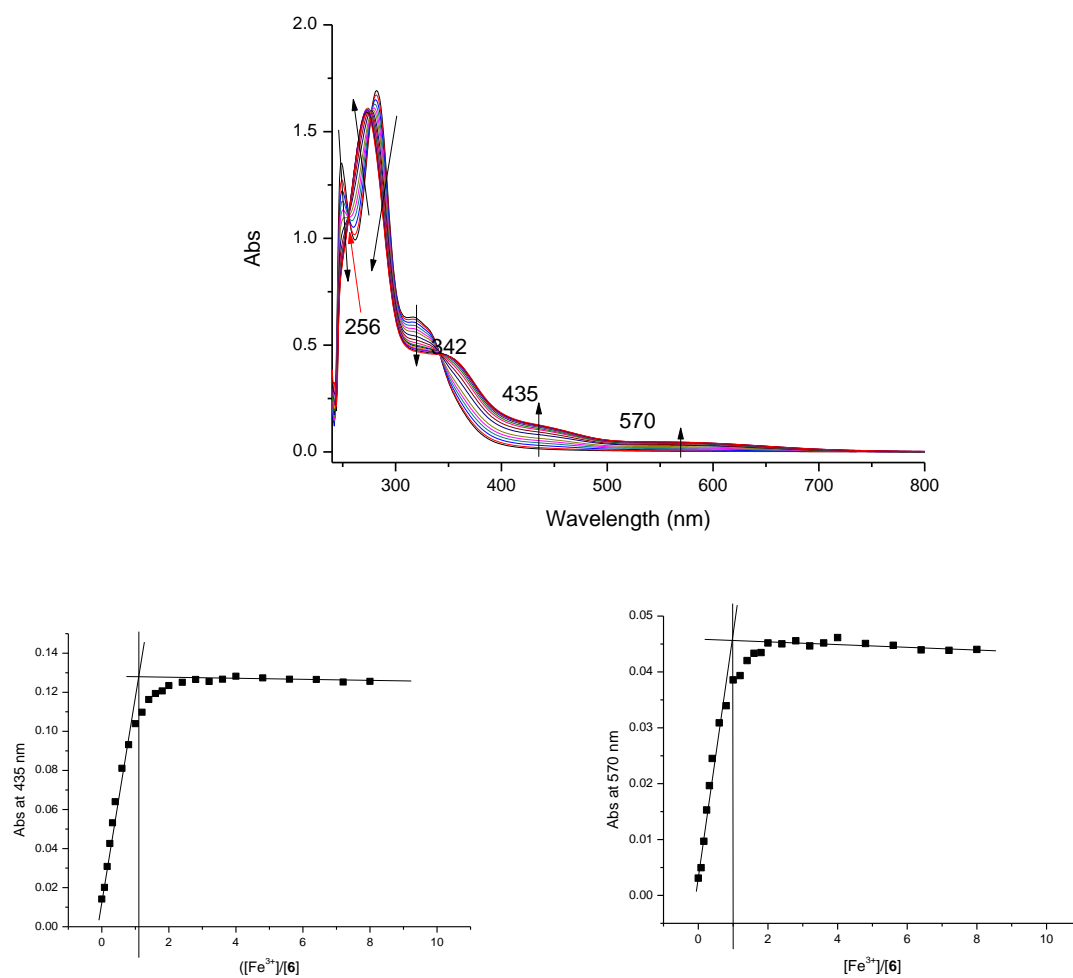


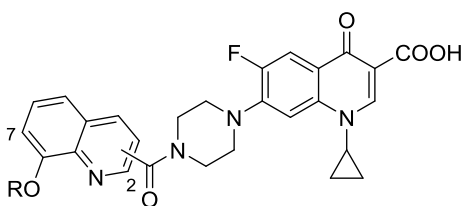
Figure 2.15. Absorption spectra in the presence of increasing concentrations of Fe-NTA (0 - 136 μM) at pH 7 and 25 ± 0.5 $^{\circ}\text{C}$ of compound **6** ($5 \cdot 10^{-5}$ M) (buffer: 50 mM HEPES - 150 mM KCl, solvent: DMSO; buffer/solvent, 1:1, v/v). Absorbance at 435 nm and 570 nm plotted against $[\text{Fe(III)}]/[\mathbf{6}]$.

In this part, we compared the iron-chelation of compounds **1**, **5** and **6**. They all formed iron-complex with the stoichiometry of 1 metal for 1 ligand, and with similar affinity constant at pH 2. However, these ligands showed different coordination mode with ferric ion. As the nitrogen of **5** is methylated, iron is complexed by the ciprofloxacin part. In compounds **1** and **6**, Cip is linked by an amide bond to 8HQ, at the 2- and 7-position, for **1** and **6**, respectively. These features induces that iron is coordinated by ciprofloxacin and hydroxyquinoline part for **1** and **6**, respectively. This will be discussed in chapter 3.

3.3. Antibacterial activity of compound 1's derivatives 5a-d, 6 and 7

The anti-*Chlamydia trachomatis* activity of the compound 1's derivatives was investigated in infected Hela cells using transformed *Chlamydia trachomatis* serovar L2 454/Bu expressing the fluorescent red protein mCherry to allow real-time monitoring of the infection cycle and screening for agents that block replication of *C. trachomatis*. Indeed, *C. trachomatis* expressing the red fluorescent protein mCherry can be detected without immunostaining [Mojica 2018]. This study was performed by Dr Åsa Gylfe (Umeå university, Umeå, Sweden).

Table 2.5 presents the half maximal effective concentration (EC₅₀) of all compounds (the greater the EC₅₀ value, the smaller antibacterial activity of compound) and the calculated octanol-water partition coefficient (clog) that features in the compounds lipophilicity. The results show that all derivatives are more potent than Cip, the parent antibiotic. Moreover, except folic acid derivative 7, they present an anti-*Chlamydia trachomatis* activity at the nanomolar range. However, only compound 6, the regioisomer, has an antibacterial activity higher than that of compound 1, reaching an excellent activity with an EC₅₀ of 10.85 nM (Table 2.5 and Figure 2.16). These results suggest that, in this series of molecules, antibacterial activity of compound 1's derivatives seems to be inversely proportional to their lipophilicity. Taking into account the macrolides lipophilic behaviour, we assume that other parameters are implicated in the good antibacterial activity of this new family of compounds. For instance, we demonstrated that the position of the carbonyl group on the 8-hydroxyquinoline heterocycle has an impact on their iron-chelation efficiency and may interfere with their antibacterial potency.

Table 2.5. The \log and EC_{50} values of compound **1**'s derivatives

Compound	CIP	1 (R=H ; C ₂ -C=O)	5a (R=Me)	5b (R=Et)	5d (R=Bn)	6 (R=H ; C ₇ -C=O)	7 (R=folic acid)
clog P ^a	-0.72	3.09	3.29	3.59	4.98	2.56	-
EC₅₀ (nM)	>50000 ^b	32.29	48.42	46.19	130.1	10.85	3416
95% confidence interval (nM)	-	30.22 - 34.49	44.85 - 52.27	42.51 - 50.18	119.5 - 141.7	10.18 - 11.58	3163- 3689

^a Computed with ChemBioDraw 13.0.0.3015

^b Minimal bactericidal concentration from [Vu 2019].

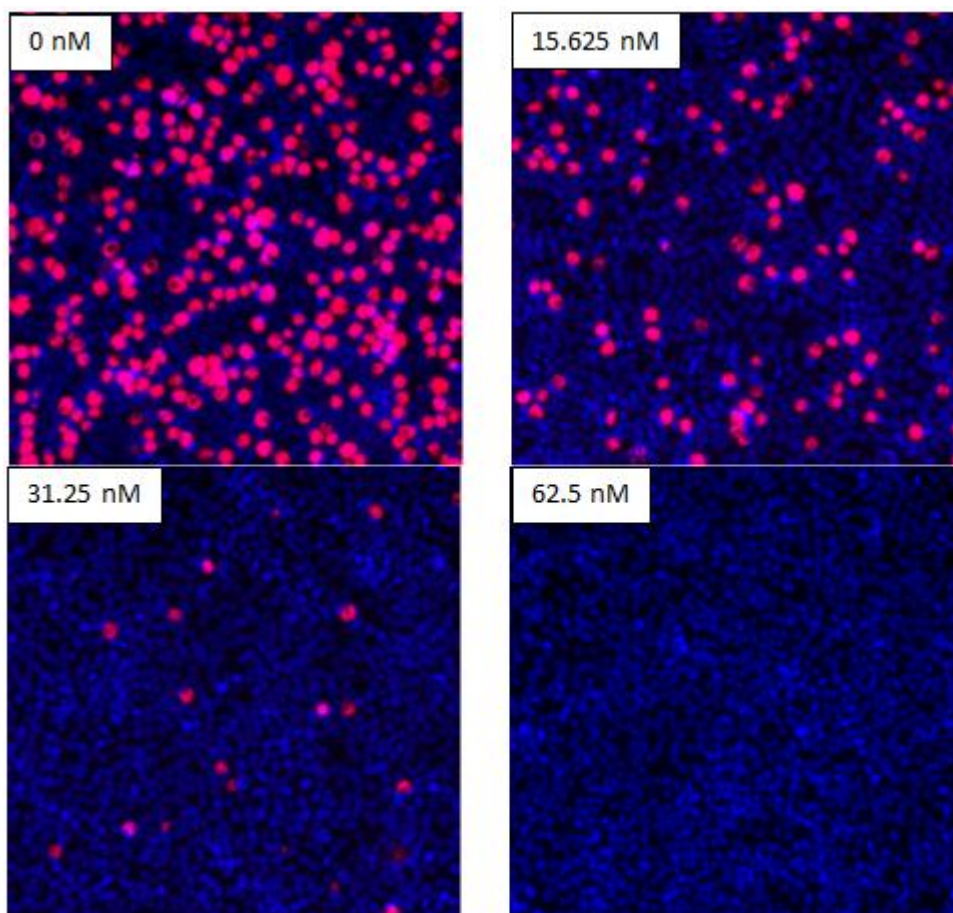


Figure 2.16. Immunofluorescence images of different concentrations of compound **6** against *C. trachomatis* L2-454/Bu infected Hela cells at 46 hours post infection (the bacterial inclusions appear in red).

4. Conclusions & Perspectives

We synthesized and characterized several Ciprofloxacin derivatives. All of them have a higher antibacterial activity than Cip against *C. trachomatis* and among them, compound **6** is the most powerful with an EC_{50} reaching 10.85 nM.

However, the antibacterial mechanism of action of this family of compounds has not been fully investigated yet. Fluoroquinolones, such as Cip, are known to block bacterial DNA synthesis by inhibiting topoisomerases II and IV. Concerning compound **1**, we demonstrated during this study that it presents a weaker IC_{50} against wild-type DNA gyrases of *M. tuberculosis* and *E. Coli* than Cip (Table 2.3). We also illustrated that its iron-chelating moiety, the 8-hydroxyquinolin heterocycle, was not implicated in its metal-chelation ability.

In order to complete this study, several suggestions are listed below.

We will evaluate Fe³⁺ ability to reverse the antibacterial activity of compound **6**. Indeed, this compound is supposed to be a stronger iron-chelator than compound **1** taking into account its salicylate coordination mode. This point will be developed in the next chapter.

We will check whether the activity of compound **7**, the folic acid-conjugate, is mediated through folic acid receptor. For this, we could set up a competitive assay where an excess of folic acid could displace compound **7** during its antibacterial evaluation.

The 8-hydroxyquinoline moiety can also form complexes with divalent transition metals such as Zn and Cu. The homeostasis of such metals is essential to avoid the deregulation of biological processes, such as amyloid- β peptide aggregation, one of the hallmarks of Alzheimer's disease, for instance [Gomes 2014]. We will therefore study in the capacities compound **1** and derivatives to complex these metals, using the methods described for iron complexation (spectrophotometry and isothermal titration calorimetry).

Finally, literature presents the fluorescent properties of 8-hydroxyquinoline derivatives and of the corresponding metal complexes [Zayed 2015] [[Jianbo 2018]. We will therefore study the fluorescent behaviour of the compounds synthesized during this study.

5. Experimental part

5.1. Organic synthesis

Materials and methods

All reagents were obtained from commercial suppliers and used without further purification. To monitor the progress of a reaction, thin-layer chromatography was performed on plastic TLC sheets of silica gel 60 F254 (layer thickness 0.2 mm) from Merck. IR, ¹H and ¹³C NMR spectra confirmed the structures of all compounds. IR spectra were recorded on a PerkinElmer Spectrum 100 FT-IR spectrometer and NMR spectra were recorded in DMSO-d₆ or CDCl₃ on a Bruker AC 400 spectrometer at 400 MHz for ¹H and 100 MHz for ¹³C. The chemical shifts are given in ppm referenced to the residual solvent signal. Coupling constants (*J*) are given in Hertz (Hz), chemical shifts in ppm, and peak multiplicities are designated as follows: s, singlet; br s: broad singlet; d, doublet; t, triplet; q, quadruplet; m, multiplet. Elemental analysis was performed by the "Service de Microanalyse" de l'Institut de Chimie des Substances Naturelles (Gif-sur-Yvette, France). High-resolution mass spectra (HRMS) were recorded at the Small Molecule Mass Spectrometry platform of IMAGIF (Centre de

Recherche de Gif - www.imagif.cnrs.fr), on a Waters spectrometer using electrospray ionization-TOF (ESI-TOF).

General procedure for ciprofloxacin coupling (compounds 1, 5a-d, 6, 7)

TBTU (1 eq.) and DIEA (1.2 eq.) were added to a solution of carboxylic acid (1 eq.) in anhydrous DMF (7 mL). After 15 min of stirring under argon, ciprofloxacin (0.9 eq.) was added and the resulting suspension stirred for 3 days. The solvent was then removed under vacuum. The residue was then triturated in a mixture of methanol and CH₂Cl₂, and recrystallization from EtOH (96%) to provide final compound.

Synthesis of 1-cyclopropyl-6-fluoro-7-(4-(8-hydroxyquinoline-2-carbonyl)piperazin-1-yl)-4-oxo-1,4-dihydroquinoline-3-carboxylic acid, (1)

From 8-hydroxyquinolin-2-carboxylic acid (0.05 g, 0.264 mmol) and following the general procedure described for Cip coupling. The residue was then triturated in a mixture of methanol and CH₂Cl₂, and recrystallization from EtOH (96%) provided compound **1** as a white powder. Yield = 22 % (0.026 g). IR (KBr, ν cm⁻¹): 1728, 1646, 1626 (C=O). ¹H NMR (DMSO-d₆) δ ppm: 1.18 (m, 2H), 1.31 (m, 2H), 3.41 (m, 2H), 3.51 (m, 2H), 3.75 (m, 3H), 3.96 (m, 2H), 7.15 (d, J = 7.3 Hz, 1H), 7.46-7.54 (m, 2H), 7.61 (d, J = 7.3 Hz, 1H), 7.74 (d, J = 8.5 Hz, 1H), 7.94 (d, J = 13.1 Hz, 1H), 8.46 (d, J = 8.5 Hz, 1H), 8.67 (s, 1H), 9.81 (s, 1H), 15.15 (br s, 1H). ¹³C NMR (DMSO-d₆) δ ppm: 7.6 (2C), 35.9, 46.3, 49.2, 49.5, 106.7, 106.8, 111.0, 112.4, 117.8, 118.8, 120.7, 128.6, 128.7, 136.8, 137.4, 139.1, 144.9, 148.1, 151.6, 153.5, 154.2, 165.9, 166.8, 176.4. Anal calcd for (C₂₇H₂₃FN₄O₅·2.5H₂O): C, 59.23; H, 5.15; N, 10.23. Found: C, 59.32; H, 4.75; N, 10.34. HRMS m/z calcd for C₂₇H₂₄FN₄O₅ [M+H]⁺ 503.1731; found 503.1724.

General procedure of alkylation of 2-methylquinolin-8-ol (compounds 2b-d)

Alkyl halide (1.5 eq.) was added to a mixture of 2-methylquinolin-8-ol and K₂CO₃ (1.5 eq.) in DMF (10 mL) and under argon. After reaction completion (TLC), DMF was removed under vacuum. Water (30 mL) was added to the crude compound and the aqueous layer was extracted twice with CH₂Cl₂ (80 mL). The combined organic layers were dried over anhydrous MgSO₄, filtered and concentrated under reduced pressure. The residue was purified by silica gel column chromatography to provide compound **2b-d** as solids.

Synthesis of 2-Methyl-8-propylquinoline (2b)

From Ethyl bromide (703.30 μ L, 9.42 mmol) and following the general procedure of alkylation. The residue was purified by silica gel column chromatography (elution: CH₂Cl₂) to obtain compound **2b** as solid. Yield = 99% (1.174 g). IR (KBr, ν cm⁻¹): 2976, 2923 (CH),

1603 (C=C_{ar}). ¹H NMR (CDCl₃) δ ppm: 1.63 (t, *J*=6.80 Hz, 3H), 2.80 (s, 3H), 4.35 (q, *J*=7.20 Hz, 2H), 7.04 (d, *J*=7.20 Hz, 1H), 7.28–7.40 (m, 3H), 8.00 (d, *J*=8.40 Hz, 1H). ¹³C NMR (CDCl₃) δ ppm: 14.4, 25.4, 64.6, 109.5, 119.3, 122.1, 125.5, 127.7, 135.8, 140.3, 154.4, 157.8.

8-Butoxy-2-méthylquinoline (2c)

From nBuBr, (1.2 g, 9.42 mmol) and following the general procedure for alkylation. The crude product was purified using silica gel chromatography with the mixture of MeOH/CH₂Cl₂ (0.5:99.5, v/v) as eluent to provide compound **2c** (1.93 g, 95%) as solid. IR (KBr, ν cm⁻¹): 2956 (-CH_{ar}), 2869 (OCH₃), 1602 (C=C_{ar}). ¹H NMR (CDCl₃) δ ppm : 1.02 (t, *J* =7.40 Hz, 3H), 1.56 (sext, *J* =7.50 Hz, 2H), 2.00 (qt, *J* =7.40 Hz, 2H), 2.76 (s, 3H), 4.22 (t, 2H, *J* =7.20 Hz), 7.03 (d, *J* =7.50 Hz, 1H), 7.35-7.25 (m, 3H), 7.98 (d, *J* =8,10 Hz, 1H). ¹³C NMR (CDCl₃) δ ppm: 13.9, 19.4, 25.7, 31.3, 69.4, 109.9, 119.5, 122.4, 125.7, 128.0, 136.0, 154.9, 158.0.

8-(Benzyloxy)-2-methylquinoline (2d)

From Benzyl bromide (1.12 mL, 9.42 mmol) and KI (104.3 mg, 0.6282 mmol) in refluxing acetone (10 mL) and following the general procedure for alkylation. The residue was crystallized in hexane (20 mL, 0°C) to provide compound **2d** (1.39 g, 88%) as solid. IR (KBr, ν cm⁻¹): 2932, 2878 (CH), 1604 (C=C_{ar}). ¹H NMR (CDCl₃) δ ppm: 2.81 (s, 3H), 5.46 (s, 2H), 7.02 (dd, *J*=7.20 Hz and 1.20 Hz, 1H), 7.26-7.39 (m, 7H), 7.52 (m, 1H), 8.0 (d, *J*=8.40 Hz, 1H). ¹³C NMR (CDCl₃) δ ppm: 25.8, 71.6, 111.5, 120.2, 122.5, 125.6, 127.6, 127.7, 128.0, 128.7, 136.1, 137.8, 140.7, 154.4, 158.2.

Oxidation using selenium dioxide – general procedure (compounds 3b-d)

2-methyl-8-alkylquinoline **2b-d** was reacted with SeO₂ (1.1 eq.) in refluxing and degassed 1,4-dioxane (10 mL) for 2.5 hours. The mixture was then cooled to room temperature; the precipitate filtered and washed several times using CH₂Cl₂. The combined filtrates were concentrated under vacuum and the residue was purified as described below.

8-Propylquinoline-2-carbaldehyde (3b)

From 2-methyl-8-propyloxyquinoline (1.164 g, 6.220 mmol) and following the general procedure using selenium dioxide. A silica gel column chromatography (solvent: MeOH/CH₂Cl₂, 1:99, v/v) provided compound **3b** (0.378 g, 31 %) as oil. IR (KBr, ν cm⁻¹): 2830, 2935, 2980 (CH), 1707 (-CHO). ¹H NMR (CDCl₃) δ ppm: 2.72 (t, *J*=6.80 Hz, 3H), 4.40 (q, *J*=7.20 Hz, 2H), 7.16 (d, *J* = 8.00 Hz, 1H), 7.46 (d, *J*=8.00 Hz, 1H), 7.60 (t, *J*=8.0 Hz, 1H),

8.06 (d, $J=8.40$ Hz, 1H), 8.27 (d, $J=8.40$ Hz, 1H), 10.30 (s, 1H). ^{13}C NMR (CDCl_3) δ ppm: 14.5, 65.0, 110.0, 117.6, 119.4, 129.5, 131.4, 137.0, 140.4, 151.61, 193.5.

8-Butoxyquinoline-2-carbaldehyde (3c)

From 8-butoxy-2-methylquinoline (665 mg, 6.28 mmol) and following the general procedure using selenium dioxide. The crude compound was used in the next step without purification. IR (KBr, ν cm^{-1}): 2958 ($-\text{CH}_{\text{ar}}$), 2873 ($-\text{OCH}_2$), 1707 ($\text{C}=\text{O}$). ^1H NMR (CDCl_3) δ ppm: 1.05 (t, $J=7.30$ Hz, 3H), 1.60 (sext, $J=7.50$ Hz, 2H), 2.04 (quint, $J=7.10$ Hz, 2H), 4.29 (t, $J=6.90$ Hz, 2H), 7.13 (d, $J=7.70$ Hz, 1H), 7.43 (d, $J=8.20$ Hz, 1H), 7.58 (t, $J=8.00$ Hz, 1H), 8.03 (d, $J=8.40$ Hz, 1H), 8.25 (d, $J=8.40$ Hz, 1H), 10.27 (s, 1H). ^{13}C NMR (CDCl_3) δ ppm: 13.9, 19.4, 31.3, 69.6, 110.4, 117.8, 119.6, 129.82, 131.6, 137.2, 151.8, 156.2, 193.8.

8-(Benzyloxy)quinolone-2-carbaldehyde (3d)

From 8-(benzyloxy)-2-methylquinoline (500 mg, 2 mmol) and following the general procedure using selenium dioxide. The mixture was then heated at 80°C under argon for 3 hours (no more starting material could be detected; TLC: DCM/MeOH 98:2). The residue was purified using silica gel column chromatography (solvent: CH_2Cl_2) to obtain compound **22** (352.7 mg, 67 %) as yellow-brown solid. IR (KBr, ν cm^{-1}): 3068-2836 (CH), 1696 ($\text{C}=\text{O}$), 1657 ($\text{C}=\text{N}$), 1614 ($\text{C}=\text{C}_{\text{ar}}$). ^1H NMR (CDCl_3) δ ppm: 5.49 (s, 2H), 7.16 (dd, $J=7.70$ Hz and 1.1 Hz, 1H), 7.31 – 7.35 (m, 1H), 7.38 – 7.42 (m, 2H), 7.47 (dd, $J=8.20$ Hz and 1.10 Hz, 1H), 7.54 (m, 3H), 8.08 (d, $J=8.40$ Hz, 1H), 8.28 (d, $J=8.50$ Hz, 1H), 10.32 (s, 1H). ^{13}C NMR (CDCl_3) δ ppm: 71.9, 112.0, 118.0, 120.4, 127.5, 128.2, 128.9, 129.8, 131.8, 137.1, 137.4, 152.1, 193.9.

General procedure for oxidation using Oxone® (compounds 4b-c)

Oxone® (1.06 eq.) was added a solution aldehydes **3b-c** in DMF. The mixture was stirred at RT for 2 hours. The DMF was then removed under vacuum. The obtained residue was treated with 1N HCl (2 mL) to dissolve the salt. Then, ethyl acetate (15 mL) was added to extract the products. The combined organic extracts were washed with water (2 mL) and brine (2 mL), dried over anhydrous MgSO_4 and filtered. After evaporation of the solvent, the crude product obtained was purified by silica gel column chromatography (elution: EtOAc/Hexane, 1:1, v/v) to provide compounds **4b-c**.

8-Propylquinoline-2-carboxylic acid (4b)

From 8-propyloxyquinoline-2-carbaldehyde **3b** (128 mg, 0.636 mmol) and following the general procedure using Oxone® in DMF (5 mL). A silica gel column chromatography (elution: EtOAc/Hexane, 1:1, v/v) provided compound **17** (72 mg, 52 %). TLC (1%

MeOH/DCM) was used to monitor during reacting and purification. IR (KBr, ν cm^{-1}): 3185 (OH), 2942, 2985 (CH), 1720 (-COOH). ^1H NMR (CDCl_3) δ ppm: 1.62 (t, $J=7.20$ Hz, 3H), 4.30 (q, $J=6.80$ Hz, 2H), 7.14 (d, $J=7.60$ Hz, 1H), 7.48 (d, $J=8.00$ Hz, 1H), 7.60 (t, $J=8.00$ Hz, 1H), 8.28 (d, $J=8.40$ Hz, 1H), 8.36 (d, $J=8.4$ Hz, 1H). ^{13}C NMR (CDCl_3) δ ppm: 14.5, 64.7, 110.2, 119.1, 119.4, 129.5, 131.2, 138.2, 138.3, 144.7, 155.0, 164.0.

8-Butoxyquinoline-2-carboxylic acid (4c)

A solution of aldehyde **5** (100 mg, 0.436 mmol) and Oxone (134.01 mg, 0.436 mmol) in DMF was stirred under argon for 16 h. After evaporation of DMF under vacuum, the residue obtained was dissolved in a 1N HCl solution and the organic phase was extracted with ethyl acetate and then washed with water, dried over MgSO_4 , evaporated and purified on silica gel column using a mixture of MeOH/ CH_2Cl_2 (5:95, v/v) as eluent to afford compound **4c** (68.1 mg, 63% yield). IR (KBr, ν cm^{-1}): 3434 (-OH), 2957 ($-\text{CH}_{\text{ar}}$), 2871 ($-\text{OCH}_2$), 1641 (C=O), 1603 (C= C_{ar}). ^1H NMR (CDCl_3) δ ppm : 1.03 (t, $J = 7.30$ Hz, 3H), 1.58 (sext, $J = 7.50$ Hz, 2H), 1.95 (qt, $J = 7.10$ Hz, 2H), 4.22 (t, $J = 6.50$ Hz, 2H), 7.13 (d, $J = 7.70$ Hz, 1H), 7.48 (d, 1H, $J = 8.30$ Hz, 1H) 7.58 (t, $J = 8.10$ Hz, 1H), 8.26 (d, $J = 8.40$ Hz, 1H), 8.35 (d, $J = 8.40$ Hz, 1H). ^{13}C NMR (CDCl_3) δ ppm: 13.9, 19.6, 31.4, 69.3, 110.5, 119.3, 119.6, 129.8, 131.5, 138.5, 138.6, 144.9, 155.4, 164.3.

8-(Benzyloxy)quinolone-2-carboxylic acid (4d)

$\text{H}_2\text{NSO}_3\text{H}$ (221.3 mg, 2.28 mmol) and NaClO_2 (206.1 mg, 2.28 mmol) were added to a cooled solution of 8-(benzyloxy)quinolone-2-carbaldehyde **3d** (150 mg, 0.57 mmol) in THF (4 mL) and H_2O (3 mL). After one hour of stirring, water (25 mL) was slowly added under sonication for 45 minutes to provide a white precipitate which was filtered, washed with water, and dried under vacuum to provide compound **5d** (144.6 mg, 91% yield). IR (KBr, ν cm^{-1}): 3490, 3360 (OH), 3065, 2918 ($-\text{CH}$), 1714 (C=O), 1504 (C= C_{ar}). ^1H NMR (CDCl_3) δ ppm: 5.35 (s, 2H), 7.21 (d, $J=7.60$ Hz, 1H), 7.35 - 7.45 (m, 3H), 7.52 (m, 3H), 7.59 (t, $J=8.00$ Hz, 1H), 8.29 (d, $J=8.40$ Hz, 1H), 8.37 (d, $J=8.40$ Hz, 1H). ^{13}C NMR (CDCl_3) δ ppm: 71.6, 111.7, 119.8, 120.0, 127.4, 128.4, 128.9, 129.7, 131.5, 136.7, 138.7, 155.1, 164.3.

7-(4-(8-(Methyloxy)quinoline-7-carbonyl)piperazin-1-yl)-1-cyclopropyl-6-fluoro-4-oxo-1,4-dihydroquinoline-3-carboxylic acid (5a)

From 8-methoxyquinoline-2-carboxylic acid (50mg, 0.248 mmol) and following general procedure for Cip coupling. Trituration in MeOH provided compound **5a** (92 mg, 71 %) as yellow solid. IR (KBr, ν cm^{-1}): 3471 (OH), 1712, 1625 (C=O). ^1H NMR ($\text{DMSO}-d_6$) δ ppm: 1.18 (m, 2H), 1.31 (m, 2H), 3.38 (m, 2H), 3.51 (m, 2H), 3.77 (m, 1H), 3.87 (m, 2H), 3.98 (m,

5H), 7.19 (d, $J=7.36$ Hz, 1H), 7.50-7.57 (m, 3H), 7.74 (d, $J=8.44$ Hz, 1H), 7.91 (d, $J=13.04$ Hz, 1H), 8.38 (d, $J=8.48$ Hz, 1H), 8.67 (s, 1H), 15.07 (s, 1H). ^{13}C NMR (DMSO- d_6) δ ppm: 7.5, 35.5, 41.4, 46.3, 49.1, 49.6, 55.7, 106.2, 106.9, 108.7, 110.9, 111.2, 119.1, 120.8, 127.8, 128.7, 136.9, 138.7, 144.5, 147.6, 151.6, 155.1, 165.7, 166.5, 176.1. HRMS m/z calcd for $\text{C}_{28}\text{H}_{26}\text{FN}_4\text{O}_5$ $[\text{M}+\text{H}]^+$ 517.1887; found 517.1894.

7-(4-(8-(Propyloxy)quinoline-7-carbonyl)piperazin-1-yl)-1-cyclopropyl-6-fluoro-4-oxo-1,4-dihydroquinoline-3-carboxylic acid (5b)

From 8-propyloxyquinoline-2-carboxylic acid (51 mg, 0.235 mmol) and following general procedure for Cip coupling. Trituration in MeOH provided compound **5b** obtained as solid. Yield = 77.9 % (97 mg). IR (KBr, ν cm^{-1}): 3458 (OH), 3041, 2895 (CH), 1719, 1619 (C=O). ^1H NMR (CDCl_3) δ ppm: 1.21 (m, 2H), 1.40 (m, 2H), 1.56 (t, $J=6.80$ Hz, 3H), 3.49-3.56 (m, 4H), 4.12 (m, 2H), 4.27 (m, 4H), 7.10 (d, $J=7.60$ Hz, 1H), 7.43 (m, 2H), 7.53 (d, $J=8.0$ Hz, 1H), 7.95 (d, $J=8.5$ Hz, 1H), 8.07 (d, $J=13.00$ Hz, 1H), 8.26 (d, $J=8.40$ Hz, 1H), 8.79 (s, 1H), 14.93 (s, 1H). ^{13}C NMR (CDCl_3) δ ppm: 8.1, 14.7, 35.1, 64.6, 104.8, 119.3, 122.0, 128.2, 136.8, 139.1, 147.4, 151.6, 155.1, 165.7, 166.5, 176.1. HRMS m/z calcd for $\text{C}_{29}\text{H}_{28}\text{FN}_4\text{O}_5$ $[\text{M}+\text{H}]^+$ 531.2044; found 531.2034.

7-(4-(8-Butoxyquinoline-2-carbonyl)piperazin-1-yl)-1-cyclopropyl-6-fluoro-8-méthoxy-4-oxo-1,4-dihydroquinoline-3-carboxylic acid (5c)

From carboxylique acid (106.7 mg, and following the general procedure for Cip coupling. Trituration in MeOH provided compound **5c** (143 mg, 77 %) obtained as solid. IR (KBr, ν cm^{-1}): 2918 (OH), 1626 (C=O). ^1H NMR (DMSO- d_6) δ ppm: 0.84 (t, $J = 7.36$ Hz, 3H), 0.99 (m, 2H), 1.26 (m, 2H), 1.49 (sext, $J = 7.44$ Hz, 2H), 1.77 (qt, $J = 6.84$ Hz, 2H), 3.37 (m, 4H), 3.56 (m, 1H), 3.94 (m, 4H), 4.16 (t, $J = 6.63$ Hz, 2H), 7.23 (d, $J = 7.28$ Hz, 1H), 7.45 (d, $J = 7.36$ Hz, 1H), 7.55 (m, 2H), 7.80 (m, 2H), 8.45 (d, $J = 8.56$ Hz, 1H), 8.47 (s, 1H). ^{13}C NMR (DMSO- d_6) δ ppm : 7.1, 13.1, 18.4, 30.4, 33.7, 41.5, 46.4, 49.3, 50.2, 68.1, 105.8, 109.9, 111.6, 118.9, 119.3, 120.8, 121.2, 127.8, 128.6, 136.7, 146.4, 166.1. HRMS m/z calcd for $\text{C}_{31}\text{H}_{32}\text{FN}_4\text{O}_5$ $[\text{M}+\text{H}]^+$ 559.2357; found 559.2366.

7-(4-(8-(Benzyloxy)quinoline-7-carbonyl)piperazin-1-yl)-1-cyclopropyl-6-fluoro-4-oxo-1,4-dihydroquinoline-3-carboxylic acid (5d)

From 8-(benzyloxy)quinoline-2-carboxylic acid **4d** (50 mg, 0.179 mmol) and following the general procedure for Cip coupling. Trituration in MeOH provided compound **5d** (75.5 mg, 71 %) obtained as solid. IR (KBr, ν cm^{-1}): 3448 (OH), 3021-2865 (CH), 1726, 1616 (C=O). ^1H NMR (CD_2Cl_2) δ ppm: 1.17 (m, 2H), 1.32 (m, 2H), 3.41 (m, 2H), 3.47 (m, 3H), 4.09 (m,

2H), 4.15 (m, 2H), 7.14–7.21 (m, 2H), 7.29 (m, 2H), 7.41 (d, $J=6.80$ Hz, 1H), 7.49–7.58 (m, 4H), 7.88 (d, $J=8.40$ Hz, 1H), 8.06 (d, $J=12.80$ Hz, 1H), 8.32 (d, $J=8.40$ Hz, 1H), 8.78 (s, 1H), 14.97 (s, 1H). ^{13}C NMR (CD_2Cl_2) δ ppm: 8.7, 35.8, 106.1, 120.6, 122.4, 128.1, 128.6, 128.7, 129.1, 130.4, 137.5, 148.2, 167.6. HRMS m/z calcd for $\text{C}_{34}\text{H}_{30}\text{FN}_4\text{O}_5$ $[\text{M}+\text{H}]^+$ 593.2221; found 593.2200.

1-Cyclopropyl-6-fluoro-7-(4-(8-hydroxyquinoline-7-carbonyl)piperazin-1-yl)-4-oxo-1,4-dihydroquinoline-3-carboxylic acid (6)

From 8-hydroxyquinoline-7-carboxylic acid (30 mg, 0.158 mmol) and following the general procedure for Cip coupling (the mixture was heated at 80°C for 24 hrs). Trituration in MeOH provided compound **6** as solid (30 mg, 37%). IR (KBr, ν cm^{-1}): 3400, 3304 (OH), 1732, 1626 ($\text{C}=\text{O}$). ^1H NMR ($\text{DMSO}-d_6$) δ ppm: 1.18 (m, 2H), 1.32 (m, 2H), 3.45 (m, 2H), 3.51 (m, 2H), 3.61 (m, 1H), 3.82 (m, 2H), 3.93 (m, 2H), 7.43 (d, $J=8.40$ Hz, 1H), 7.49 (d, $J=8.80$ Hz, 1H), 7.59 – 7.66 (m, 2H), 7.93 (d, $J=13.20$ Hz, 1H), 8.39 (dd, $J=8.00$ Hz and 1.20 Hz, 1H), 8.67 (s, 1H), 8.93 (dd, $J=4.1$ and 1.5 Hz, 1H), 15.19 (s, 1H). ^{13}C NMR ($\text{DMSO}-d_6$) δ ppm: 7.2, 35.4, 49.2, 117.7, 118.7, 122.3, 126.0, 135.8, 138.9, 147.5, 148.5, 148.7, 165.2, 166.6, 175.9. HRMS m/z calcd for $\text{C}_{27}\text{H}_{24}\text{FN}_4\text{O}_5$ $[\text{M}+\text{H}]^+$ 503.1731; found 503.1706.

7-(4-(4-(4-(((2-Amino-4-hydroxyptéridin-6-yl)méthyl)amino)benzamido)-4-carboxybutanoyl)pipérazin-1-yl)-1-cyclopropyl-6-fluoro-4-oxo-1,4-dihydroquinoline-3-carboxylic acid (7)

From folic acid (100 mg, 0.226 mmol) and following the general procedure for Cip coupling. The residue was first recrystallized hot from water. A second recrystallization in EtOH provided compound **7** as solid ($m = 81$ mg, 48%). IR (ATR, ν cm^{-1}): 3347 (OH), 1701, 1627 ($\text{C}=\text{O}$), 1607 ($\text{C}=\text{C}_{ar}$). ^1H NMR ($\text{DMSO}-d_6$) δ ppm: 1.05 (m, 2H), 1.29 (m, 2H), 1.90–2.08 (m, 4H), 3.64–3.88 (m, 5H), 4.34 (m, 1H), 4.47 (m, 2H), 4.99 (m, 1H), 6.63 (m, 2H), 6.93 (m, 3H), 7.53 (m, 1H), 7.66 (m, 2H), 8.15 (m, 1H), 8.65 (m, 2H), 11.45 (br s, 1H), 15.18 (br s, 1H). ^{13}C NMR ($\text{DMSO}-d_6$) δ ppm: 7.2, 28.7, 30.2, 35.0, 35.4, 45.7, 49.0, 51.5, 51.8, 106.7, 110.6, 110.8, 111.0, 127.6, 128.5, 128.6, 138.8, 147.5, 148.1, 150.4, 153.4, 165.4, 166.0, 171.0, 174.5, 176.0. HRMS m/z calcd for $\text{C}_{36}\text{H}_{34}\text{FN}_{10}\text{O}_8$ $[\text{M}-\text{H}]^+$ 753.2545; found 753.2556.

5.2. Biology

5.2.1. Compound 1

Chlamydia trachomatis: bacteria, cell culture and biological reagents- Collaboration with Dr Philippe Verbeke, U1139, Hôpital Bichat, Paris, France).

HeLa cells were obtained from and cultured as recommended by ATCC (Manassas, VA), in 75 cm² tissue culture flasks for maintenance and in 24-well, 48-well or 96-well plates for assays. *C. trachomatis* serovar L2 was from ATCC. A stock of bacteria was prepared in HeLa cells as previously described and stored at -80 °C in sucrose-phosphate-glutamic acid (SPG) buffer (10 mM sodium phosphate [8 mM Na₂HPO₄ - 2 mM NaH₂PO₄], 220 mM sucrose, 0.50 mM L-glutamic acid) for later use [Dumoux 2013]. The number of bacterial inclusion-forming units (IFU) was determined using a method described previously [Abdelsayed 2014]. DMEM (Dulbecco's Modified Eagle's medium) and fetal calf serum (FCS) were purchased from Invitrogen (Carlsbad, CA, USA). Anti-*Chlamydia* genus-FITC (Fluorescein isothiocyanate) antibody was from Argene (Argene Biosoft 12-114, Varhiles, France). Toxicity of the molecules was assayed on mouse embryonic fibroblasts and HeLa cells. Briefly, cells were grown in 24-well plates, were incubated with different concentrations of the molecules (0–200 µM) and cultivated for 24 to 48 h. Cell proliferation was measured by counting the cells in each well and comparing with control cells incubated without any product. Cell death was measured by Trypan Blue exclusion 24 to 48 h after incubation with the molecules.

Inhibition of M. tuberculosis and E. coli DNA gyrases (DNA supercoiling assays, IC₅₀ determination) - Collaboration with Pr Alexandra Aubry, AP-HP, Hôpital Pitié-Salpêtrière, Centre National de Référence des Mycobactéries et de la Résistance des Mycobactéries aux Antituberculeux, F-75013 Paris, France.

DNA supercoiling activity was tested with various ratios of purified *M. tuberculosis* and *E. coli* GyrA and GyrB subunits. The reaction mixture (total volume, 30 µL) contained DNA gyrase assay buffer (40 mM Tris-HCl [pH 7.5], 25 mM KCl, 6 mM magnesium acetate, 2 mM spermidine, 4 mM dithiothreitol, bovine serum albumin [0.36 mg/mL], 100 mM potassium glutamate (except for *E. coli*), 0.1 mM EDTA, 1 mM ATP) (pH 8.0) and relaxed pBR322 DNA (0.4 µg) as the substrate. Gyrase proteins were added, and the reaction mixtures were incubated at 37 °C for 1 h. Reactions were terminated by the addition of 50% glycerol containing 0.25% bromophenol blue, and the total reaction mixture was subjected to electrophoresis in a 1% agarose gel in 0.5× TBE (Tris-borate-EDTA, pH 8.3) buffer. After

running for 16h at 40 V, the gel was stained with ethidium bromide (0.7 µg/mL). One unit of enzyme activity was defined as the amount of DNA gyrase that converted 300 ng of relaxed pBR322 to the supercoiled form in 1h at 37°C. Inhibition of supercoiling activity of the recombinant DNA gyrases was performed by the method described previously [Pan 1999]. In brief, a reaction mixture containing 1 U of purified DNA gyrase and increasing concentrations of quinolones was incubated as described above. The inhibitory effect of quinolones on DNA gyrase was assessed by determining the concentration of drug required to inhibit the supercoiling activity of the enzyme by 50% (IC₅₀). Supercoiling activity was assessed by tracing the brightness of the bands corresponding to the supercoiled pBR322 DNA with Molecular Analyst software (Bio-Rad).

Antimicrobial susceptibility tests for bacteria from the ESKAPE group - Collaboration with Pr Patrick Plésiat, Centre National de Référence de la résistance aux antibiotiques, Hôpital Jean Minjoz, boulevard Fleming, 25030 Besançon, France.

Drug susceptibility testing was performed as recommended by the Clinical and Laboratory Standards Institute [Patel 2015], by using the conventional microdilution method (in a final volume of 100 µL per well), Mueller-Hinton broth and sterile microtiter plates.

Statistical analysis

Data are presented as the mean ± standard deviation of experiments, and p values were calculated using a two-tailed two-sample equal-variance Student's t test. Statistically significant differences are noted as follows: * p<0.05, ** p<0.01, *** p<0.001.

5.2.2. Compound 1's derivatives (5a, 5b, 5d, 6, 7) - Collaboration with Dr Åsa Gylfe, Umeå university, Umeå, Sweden).

Cell culture and Chlamydia propagation

HeLa 229 cells (CCL-2.1; ATCC) were cultured at 37°C (5% CO₂) in RPMI-1640 medium (HyClone) with 25 mM HEPES and 2.0527mM L-glutamine, supplemented with 10% fetal bovine serum (FBS) (Sigma-Aldrich). Transformed *Chlamydia trachomatis* serovar L2 454/Bu (VR902B; ATCC) expressing the fluorescent red protein mCherry (CT L2 mCherry) [Mojica 2018] was cultured in HeLa cells. Stocks of CT L2 mCherry elementary bodies were purified as described by Caldwell *et al.* [Caldwell 1981] and stored at -80 °C in SPG buffer (0.25 M Sucrose, 10 mM sodium phosphate and 5 mM L-glutamic acid)

Reinfection assay

Reinfection experiments were performed as previously described [Good 2016] with adjustments to enable detection of the mCherry expressing *C. trachomatis* strain. HeLa cells were infected with CT L2 mCherry purified elementary bodies in Hank Balanced Salt Solution (HBSS) at a multiplicity of infection (MOI) of 0.5 in 96 well-plates. After 1h, the HBSS was replaced with cell culture media containing test compounds diluted in DMSO. The final concentration of DMSO was 0.2%. Progeny *Chlamydia* was harvested 46h post infection, through osmotic host cell lysis by addition of cold Milli-Q water. 4X SPG was added to get a final concentration of 1X SPG and 10-fold serial dilutions were performed in HBSS. Fresh HeLa cells were infected with the diluted progeny. HBSS was substituted with cell culture medium 1 h post infection. At 44 h post infection Hoechst 33342 (Thermo Scientific), 0.1ug per well, was added 20 min prior to fixation with 4% formaldehyde (Sigma-Aldrich) for 15min followed by washing in PBS. The 96 well plate was analyzed by Arrayscan automated microscopy (ArrayScan VTI HCS, Thermo Scientific). Images of nuclei (Hoechst-ex386/23nm) and Chlamydia inclusions (mCherry: ex549/15nm) were acquired in 10 visual fields with the 10x objective and inclusion forming units (IFUs) were counted with the built in software. To exclude small underdeveloped inclusions as well as red fluorescent artefacts, a size cut off was determined based on Chlamydia inclusions in DMSO control wells. The images were also manually inspected to exclude any field that had lost cells during the washing process. Relative infection was calculated as the percentage of IFUs compared to DMSO treated controls. All experiments were performed three times with three technical replicates in each experiment.

EC₅₀

EC₅₀ was calculated using GraphPad Prism. Values from three individual experiments were normalized by setting DMSO treated infections to 100% and calculating the relative infection for each compound concentration. Concentrations were transformed to log scale and a non-linear regression curve fit was performed using log(inhibitor) vs normalized response-variable slope.

5.3. Metal chelation

5.3.1. Stock solutions

Because of its poor solubility in aqueous media, compound **1** and its derivatives were first dissolved in DMSO at 10^{-2} M. The complexation experiments were performed in a H₂O/DMSO mixture (1:1, v/v) at a concentration of $1 \cdot 10^{-4}$ M of **1**, in HCl at pH 2 or HEPES buffer (50 mM HEPES, 150 mM KCl, pH 7.0). FeCl₃ solutions were prepared in acidic media (pH 2). FeNTA solutions were prepared as previously described.

5.3.2. Spectrophotometric measurements

Affinity constants were determined spectrophotometrically by the use of the SPECFIT32 Global Analysis program [Binstead 2003]. Spectroscopic measurements were performed at 25.0 ± 0.5 °C on a Cary 4000 spectrophotometer.

CHAPTER III: INFLUENCE OF THE CARBONYL GROUP OF THE 8-HYDROXYQUINOLINE MOIETY ON ITS METAL CHELATING PROPERTIES

1. Introduction

8-Hydroxyquinoline (HQ) is a well-known ligand within the fields of materials science, supramolecular and medicinal chemistry. The deprotonation of its phenolic-like function added to the proximity of its heterocyclic nitrogen imparts it a strong bidentate character allowing the formation of stable hexa- or tetra-coordinated complexes with a broad range of transition metal and lanthanide cations [Al-Busafi 2014] [Türke 2013] [Zuki 2012] [Li 2008]. Over the past 20 years, its popularity has never stopped to grow as an aluminium (III) chelating agent. It produces the tris(8-hydroxyquinoline)aluminium(III) [Al(HQ)₃], a hexa-coordinated complex widely involved in promising low-molecular-weight precursor suitable for organic light emitting diode (OLED) applications [Chen 1998] [Tang 1987] [Tang 1989].

In parallel, the interest in HQ has increased for medicinal inorganic chemistry as a robust alternative to the usual catechol, hydroxamic acid and α -hydroxycarboxylic acid chelating agents [Pierre 2003]. Some of its derivatives were recently reported for their anti-microbial, anti-cancer, anti-bacterial, and/or anti-neurodegenerative activities [Cherdrakulkiat 2016] [Oliveri 2016] [Prachayasittikul 2013]. One of the pharmacological responses to HQ derivatives *in vivo* is their interaction with metals, such as Cu, Zn or Fe. Iron plays a crucial part in the growth process of living organisms [Crichton 2001]. For example, it participates in respiration mechanisms with the transport of molecular oxygen, DNA synthesis and repair catalyzed by ribonucleotide reductase, and electron transport chains across membranes. Nevertheless, iron is also involved in Fenton- and Haber-Weiss-type chemistry which generates highly reactive oxygen radicals that cause irreversible damage to cells and their environment [Koppenol 2001]. Furthermore, in its most stable oxidation state (*i.e.*, iron(III)), the cation is insoluble in physiological conditions and precipitates as an iron(III) oxide. For this reason, in microorganisms, the metal is chelated by low-molecular-weight ligands called siderophores with affinities between 10^{15} and 10^{40} [Saha 2012] [Hider 2010].

In case of iron-overload disorders such as thalassemia or haemochromatosis, chelation therapies with natural or synthetic siderophores are carried out to remove the excess of iron from the organism [Hider 2013] [Ma 2012] [Tilbrook 1998]. Deferoxamine is a common example of natural siderophore extracted from the bacteria *Streptomyces pilosus* [Rakba 1995]. However, the development of synthetic siderophores is of particular interest since they allow the development of new metal chelators with improved selectivity and affinities.

Within this framework, a tripodal tris(bidentate) family of ligands containing three HQ units was synthesized. They present biological functions as cellular protection, antiproliferative and apoptotic effects [Lescoat 2012] [Crisponi 2008] [Du Moulinet d'Hardemare 2006] [Liu 2002]. Known as TRENTOX, the skeleton of the tripodal ligand consists of 3 HQ-5-sulfonate subunits linked by amide bond to tris(2-aminoethyl) amine (TREN) (Figure 3.1). According to the HQ substitution position (*i.e.*, at 7- or 2-position, see Figure 3.3), the tripodal ligand is dubbed O-TRENTOX or N-TRENTOX, respectively. Both chelators exhibit a high affinity for iron (III), but the pFe value of N-TRENTOX is calculated as 7 orders of magnitude lower than that of O-TRENTOX (22.5 versus 29.5, respectively) [Serratrice 1997] [Caris 1996].

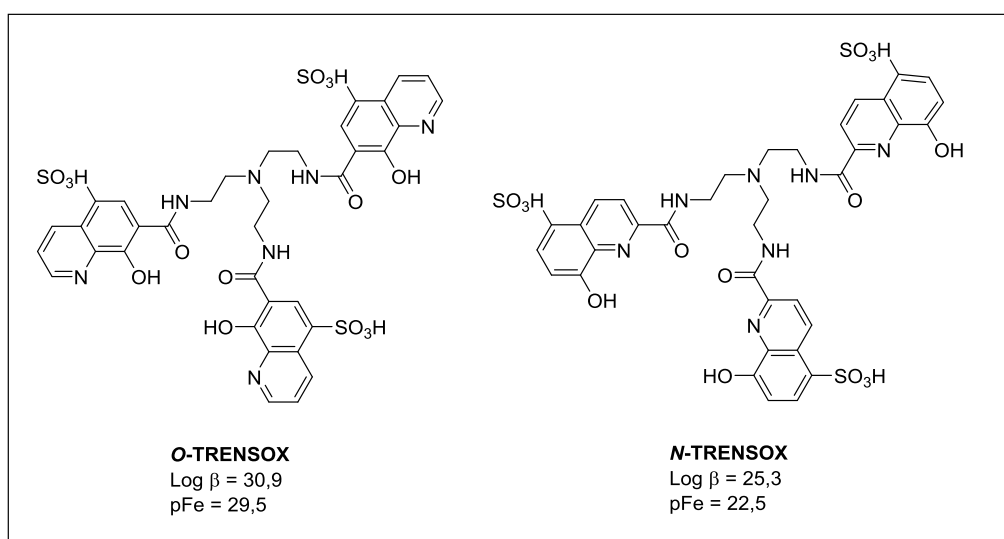


Figure 3.1. Structures of O- and N-TRENTOX and their iron chelating capacities.

Furthermore, we synthesized a 3-isoxazolidone derivative and a ciprofloxacin conjugate, both bearing by an amide bond HQ at position 2 (Figure 3.2). These molecules present high activities against *Chlamydia trachomatis* but are not able to chelate iron(III) through their HQ moieties [Vu 2018] [Abdelsayed 2014].

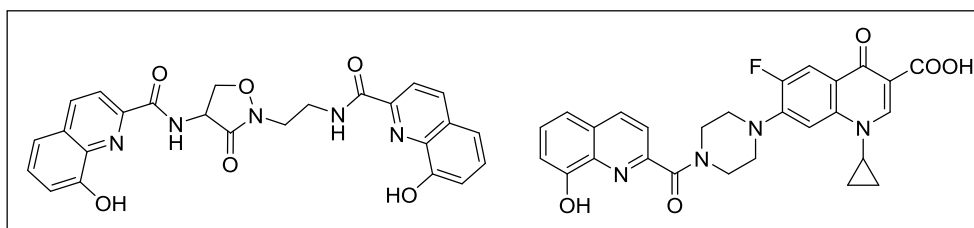


Figure 3.2. Previously 8-hydroxyquinoline derivatives obtained in the group.

Out of some macroscopic conclusions, the iron(III) affinities measured for 2- and 7-substituted HQ by electron withdrawing groups still remain non-rationalized. To disentangle the different effects acting on this chelation mechanism, we propose to assess a mixed experimental and theoretical spectroscopic study aiming at understanding the ability of 2- and 7-ester HQ, dubbed here as NHQ and OHQ, respectively, to chelate the metal cation (Figure 3.3). This study has been performed in collaboration with Dr Eric Brémond and Dr Mahamadou Seydou (ITODYS, Université de Paris).

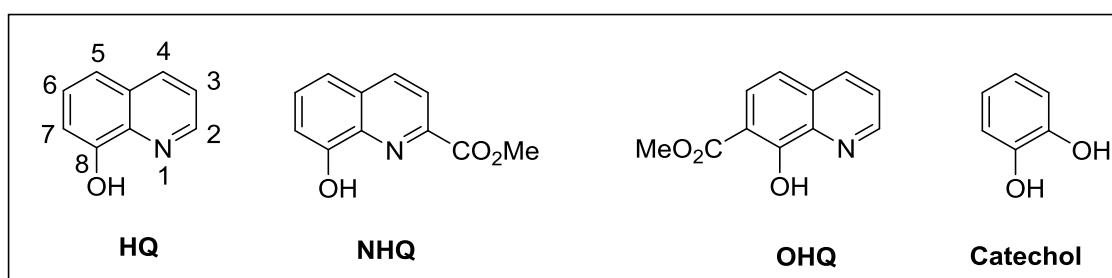


Figure 3.3. Representation of the free ligands investigated.

Among theoretical methods, the Kohn-Sham approach [Kohn 1965] of density-functional theory [Hohenberg 1964] (DFT) and its time-dependent variant [Runge 1984] (TDDFT) in its linear-response formulation [Casida 1995] are the best suitable methods to study the targeted metalloquinolate complexes.

Their trade-off between computational cost and accuracy, enriched by the recurrent developments led to improve the estimate of the unknown exchange-correlation energy, turn them into an approach of choice to study the spectroscopic properties of systems of hundreds of atoms [Brémond 2013]. In their global and range-separated variants, hybrid and double-hybrid density functional approximations [Brémond 2019] [Brémond 2018] partly cure the self-interaction error in DFT (SIE) [Cohen 2008]. In this respect, they are underlined by several benchmark tests to be part of the most accurate class of approximation to estimate ground- and excited-state properties of organic molecular systems [Goerigk 2017] [Brémond 2016] [Brémond 2015]. However, due to their large variety of possible spin states and the low

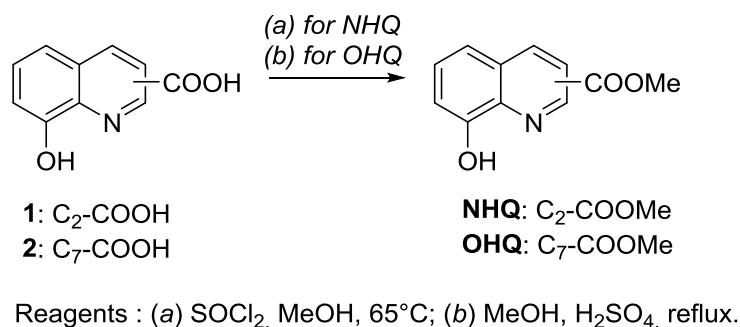
energy gap between themselves, transition metal complexes are still a challenge for DFT approaches. Numerous investigations show that a too large excess of exact-like exchange (EXX > 25%) may emphasize a stabilization of the high-spin (HS) state while semilocal density functionals (EXX = 0%) tend to favour a low-spin (LS) state configuration as ground-electronic state [Rousseau 2018] [Wilbraham 2018] [Swart 2008]. This methodological ambiguity avoids systematic and blind investigations and requires a careful check of all the accessible states using different levels of theory, especially when the investigations deal with the computations of spectroscopic features [Saureu 2016].

By carefully analyzing all the possible spin states and computing the absorption spectroscopic features of a declination of iron(III) complexes chelated by quinolate derivatives, comparing them with experimental measurements, we intend here to rationalize and explain the different affinities of NHQ, HQ and OHQ for the metal cation.

2. Results and discussions

2.1. Organic synthesis

The esters NHQ and OHQ were obtained after esterification of the corresponding acid in thionyl chloride or, refluxing methanol and sulfuric acid, respectively (Scheme 3.1).



Scheme 3.1. Synthesis of NHQ and OHQ.

2.2. Free ligands

2.2.1. UV-vis absorbance spectra of the ligands

The scaffold of HQ and its both NHQ and OHQ ester derivatives consists of a quinoline core substituted in 8-position by a phenol-like hydroxyl function (Figure 3.3). The resulting electronic delocalization over the whole molecule, modulated by a functionalization in 2- or

7-position by an electron withdrawing group (NHQ and OHQ, respectively), induces large absorption bands within the UV/vis region. The position of these bands is experimentally demonstrated as sensitive to the pH and results from the protonation state of the hydroxyl phenol-like function and the nitrogen atom carried by the heterocyclic quinoline skeleton.

Figure 3.4 depicts the influence of the pH on the absorption properties of HQ. The first set of absorption spectra is recorded from pH 6.10 to 2.35 in acetate buffer. The resulting spectra show an absorbance increase (decrease) of the low-lying band at 369 (308) nm, gone along with a red shift of the maximum of absorption from 242 to 252 nm. These variations generate the appearance of 3 isosbestic points at 245, 265 and 335 nm. We ascribe these spectroscopic changes to the protonation of the nitrogen atom belonging to the heterocyclic quinoline core. Computations at TD-PBE0 level accurately confirm and precise the pH sensitivity of HQ with an error lower than 0.1 eV on the positions of the first low-lying transitions (Table 3.1). The protonation of the nitrogen atom induces a red shift of the first low-lying vertical electronic transition from 319 to 369 nm (3.88 to 3.36 eV, respectively), accompanied by a decrease of the corresponding oscillator strength from 0.06 to 0.04. In both case, the low-lying vertical absorption is of $\pi \rightarrow \pi^*$ type and is governed by a highest occupied to a lowest unoccupied molecular orbital (HOMO \rightarrow LUMO) transition delocalized over the whole quinoline core. The red shift of the maximum of absorption is also accurately modelled when the pH decreases. It goes from 229 nm (5.40 eV) for the neutral HQ molecule to 236 nm (5.25 eV) for the nitrogen-protonated system.

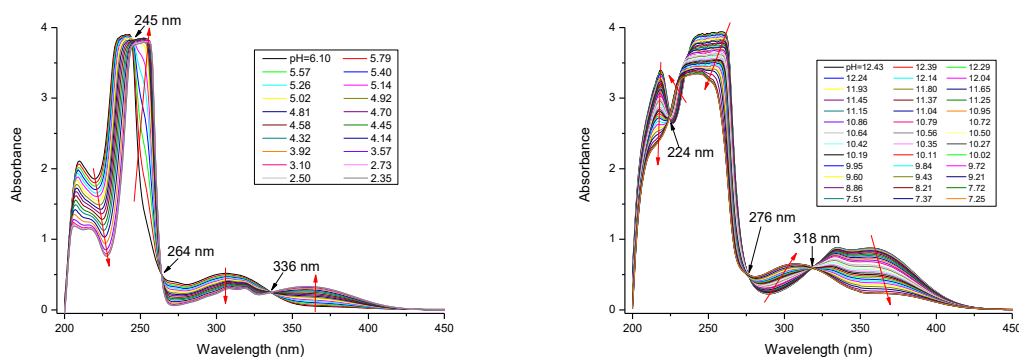


Figure 3.4. Experimental absorption spectra of HQ (5.10^{-4} M) acquired at different pH values in (left) sodium acetate 50 mM, KCl 140 mM, 20% EtOH, pH 2.35–6.10; in (right) carbonate 50 mM, KCl 150 mM, 20% EtOH, pH 7.35–12.45. All the experiments are performed at $25 \pm 0.5^\circ\text{C}$. Arrows indicate the direction of spectral changes when pH value decreases.

A second series of absorption spectra is acquired in carbonate buffer (Figure 3.4) making the pH to vary from 12.45 to 7.35. We observe a concomitant blue shift and absorbance decrease of both characteristic absorption bands from 334 (at pH 12.45) to 308 nm (at pH 7.35) and from 260 (at pH 12.45) to 252 nm (at pH 7.35), together with the appearance of a low-lying band at 360 nm. Three isosbestic points at 224, 276 and 318 nm come out from these spectral variations. Computations show that the modification of the absorption spectrum comes from the deprotonation of the phenol-like hydroxyl function (Table 3.1). Indeed, for the anionic system, TDDFT models the outbreak of a new low-lying $\pi \rightarrow \pi^*$ absorption band at 408 nm (3.04 eV) governed by a HOMO \rightarrow LUMO transition, and the persistence of both other $\pi \rightarrow \pi^*$ bands at 320 and 243 nm (3.87 and 5.10 eV), respectively. In direct comparison with experiment, the $S_0 \rightarrow S_1$ absorption band computed at TD-PBE0 level of theory is red-shifted by 0.4 eV (Table 3.1). This larger error with respect to the neutral and cationic HQ molecules is rationally explained by the expansion of the electronic conjugation of the system. In this specific case, semilocal or hybrid density functionals casting a low fraction of exact-like exchange over delocalize the density due to SIE [Cohen 2008]. At excited state, this error is translated by a stronger charge transfer character of the transition which results in a small electronic overlap between the donor and acceptor regions of the molecule [Le Bahers 2011] [Peach 2008] [Dreuw 2004]. The analysis of the DCT index value, which provides an information about the mean charge-transfer distance between donor and acceptor centers [Le Bahers 2011], agrees and provides a small increase of charge-transfer length when going to the anionic form (2.1 to 2.2 Å). The computation of the vertical transitions with the CAM-B3LYP range-separated hybrid density functional confirms this hypothesis (Table 3.1) and finds the positions of the 3 absorption bands of the anionic system at 368, 309 and 238 nm (3.37, 4.02 and 5.21 eV, respectively).

The spectra of NHQ and OHQ were also recorded depending on pH values (Figure 3.5). Their experimental absorption spectra present similar features and TDDFT confirms the nature and assignation of the bands, keeping an excellent agreement with experiments (Table 3.2).

Table 3.1. Energies (e , in eV), wavelengths (λ , in nm), oscillator strengths (f , in a.u.) and charge-transfer distance (DCT in Å) of the main vertical electronic transitions computed for the acid (LH_2^+), neutral (LH) and basic (L^-) forms of the HQ molecule at PCM-TD-PBE0 and PCM-TD-CAM-B3LYP level of theory with the 6-31+G* basis set. Only transitions with sufficiently large enough oscillator strength are retained. Experimental energies and wavelengths of the main absorption bands are provided as a matter of comparison.

HQ	type	exp.		PBE0				CAM-B3LYP			
		e (eV)	λ (nm)	e (eV)	λ (nm)	f (a.u.)	D _{CT} (Å)	e (eV)	λ (nm)	f (a.u.)	D _{CT} (Å)
LH_2^+	$\pi \rightarrow \pi^*$	3.36	369	3.36	369	0.04	2.1	3.71	334	0.06	2.1
	$\pi \rightarrow \pi^*$	5.12	242	5.25	236	0.83	2.0	5.40	229	0.88	1.7
LH	$\pi \rightarrow \pi^*$	4.02	308	3.88	319	0.06	2.1	4.21	295	0.09	2.0
	$\pi \rightarrow \pi^*$	4.92	252	5.40	229	0.87	1.7	5.53	224	0.96	1.5
L^-	$\pi \rightarrow \pi^*$	3.44	360	3.04	408	0.08	2.2	3.37	368	0.09	2.2
	$\pi \rightarrow \pi^*$	3.71	334	3.87	320	0.14	1.5	4.02	309	0.14	1.3
	$\pi \rightarrow \pi^*$	4.77	260	5.10	243	0.40	1.3	5.21	238	0.42	0.4

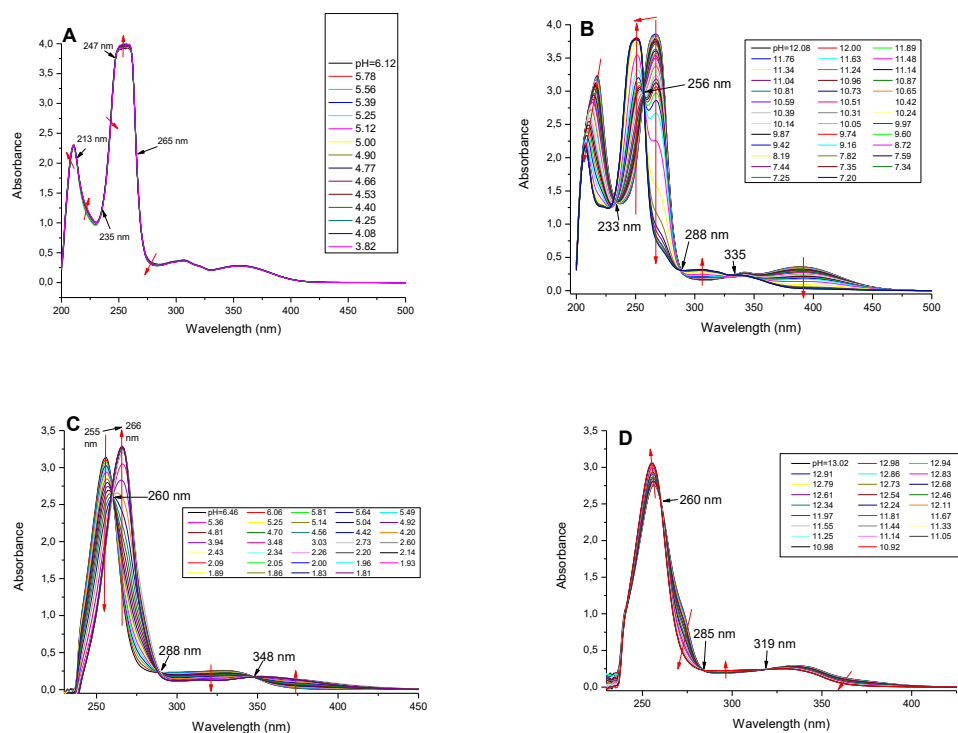


Figure 3.5. Absorption spectra of (A) NHQ (5.10^{-4} M) in sodium acetate 50 mM, KCl 140 mM, 20 % DMSO, pH 3.82–6.12 (B) NHQ (5.10^{-4} M) in carbonate 50 mM, KCl 150 mM, 20 % DMSO, pH 7.34–12.08 (C) OHQ (5.10^{-4} M) in sodium acetate 50 mM, KCl 140 mM, 20 % DMSO, pH 1.81–6.46 (D) OHQ (5.10^{-4} M) in carbonate 50 mM, KCl 150 mM, 20 % DMSO, pH 10.92–13.02 at 25 ± 0.5 °C. Arrows indicate the direction of spectral changes when pH value decreases.

Table 3.2. Energies (e , in eV), wavelengths (λ , in nm) and oscillator strengths (f , in a.u.) of the main vertical electronic transitions computed for the acid (LH_2^+), neutral (LH) and basic (L^-) forms of the NHQ and OHQ molecules at PCM-TD-PBE0 and PCM-TD-CAM-B3LYP level of theory with the 6-31+G* basis set. Only transitions with sufficiently large enough oscillator strength are retained. Experimental energies and wavelengths of the main absorption bands are provided as a matter of comparison.

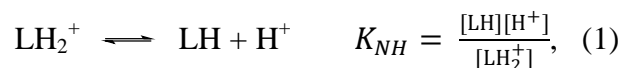
NHQ	type	exp.		PBE0			CAM-B3LYP		
		e (eV)	λ (nm)	e (eV)	λ (nm)	f (a.u.)	e (eV)	λ (nm)	f (a.u.)
LH_2^+	$\pi-\pi^*$	3.49	355	2.91	426	0.02	3.30	375	0.04
	$\pi-\pi^*$	4.88	254	4.82	257	0.97	5.05	245	1.04
LH	$\pi-\pi^*$	3.58	346	3.42	363	0.06	3.80	326	0.08
	$\pi-\pi^*$	4.96	250	4.96	250	1.02	5.19	239	1.13
L^-	$\pi-\pi^*$	3.23	384	3.62	373	0.12	2.93	423	0.16
	$\pi-\pi^*$	3.63	342	3.57	348	0.14	3.81	326	0.15
	$\pi-\pi^*$	4.65	266	4.73	262	0.50	4.94	251	0.69

OHQ	type	exp.		PBE0			CAM-B3LYP		
		e (eV)	λ (nm)	e (eV)	λ (nm)	f (a.u.)	e (eV)	λ (nm)	f (a.u.)
LH_2^+	$\pi-\pi^*$	3.60	344	3.37	368	0.04	3.71	334	0.06
	$\pi-\pi^*$	4.63	268	4.92	252	0.99	5.40	229	0.88
LH	$\pi-\pi^*$	3.79	327	3.85	321	0.07	4.12	301	0.08
	$\pi-\pi^*$	4.84	256	5.06	245	1.01	5.21	238	1.12
L^-	$\pi-\pi^*$	-	-	3.28	378	0.04	3.59	345	0.09
	$\pi-\pi^*$	3.69	336	3.62	342	0.31	3.84	323	0.34
	$\pi-\pi^*$	4.82	257	4.99	248	0.51	5.11	243	0.49

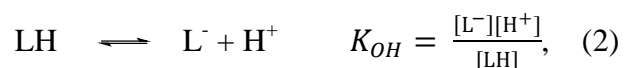
2.2.2. Determination of the thermodynamic constant

The pH-sensitivity of the absorption spectra allows the determination of the K_{NH} and K_{OH} acid-base dissociation constants of the 3 HQ derivatives. The former describes the

deprotonation of the nitrogen center positioned on the quinoline scaffold and is defined such as



where LH_2^+ and LH are the cationic and neutral form of the ligand, respectively. The latter represents the deprotonation of the phenol-like hydroxyl function and is governed by



with L^- the anionic form of the ligand.

Table 3.3 reports both constants obtained by a Specfit analysis of the absorption spectra of HQ and its NHQ and OHQ ester derivatives. Results are in line with those previously reported at experimental or theoretical levels in Refs [Türkel 2013] [Oliveri 2016] [Bahers 2009] [Boukhalfa 2002] [Bardez 1997]. The first dissociation constant ($\text{p}K_{\text{NH}}$) is measured as independent of the electron withdrawing effects induced by the ester substituents and is merely determined as 4.8 for the three ligands. However, the $\text{p}K_{\text{OH}}$ of OHQ (12.5) is estimated as 2 units higher than the ones of HQ and NHQ (10.3 and 9.5, respectively). Indeed, computations show that the energy minimum structure of the neutral OHQ molecule involves the formation of a planar 6-member ring governed by an intramolecular hydrogen bond between the hydroxyl and ester groups. Previously hypothesized by Carris and coworkers [Carris 1996], this spatial arrangement, which can only occur in case of OHQ, confirms the improved stability of the neutral form and its higher $\text{p}K_{\text{OH}}$ value.

Table 3.3. Acid-base dissociation constants of the HQ ligand and its NHQ and OHQ ester derivatives in absence or presence of iron(III).

Ligands	Without Fe^{3+}		With Fe^{3+}	
	$\text{p}K_{\text{NH}}$	$\text{p}K_{\text{OH}}$	$\text{p}K_{\text{NH}^+}$	$\text{p}K_{\text{OH}^+}$
HQ	4.85±0.05	10.30±0.02	3.00±0.04	5.00±0.05
NHQ	4.90±0.10	9.50±0.05	3.05±0.05	5.50±0.05
OHQ	4.70±0.10	12.50±0.10	3.00±0.10	4.85±0.05

2.3. Formation of the iron (III) complexes

2.3.1. Stoichiometry of the iron(III) complexes

Owing to their bidentate character, HQ and both NHQ and OHQ ester derivatives are expected to strongly chelate iron(III). One equivalent of FeCl_3 was added to a solution of HQ, and the absorption spectra were acquired first in formiate and then in acetate buffer (see Table 3.3 and Figure 3.6). The Specfit analysis of the spectra shows that in the presence of iron(III), the $\text{p}K_{\text{NH}'}$ and $\text{p}K_{\text{OH}'}$ values (Eqs. (1) and (2), the prime factor exponent notation depicting the presence of iron(III)) are decreased by around 1.9 and 5.3 units, respectively. It thus demonstrates the complexation of Fe^{3+} by both acid-base sites of HQ. In the same experimental conditions, the $\text{p}K_{\text{NH}'}$ of NHQ and OHQ decreases by 1.9 and 1.7 units, while the $\text{p}K_{\text{OH}'}$ decrease is estimated to 4.0 and 7.6, respectively. In case of OHQ, the larger $\text{p}K_{\text{OH}'}$ variation indicates the breaking of the 6-member intramolecular hydrogen-bonded ring stabilizing the structure and the formation of an iron(III) complex involving its 2 acid-base functions.

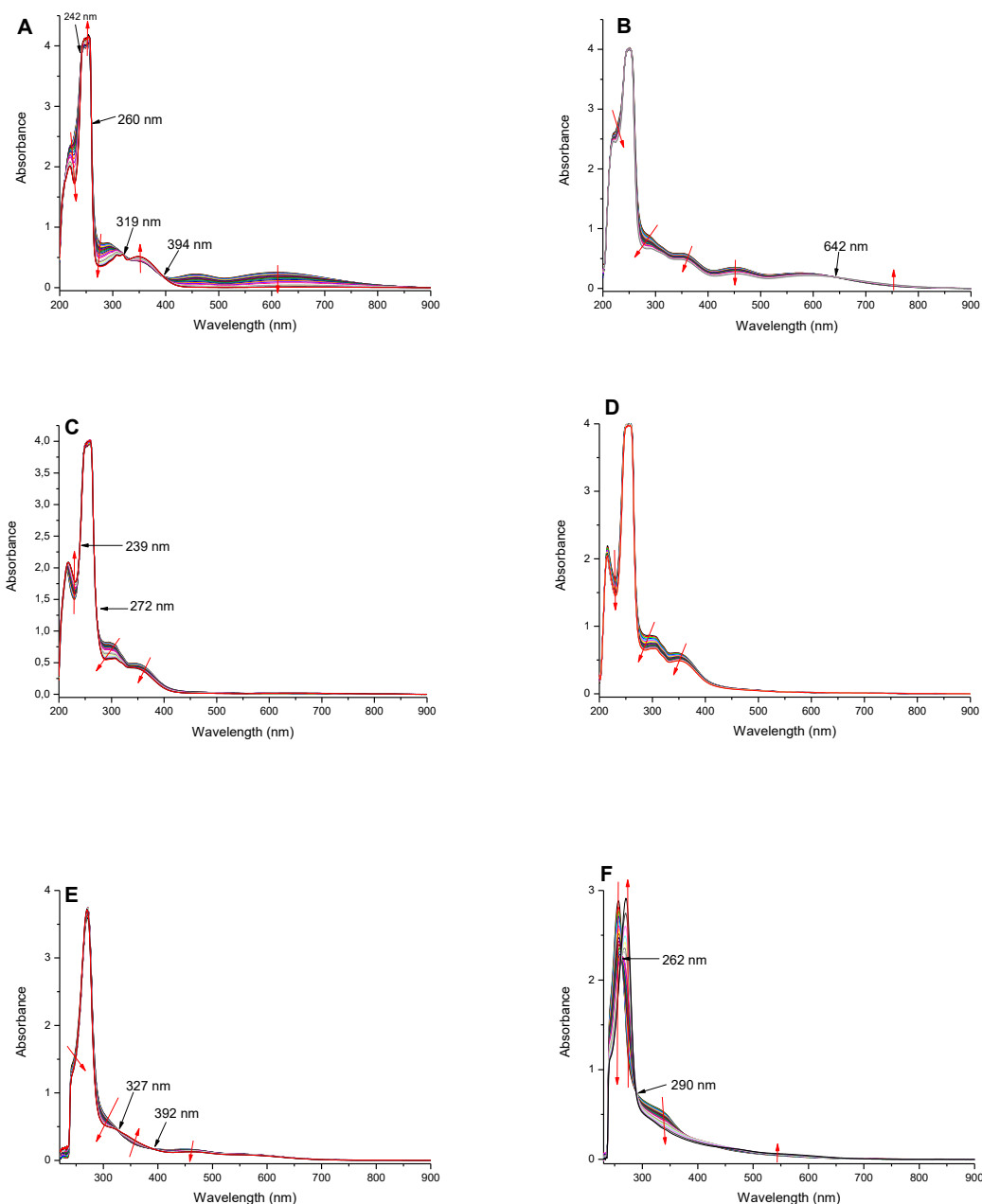


Figure 3.6. Absorption spectra in the presence of iron of (A) HQ (5.10^{-4} M) in sodium formiate 50 mM, KCl 140 mM, 20 % DMSO, pH 2.11–3.95 (B) HQ (5.10^{-4} M) in sodium acetate 50 mM, KCl 150 mM, 20 % DMSO, pH 4.52–6.34 (C) NHQ (5.10^{-4} M) in sodium formiate 50 mM, KCl 140 mM, 20 % DMSO, pH 2.09–4.00 (D) NHQ (5.10^{-4} M) in sodium acetate 50 mM, KCl 150 mM, 20 % DMSO, pH 4.20–6.41 at 25 ± 0.5 °C. (E) OHQ (5.10^{-4} M) in sodium formiate 50 mM, KCl 140 mM, 20 % DMSO, pH 2.09–4.00 (F) OHQ (5.10^{-4} M) in sodium acetate 50 mM, KCl 150 mM, 20 % DMSO, pH 3.32–6.25 at 25 ± 0.5 °C. Arrows indicate the direction of spectral changes when pH value decreases.

The formation of the iron(III) complexes with HQ derivatives is further confirmed by direct and reverse isothermal titration calorimetry (ITC) titrations (Figure 3.7). At pH 2.0, the direct titration, *i.e.* the titration of HQ by FeCl₃, provides a stoichiometry of 0.4 ± 0.1 equivalents of iron(III) cation and an affinity constant of $(2.8 \pm 1.3) \times 10^3$. The reverse titration agrees with the direct one and shows a metal cation chelated by (3.2 ± 0.3) equivalents of HQ and an affinity constant merely equals to the previous one within the uncertainty limits, *i.e.* $(2.1 \pm 0.3) \times 10^3$. As a result, both titrations converge to the thermodynamically favoured formation of an iron(III) complex coordinated by 3 HQ molecules. More precisely, the ITC analysis shows that at room temperature and acid pH, the reaction is endothermic ($\Delta H = 0.5 \pm 0.1$ kJ mol⁻¹) and driven by entropy ($|T\Delta S| > |\Delta H|$), *i.e.* that the water/HQ ligand exchanges increase the entropy and drive the reaction to the formation of the complex. At pH 7.4, the direct titration of HQ by ferric citrate confirms the thermodynamically favoured hexa-coordination of iron(III) with three HQ molecules ($n = 0.46 \pm 0.15$, Figure 3.7). However, like previously observed for the catechol ligand [Yang 2014], the reaction is found to be exothermic ($\Delta H = -(53 \pm 1)$ kJ mol⁻¹) in neutral medium. Thus, it implies that the formation of the coordination bond between the ferric cation and HQ is energetically more important than the decoordination and release of water within the solution ($|\Delta H| > |T\Delta S|$).

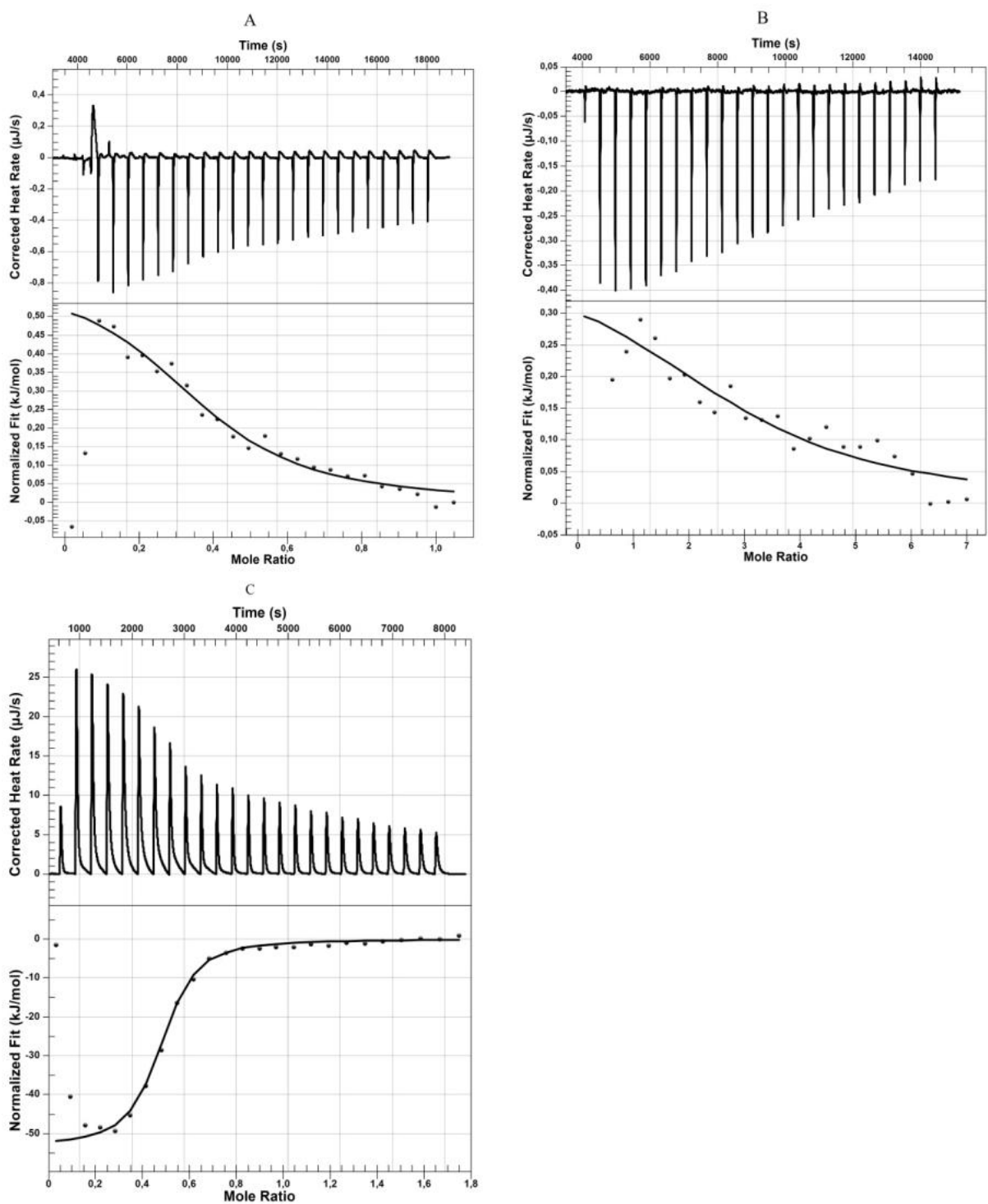


Figure 3.7. Isothermal titration data for the titration at 25°C of: (A) HQ (5 mM) with Fe³⁺ (15 mM) at pH 2.0, (B) Fe³⁺ (0.5 mM) with HQ (10 mM) at pH 2.0, (C) HQ (2 mM) with Fe(citrate) (10 mM) at pH 7.0. The first two data points were deleted before curve fitting.

2.3.2. Structure of the iron(III) complexes

The iron(III) complex chelated by three HQ ligands can adopt three ground-state electronic configurations, each one characterized by a different population of the $3d$ orbitals of the metal by its five valence electrons. In its low-, intermediate- or high-spin state (LS, IS or HS, respectively), iron(III) adopts a $(t_{2g})^5$, $(t_{2g})^4 (e_g)^1$, or $(t_{2g})^3 (e_g)^2$ electronic configuration. A structure optimization of the neutral form of the complex $[\text{Fe}(\text{HQ})_3]$ in its 3 allowed spin states demonstrates that the HS configuration is by far the most stable state of the complex (Table 3.4). PBE0 models the HS state 10.0 (14.4) kcal mol^{-1} more stable than the LS (IS) one. Even if global hybrids are known to overstabilize the HS configuration [Rousseau 2018] [Song 2018] [Wilbraham 2018] [Swart 2016], the OPBE semilocal approximation confirms the state ordering (HS being 6.0 and 11.8 kcal mol^{-1} more stable than LS and IS, respectively) and imposes the HS configuration as the most stable electronic state of the complex.

Table 3.4. Energy gaps (kcal mol^{-1}) between the low- and high-spin states ($\Delta_{\text{LS-HS}}$) and intermediate- and high-spin states ($\Delta_{\text{IS-HS}}$) for a series of iron(III) complexes computed at the PCM-DFT level of theory with different density functionals and the 6-31+G* basis set. For all iron(III) complexes, the high-spin state is found as the most stable electronic state.

Iron(III) complexes		OPBE	PBE0	CAM-B3LYP
$\text{Fe}(\text{HQ})_3$	$\Delta_{\text{LS-HS}}$	6.00	9.96	2.07
	$\Delta_{\text{IS-HS}}$	11.78	14.42	10.96
$\text{Fe}(\text{NHQ})_3$	$\Delta_{\text{LS-HS}}$	23.57	29.95	20.64
	$\Delta_{\text{IS-HS}}$	14.49	13.45	8.56
$\text{Fe}(\text{OHQ})_3$	$\Delta_{\text{LS-HS}}$	4.13	8.90	1.12
	$\Delta_{\text{IS-HS}}$	11.65	13.99	10.22
$\text{Fe}_{\text{OO}}(\text{OHQ})_3$	$\Delta_{\text{LS-HS}}$	24.09	22.92	14.03
	$\Delta_{\text{IS-HS}}$	17.31	18.21	14.87

Within the sextet spin state multiplicity, the structure of the complex is slightly distorted with respect to an ideal octahedral coordination due to the formation of a constrained 5-member ring between Fe and the coordination sites of the ligand. Indeed, the Fe-O and Fe-N mean

distances are estimated to be 1.973 and 2.181 Å, respectively (Table 3.5), with a spin density of about 5.0, 0.1 and 0.0 a.u. localized on the Fe, O and N atoms, respectively. The addition of the D3(bj) empirical dispersion correction does not modify the structure of the complex and confirms the reliability of PBE0 with respect to these systems.

Table 3.5. Coordination bond distance (Å) between iron(III) and the different chelating sites for a selection of HQ-based complexes. Bond distances are optimized at PCM-PBE0 level of theory with (+D3(bj)) or without (noCor) empirical dispersion corrections with the 6-31+G* basis set. Crystallographic structure parameters of the O-TRENTOX-based complex are reported as a matter of comparison.

Iron (III) complexes	Fe-O		Fe-N		Fe-O(C=O)	
	noCor	+D3(bj)	noCor	+D3(bj)	noCor	+D3(bj)
[Fe(HQ) ₃] ^a	1.973	1.974	2.181	2.185	-	-
[Fe(NHQ) ₃] ^a	1.970	1.977	2.307	2.274	-	-
[Fe(OHQ) ₃] ^a	1.970	1.970	2.168	2.184	-	-
[Fe _{OO} (OHQ) ₃] ^a	1.937	1.931	-	-	2.083	2.090
[Fe(O-TRENTOX) ₃] ^b		1.940	-	-		2.034

^a Computed at DFT level

^b Crystallographic structure from Ref. [Serratrice 1999]

Same computations performed on the neutral form of the [Fe(NHQ)₃] or [Fe(OHQ)₃] complex show similarly that iron(III) is hexacoordinated by three NHQ or OHQ ligands, and lead to an energetically favoured HS state configuration. Due to a larger steric hindrance, both resulting complexes are more distorted than [Fe(HQ)₃] (Figure 3.8). The Fe-O mean distance is measured as 1.970 Å and is very similar to the one of [Fe(HQ)₃] (Table 3.5). However, the Fe-N mean distance is significantly larger (shorter) for [Fe(NHQ)₃] ([Fe(OHQ)₃]) with respect to the one of [Fe(HQ)₃] and is estimated to be 2.307 (2.168) Å versus 2.181 Å. This difference in structure impoverishes the spin density of Fe in the NHQ-based complex (4.7 versus 5.0 a.u.) and reinforces it to 5.2 a.u. in case of the OHQ-based one. Particularly for [Fe(NHQ)₃], these deviations with respect to the ideal octahedral environment of the metal may lead to the formation of less stable complexes with respect to [Fe(HQ)₃]. The OHQ ligand allows however to consider another chelation environment for iron(III). Indeed, the

spatial proximity of the carbonyl group and phenol-like hydroxyl function of this ligand allows the formation of a less constrained 6-member ring between Fe and both oxygen donor sites. The resulting complex is dubbed $[\text{Fe}_{\text{oo}}(\text{OHQ})_3]$. With this salicylate coordination, the complex adopts a quasi-ideal octahedral geometry with a Fe–O mean distance estimated to 1.937 and 2.083 Å for the hydroxyl and carbonyl sites, respectively (Table 3.5, Figure 3.8). These findings agree with previous works reported by Serratrice and co-workers [Serratrice 1997] [Caris 1996]. They first demonstrated the iron chelation by the carbonyl group by IR spectroscopy, the carbonyl characteristic band being blue-shifted in presence of Fe^{3+} [Serratrice 1997]. They then confirmed this coordination scheme by crystallizing the iron(III) complex by O-TRENTOX [Serratrice 1999]. In this specific case, the distance between the metal cation and the hydroxyl group is in perfect match (1.940 Å). Its distance with the carbonyl site is however 0.04 Å shorter (2.034 Å).

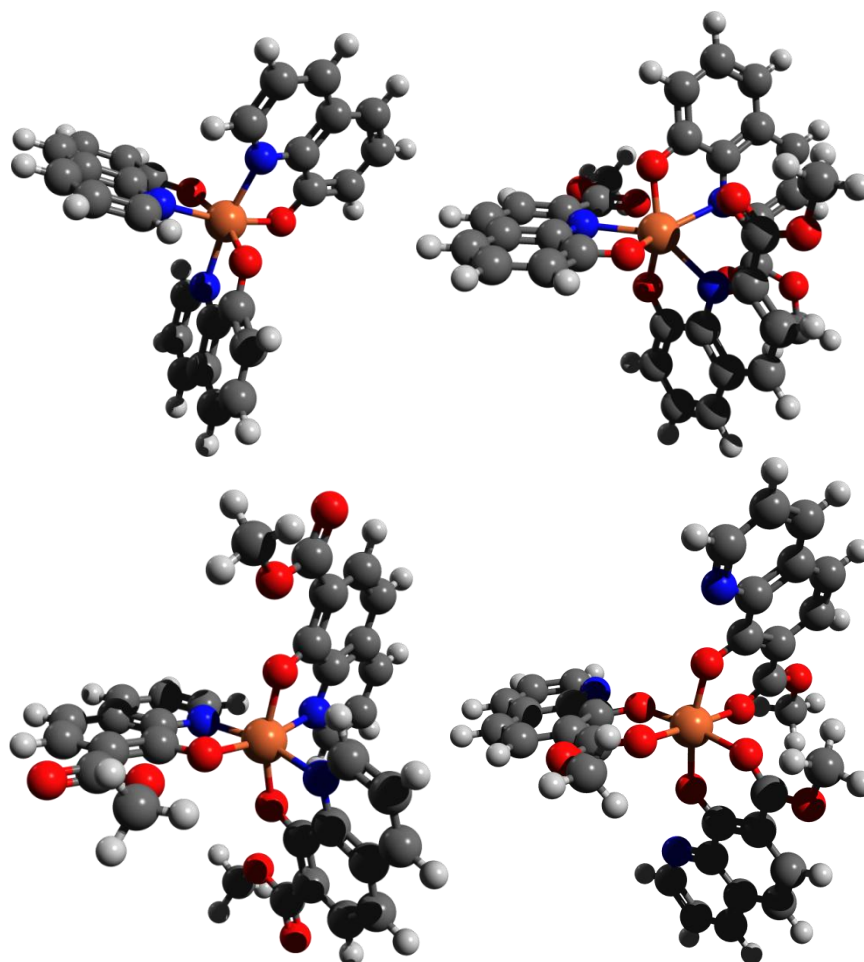


Figure 3.8. Low energy computational model of (A) $\text{Fe}(\text{HQ})_3$, (B) $\text{Fe}(\text{NHQ})_3$, (C) $\text{Fe}(\text{OHQ})_3$ and (D) $\text{Fe}_{\text{oo}}(\text{OHQ})_3$

2.3.3. UV/vis spectra of the iron(III) complexes

The formation of the iron(III) complex by HQ-based ligands was then analyzed by UV/vis absorption spectroscopy (Figure 3.9). The addition of FeCl_3 to a solution of HQ at pH 2.0 leads to the appearance of two new absorption bands within the visible region (653 and 452 nm), and the persistence of the characteristic $\pi \rightarrow \pi^*$ band of the HQ ligand in acidic medium (369 nm) (Table 3.6). These UV/vis features are in line with what observed experimentally for (8-hydroxyquinoline-5-sulfonic acid) iron(III) and quinolobactine complexes [du Moulinet d'Hardemare 2004] [Imbert 2002] [Gerard 1995]. The same experiment performed at pH 7.4 leads to a slightly modified absorption spectrum characterized by an absorbance decrease and blue shift of the first low-lying band from 653 to 582 nm, followed by the persistence of both others at 455 and 369 nm, respectively (Figure 3.9). The spectrum presents an isosbestic point in the visible region. This feature confirms the ITC experiments (considering a one-third ratio equivalent of iron(III)) and is the signature of the formation of a unique complex with a fixed stoichiometry.

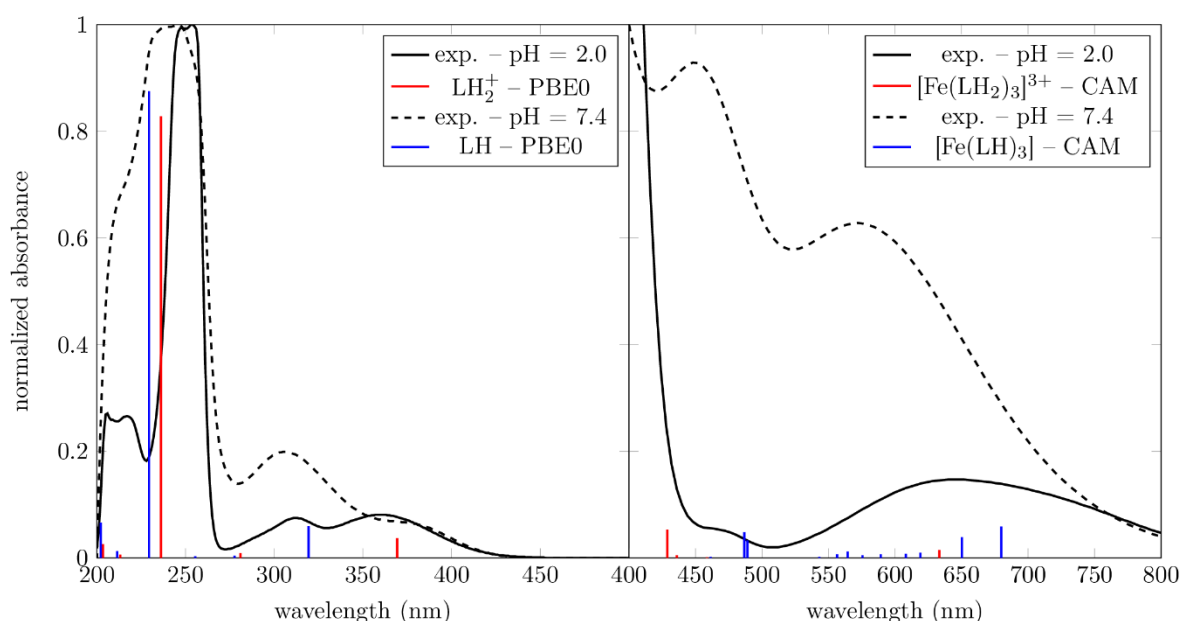


Figure 3.9. Experimental absorption spectra function of the pH (2.0 and 7.4) and the corresponding vertical electronic transitions function of the acid (LH_2^+) and neutral (LH) form of HQ in case of the (left) free ligand and (right) iron(III) complex. Vertical excitations are computed with the 6-31+G* basis set at PCM-TD-PBE0 and PCM-TD-CAM-B3LYP levels of theory for the free ligand and iron(III) complex, respectively. Both insets depict the absorption spectra Gaussian convolution of the vertical excitations.

Computations performed at the TD-PBE0 level of theory on the acid and neutral forms of the complex ($[\text{Fe}(\text{HQ})_3]^{3+}$ and $[\text{Fe}(\text{HQ})_3]$, respectively) show the raising of two new low energy vertical transitions within the visible region of the spectrum (Table 3.6). Both of them are quasi-degenerated due to the quasi-symmetry of the complex and present a charge-transfer character depicted by a DCT index value varying between 1.3 and 2.6 Å according to the transition type and protonation state.

Table 3.6. Energies (e , in eV), wavelengths (λ , in nm), oscillator strengths (f , in a.u.) and charge-transfer distance (DCT in Å) of the main vertical electronic transitions computed for the acid ($[\text{Fe}(\text{HQ})_3]^{3+}$, pH 2.0) and neutral ($[\text{Fe}(\text{HQ})_3]$, pH 7.4) forms of the iron(III) complex chelated by 3 HQ ligands at PCM-TD-PBE0 and PCM-TD-CAMB3LYP level of theory with the 6-31+G* basis set. Only transitions with sufficiently large enough oscillator strengths and one among the quasi-generated states are retained. Experimental energies and wavelengths of the main absorption bands are provided as a matter of comparison.

iron(III) complexes	type	exp.		PBE0				CAM-B3LYP			
		e (eV)	λ (nm)	e (eV)	λ (nm)	f (a.u.)	D_{CT} (Å)	e (eV)	λ (nm)	f (a.u.)	D_{CT} (Å)
$[\text{Fe}(\text{HQ})_3]^{3+}$	MLCT	1.90	653	0.96	1297	0.02	2.6	1.96	633	0.02	3.5
	LLCT	2.76	450	2.63	472	0.05	1.7	2.89	429	0.05	3.9
	$\pi \rightarrow \pi^*$	3.36	369	3.27	379	0.03	2.3	3.68	336	0.05	0.7
$[\text{Fe}(\text{HQ})_3]$	MLCT	2.13	582	1.60	773	0.05	1.9	1.82	680	0.06	1.9
	LLCT	2.72	455	2.44	509	0.02	1.3	2.55	487	0.05	1.0
	$\pi \rightarrow \pi^*$	3.36	369	3.27	379	0.07	1.4	3.57	347	0.08	1.2

The analysis of the density difference between the first excited and ground states depicts a strong metal-to-ligand-charge-transfer (MLCT) character characterized by a strong density depletion on the metal and one of its surrounding ligand, compensated by a density increase mainly located on the other ligands (Figure 3.10). The D_{CT} index value is here computed as 2.6 and 1.9 Å for the cationic and neutral forms of the complex, respectively. In this specific case, the PBE0 global hybrid is expected to suffer from spurious SIE and to strongly

underestimate the energy of the MLCT transitions. Indeed, it models the first low-lying excitation at 1297 nm and 773 nm (0.96 and 1.60 eV) for the acid and neutral forms of the complex, respectively, while the experimental determination of the position of the first absorption band lies at 653 and 582 nm (1.90 and 2.13 eV), namely an error larger than 0.9 and 0.5 eV, respectively (Table 3.6). Switching to the CAM-B3LYP range-separated density functional partially corrects SIE and models the first low-lying band at 633 and 680 nm (1.96 and 1.82 eV), respectively, thus reducing the error to 0.2 eV (Table 3.6). Moreover, TDDFT confirms here that the increase of the pH, increases the absorbance of the first absorption band with an oscillator strength going from 0.02 for the protonated $[\text{Fe}(\text{HQ})_3]^{3+}$ complex to 0.06 for its neutral form.

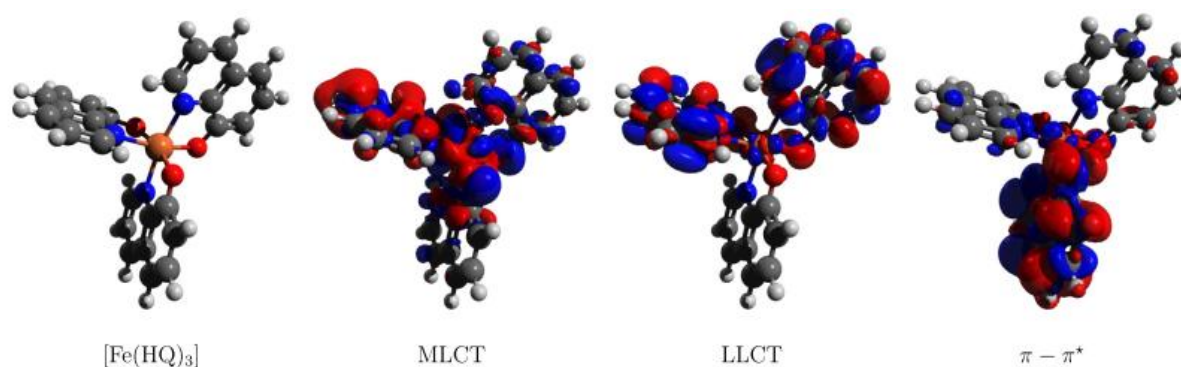


Figure 3.10. Computed electronic density variations ($\Delta\rho$, isovalue 0.0004 a.u.) for the main vertical electronic transitions of the neutral form of the $[\text{Fe}(\text{HQ})_3]$ complex. The blue and red surfaces represent a density increase and depletion upon excitation, respectively.

The second absorption band is prone to a ligand-to-ligand-charge transfer (LLCT) character which is ruled by a through space charge transfer between two ligands with a D_{CT} index value estimated to 1.7 and 1.3 Å for the cationic and neutral forms of the complex (Figure 3.10). In this specific case, PBE0 is expected to be particularly prone to SIE because of the through space character of the transition. Indeed, PBE0 overestimates the energy of the transition with an error larger than 0.3 eV. It computes it at 472 and 509 nm (2.63 and 2.44 eV) for the acid and neutral form of the complex, respectively (Table 3.6). CAM-B3LYP corrects this spurious behavior and models it at 429 and 487 nm (2.89 and 2.55 eV), thus lowering the error to 0.2 eV. The last intense absorption band observed as the maximum of absorption is pH independent. It is experimentally measured at 369 nm (3.36 eV), and modelled as quasi-degenerated at 379 nm (3.27 eV) with the PBE0 global hybrid (Table 3.6). The good agreement between experiment and theory points here the character change of the transition.

Figure 3.10 shows that it is characterized by a local $\pi \rightarrow \pi^*$ excitation located on the ligand itself. CAM-B3LYP confirms this trend and estimates it with a slightly larger error at 336 and 347 nm (3.68 and 3.57 eV) for the acid and neutral form of the complex.

The absorption spectra of NHQ- and OHQ-based complexes in acid and neutral media present similar spectroscopic features with respect to $[\text{Fe}(\text{HQ})_3]^{3+}$ and $[\text{Fe}(\text{HQ})^3]$, respectively (Figure 3.11). Within the visible region, the absorption bands of the OHQ-based complexes are however largely blue-shifted and lie around 560 and 462 nm (2.21 and 2.68 eV) for the acid form, and 525 and 425 nm (2.36 and 2.92 eV) for the neutral form.

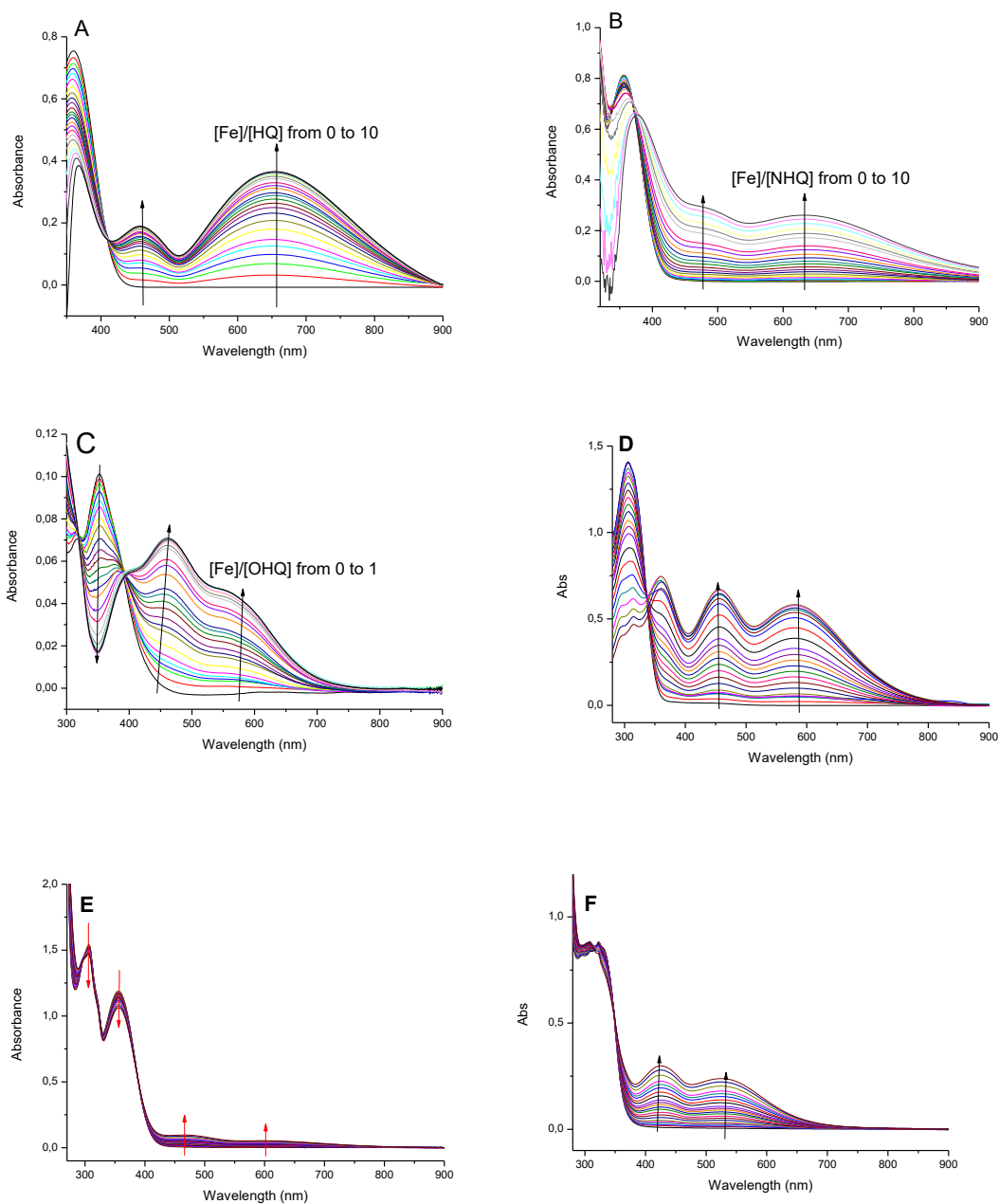


Figure 3.11. Experimental absorption spectra of (A) HQ (5.10^{-4} M), (B) NHQ (5.10^{-4} M), and (C) OHQ (1.10^{-4} M) in presence of an increasing concentration of FeCl_3 at pH 2.0. Same experiments for (D) HQ (5.10^{-4} M), (E) NHQ (1.10^{-4} M), and (F) OHQ (5.10^{-4} M) in presence of an increasing concentration of Fe(III)-NTA at pH 7.4. All the experiments are performed at $25 \pm 0.5^\circ\text{C}$. Arrows indicate the direction of spectral changes when the concentration in iron(III) increases.

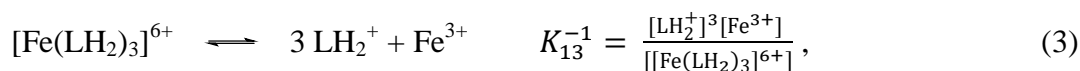
CAM-B3LYP provides an accurate estimate of the three types of transitions involved in the UV/vis spectrum of $[\text{Fe}(\text{NHQ})_3]$ with an error of about 0.2 eV (Table 3.7). However for $[\text{Fe}(\text{OHQ})_3]$, it models the MLCT, LLCT and $\pi \rightarrow \pi^*$ transitions with deviations larger than 0.4, 0.7 and 0.2 eV, respectively. This larger error range lets us suppose that $[\text{Fe}(\text{OHQ})_3]$ is not the iron(III) complex formed preferentially in solution, and that the hydroxyl/nitrogen chelation sites of the OHQ is not the one observed. Indeed, the same computations performed on the $[\text{Fe}_{\text{oo}}(\text{OHQ})_3]$, namely the iron(III) metal chelated by the phenol-like hydroxyl and ester donor sites of the OHQ ligand, provide a better estimate of the three types of transitions with an error of about 0.2 eV (Table 3.7). More than a structure argument as discussed above, the UV/vis spectrum of the OHQ-based complex goes in favour to a salicylate chelation of the iron(III) cation.

Table 3.7. Energies (e , in eV), wavelengths (λ , in nm), oscillator strengths (f , in a.u.) and charge-transfer distance (D_{CT} in Å) of the main vertical electronic transitions computed for the neutral $[\text{Fe}(\text{NHQ})_3]$, $[\text{Fe}(\text{OHQ})_3]$ and $[\text{Fe}_{\text{oo}}(\text{OHQ})_3]$ forms of the iron(III) complex (pH 7.4) at PCM-TD-PBE0 and PCM-TD-CAM-B3LYP level of theory with the 6-31+G* basis set. Only transitions with sufficiently large enough oscillator strengths and one among the quasi-generated states are retained. Experimental energies and wavelengths of the main absorption bands are provided as a matter of comparison.

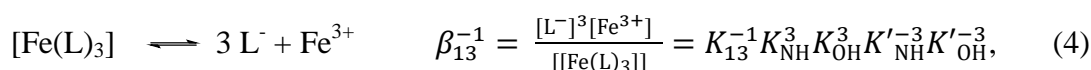
iron(III) complexes	type	exp.		PBE0				CAM-B3LYP			
		e (eV)	λ (nm)	e (eV)	λ (nm)	f (a.u.)	D_{CT} (Å)	e (eV)	λ (nm)	f (a.u.)	D_{CT} (Å)
$[\text{Fe}(\text{NHQ})_3]$	MLCT	2.05	605	1.60	775	0.06	1.5	1.79	692	0.06	1.6
	LLCT	2.66	465	2.16	573	0.01	1.7	2.35	527	0.03	1.5
	$\pi \rightarrow \pi^*$	3.28	378	2.81	441	0.04	1.9	3.22	384	0.10	1.8
$[\text{Fe}(\text{OHQ})_3]$	MLCT	2.36	525	1.70	729	0.05	1.7	1.95	636	0.06	1.9
	LLCT	2.92	425	2.51	494	0.03	1.2	2.66	466	0.06	1.3
	$\pi \rightarrow \pi^*$	3.20	387	3.36	369	0.07	1.8	3.44	360	0.07	1.2
$[\text{Fe}_{\text{oo}}(\text{OHQ})_3]$	MLCT	2.36	525	1.75	709	0.08	2.1	2.05	604	0.08	1.5
	LLCT	2.92	425	2.64	470	0.02	0.1	2.75	451	0.03	0.7
	$\pi \rightarrow \pi^*$	3.20	387	3.23	384	0.04	1.5	3.26	380	0.03	1.0

2.3.4. Determination of the thermodynamic constants

The Specfit analysis of the absorption spectra of HQ-, NHQ-, and OHQ-based iron(III) complexes in acid medium (Figure 3.11) allows the determination of an apparent affinity constant K_{13} at pH 2.0:



where LH_2^+ and $[\text{Fe}(\text{LH}_2)_3]^{6+}$ are the cationic forms of the ligand and iron(III) complex predominant at pH 2.0, respectively. The experimental determination of K_{13} at pH 2.0 and the acid-base constants of the free and complexed ligands allow deducing a global stability constant β_{13} , as a combination of the laws of mass action described by Eqs. (1), (2) and (3) such as:



with L^- and $[\text{Fe}(\text{L})_3]$ are the deprotonated forms of the ligand and iron (III) complex, respectively.

To extend the comparison with other experimental studies performed in biological media [Li 2008] [Martell 1992], pFe of the three different ligands was determined. It is defined as the negative logarithm of the free iron(III) concentration ($\text{pFe} = -\log[\text{Fe}^{3+}]$) at pH 7.4 with an analytical ligand and Fe^{3+} concentration of 10^{-5} and 10^{-6} M, respectively. Table 3.8 reports both pFe and $\log \beta_{13}$ characteristic constants for the three studied ligands and catechol, another well-known chelator in literature (Figure 3.3) [Pierre 2003].

Table 3.8. Formation constants of the $[\text{Fe}(\text{L})_3]$ complex for a selection of ligands L.

$[\text{Fe}(\text{L})_3]$	$\log K_{13}^a$	$\log \beta_{13}^b$	pFe ^c
HQ	9.70±0.05	31.1	13.5
NHQ	7.80±0.10	25.3	10.5
OHQ	13.40±0.40	41.5	17.1
Catechol	10.00±0.40	45.7	21.0

^a Affinity constant measured at pH 2.0 by spectroscopy.

^b Overall stability constant.

^c $\text{pFe} = -\log[\text{Fe}^{3+}]$ when $[\text{Fe}^{3+}]_{\text{total}} = 10^{-6}$ M and $[\text{L}]_{\text{total}} = 10^{-5}$ M at pH 7.4.

Independently on the ligand type, the logarithm of the formation constants of the iron(III) complex is calculated as 3 or 4 times larger at basic than at acid pH. This larger affinity in basic medium is explained by the non-protonation of both chelating sites which facilitates the formation of coordination bonds. The best affinity for the metal cation is found for OHQ and catechol with a $\log K_{13}$ and $\log \beta_{13}$ larger than 10.0 and 40.0, respectively. Among them, catechol is by far the best ligand with a $\log \beta_{13}$ of 45.7. Its small size limits the steric hindrance and allows the formation of a very stable hexa-coordinated iron(III) complex by both phenol-like hydroxyl functions [Martell 1992]. By difference, $\log \beta_{13}$ value of OHQ is about 4 units lower (Table 3.6). This trend discrepancy depicts a coordination of the metal through the phenol-like hydroxyl and ester groups which allows the formation of a structure very close to the ideal octahedral environment with a less strong coordination binding since the basic character of the ester function is lower than the one of the hydroxylate.

Furthermore, the worse affinity constant is by far determined for NHQ with a $\log \beta_{13}$ of about 25.3. Here, it is drastically decreased due to the strong steric hindrance which leads to a strongly distorted structure of the resulting hexa-coordinated complex.

The iron(III)-HQ complex presents an affinity constant in between both previously reported cases $\log \beta_{13}=31.1$ since its structure is less prone to steric hindrance than $[\text{Fe}(\text{NHQ})_3]$ but is computed as more distorted than $[\text{Fe}_{\text{oo}}(\text{OHQ})_3]$ in comparison with the ideal octahedral environment.

The pFe values confirm this trend (Table 3.8). For OHQ and catechol, the values are much closed to the ones of other bidentate ligands reported in literature like 1-hydroxypyridin-2-one (pFe = 16.0), and Deferiprone (pFe = 19.0) [Li 2008]. Similar conclusions can be drawn for the HQ and NHQ ligands which lead to less stable iron(III) complexes, the pFe value of NHQ being 6.6 units lower than that of OHQ. Such a trend supports the conclusions drawn by Serratrice and coworkers for the N-TRENTOX and O-TRENTOX ligands [Serratrice 1997] and correlates with our previous investigations dealing with tuned ciprofloxacin and D-cycloserine ligands [Vu 2018] [Abdelsayed 2014]. It shows that the ester functionalization in 2-position of their HQ moieties increases the steric hindrance and disfavours the formation of an iron(III) hexa-coordinated complex, while its ester functionalization in 7-position allows the formation of an ideal-like octahedral complex, and thus favours a coordination of iron(III) through the salicylate function.

This phenomenon is once again illustrated with compounds **1** and **6** presented in the previous chapter (Chapter 2). Indeed, compound **1** with a carbonyl in 2-position of 8-HQ does not complex iron with this heterocycle, while this is possible with compound **6**, substituted in 7-position.

3. Conclusions & Perspectives

In this study, we performed a joined experimental and theoretical investigation aiming at understanding the formation of iron(III) complexes chelated by bidentate 8-HydroxyQuinoline-based derivatives, and the relative stability of the resulting complexes with respect to a functionalization of their ligands by electron withdrawing groups in 2- or 7-positions. More precisely, we succeeded to raise a protocol able to characterize and follow by UV/vis spectroscopy the formation of the iron(III) complexes. DFT computations performed with the PBE0 global-hybrid and confirmed with the OPBE semilocal density functional, showed that the hexa-coordinated complex was stabilized in its ground electronic state by adopting a high spin state configuration. They demonstrated that according to the position of the withdrawing group on the heterocyclic skeleton, the steric hindrance can destabilize the iron(III) complex by forcing it to adopt a distorted structure far from the ideal octahedral environment. In this respect, we found that the ester functionalization of HQ in 2-position weakens the iron(III) complex while its functionalization in 7-position allows a salicylate coordination of the metal very close to the ideal octahedral environment. UV/vis spectroscopic investigations at experimental and theoretical levels confirmed the existence of these complexes by providing matching signatures with an error close to 0.2 eV. TDDFT computations performed with the CAM-B3LYP range-separated hybrid proved that the two degenerated low-lying absorption bands of the experimental spectra correspond to strong charge-transfer excitations with metal-to-ligand and ligand-to-ligand characters, respectively. Moreover, in case of the 7-position functionalization, they confirmed that the ester/hydroxyl chelation prevails over the nitrogen/ester one by modelling similar chemical shifts of the bands.

These results have been published in 2020 in *J. Inorg. Biochem.*

As mentioned in the introduction, HQ can also form complexes, through chelation, with various divalent transition metals, such as Zn and Cu. The homeostasis of such metal is essential to avoid the deregulation of biological processes, such as amyloid- β peptide aggregation, one of the hallmarks of Alzheimer's disease, for instance [Gomes 2014]. It could

be then interesting to study the ability of OHQ and NHQ to complex these metals, as well as determining, as for iron(III), whether their metal affinities depend on the position of the ester group on the quinoline group.

4. Experiments

4.1. Materials and methods

All reagents were obtained from commercial suppliers and used without further purification. To monitor the progress of a reaction, thin-layer chromatography was performed on plastic TLC sheets of silica gel 60 F254 (layer thickness 0.2 mm) from Merck. IR, ^1H and ^{13}C NMR spectra confirmed the structures of all compounds. NMR spectra were recorded in DMSO- d_6 or CD_3OD on a Bruker AC 400 spectrometer at 400 MHz for ^1H and 100 MHz for ^{13}C . The chemical shifts are given in ppm referenced to the residual solvent signal. Coupling constants (J) are given in hertz (Hz), chemical shifts in ppm, and peak multiplicities are designated as follows: s, singlet; br s: broad singlet; d, doublet; t, triplet; q, quadruplet; m, multiplet. High-resolution mass spectra (HRMS) was recorded at the Small Molecule Mass Spectrometry platform of IMAGIF (Centre de Recherche de Gif - www.imagif.cnrs.fr), on a Waters spectrometer using electrospray ionization-TOF (ESI-TOF).

4.2. Methyl 8-hydroxyquinoline-2-carboxylate (NHQ) synthesis

Thionyl chloride (0.127 mL, 1.74 mmol) was added dropwise to a cooled suspension of 8-hydroxyquinoline-2-carboxylic acid (0.22 g, 1.16 mmol) in MeOH (5 mL). The yellow suspension was heated at 65°C for 4 h. After cooling at room temperature, water (10 mL) was added dropwise to the solution. Then, the suspension was filtered under vacuum to provide NHQ as yellow solid (0.200 g, 85%). IR ($\nu\text{ cm}^{-1}$): 3333, 1657, 1610. ^1H NMR (CD_3OD) δ ppm: 8.36 (d, $J = 8.60$ Hz, 1H), 8.33 (d, $J = 8.56$ Hz, 1H), 7.54 (t, $J = 8.04$ Hz, 1H), 7.38 (dd, $J = 8.24$ and 1.08, 1H), 7.15 (dd, $J = 7.68$ and 1.12 Hz, 1H), 4.06 (s, 3H). ^{13}C NMR (CD_3OD) δ ppm: 164.0, 152.7, 145.1, 143.9, 134.8, 132.9, 132.6, 122.4, 119.6, 116.3, 54.7. HRMS m/z calcd for $\text{C}_{11}\text{H}_9\text{NO}_3$ $[\text{M}+\text{H}]^+$ 204.0661; found: 204.0659.

4.3. Methyl 8-hydroxyquinoline-7-carboxylate (OHQ) synthesis

Five drops of sulfuric acid were added to a solution of 8-hydroxyquinoline-7-carboxylic acid (0.050 g, 0.26 mmol) in MeOH (5 mL). The reaction mixture was heated to reflux and stirred for 6 h. Then, the solvent was removed in vacuum and the crude residue purified by dematellated silica gel chromatography (eluent: CH₂Cl₂/MeOH, 85:15, v/v) to afford OHQ as solid (0.054 g, quantitative). IR (ν cm⁻¹): 1550, 1597, 2843. ¹H NMR (DMSO-*d*₆) δ ppm: 9.01 (dd, *J* = 4.8 and 1.5 Hz, 1H), 8.81 (dd, *J* = 8.4 and 1.4 Hz, 1H), 8.0 (d, *J* = 8.7 Hz, 1H), 7.94 (dd, *J* = 8.4 and 4.8 Hz, 1H), 7.49 (d, *J* = 8.72 Hz, 1H), 3.37 (s, 3H). ¹³C NMR (DMSO-*d*₆) δ ppm: 170.8, 158.0, 146.2, 142.2, 133.9, 132.1, 128.1, 124.2, 115.7, 112.5, 52.8. HRMS *m/z* calcd for C₁₁H₉NO₃ [M+H]⁺ 204.0661; found: 204.0655.

4.4. Stock solutions

Because of their poor solubility in aqueous media, the compounds synthesized were first dissolved in EtOH or DMSO at 10⁻² or 10⁻³ M. These solutions were then diluted to 1 or 5 · 10⁻⁴ M in the final buffer. Solutions at pH < 2.0 were not buffered; formiate, acetate, Hepes and carbonate buffers were used for pH 2.0–3.5, pH 3.5–6.0, pH 6.0–8.5 and pH > 8.5, respectively. Buffer salt concentration was 50 mM, and the ionic strength was adjusted to 0.2 with KCl. The final pH was reached by micro-injections of concentrated HCl or NaOH. FeCl₃ solutions were prepared in acidic media (pH 2.0). The Fe³⁺ complexes were prepared in acidic media by adding the required amount of FeCl₃ to the ligands. Then, the pH was gently raised to the final values by micro-injections of a concentrated NaOH solution. Fe(III)-citrate was prepared as previously described [Yang 2014].

4.5. pH Measurements

pH values were measured at 25.0 ± 0.5°C with a Jenco pH-meter equipped with an “Ingold” combined calomel/glass microelectrode. The pH-meter was standardized at 25.0 ± 0.5°C by the standard pH buffer values of 7.00 and 10.01 (Sigma). In the presence of DMSO and EtOH, the pH values were corrected according to published procedures [Bates 1973].

4.6. Spectrophotometric measurements

Affinity constants and acid-base constants were determined spectrophotometrically with the SPECFIT32 Global Analysis program [Binstead 2003] [Eigen 1963]. Spectroscopic measurements were performed at $25.0 \pm 0.5^\circ\text{C}$ on a Cary 4000 spectrophotometer equipped with a Peltier-thermostated cell-carrier.

4.7. Microcalorimetry

Isothermal titration calorimetry (ITC) experiments were carried out on a TA Instruments microcalorimeter system with a gold cell and an active cell volume of $166 \mu\text{L}$. All ITC titrations were performed at 25.0°C and a stirring rate of 250 rpm, using a titrating syringe volume of $50 \mu\text{L}$. Typically, an automated sequence of 24 injections, each of $2 \mu\text{L}$ FeCl_3 or $\text{Fe}(\text{citrate})$, titrant into the sample cell containing the ligand, spaced at 7.5 min intervals, at pH 2.0 or pH 7.0, respectively. Reverse titrations were also performed with an automated sequence of 24 injections of ligand into the cell containing the metal solution, spaced at 7.5 min intervals. The ITC data were analyzed after subtraction of the control injection in buffer alone, using the Nanoanalyze software, to yield the association constant, stoichiometry, and the enthalpy variation of the binding reactions.

4.8. Computational details

All the computations were performed with the release B.01 of the Gaussian'16 program package [Frisch 2016]. The structures of the free ligands and hexa-coordinated iron(III) complexes in their low, intermediate and high spin electronic states were fully optimized at DFT level with the PBE0 global-hybrid density functional [Adamo 1999] [Ernzerhof 1999] using the Pople 6-31+G* double- ζ basis set for the H, C, N and O atoms [Hehre 1972] [Franci 1982], and the LanL2DZ double- ζ basis set associated to the corresponding pseudopotential for Fe [Hay 1985]. Structure optimizations of the high spin state complexes were also performed at the PBE0-D3(bj) level of theory by adding on top of the PBE0 density functional the D3(bj) empirical dispersion correction [Goerigk 2011]. Bulk solvent effects were added in an implicit fashion employing the polarizable continuum model (PCM) and setting the dielectric constant to the one of water [Tomasi 2005]. To confirm the spin multiplicity of the ground electronic state of each iron(III) complex, structure optimizations were also carried out with OPBE [Cohen 2000] [Perdew 1996], a semilocal density

functional recognized to provide a reliable estimate of the high- and low-spin energy gaps [Rousseau 2018]. Excited-state properties were computed with linear response TDDFT using the methodology mentioned above. More precisely, the first 30 vertical electronic excitations were estimated with the PBE0 global- and CAM-B3LYP [Yanai 2004] range-separated hybrid density functionals from the PBE0 optimized structures with the same basis sets and pseudopotentials as mentioned above. Both density functionals and basis sets are recognized to provide reliable energies depending on the type of electronic transitions [Le Bahers 2014], and a sufficient enough energy convergence [Jacquemin 2009] [Jacquemin 2009], respectively. The band-shaped absorption spectra were obtained by convoluting the stick spectrum (energy and oscillator strength) into a sum of Gaussian functions centered on each vertical transition, fitting the full width at half maximum of each Gaussian function to the corresponding experimental spectra [Brémond 2010] [Brémond 2014]. Density-based analyzes and the mean charge transfer distance D_{CT} index values were computed from ground- and excited-cube densities according to the model described by Ciofni and coworkers [Le Bahers 2011].

CHAPTER IV:

THE USE OF NANOPARTICLES TO OVERCOME *CHLAMYDIA TRACHOMATIS* INFECTION

1. The use of nanoparticles to overcome *C. trachomatis* infection – state of art

The contribution of nanotechnologies is a very developed aspect in the search for a vaccine directed against *C. trachomatis* [Sahu 2018] [Lin 2018] but will not be developed here as we chose to focus on the delivery of antibiotics or similar.

Antibiotics activity against *Chlamydia* is hampered by insufficient accumulation of active drugs at the intracellular target site. Antibiotics often have to cross many membrane barriers (cell membrane, inclusion membrane and membrane of EBs or RBs) and this can substantially reduce the concentration of the drugs at the target site and limit thus their action. Therefore, successful therapy with antibiotics may require specialized drug carriers that can enhance delivery to cytoplasmic inclusions in order to inhibit both acute and persistent infections. Nanoparticles (NPs) may play this role. Their small size, surface chemical reactivity toward biomolecule grafting, their intrinsic physical properties (magnetic, optic, etc.) giving them the opportunity to be stimulated by an external electromagnetic field among others, make them particularly valuable for drug transport and delivery. Several examples have been described in the literature and are presented below.

1.1. Metallic nanoparticles

Metal nanoparticles have been explored for their putative biomedical applications against a wide range of pathogens. Among them, silver NPs were the most tested one against *C. trachomatis* infection. For instance, Yilma *et al.* described the ability of silver NPs (Ag NPs), particularly small Ag NPs coated with a poly(vinylpyrrolidone) thin shell, to decrease inflammation initiated in *C. trachomatis* J774 macrophages infected mouse [Yilma 2013]. Indeed, they demonstrated that the production of many chemokines and cytokines secreted during the bacterial infection is downregulated in macrophages exposed to Ag NPs.

A complete review dealing with Ag NPs and their applications was published by Marin *et al* in 2015 for such a purpose [Marin 2015].

1.2. Polymeric nanoparticles

Chlamydiae are known to divert the host mammalian cell machinery to acquire nutrients from extracellular sources. Following a chlamydial infection, cellular lipid droplets (~100 nm in diameter) are actively trafficked to the inclusions [Cocchiaro 2008]. A number of studies have shown that polymeric nanoparticles in the similar size range can also enter mammalian cells efficiently and deliver encapsulated drugs intracellularly [Panyam 2003]. Based on this, Toti *et al.* hypothesized that polymeric nanoparticles can be used to enhance antibiotic delivery to the chlamydial inclusions. Furthermore, the sustained release profile of antibiotics from nanoparticles can prolong therapeutic efficacy and inhibit persistent infections. Previously, their group used NPs based on poly(lactide-co-glycolide) (PLGA) polymer to enhance the delivery of antibiotics to chlamydial inclusions [Toti 2011]. PLGA NPs entered these inclusions rapidly into both acute and persistently infected cells. Furthermore, nanoparticle encapsulating rifampin, a form of azithromycin, one of the two first-line chlamydial antibiotics, reduced inclusion numbers in infected cells more than the soluble form. This means that nanoparticle may act as valuable drug delivery platforms, increasing drug antimicrobial activity. Similar results were reported in other results [Mohammadi 2010] [Azhdarzadeh 2012], confirming the ability of encapsulating type nanoparticle to improve the antibiotic activity.

In 2011 Mishra *et al.* conjugated azithromycin to poly(amidoamine) (PAMAM) dendrimers, another class of nanoscale drug delivery carrier, and evaluated the antibacterial activity of the resulting NPs in acute and persistent chlamydial infections [Mishra 2011]. They demonstrated that the nanohybrids were more efficient than the free drugs in chlamydial inclusions penetration, when contacted to HEp-2 cells. They evidenced an effective protection of these cells.

One of the key features of polymeric nanoparticles is that their physicochemical characteristics, including size, shape and antibiotic release kinetics, can be fine-tuned to further enhance the antimicrobial activity of the drugs [Xiong 2014] [Zhang 2010] [Abed 2014]. This versatility, coupled with the use of polymers that are safe for human use, should enable their rapid clinical translation.

Introducing a targeting ligand onto the surface of NPs can also improve *in vivo* efficacy of antibiotic-loaded NPs. In a recent study by Benchaala *et al.*, folic acid was used as a targeting

moiety to enhance delivery of antibiotics to infected tissues *in vivo* [Benchaala 2014]. The choice of folic acid was driven by recent results, which have been demonstrated that mammalian cells infected with *C. trachomatis* overexpress folate receptors and that folate-conjugated delivery systems are able to target almost specifically such cells [Panyam 2014]. Benchaala *et al.* demonstrated that folate-functionalized dendrimers can be concentrated (3-4 times higher than non-folate conjugated systems) in the infected paws and genital tracts of mice exhibiting *C. trachomatis* induced inflammation and infection. These results pave the way of an effective *in vivo* antimicrobial activity enhancement by the systematic use of specific ligand-functionalized NPs. In this context, other expressed targets on *C. trachomatis* can be addressed through real nanotherapeutic strategies: Protein Disulfide Isomerase (PDI), heparan sulfate and N-linked high-mannose type oligosaccharides [Kuo 1996] [Davis 2002] [Su 1996]. But to date, folic acid appears as the most promising one [Panyam 2014] [Benchaala 2014].

1.3. From Folate-based polymeric NPs to Folate-based carbon dots

As previously presented, Benchaala *et al.* proposed folic acid-functionalized dendrimers to targeting *Chlamydia-infected tissues* in a reactive arthritis mouse model [Benchaala 2014]. Especially, they developed a folate-PAMAM dendrimer-Cy5.5 conjugate, in which the Cy5.5 chromophores allow their imaging during the entire cell contacting process. Upon systemic administration and comparison with non-folate-functionalized NPs, they observed a higher concentration of folate-based NPs in paws and genital tracts, two major sites of infection and inflammation, as a consequence of the folic acid - folic acid receptor recognition. Indeed, folate receptors (FA-Rs), high-affinity folate-binding proteins ($K_d = 10^{-10}$ M; [Chen 2013]), are known to be overexpressed on the membranes of many cells during physiopathological conditions, but minimally expressed on normal cells [Merzel 2017a] [Merzel 2017b]. All the experimental observations fit with an overexpression of the FA-Rs in *C. trachomatis*-infected and inflamed tissues and folate-based NPs uptake through endocytosis.

Based on such an approach, it could be interesting to replace the Cy5.5 chromophore by a light emitting NPs with better optical properties (wide wavelength excitation range, high quantum yield, etc.). Among these NPs, carbon dots are certainly the most promising, since they exhibit powerful luminescence properties and non-toxicity [Sciortino 2018a]. As small solid particles they can also replace the polymer or the dendrimer type carriers, making them useful for specific drug delivery when additionally functionalised with acid folic. This is what

exactly did Bhunia *et al.* for imaging cancer cells overexpressing the FA-Rs on their-surface. They thermally decomposed folic acid and obtained carbon dots with luminescent properties in the visible light range, functionalized at their surface by folic acid residue (FA-CDs). They showed that thanks to their adsorbates, the resulting nanohybrides can be concentrated in the investigated cancer cells and thanks to their inorganic core they can be imaged by fluorescence microscopy (Figure 4.1) [Bhunia 2016].

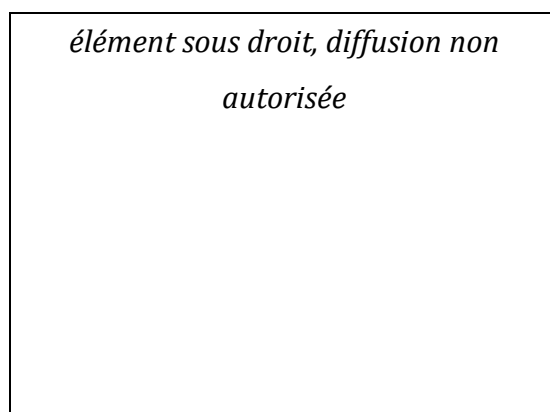


Figure 4.1. Fluorescence emission intensity as a function of the cell type incubated with the FA-CDs [Bhunia 2016].

FA-CDs based drug delivery systems were scarcely tested as antibacterial nanocarriers and they were never contacted with *C. trachomatis* infected cells for their treatment, despite they large applicative potential. To date, crossing "chlamydia" and "carbon dots" keywords does not provide any results in PubMed and Web of Sciences search engines. To the best of our knowledge, there is only the work of Hou *et al.*, in which the authors prepared carbon dots by hydrothermal decomposition of ciprofloxacin hydrochloride (Cip), a well-known antibiotic [Hou 2017]. The authors showed that the resulting Cip-CDs nanohybrides maintain antibacterial effects towards *Staphylococcus aureus* (Gram-positive) and *Escherichia coli* (Gram-negative), underlining the ability of the engineered systems to act alone as an antibacterial agent.

Carbon dots (CDs) are an emerging new type of carbon nanomaterials. They were discovered accidentally in 2004, by Xu *et al.* [Xu 2004] and since then, a variety of synthesis methods have been developed for their production [Rani 2020]: sonication, electrochemical exfoliation, laser ablation, microwave irradiation. Most CDs exhibit blue or/and green emissions, despite the different routes and precursors used for their fabrication. They are typically green substitutes of the prior toxic CdSe quantum dots (QDs) [Sharma 2017]. Their building block is made out of carbon [Bakker 2010], with some doped heteroatoms, creating a

nanoparticle that is more biocompatible, soluble in water and less toxic compared with QDs [Havrdova 2016]. Moreover, CDs demonstrate ease surface functionalization [Tian 2019]. Thanks to these unique properties, the number of related publications about their syntheses, properties and applications increased exponentially every year and a rapid expansion into various applications, including biomedical use, is observed [Farshbaf 2018]. However, elucidating the molecular origin and key factors controlling their physiochemical properties remains challenging. Zhu *et al* proposed that some properties, e.g. toxicity, are dictated primarily by the CDs core, while other properties, e.g. dispersibility, are derived primarily from their surface functional groups [Zhu 2015]. Zhi *et al.* reviewed prevalent hypotheses regarding the origin of the CDs photoluminescence, highlighting the role of the surface groups, with their trapped energy levels in the band gap of these semiconductors, in the radiative desexcitation processes [Zhi 2019].

CDs as semiconductive nanoparticles, are commonly characterized using methods including UV/Vis absorption and fluorescence spectroscopies, Raman, dynamic light scattering (DLS), atomic force microscopy (AFM), transmission electron microscopy (TEM), FTIR, Mass, NMR, zeta potentiometry and X-ray photoelectron spectroscopy (XPS). Their exact structure is still under debates. What we can say that it is strongly dependent on their preparation conditions. To date, several crystallographic features were identified. CDs can be nitride carbon semiconductor C_3N_4 [Sciortino 2018b], nanographene and/or nanographene oxide [Yuan 2018] and polymeric particles [Yang 2018]. Only TEM and High resolution TEM measurements coupled to Electron Energy Loss Spectroscopy (EELS) would allow the discrimination between all these structures.

2. Pioneer study on CDs as antibacterial agents against *C. trachomatis* infection

Folate-based CDs (FA-CDs) offer an unambiguous efficient tool toward *C. trachomatis* infection fighting. These "all in one" NPs would allow:

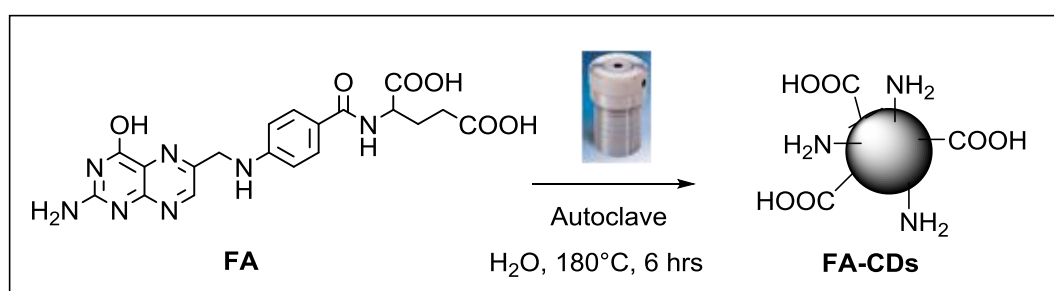
- (i) infected cells targeting through the recognition FA-CDs/FA-Rs;
- (ii) cell internalization, as suggested by previous studies, which pointed out that FA-CDs may internalize FR-positive HeLa cells [Slastnikova 2017];
- (iii) drug delivery when antibiotics are judiciously grafted to their surface;
- (iv) imaging the infected cells through the luminescent properties of the FA-CDs.

For these reasons, we synthesized FA-CDs by folic acid hydrothermal thermal decomposition [Bhunia 2016]. The produced FA-CDs were then well-characterized and provided to Dr Åsa Gylfe (Umeå university, Sweden) to evaluate their ability to interact with *C. trachomatis* infected HeLa cells. To be as exhaustive as possible in our investigations, we also prepared Cip-CDs by ciprofloxacin hydrochloride hydrothermal decomposition [Hou 2017]. Cip-CDs were also well-characterized and tested for their antibacterial activity against *C. trachomatis*.

3. Results and discussion

3.1. Synthesis and characterizations of FA-CDs

FA-CDs were synthesized by a hydrothermal method using folic acid as the carbon source. We first tried to reproduce the synthesis proposed by Bhunia *et al* [Bhunia 2016]. Indeed, they described a simple one-step synthetic route in which folic acid was mixed with sodium hydroxyde and heated at 90°C for 2 hours to induce carbonization. However, our trials did not provide luminescent objects. We then modified the experimental procedure increasing the temperature up to 180°C, without however obtaining FA-CDs. Finally, removing sodium hydroxide from the reaction medium and heating up to 180°C led to a yellow suspension with a fluorescent behaviour which is not observed in the free FA under UV irradiation (Figure 4.2). The latter was then purified by filtration through a 0.22 µm filter, dialyzed against milliQ water and lyophilized to provide the desired FA-CDs as yellow powder. The extension of the reaction time to 6 hours allowed an increase in the reaction yield from 3.3 % for two hours to 23.3 % for 6 hours (Scheme 4.1). FA-CDs obtained after 6 hours of reaction were selected for characterization.



Scheme 4.1. Schematic FA-CDs synthesis from folic acid

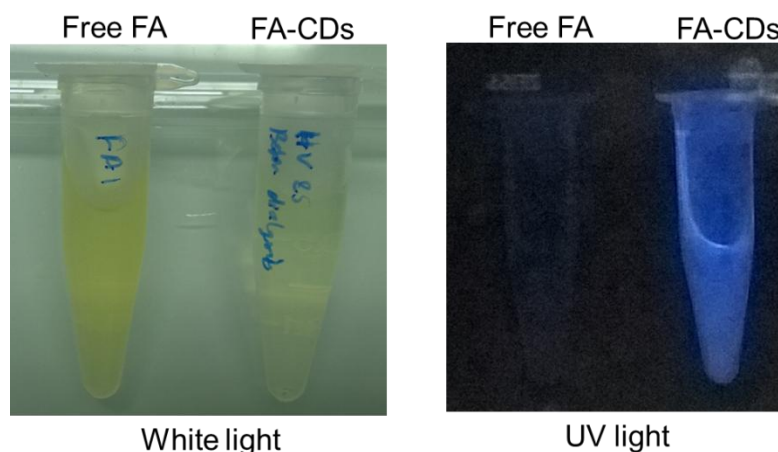


Figure 4.2. Solution of free FA and FA-CDs in water under white light and under UV irradiation at 365 nm.

Statistical analysis of particle size, extracted from Dynamic Light Scattering (DLS) data, indicated that the synthesized FA-CDs exhibited a size distribution of 2.5–8 nm with an average diameter about 4 ± 1 nm (Figure 4.3).

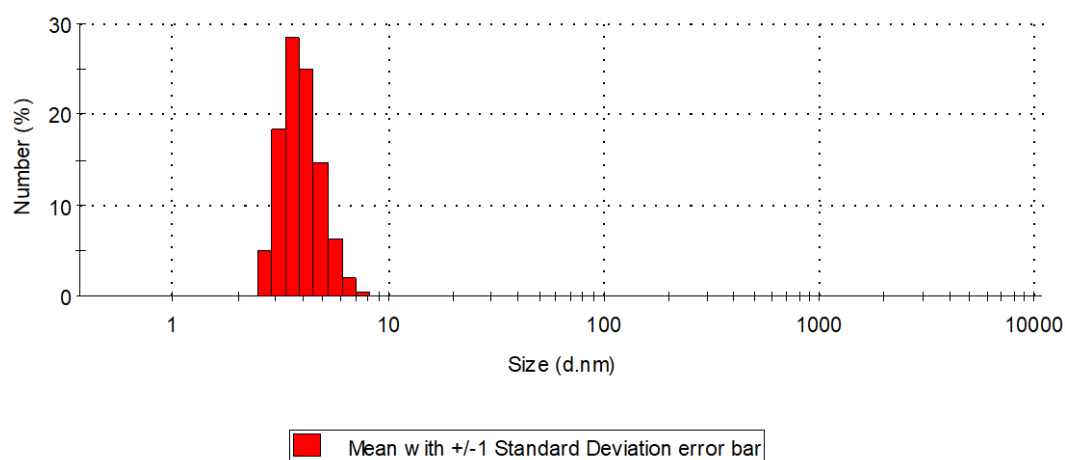


Figure 4.3. Size distribution histogram of FA-CDs, extracted from the DLS experiments in water.

TEM experiments are actually in progress to confirm FA-CDs size and to provide information about their crystalline structure (Pr Nicolas Menguy, *Institut de Minéralogie, de Physique des Matériaux et de Cosmochimie*, Sorbonne University).

The optical absorption and emission spectra of the filtrated aqueous FA-CDs solution were recorded and plotted in Figures 4.4 and 4.5, respectively. FA-CDs display several absorption bands (Figure 4.4). Two main features can be highlighted. First, a systematic blue shift is

observed on the FA characteristic UV bands in the FA-CDs spectrum, 255 to 236 nm and 284 to 277 nm, with a significant relative intensity variation. These bands are usually attributed to the π - π^* transition of the aromatic sp^2 carbon atoms [Li 2012] [Bhunia 2016] and their evidence suggest that FA molecules are still present on CDs surface. A last FA signature in the FA-CDs spectrum is that of the band at 365 nm. It consists of a net peak in free FA spectrum and a shoulder in FA-CDs one. It is assigned to the π - π^* transition localized on the pterin ring in FA [Li 2012] [Baibarak 2019] [Mitchell 1944].

Second, new bands at 313 and 342 nm are observed in the FA-CDs spectrum potentially attributed to the CDs cores, like their band-to-band transition and/or specific transitions involving their surface states, or attributed to intrinsic transitions of other residual adsorbates, like the n - π^* transitions of carbonyl groups [Sciortino 2018a]. At this stage, without the exact structure of the produced CDs we cannot definitively attribute these last bands.

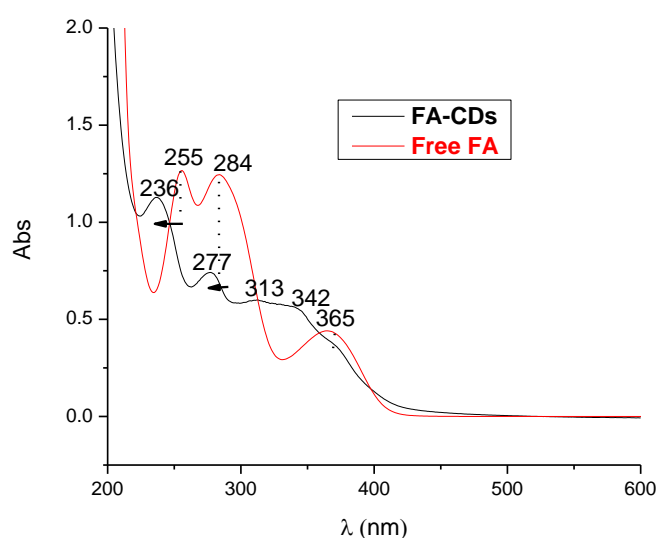


Figure 4.4. Ultraviolet-visible (UV/Vis) absorption spectra of FA-CDs (50 $\mu\text{g}/\text{mL}$ in water, black line) and free FA (25 $\mu\text{g}/\text{mL}$ in water, red line) in aqueous solution

With continuously increasing the excitation wavelengths from 300 to 410 nm, no obvious wavelength shift was observed in the fluorescence emission spectra of FA-CDs (Figure 4.5), implying an excitation-independent fluorescent behavior, which is quite typical of CDs [Sciortino 2018a]. Indeed, whereas organic chromophores require an excitation at a wavelength close to the involved LUMO-HOMO transition energy, CDs can be excited over a wider range of wavelengths, as long as their corresponding energies remain higher than those

required for the band-to-band or surface state within the band gap transitions [Sciortino 2018a]. The fluorescence spectra showed that the optimum emission of FA-CDs was located at 444 nm when excited at 355 nm, the wavelength giving the highest luminescence intensity. At this excitation, a fluorescent quantum yield of 13% was obtained (calculated with respect to quinine sulfate standard) (Figure 4.6, Table 4.1), 1.5 times higher than that reported by Bhunia *et al.* in his previous works [Bhunia 2016]. At the same excited wavelength (355 nm), photoluminescence spectra of free FA and FA-CDs show distinct differences in measured fluorescence intensity, which is in favor to FA-CDs, as shown in Figure 4.7.

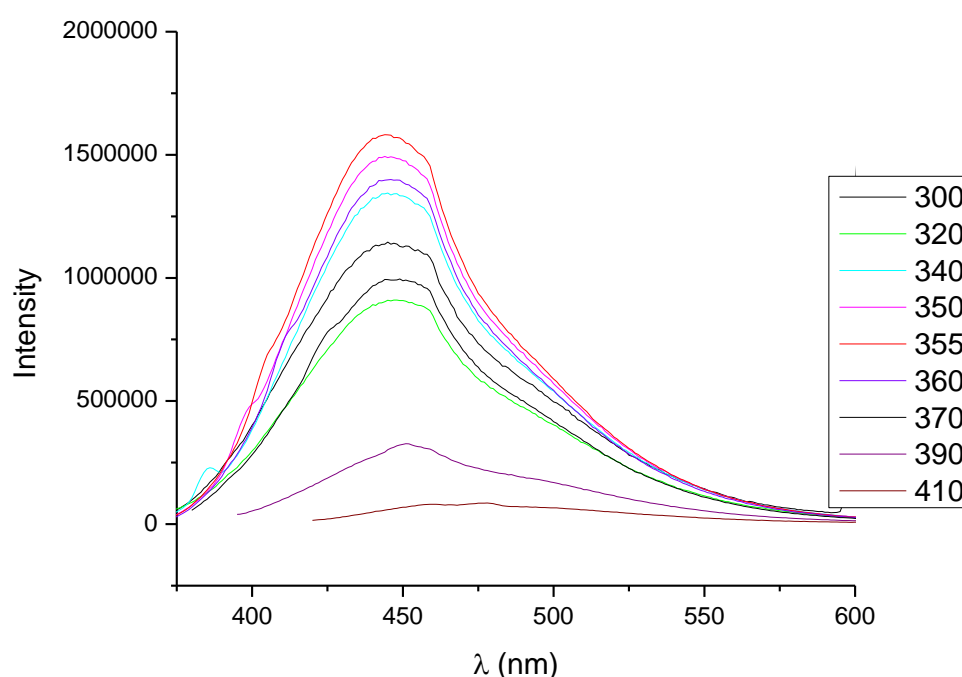


Figure 4.5. Photoluminescence spectra of FA-CDs (1 $\mu\text{g}/\text{mL}$ in water) for various excitation wavelengths.

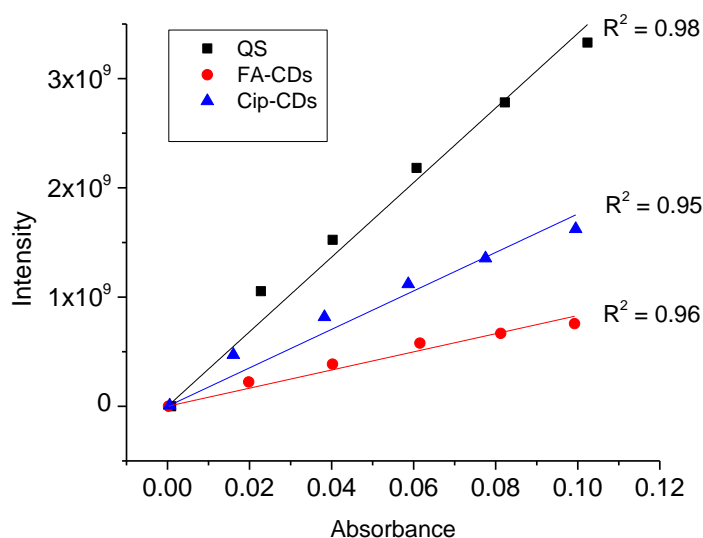


Figure 4.6. Slope method for the calculation of fluorescence quantum yield.

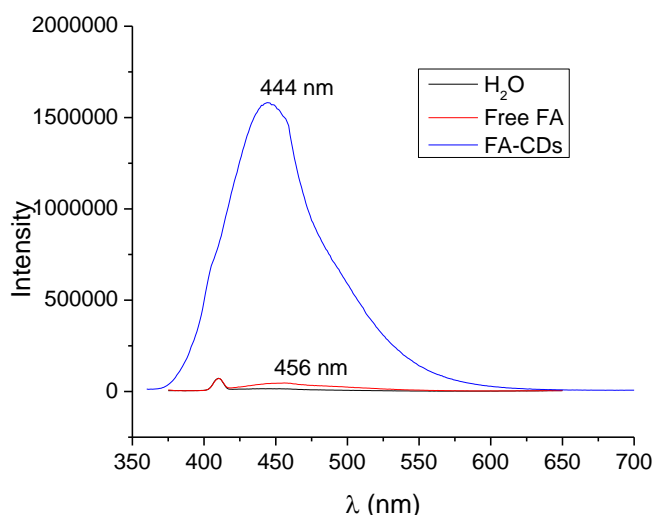


Figure 4.7. Photoluminescence spectra of free FA (1 µg/mL in water) and FA-CDs (1 µg/mL in water), $\lambda_{exc} = 355$ nm.

Fourier transform infrared (FT-IR) spectrum of FA-CDs (KBr method) was recorded and compared to that of free FA (Figure 4.8). FA-CDs spectrum appears to be less rich than that of free FA. Nevertheless, it evidences several signatures of carbon-bonded, nitrogen bonded and oxygen-bonded units. The vibration bands of a variety of hydrophilic functional groups can be identified: the broad peak at 3211 cm^{-1} ascribed to the OH or/and NH and/or NH_2 stretching vibration, the strong peak at 1679 cm^{-1} assigned to COO stretching vibration and the peaks at 1403 , 1294 and 1108 cm^{-1} agreed with the C–O and C–N stretching vibrations.

They can be be affiliated to those observed for free FA: 3543, 3416 and 3322 cm^{-1} for amino and hydroxyl moieties; 1693 and 1638 cm^{-1} for carbonyl groups. As they can be assigned to new hydrophilic species generated during hydrothermal treatment. Indeed, it was reported that reaction between carboxyl and amino groups, which are present in the FA structure, under hydrothermal conditions contributes to the bonding of hydrophilic functional structures on the surface of carbon dots [Krysmann 2012] [Zhang 2016] [Hou 2017]. So at this stage it is not easy to conclude about the exact nature of the organic adsorbates on CDs surface. FA as well as FA residues can be present. Nevertheless, an attentive observation of FA-CDs FTIR spectrum evidences a peak at 1587 cm^{-1} which is usually assigned to aromatic carbon-carbon double bonds. This peak can be a signature of FA persistence, even if one can not exclude other hydrophilic species on CDs's surface.

So, this chemical richness of FA-CDs surface with several hydroxyl, amino and carbonyl groups attached on, whatever their origin, offers an additional advantageous to these particles, their ability, through a judicious surface chemistry, to be covalently decorated with supplementary functional molecules (drugs).

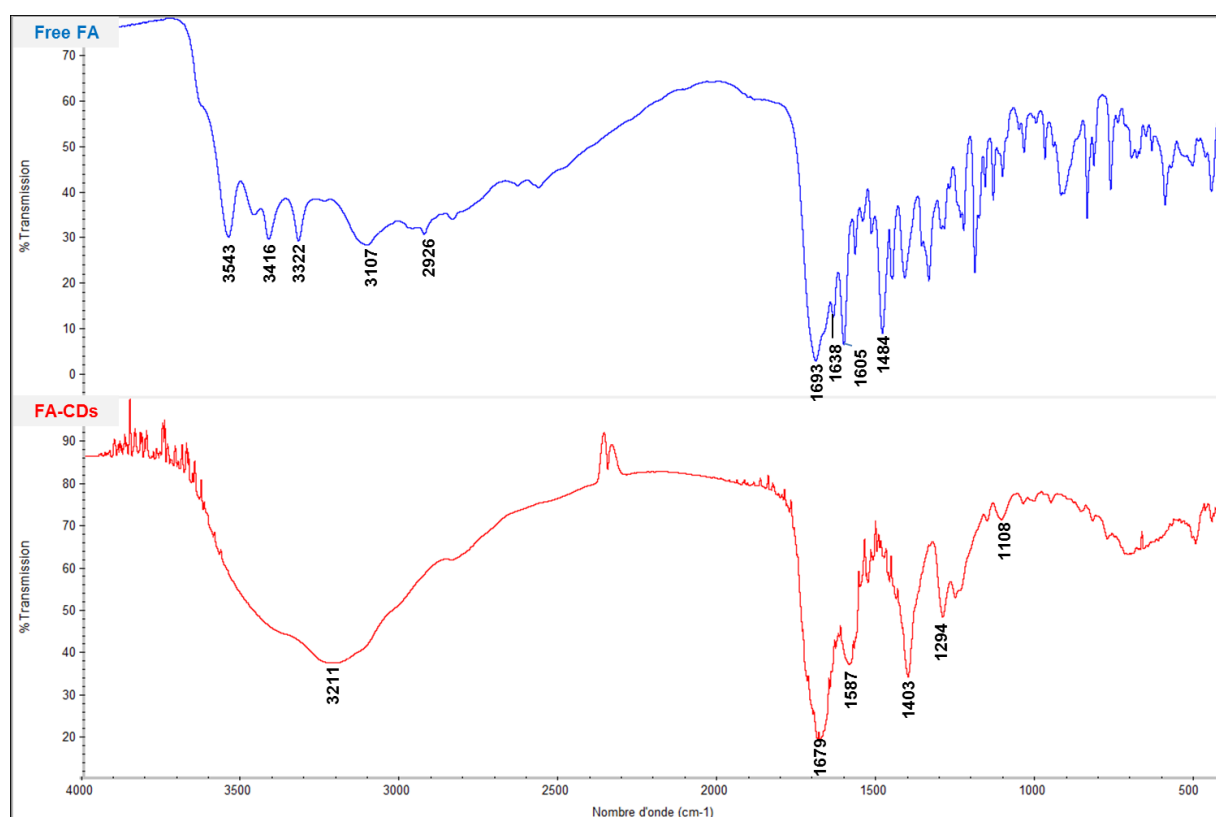


Figure 4.8. FT-IR spectra of free FA (upper spectrum) and FA-CDs (lower spectrum).

Zeta potential is an indicative measure of the stability of an aqueous dispersion of NPs. It defines the charge surface around the particles and it is directly related to the type of attached groups to this surface. Since these groups are dependent on the pH of the solution, the Zeta potential can be varied by changing the pH in the sense of an alteration or improvement of the NP suspension stability. Indeed, whereas negatively charged carboxylate groups at the surface of NPs stabilize their aqueous suspension at $\text{pH} > 4$ (average pK_a of carboxylate/carboxylic system) and lead a strongly negative Zeta potential value in this pH range, positively charged ammonium groups do that at $\text{pH} < 9$ (average pK_a of ammonium/amino system) and lead a strongly positively charged Zeta potential value only in this pH range.

Hence, it is important to determine how pH affects the Zeta potential of our aqueous FA-CDs dispersion. As a point of reference, according colloid chemistry principles, an electrostatically stabilized dispersion system loses stability when the absolute value of the zeta potential decreases to less than 30 mV. In the present case, FA-CDs suspension exhibits a Zeta potential of -13 mV at $\text{pH} = 4$, meaning that the produced particles are globally negatively charged at their surface, with a relative weak colloidal stability. At such pH value, FA-CDs are likely agglomerated (Figure 4.9). It exhibits a Zeta potential of -35 mV at $\text{pH} = 7$ (Figure 4.10), meaning that the produced particles are strictly negatively charged at their surface, with a high colloidal stability. At such pH value, FA-CDs are likely individualized particles

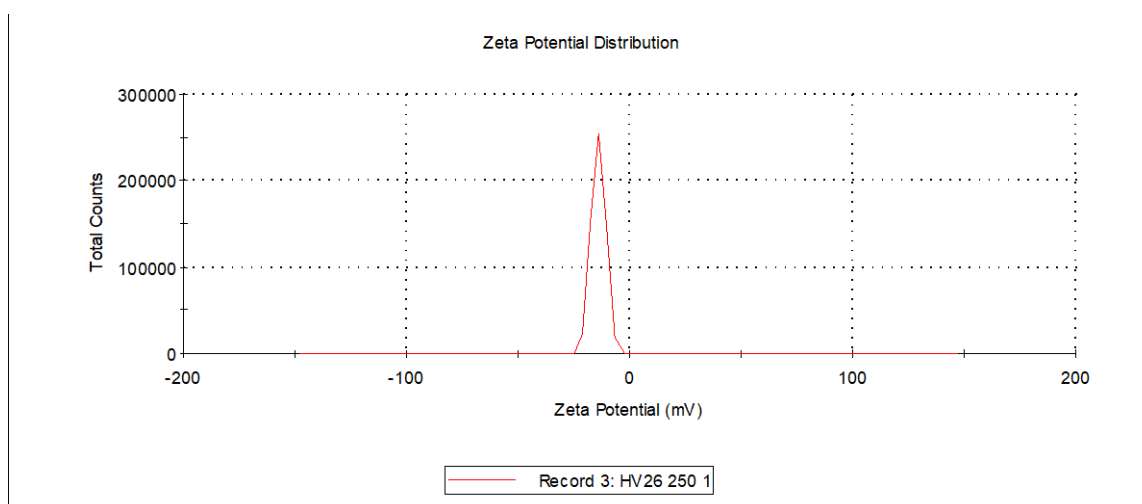


Figure 4.9. Aqueous FA-CDs suspension zeta potential distribution at pH 4.

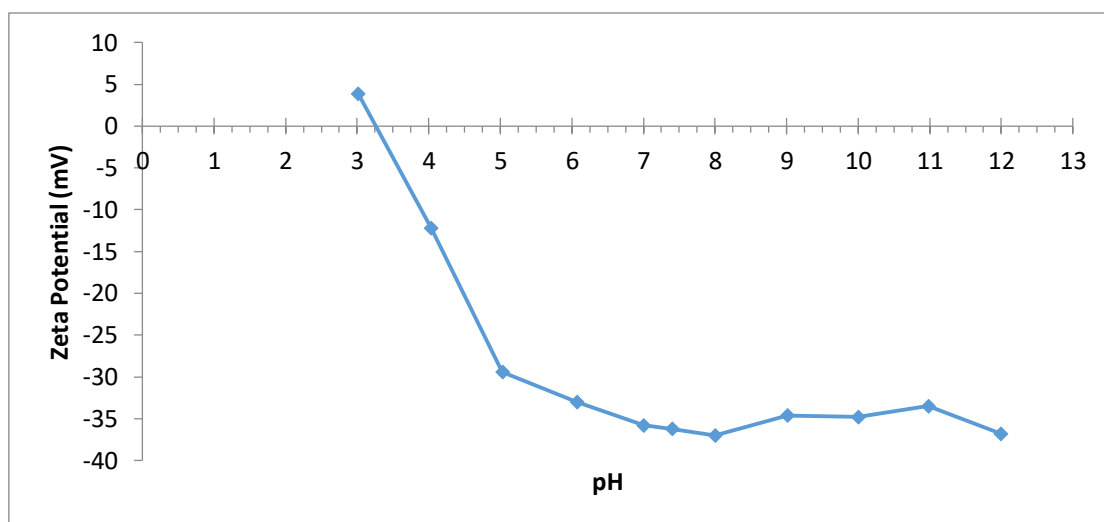
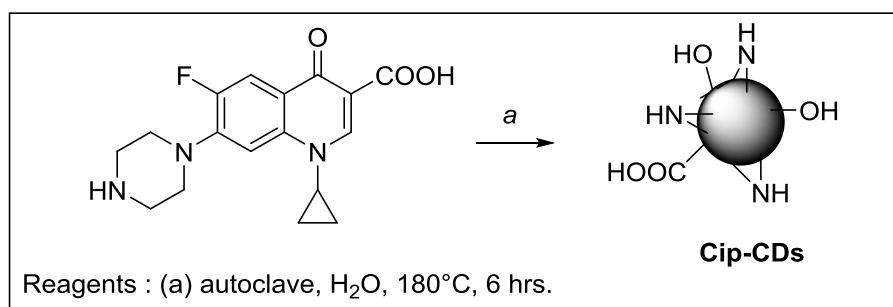


Figure 4.10. Variation of the measured Zeta potential of an aqueous FA-CDs suspension at different pH values. The isoelectric point was defined at the intersection between the Zeta potential vs. pH plot and the abscise axis. It is found to be about pH 3.2.

This result must be underlined because its highlight the fact that aqueous FA-CDs suspensions form stable colloids at physiological pH values, which is important for all our further biological and pharmacological assays.

3.2. Synthesis and characterizations of Cip-CDs

A hydrothermal synthesis was also performed to obtain CDs from Cip as source of carbon (Cip-CDs) following the procedure described by Hou *et al.* [Hou 2017]. It consists of heating, in an autoclave, at 180°C for 6 hours a Cip aqueous solution (Scheme 4.2). Herein, they proposed a method allowing the production of CDs with functional groups on their surface, which could effectively avoid and exclude further functional modification steps. The as-prepared CDs are thus expected to preserve the structural feature of Cip at their surface and to conserve its antibacterial properties.



Scheme 4.2. Cip-CDs synthesis from Ciprofloxacin.

As for FA-CDs, the recovered suspension is yellow and appears blue under UV illumination. It was then analyzed by DLS to determine the average size of the produced particles. The statistical analysis of particle size, extracted from these measurements indicated that the synthesized Cip-CDs exhibited a size distribution ranging between 3.5 and 9 nm, with an average size value of 5 ± 1 nm (Figure 4.11).

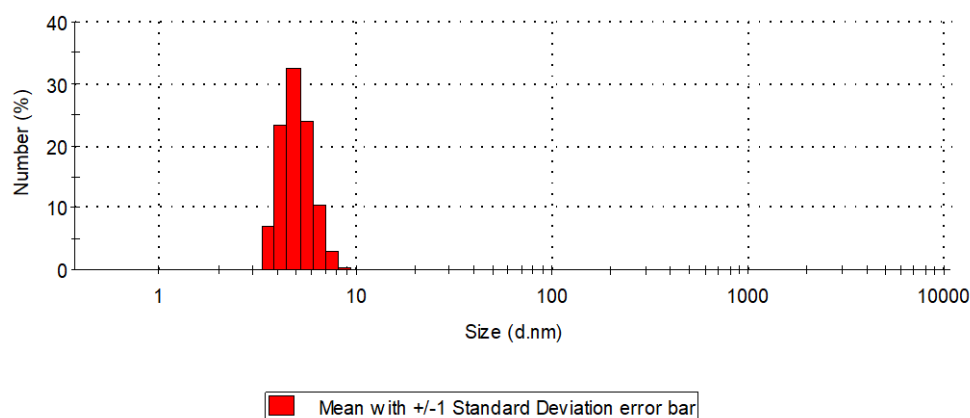


Figure 4.11. Size distribution histogram of Cip-CDs, extracted from the DLS experiments in water

TEM experiments are actually in progress to confirm Cip-CDs size and to provide information about their crystalline structure (Pr Nicolas Menguy, *Institut de Minéralogie, de Physique des Matériaux et de Cosmochimie*, Sorbonne University).

The UV-vis absorption spectrum of Cip-CDs displays two characteristic peaks at 271 and 322 nm (Figure 4.12), assigned to the $\pi-\pi^*$ and $n-\pi^*$ Cip transitions, respectively. Importantly, compared with the UV-vis absorption spectrum of free Cip, these transitions are shifted by about 5-7 nm, in agreement with Cip adsorption (probably chemisorption) at the surface of CDs. The band at 334 nm in Cip-CDs spectrum is also present around 328 nm in free Cip spectrum. One must also notice that no additional bands are observed in Cip-CDs spectrum, like for FA-CDs one. But the observed increase of its band intensity, particularly around 330 nm may traduce a superposition with characteristic carbon dots bands.

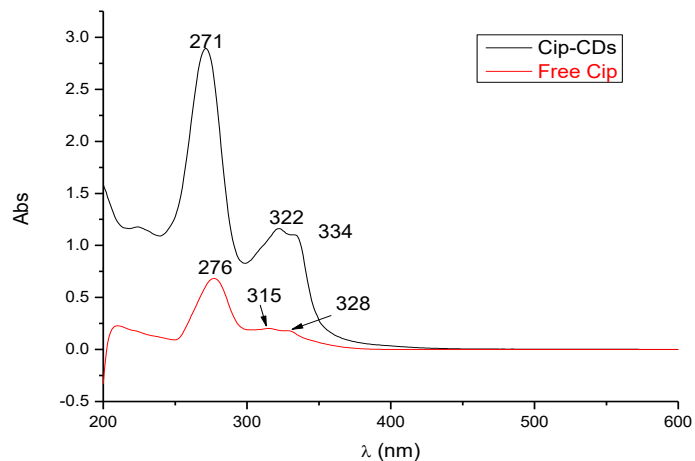


Figure 4.12. UV-visible absorption spectra of free Cip (25 $\mu\text{g}/\text{mL}$ in 0.1N HCl, red line) and Cip-CDs (50 $\mu\text{g}/\text{mL}$ in H_2O , black line)

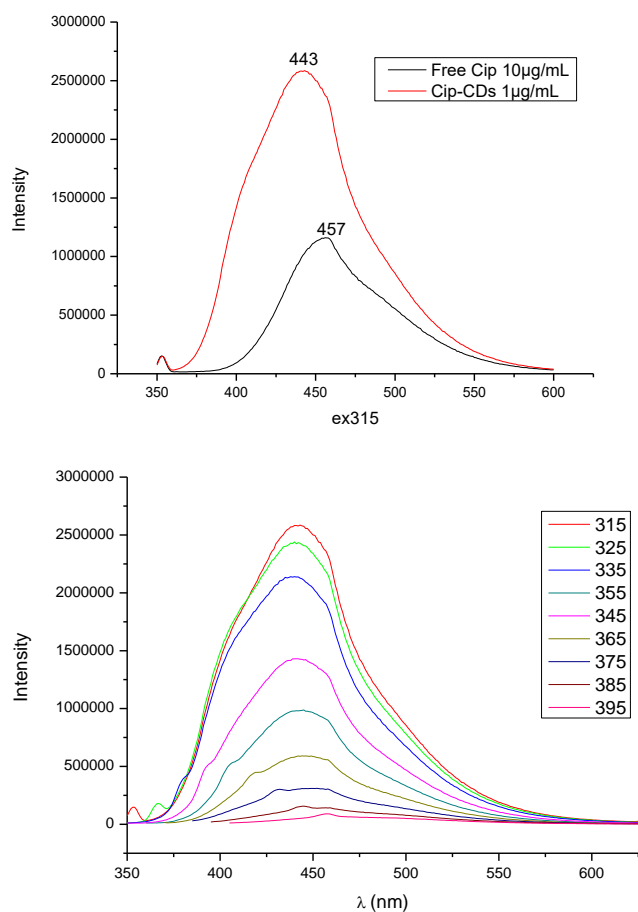


Figure 4.13. Photoluminescence spectra of (upper) free Cip (10 $\mu\text{g}/\text{mL}$ in 1N HCl) and Cip-CDs (1 $\mu\text{g}/\text{mL}$ in water), $\lambda_{\text{ex}} = 315 \text{ nm}$; and (lower) Cip-CDs (1 $\mu\text{g}/\text{mL}$ in water) for various excitation wavelengths.

With continuously increasing the excitation wavelengths from 300 to 400 nm, we recorded the photoluminescence spectra of Cip-CDs (Figure 4.13). As expected the former exhibits an excitation-independent fluorescent behavior. A maximum of fluorescence at 443 nm was reached at an excitation of 315 nm for Cip-CDs with a photoluminescence quantum yield (QY) of 18 %, calculated with respect to quinine sulfate standard by the slope method (Figure 4.6, Table 4.1). At the same excited wavelength (315 nm), photoluminescence spectra of free Cip and Cip-CDs show distinct differences in measured fluorescence intensity as shown in Figure 4.13.

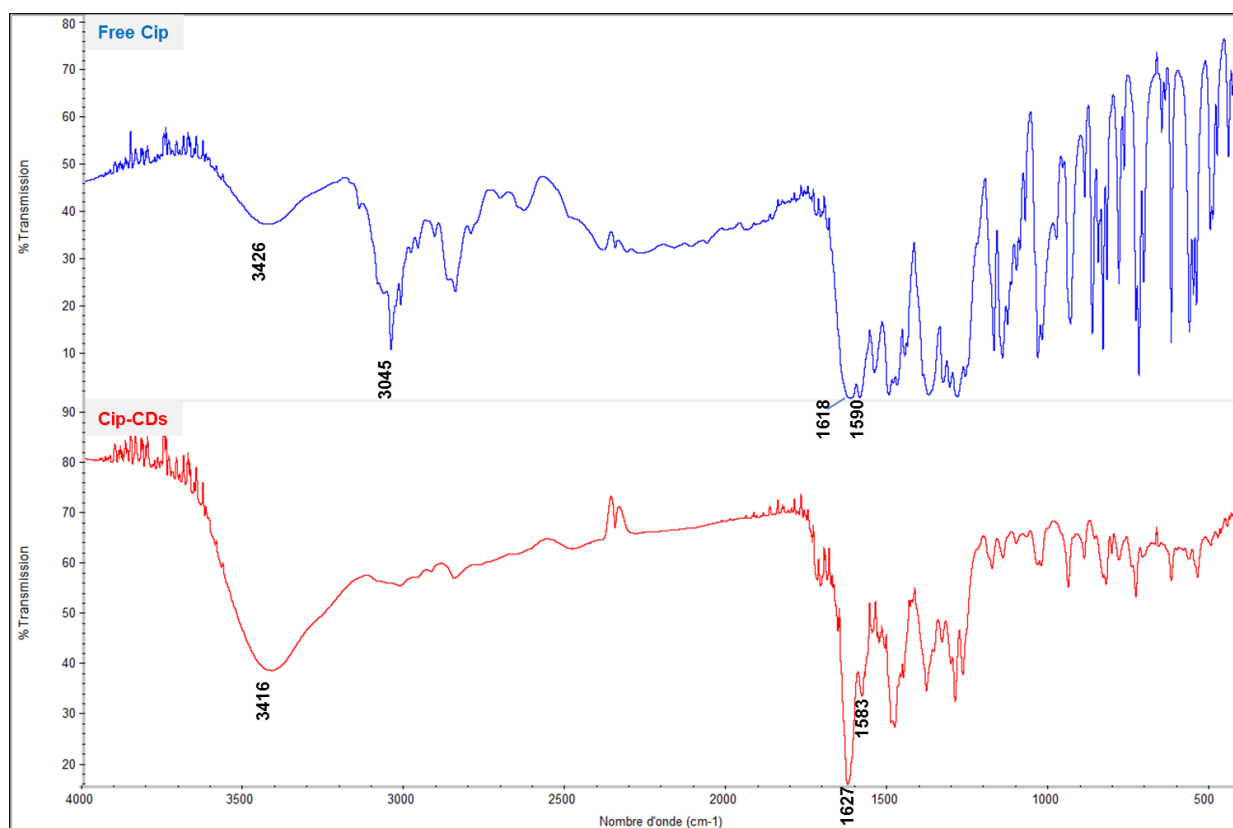


Figure 4.14. FT-IR spectra of Cip (blue spectrum) and Cip-CDs (red spectrum).

As for FA-CDs, the FT-IR spectrum of Cip-CDs is less rich than that of free Cip. Once again it evidences the signature of various hydrophilic groups (Figure 4.14) like the O-H and -NH- through their stretching vibration bands at around 3045 cm⁻¹ the CO carbonyl through its stretching vibration bands at 1627 cm⁻¹. It also evidences the signature of aromatic carbon-carbon double bonds at 1580-1590 cm⁻¹, which is one of the Cip characteristic bands. As previously, one may assume that the condensation reaction, which should occur between amino and carboxylic acid groups of Cip, during the hydrothermal treatment, contributes to the formation of carbon cores and their surface fictionalization with hydrophilic groups

without excluding Cip grafting without altering its structure. This is very important, because, the persistence of Cip on the surface of Cip-CDs is required to maintain any antibacterial activity.

To complete our characterizations, we measured the Zeta potential of our engineered nanohybrides, at different pH values, to check their colloidal stability in water. At pH 4 to begin, the zeta potential of the Cip-CDs is found to be close to 0 mV. This indicates that Cip-CDs surface are globally not charged (Figure 4.15) and that they form aggregates in the solution, breaking rapidly the colloidal stability, which is not recommended for the desired application. This study will be continued once containment is completed.

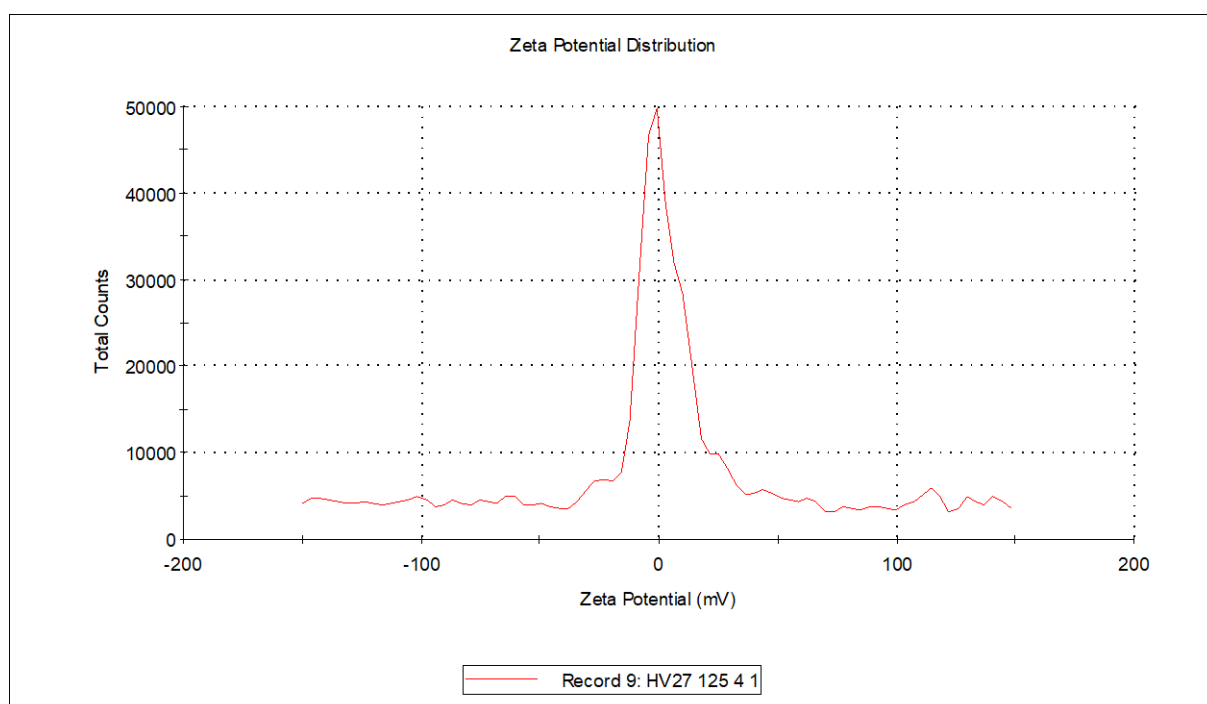


Figure 4.15. Aqueous Cip-CD suspension zeta potential distribution at pH 4.

4. Conclusions and Perspectives

We synthesized successfully and characterized Carbon dots from folic acid, in one hand, and from Ciprofloxacin, in the other hand, by a hydrothermal method and demonstrated their luminescent properties. These nanoparticles have been provided to Dr Åsa Gylfe (university of Umeå, Sweden) to evaluate their ability to interact with folic acid receptor and to inhibit *C. trachomatis* growth, respectively. Experiments are actually under progress.

We plan, in a second step, to covalently couple, or not, the FA-CDs with a drug active against *C. trachomatis* to evaluate their drug delivery ability.

The putative antibacterial activity of Cip-CDs will enable us to extend this strategy to other active molecules, like those described in this manuscript.

5. Experimental section

5.1. Chemicals

Folic acid, Ciprofloxacin, and Quinine sulfate dihydrate were obtained from commercial suppliers (from Sigma-Aldrich).

5.2. Apparatus and characterization

All the UV–visible absorption spectra were recorded at $25.0 \pm 0.5^\circ\text{C}$ on a Cary 4000 spectrophotometer in a transmission mode. All fluorescence spectra were performed on Fluorolog® HORIBA JOBIN YVON spectrofluorometer equipped with a quartz cell (1×1 cm). The DLS and the zeta potentials experiments were performed on Malvern Zetasizer Nano ZS (Red badge) ZEN3600 3000HSa (He-Ne laser, 633 nm). FTIR spectra were recorded on a PerkinElmer Spectrum 100 FT-IR spectrometer.

5.3. FA-CDs hydrothermal synthesis

The FA-CDs were synthesized by a typical hydrothermal method. Briefly, FA (0.15 g) was dissolved in 50 mL ultrapure water. Then the solution was sonicated for 30 min and transferred to a poly (tetrafluoroethylene)-lined autoclave (25 mL) and heated at 180°C for 6 hours. The yellow solution was then filtered through a $0.22 \mu\text{m}$ syringe filter. The resulting solution was dialyzed against water (MWCO = 100 - 500 kDa). The liophilization of the yellow solution provided FA-CDs as yellow powder which was stored at 4°C for further experiments.

5.4. Cip-CDs hydrothermal synthesis

Typically, 21 mg of ciprofloxacin hydrochloride was dissolved in 50 mL double deionized water, and then, the solution was transferred to a Teflon-lined stainless steel autoclave and heated at around 180°C for 4 h. The reactor was gradually cooled down to room temperature naturally after the reaction, and a yellow solution was obtained. The solution was dialysed for 48 h (molecular-weight cut-off of 500 Da) to remove excess ciprofloxacin, water was changed every two hours in the first twelve hours and then every eight hours for the remaining time. Finally, pure g-CDs were concentrated by freezing (-80°C) and drying under vacuum. Yield = 47% (10 mg, yellow solid).

5.5. Quantum yield (QY) measurement

The quantum yields of the produced carbon dots were computed by slope method, where the quinine sulfate (QS) solution (dissolved in 0.1 M sulfuric acid; quantum yield = 0.54) was used as a reference. The electronic absorption intensity of the FA-CDs, Cip-CDs and QS solutions for five different concentrations in 355, 315 and 346 nm wavelengths were determined using UV–visible Cary 4000 spectrophotometer. The corresponding photoluminescence spectra were recorded on the same solutions, around 450 nm, for the 355, 315 and 346 nm excitation wavelengths. The photoluminescence intensities were regressed on the absorbance for five solutions of each material. Thereby, we calculate grad values (Table 4.1). Finally, the follows equation was used to determine the quantum yield:

$$QY = QY_{ST} (\eta^2 / \eta_{ST}^2) (Grad / Grad_{ST})$$

Where QY is the quantum yield, ST indicates the standard, Grad is the gradient obtained from the plot of integrated fluorescence intensity versus absorbance (the slope), and η is the refractive index of the solvent. It was fixed to 1.33 for both water (for CDs) and 0.1 M sulfuric acid solution (for quinine sulfate). The absorption intensity never exceeded 0.1.

Table 4.1. Slope method for the calculation of fluorescence quantum yield of FA-CDs and Cip-CDs

	η	Grad	R ²
QS	1.33	3.41E10	0.98
FA-CDs	1.33	8.31E9	0.96
Cip-CDs	1.33	1.11E10	0.99

CHAP V:

GENERAL CONCLUSIONS

The work carried out during this study revolves around the search for new tools to try to fight a bacterial infection affecting more than 100 million people each year, *Chlamydia trachomatis* infection.

Several strategies have been proposed.

The first is based on the structural modification of Ciprofloxacin, an antibiotic available on the market but whose efficacy does not allow its use against this infection.

Taking into account the iron requirements of this bacterium to grow, we coupled the antibiotic with an 8-hydroxyquinoline heterocycle. The corresponding conjugate, compound **1**, has been shown to be not only more active than Ciprofloxacin but also just as potent as the two drugs used to treat this infection, Azythromycin and Doxycycline, *in vitro*.

We then used this molecule as a lead compound for the synthesis of new derivatives, obtained after modulation of physicochemical parameters such as lipophilicity. All new compounds proved to be more active than the parent antibiotic, one of them reaching nanomolar efficiency.

The mode of action of this new family of compounds has not been identified to date. We already know that compound **1** does not efficiently inhibit topoisomerases, the fluoroquinolones targets, a family of antibiotics to which Ciprofloxacin belongs to.

In addition, the metal chelating properties of the 8-hydroxyquinoline moiety led us to study, using UV-visible spectrophotometry and isothermal calorimetric titration, the ability of these new molecules to complex iron(III), an essential metal for the bacterial growth. Our results showed that, except for the conjugate **6**, an isomer of compound **1**, the metal is chelated by the fluoroquinolone entity and not by its 8-hydroxyquinoline heterocycle.

We then tried to understand this absence of chelation and suspected an influence of the positioning of the carbonyl present on the 8-hydroxyquinoline. For this, we synthesized simple model-molecules presenting a carbonyl, in the form of ester functions, in position 2 or 7 of the 8-hydroxyquinoline moiety and carried out a study mixing computational calculations (DFT computations) and experimental measurements (spectrophotometric and calorimetric

titrations). These results showed a significant difference in stability between the complexes resulting from the different ligands. Indeed, they demonstrated that according to the position of the withdrawing group on the heterocyclic skeleton, the steric hindrance can destabilize the iron(III)-complex by forcing it to adopt a distorted structure far from the ideal octahedral environment. In this respect, we found that the ester functionalization of HQ in 2-position weakens the iron (III)-complex while its functionalization in 7-position allows a salicylate coordination of the metal, very close to the ideal octahedral environment. The region-isomer **6** has a carbonyl function allowing this type of iron coordination. Its antibacterial activity is approximately 3 times greater. We still have to establish whether this activity is directly linked to its metal chelating properties.

The last tool proposed in this work is based on the use of nanomaterials, whose interest in therapy is well established. We were particularly interested in nanoparticles not yet described to fight *C. trachomatis* infection, the Carbon dots. These nano-objects possess multiple interests such as their easy synthesis and functionalization, their solubility in water, their biocompatibility by an absence of toxicity and their luminescent properties.

We used folic acid as starting material for these syntheses. Indeed, this essential vitamin is recognized by its receptor on the surface of many cells and is internalized by an endocytosis pathway. This specific recognition phenomenon explains why many publications are describing folic acid as a vector of drugs, anticancer in particular, because several physiopathological conditions, such as cancer or *C. trachomatis* infection, result in the overexpression of this receptor on the cell surface.

We therefore synthesized and characterized Carbon dots from folic acid in order to use them as tools allowing both to target the infected cells but also to verify the interaction of these nano-objects with folic acid receptor, through their luminescent properties. At the same time, we synthesized compound **7**, a folic acid-Ciprofloxacin conjugate. Indeed, we assumed an increase in the membrane permeability of the antibiotic by its internalization through folic acid receptor and therefore, a better reach of this intracellular bacterium. The corresponding conjugate **7** is more active than Ciprofloxacin, as expected.

We also synthesized Carbon dots from Ciprofloxacin to study their intrinsic antibacterial activity against *C. trachomatis*. Indeed, literature describes them active against *E. coli*, for instance. These studies are currently underway with our colleague, Dr. Åsa Gylfe, at the University of Umeå, Sweden.

Thus, this multidisciplinary study, at the interface of organic synthesis, physicochemistry, nanochemistry and biology, demonstrates the interest of the 8-hydroxyquinoline moiety in the fight against *C. trachomatis* infection and has made it possible to obtain new and potent molecules against this bacterium. However, many questions remain unanswered. They will be, at least partially, raised by the perspectives presented within each chapter.

REFERENCES

- Abdelrahman YM, and Belland RJ. The chlamydial developmental cycle. *FEMS Microbiol. Rev.* **2005**, 29(5), 949-959.
- Abdelsayed S, Ha Duong NT, Hai J, Hémadi M, El Hage Chahine JM, Verbeke P, and Serradji N. Design and synthesis of 3-isoxazolidone derivatives as new *Chlamydia trachomatis* inhibitors. *Bioorg Med Chem Lett.* **2014**, 24(16), 3854-3860.
- Abed N, and Couvreur P. Nanocarriers for antibiotics: A promising solution to treat intracellular bacterial infections. *Int J Antimicrob Agents.* **2014**, 43(6), 485-496.
- Adamo C, and Barone V. Toward reliable density functional methods without adjustable parameters: the PBE0 model. *J Chem Phys.* **1999**, 110(13), 6158-6170.
- Agbowuro AA, Hwang J, Peel E, Mazraani R, Springwald A, Marsh JW, McCaughey L, Gamble AB, Huston WM, and Tyndall JDA. Structure-activity analysis of peptidic *Chlamydia* HtrA inhibitors. *Bioorg Med Chem.* **2019**, 27(18), 4185-4199.
- Al-Busaf SN, Suliman FEO, and Al-Alawi ZR. 8-Hydroxyquinoline and its derivatives: synthesis and applications. *Res Rev J Chem.* **2014**, 3(1), 1-10.
- Al-Younes HM, Rudel T, Brinkmann V, Szczepek AJ, Meyer TF. Low iron availability modulates the course of *Chlamydia pneumoniae* infection. *Cell Microbiol.* **2001**, 3(6), 427-437.
- Arnott JA, and Planey SL. The influence of lipophilicity in drug discovery and design. *Expert Opin Drug Discov.* **2012**, 7(10). 863-875.
- Aubry A, Pan XS, Fisher LM, Jarlier V, and Cambau E. *Mycobacterium tuberculosis* DNA gyrase: interaction with quinolones and correlation with antimycobacterial drug activity. *Antimicrob Agents Chemother.* **2004**, 48(4),1281-1288.
- Azhdarzadeh M, Lotfipour F, Zakeri-Milani P, Mohammadi G, and Valizadeh H. Anti-bacterial performance of azithromycin nanoparticles as colloidal drug delivery system against different gram-negative and gram-positive bacteria. *Adv Pharm Bull.* **2012**, 2(1), 17-24.

- Bahers** TL, Adamo C, Ciofni I. Theoretical determination of the pKas of the 8-hydroxyquinoline-5-sulfonic acid: a DFT based approach. *Chem Phys Lett.* **2009**, 472(1), 30-34.
- Baibarac M, Smaranda I, Nila A, and Serbschi C. Optical properties of folic acid in phosphate bufer solutions: the influence of pH and UV irradiation on the UV-VIS absorption spectra and photoluminescence. *Sci Rep.* **2019**, 9:14278.
- Baker SN, and Baker GA. Luminescent carbon nanodots: emergent nanolights. *Angew Chem Int Ed.* **2010**, 49, 6726-6744.
- Balakrishnan A, Patel B, Sieber SA, Chen D, Pachikara N, Zhong G, Cravatt BF, and Fan H. Metalloprotease inhibitors GM6001 and TAPI-0 inhibit the obligate intracellular human pathogen *Chlamydia trachomatis* by targeting peptide deformylase of the bacterium. *J. Biol. Chem.*, **2006**, 281(24), 16691-16699.
- Balakrishnan A, Wang L, Li X, Ohman-Strickland P, Malatesta P, and Fan H. Inhibition of chlamydial infection in the genital tract of female mice by topical application of a peptide deformylase inhibitor. *Microbiol. Res.*, **2009**, 164(3), 338-346.
- Bao X, Gylfe A, Sturdevant GL, Gong Z, Xu S, Caldwell HD, Elofsson M, and Fan H. Benzylidene acylhydrazides inhibit chlamydial growth in a type III secretion- and iron chelation-independent manner. *J. Bacteriol.* **2014**, 196(16), 2989-3001.
- Bao X, Pachikara ND, Oey CB, Balakrishnan A, Westblade LF, Tan M, Chase T Jr, Nickels BE, Fan H. Non-coding nucleotides and amino acids near the active site regulate peptide deformylase expression and inhibitor susceptibility in *Chlamydia trachomatis*. *Microbiology*, **2011**, 157, 2569-2581.
- Bardez E, Devol I, Larrey B, and Valeur B. Excited-state processes in 8-Hydroxyquinoline: photoinduced tautomerization and solvation effects. *J Phys Chem.* **1997**, 101, 7786-7793.
- Bates RG. Determination of pH - Theory and Practice. *Wiley - Interscience, New York.* **1973**.
- Bednar MM, Jorgensen I, Valdivia RH, McCafferty DG. *Chlamydia* protease-like activity factor (CPAF): characterization of proteolysis activity in vitro and development of a nanomolar affinity CPAF zymogen-derived inhibitor. *Biochemistry*, **2011**, 50, 7441-7443.

- Benchaala I, Mishra MK, Wykes SM, Hali M, Kannan RM, and Whittum-Hufson J. Folate-functionalized dendrimers for targeting Chlamydia-infected tissues in a mouse model of reactive arthritis. *Int J Pharm.* **2014**, 466(1-2), 258-265.
- Bhunia SK, Maity AR, Nandi S, Stepensky D, and Jelinek R. Imaging Cancer Cells Expressing the Folate Receptor with Carbon Dots Produced from Folic Acid. *ChemBioChem.* **2016**, 17(7), 614-619.
- Binstead RA, Zuberbuhler AD, Jung B. SPECFIT global analysis system version 3.04.34. **2003**.
- Bommana S, and Polkinghorne A. Chlamydial infections in animals: current practices and issues. *Front Microbiol.* **2019**, 10, article 113.
- Bongers S, Hellebrekers P, Leenen LPH, Koenderman L, and Hietbrink F. Intracellular penetration and effects of antibiotics on Staphylococcus aureus inside human neutrophils: A comprehensive review. *Antibiotics (Basel).* **2019**, 8(2), 54.
- Boukhalfa H, and Crumbliss AL. Chemical aspects of siderophore mediated iron transport. *Biometals.* **2002**, 15(4), 325-339.
- Brémond E, Alberto ME, Russo N, Ricci G, Ciofni I, Adamo C. Photophysical properties of NIR-emitting fluorescence probes: insights from TD-DFT. *Phys Chem Chem Phys.* **2013**, 15(25), 10019-10027.
- Brémond E, Bahers TL, Ricci G, Ciofni I, Adamo C. In silico assessment of the HPLC-UV response coefficients, *Comput. Theor Chem.* **2014**, 1040-1041, 1-5.
- Brémond E, Ciofni I, Sancho-García JC, Adamo C. Nonempirical double-hybrid functionals: an effective tool for chemists. *Acc Chem Res.* **2016**, 49(8), 1503-1513.
- Brémond E, Kieffer J, Adamo C. A reliable method for fitting TD-DFT transitions to experimental UV-visible spectra. *J Mol Struct.* 2010, 954(1-3), 52-56. <https://doi.org/10.1016/j.theochem.2010.04.038>.
- Brémond É, Pérez-Jiménez ÀJ, Sancho-García JC, Adamo C. Range-separated hybrid density functionals made simple. *J Chem Phys.* **2019**, 150(20), 201102.
- Brémond E, Savarese M, Pérez-Jiménez AJ, Sancho-García JC, Adamo C. Range-separated double-hybrid functional from nonempirical constraints. *J Chem Theory Comput.* **2018**, 14(8), 4052-4062.

- Brémond E, Savarese M, Pérez-Jiménez AJ, Sancho-García JC, Adamo C. Systematic improvement of density functionals through parameter-free hybridization schemes. *J Phys Chem Lett.* **2015**, 6(18), 3540-3545.
- Buckner L R, Amedee A M, albritton H L, Kozlowski P A, Lacour N, McGowin C L, Schust D J, and Quayle A J. Chlamydia trachomatis infection of endocervical epithelial cells enhances early HIV transmission events. *PloS One.* **2016**, 11(1), 0146663-0146682.
- Burger K. Organic reagents in metal analysis. *Elsevier.* **1973**, p 22.
- Caini S, Gandini S, Dudas M, Bremer V, Severi E, Gherasim A. Sexually transmitted infections and prostate cancer risk: a systematic review and meta-analysis. *Cancer Epidemiol.* **2014**, 38(4), 329-338.
- Caldwell HD, Kromhout J, Schachter J. Purification and partial characterization of the major outer membrane protein of *Chlamydia trachomatis*. *Infect Immun.* **1981**, 31, 1161-1176.
- Campoli-Richards DM, Monk JP, Price A, Benfield P, Todd PA, and Ward A. Ciprofloxacin. A review of its antibacterial activity, pharmacokinetic properties and therapeutic use. *Drugs.* **1988**, 35(4), 373-447.
- Caris C, Baret P, Pierre JL, Serratrice G. Synthesis and NMR study of two lipophilic iron(III) sequestering agents based on 8-hydroxyquinoline; H-bonding and conformational changes. *Tetrahedron.* **1996**, 52(13), 4659-4672.
- Casida ME. Time-dependent density-functional response theory for molecules. *in: D.P. Chong (Ed.), Recent Advances in Density Functional Methods, World Scientific, Singapore, 1995*, 1, 155–192.
- Ceci A, Baiardi P, Felisi M, Cappellini MD, Carnelli V, De Sanctis V, Galanello R, Maggio A, Masera G, Piga A et al. The safety and effectiveness of deferiprone in a large-scale, 3-year study in Italian patients. *Br J Haematol.* **2002**, 118, 330–336.
- Cézard C, Farvacques N, Sonnet P. Chemistry and biology of pyoverdines, *Pseudomonas* primary siderophores. *Curr Med Chem.* **2015**; 22(2), 165-186.
- Chan GC, Chan S, Ho PL, Ha SY. 2009. Effects of chelators (deferoxamine, deferiprone and deferasirox) on the growth of *Klebsiella pneumoniae* and *Aeromonas hydrophila* isolated from transfusion-dependent thalassemia patients. *Hemoglobin*, **2009**, 33, 352-360.

- Chang JH, Lee IS, Kim HK, Cho YK, Park JM, Kim SW, Choi MG, Chung IS. Nafamostat for Prophylaxis against Post-Endoscopic Retrograde Cholangiopancreatography Pancreatitis Compared with Gabexate. *Gut Liver*. **2009**, 3(3), 205-210.
- Chen C, Ke J, Zhou XE, Yi W, Brunzelle JS, Li J, Yong EL, Xu HE, and Melcher K. Structural basis for molecular recognition of folic acid by folate receptor. *Nature*. **2013**, 500(7463), 486-489.
- Chen CH, and Shi J. Metal chelates as emitting materials for organic electroluminescence. *Coord Chem Rev*. **1998**, 171, 161-174.
- Cherdtrakulkiat R, Boonpangrak S, Sinthupoom N, Prachayasittikul S, Ruchirawat S, Prachayasittikul V. Derivatives (halogen, nitro and amino) of 8-hydroxyquinoline with highly potent antimicrobial and antioxidant activities. *Biochem Biophys Reports*. **2016**, 6, 135-141.
- Cherny RA, Atwood CS, Xilinas ME, et al. Treatment with a copper-zinc chelator markedly and rapidly inhibits β -amyloid accumulation in Alzheimer's disease transgenic mice. *Neuron*. **2001**, 30, 665–676.
- Christian JG, Heymann J, Paschen SA, Vier J, Schauenburg L, Rupp J, Meyer TF, Häcker G, Heuer D. Targeting of a chlamydial protease impedes intracellular bacterial growth. *PLoS Pathog*. **2011**, 7(9), e1002283.
- Chu H, Slepkin A, Elofsson M, Keyser P, de la Maza LM, Peterson EM. Candidate vaginal microbicides with activity against *Chlamydia trachomatis* and *Neisseria gonorrhoeae*. *Int J Antimicrob Agents*. **2010**, 36(2), 145-150.
- Cocchiari JL, Kumar Y, Fischer ER, Hackstadt T, and Valdivia RH. Cytoplasmic lipid droplets are translocated into the lumen of the *Chlamydia trachomatis* parasitophorous vacuole. *Proc Natl Acad Sci USA*. **2008**, 105(27), 9379-9384.
- Cohen AJ, Handy NC. Assessment of exchange correlation functionals. *Chem Phys Lett*. **2000**, 316(1-2), 160–166.
- Cohen AJ, Mori-Sánchez P, Yang W. Insights into current limitations of density functional theory. *Science*. **2008**, 321(5890), 792-794.
- Corcé V, Renaud S, Cannie I, Julienne K, Gouin S G, Loréal O, Gaboriau F, Deniaud D. Synthesis and biological properties of quilamines II, new iron chelators with antiproliferative activities. *Bioconjug Chem*. **2014**, 25(2), 320-334.

- Cram ED, Rockey DD, Dolan BP. *Chlamydia spp.* development is differentially altered by treatment with the LpxC inhibitor LPC-011. *BMC Microbiol.* **2017**, 17, 98.
- Crichton RR. Inorganic Biochemistry of Iron Metabolism. *John Wiley & Sons Chichester.* **2001**.
- Crisponi G, Remelli M. Iron chelating agents for treatment of iron overload. *Coord Chem Rev.* **2008**, 252, 1225-1240.
- Cui HJ, He HY, Yang AL, Zhou HJ, Wang C, Luo JK, Lin Y, Tang T. Efficacy of deferoxamine in animal models of intracerebral hemorrhage: a systematic review and stratified meta-analysis. *PloS one.* **2015**, 10(5), e0127256.
- D**ai W, and Li Z. Conserved type III secretion system exerts important roles in *Chlamydia trachomatis*. *Int J Clin Exp Pathol.* **2014**, 7(9), 5404-5414.
- Davis CH, Raulston JE, and Wyrick PB. Protein Disulfide Isomerase, a component of the estrogen receptor complex, is associated with *Chlamydia trachomatis* serovar E attached to human endometrial epithelial cells. *Infect Immun.* **2002**, 70(7), 3413-3418.
- Dean D, Suchland R, and Stamm W. Evidence for long-term cervical persistence of *Chlamydia trachomatis* by omp1 genotyping. *J Infect Dis.* **2000**, 182, 909-916.
- Dhungana S, Harrington JM, Gebhardt P, Mollmann U, Crumbliss AL. Iron chelation equilibria, redox, and siderophore activity of a saccharide platform ferrichrome analogue. *Inorg Chem.* **2007**, 46, 8362-8371.
- Dibrov P, Dibrov E, Maddaford TG, Kenneth M, Nelson J, Resch C, Pierce GN. Development of a novel rationally designed antibiotic to inhibit a nontraditional bacterial target. *Can J Physiol Pharmacol.* **2017**, 95, 595-603.
- Dreses-Werringloer U, Padubrin I, Jurgens-Saathoff B, Hudson AP, Zeidler H, and Kohler L. Persistence of *Chlamydia trachomatis* is induced by ciprofloxacin and ofloxacin in vitro. *Antimicrob Agents Chemother.* **2000**, 44(12), 3288-3297.
- Dreuw A, Head-Gordon M. Failure of time-dependent density functional theory for long-range charge-transfer excited states: the Zincbacteriochlorin-Bacteriochlorin and Bacteriochlorophyll-Spheroidene complexes. *J Am Chem Soc.* **2004**, 126(12), 4007-4016.
- Du Moulinet d'Hardemare A, Serratrice G, Pierre JL. Synthesis and iron-binding properties of quinolobactin, a siderophore from a pyoverdine-deficient *Pseudomonas fluorescens*. *Biometals.* **2004**, 17, 691-697.

- Du Moulinet d'Hardemare A, Torelli S, Serratrice G, Pierre JL. Design of iron chelators: syntheses and iron (III) complexing abilities of tripodal tris-bidentate ligands. *Biometals*. **2006**, 19, 349-366.
- Dumoux M, Le Gall SM, Habbedine M, Delarbre C, Hayward RD, Kanellopoulos-Langevin C, and Verbeke P. Penicillin kills *Chlamydia* following the fusion of bacteria with lysosomes and prevents genital inflammatory lesions in *C. muridarum*-infected mice. *PLoS One*. **2013**, 8, e83511.
- Dumoux M, Nans A, Saibil H R, Hayward R D. Making connections: snapshots of chlamydial type III secretion systems in contact with host membranes. *Cur Opin Microbiol*, **2015**, 23, 1-7.
- E**igen M, DeMaeyer L. Relaxation methods, in: S.L. Friess, E.S. Lewis, A. Weissberger (Eds.), *Techniques of organic chemistry - Investigation of Rates and Mechanism of Reactions*, part II, vol. 8 Wiley Intersciences, New York, 1963, 895-1029.
- Engström P, Krishnan KS, Ngyuen BD, Chorell E, Normark J, Silver J, Bastidas RJ, Welch MD, Hultgren SJ, Wolf-Watz H, Valdivia RH, Almqvist F, Bergström S. A 2-pyridone-amide inhibitor targets the glucose metabolism pathway of *Chlamydia trachomatis*. *MBio*, **2014**, 6(1), e02304-e02314.
- Enquist PA, Gylfe A, Hägglund U, Lindström P, Norberg-Scherman H, Sundin C, and Elofsson M. Derivatives of 8-hydroxyquinoline-antibacterial agents that target intra- and extracellular Gram-negative pathogens. *Bioorg Med Chem Lett*. **2012**, 22(10), 3550-3553.
- Ernzerhof M, Scuseria GE. Assessment of the Perdew-Burke-Ernzerhof exchange-correlation functional. *J Chem Phys*. **1999**, 110(11), 5029-5036.
- Evans JR, Solomon AW, Kumar R, Perez Á, Singh BP, Srivastava RM, and Harding-Esch E. Antibiotics for trachoma. *Cochran Database Syst Rev*. **2019**, 9, CD001860.
- F**ardeau S, Dassonville-Klimpt A, Audic N, Sasaki A, Pillon M, Baudrin E, Mullié C, and Sonnet P. Synthesis and antibacterial activity of catecholate-ciprofloxacin conjugates. *Bioorg Med Chem*. **2014**, 22, 4049-4060.
- Farshbaf M, Davaran S, Rahimi F, Annabi N, Salehi R, and Akbarzadeh A. Carbon quantum dots: recent progresses on synthesis, surface modification and applications. *Artif Cells Nanomed Biotechnol*. **2018**, 46(7), 1331-1348.

- Forslund O, Hjelm M, El-Ali R, Johnsson A, and Bjartling C. Mycoplasma genitalium and macrolide resistance-associated mutations in the skåne region of southern Sweden 2015. *Acta Derm Venereol.* **2017**, 97(10), 1235-1238.
- Francl MM, Pietro WJ, Hehre WJ, Binkley JS, Gordon MS, DeFrees DJ, Pople JA. Self-consistent molecular orbital methods. XXIII. A polarization-type basis set for second-row elements. *J Chem Phys.* **1982**, 77(7), 3654-3665.
- Frisch MJ, Trucks GW, Schlegel HB, Scuseria GE, Robb MA, Cheeseman JR, Scalmani G, Barone V, Petersson GA, Nakatsuji H, Li X, Caricato M, Marenich AV, Bloino J, Janesko BG, Gomperts R, Mennucci B, Hratchian HP, Ortiz JV, Izmaylov AF, Sonnenberg JL, Williams-Young D, Ding F, Lipparini F, Egidi F, Goings J, Peng B, Petrone A, Henderson T, Ranasinghe D, Zakrzewski VG, Gao J, Rega N, Zheng G, Liang W, Hada M, Ehara M, Toyota K, Fukuda R, Hasegawa J, Ishida M, Nakajima T, Honda Y, Kitao O, Nakai H, Vreven T, Throssell K, Montgomery Jr JA, Peralta JE, Ogliaro F, Bearpark MJ, Heyd JJ, Brothers EN, Kudin KN, Staroverov VN, Keith TA, Kobayashi R, Normand J, Raghavachari K, Rendell AP, Burant JC, Iyengar SS, Tomasi J, Cossi M, Millam JM, Klene M, Adamo C, Cammi R, Ochterski JW, Martin RL, Morokuma K, Farkas O, Foresman JB, Fox DJ. Gaussian 16 Revision B.01, **2016**.
- G**allegos KM, Taylor CR, Rabulinski DJ, Del Toro R, Girgis DE, Jourha D, Tiwari V, Desai UR, and Ramsey KH. A synthetic, small, sulfated agent is a promising inhibitor of *Chlamydia spp.* Infection *in vivo*. *Front Microbiol.* **2019**, 9, 3269.
- Gerard C, Chehhal H, Hugel RP. Complexes of iron(III) with ligands of biological interest: dopamine and 8-hydroxyquinoline-5-sulfonic acid. *Polyhedron.* **1994**, 13(4), 591-597.
- Ghosh B, Antonio T, Reith MEA, and Dutta AK. Discovery of 4-(4-(2-((5-hydroxy-1,2,3,4-tetrahydronaphthalen-2-yl)(propyl)amino)ethyl)piperazin-1-yl)quinolin-8-ol and its analogues as highly potent dopamine D2/D3 agonists and as iron chelator: In vivo activity indicates potential application in symptomatic and neuroprotective therapy for Parkinson's disease. *J Med Chem.* **2010**, 53, 2114-2125.

- Glasauer SM, Beveridge TJ, Burford EP, Harper FA, and Gadd GM. Metals and Metalloids, transformation by microorganisms. *Reference Module in Earth Systems and Environmental Sciences*. **2013**.
- GLoeck S, Ong VA, Patel P, Tyndall JD, Timms P, Beagley KW, Allan JA, Armitage CW, Turnbull L, Whitchurch CB, Merdanovic M, Ehrmann M, Powers JC, Oleksyszyn J, Verdoes M, Bogyo M, and Huston WM. Identification of a serine protease inhibitor which causes inclusion vacuole reduction and is lethal to *Chlamydia trachomatis*. *Mol Microbiol*. **2013**, 89(4), 676-689.
- Goerigk L, Grimme S. Efficient and accurate double-hybrid-meta-GGA density functionals evaluation with the extended GMTKN30 database for general main group thermochemistry, kinetics, and noncovalent interactions. *J Chem Theory Comput*. **2011**, 7(2), 291-309.
- Goerigk L, Hansen A, Bauer C, Ehrlich S, Najibi A, Grimme S. A look at the density functional theory zoo with the advanced GMTKN55 database for general main group thermochemistry, kinetics and noncovalent interactions. *Phys Chem Chem Phys*. **2017**, 19(48), 32184-32215.
- Gomes LM, Vieira RP, Jones MR, Wang MC, Dyrager C, Souza-Fagundes EM, Da Silva JG, Storr T, and Beraldo H. 8-hydroxyquinoline Schiff-base compounds as antioxidants and modulators of copper-mediated A β peptide aggregation. *J Inorg Biochem*. **2014**, 139, 106-116.
- Good JA, Silver J, Nunez-Otero C, Bahnan W, Krishnan KS, Salin O, Engstrom P, Svensson R, Artursson P, Gylfe Å, Bergstrom S, Almqvist F. Thiazolino 2-pyridone amide inhibitors of *Chlamydia trachomatis* infectivity. *J Med Chem*. **2016**, 59, 2094-2108.
- Good JAD, Kulén M, Silver J, Krishnan KS, Bahnan W, Núñez-Otero C, Nilsson I, Wede E, de Groot E, Gylfe Å, Bergström S, and Almqvist F. Thiazolino 2-Pyridone Amide Isosteres As Inhibitors of *Chlamydia trachomatis* Infectivity. *J Med Chem*. **2017**, 60(22), 9393-9399.
- Gordon FB, and Quan AL. Isolation of the trachoma agent in cell culture. *Proc Soc Exp Biol Med*. **1965**, 118, 354-359.
- Gordon FB, and Quan AL. Susceptibility of *Chlamydia* to antibacterial drugs: test in cell culture. *Antimicrob Agents Chemother*. **1972**, 2(3), 242-244.

- Grieshaber S, Swanson JA, and Hackstadt T. Determination of the physical environment within the *Chlamydia trachomatis* inclusion using ion-selective ratiometric probes. *Cell Microbiol.* **2002**, 4(5), 273-283.
- Grishin AV, Luyksaar SI, Kapotina LN, Kirsanov DD, Zayakin ES, Karyagina AS, Zigangirova NA. Identification of chlamydial T3SS inhibitors through virtual screening against T3SS ATPase. *Chem Biol Drug Des.* **2018**, 91(3), 717-727.
- Guariglia R, Martorelli MC, Villani O, Pietrantuono G, Mansueto G, D'Auria F, Grieco V, Bianchino G, Lerose R, Bochicchio GB, et al. Positive effects on hematopoiesis in patients with myelodysplastic syndrome receiving deferasirox as oral iron chelation therapy: A brief review. *Leuk Res.* **2011**, 35, 566–570.
- Guo J, Schlich M, Cryan JF, O'Driscoll CM. Targeted drug delivery via folate receptors for the treatment of brain cancer: Can the promise deliver? *J Pharm Sci.* **2017**, 106(12), 3413-3420.
- Guy Serratrice, Hakim Boukhalfa, Claude Béguin, Paul Baret, Catherine Caris, Jean-Louis Pierre. O-TRENDOX, a new tripodal iron chelator based on 8-hydroxyquinoline subunits: Thermodynamic and kinetic studies. *Inorg Chem.* **1997**, 36, 3898-3919.
- Gyparaki M, Porter JB, Hirani S, Streater M, Hider RC, Huehns ER. In vivo evaluation of hydroxypyridone iron chelators in a mouse model. *Acta Haematol* **1987**, 78, 217-21.
- H**alberstaedter L and von Prowazek S. Zur atologie des trachoms. *Dtsch Med Wochenschr.* **1907**, 33, 1285-1287.
- Hansch C, Leo A, and Hoekman D. Exploring QSAR – hydrophobic, electronic, and steric constants. *Washington, DC: American Chemocal Society.* **1995**, p51.
- Hanski L, Genina N, Uvell H, Malinovskaja K, Gylfe Å, Laaksonen T, Kolakovic R, Mäkilä E, Salonen J, Hirvonen J, Elofsson M, Sandler N, Vuorela PM. Inhibitory activity of the isoflavone biochanin A on intracellular bacteria of genus *Chlamydia* and initial development of a buccal formulation. *PloS One.* **2014**, 9(12), e115115.
- Havrdova M, Hola K, Skopalik J, Tomankova K, Petr M, Cepe K, Polakova K, Tucek J, Bourlinos AB, and Zboril R. Toxicity of carbon dots – Effect of surface functionalization on the cell viability, reactive oxygen species generation and cell cycle. *Carbon.* **2016**, 99, 238-248.

- Hay PJ, Wadt WR. Ab initio effective core potentials for molecular calculations. Potentials for the transition metal atoms Sc to Hg. *J Chem Phys.* 1985, 82(1), 270-283.
- He W, Yang C, Zhao X, Wang Y. Antimicrobial activity of bitespiramycin, a new genetically engineered macrolide. *Bioorg Med Chem Lett.* **2017**, 27(19), 4576-4577.
- Hehre WJ, Ditchfeld R, Pople JA. Self-consistent molecular orbital methods. XII. Further extensions of Gaussian-type basis sets for use in molecular orbital studies of organic molecules. *J Chem Phys.* **1972**, 56(5), 2257-2261.
- Hershko C, Konijn AM, Nick Blood HP, 97: 1115-22, 2001. ICL670A: a new synthetic oral chelator: evaluation in hypertransfused rats with selective radioiron probes of hepatocellular and reticuloendothelial iron stores and in iron-loaded rat heart cells in culture Hider RC, Ma Y, Molina-Holgado F, Gaeta A, Roy S. Iron chelation as a potential therapy for neurodegenerative disease. *Biochem Soc Trans.* **2008**, 36, 1304-1308.
- Hider RC, and Kong X. Chemistry and biology of siderophores. *Nat Prod Rep.* **2010**, 27(5), 637-657.
- Hider RC, and Kong X. Iron: effect of overload and deficiency. *Met Ions Life Sci.* **2013**, 13, 229-294.
- Hider RC, Kontoghiorghes G, Silver J. Pharmaceutical compositions: UK Patent GB2118176, **1983** (Priority date 1982).
- Hogan RJ, Mathews SA, Mukhopadhyay S, Summersgill JT, and Timms P. Chlamydial persistence: beyond the biphasic paradigm. *Infect Immun.* **2004**, 72, 1843-1855.
- Hohenberg P, Kohn W. Inhomogeneous electron gas. *Phys Rev.* **1964**, 136(3B), B864-B871.
- Horner PJ. Azithromycin antimicrobial resistance and genital Chlamydia trachomatis infection: duration of therapy may be the key to improving efficacy. *Sex Transm Infect.* **2012**, 88, 154-156.
- Hou P, Yang T, Liu H, Li YF, and Huang CZ. An active structure preservation method for developing functional graphitic carbon dots as an effective antibacterial agent and a sensitive pH and Al(III) nanosensor. *Nanoscale.* **2017**, 9(44), 17334-17341.
- Ibana JA, Belland RJ, Zea AH, Schust DJ, Nagamatsu T, AbdelRahman YM, Tate DJ, Beatty WL, Aiyar AA, Quayle AJ. Inhibition of indoleamine 2,3-dioxygenase activity by levo-1-methyl tryptophan blocks gamma interferon-induced *Chlamydia trachomatis* persistence in human epithelial cells. *Infect Immun.* **2011**, 79(11), 4425-4437.

- Imbert D, Baret P, Gaude D, Gautier-Luneau I, Gellon G, Thomas FS, Pierre JL. Hydrophilic and lipophilic iron chelators with the same complexing abilities. *Chem Eur J.* **2002**, 8(5), 1091-1100.
- Inman RD, Chiu B. Nafamostat mesylate, a serine protease inhibitor, demonstrates novel antimicrobial properties and effectiveness in Chlamydia-induced arthritis. *Arthritis Res Ther.* **2012**, 14(3), R150.
- Irschik H, Jansen R, Hofle G, Gerth K and Reichenbach H. The coralopyronins, new inhibitors of bacterial RNA synthesis from Myxobacteria. *J. Antibiot.* **1985**, 38, 145-152.
- J**ack DB. Recent advances in pharmaceutical chemistry. The 4-quinolone antibiotics. *J Clin Hosp Pharm.* **1986**, 11(2), 75-93.
- Jacquemin D, Perpète EA, Ciofni I, and Adamo C. Accurate simulation of optical properties in dyes. *Acc Chem Res.* **2009**, 42(2), 326-334.
- Jacquemin D, Wathelet V, Perpète EA, and Adamo C. Extensive TD-DFT benchmark: singlet-excited states of organic molecules. *J Chem Theory Comput.* **2009**, 5(9), 2420-2435.
- Jianbo H, Tingting Z, Yongjing C, Yuanyuan Z, Weiqing Y, Menglin M. Study on relationship between fluorescence properties and structure of substituted 8-hydroxyquinolin zinc complexes. *J Fluoresc.* **2018**, 28(5), 1121-1126.
- Jisha B, Resmi MR, Maya RJ, and Varma RL. Colorimetric detection of Al(III) ions based on triethylene glycol appended 8-propyloxy quinoline ester. *Tetra Lett.* **2013**, 54, 4232-4236.
- Johnston WD, and Freiser H. Structure and behavior of organic analytical reagents. III. Stability of chelates of 8-hydroxyquinoline and analogous reagents. *J Am Chem Soc.* **1952**, 72(21), 5239-5242.
- K**anizsai I, Madácsi R, Hackler LJ, Gyuris M, Szebeni GJ, Huzián O, and Puskás LG. Synthesis and cytoprotective characterization of 8-hydroxyquinoline betti products. *Molecules.* **2018**, 23, 1934-1958.
- Karpishin TB, Gebhard MS, Solomon EI, Raymond KN. Spectroscopic studies of the electronic structure of iron(III) tris(catecholates). *J Am Chem Soc.* **1991**, 113, 2977-2984.

- Kaur D, Yantiri F, Rajagopalan S, Kumar J, Mo JQ, Boonplueang R, Viswanath V, Jacobs R, Yang L, Beal MF, DiMonte D, Volitaskis I, Ellerby L, Cherny RA, Bush AI, Andersen JK. Genetic or pharmacological iron chelation prevents MPTP-induced neurotoxicity *in vivo*: a novel therapy for Parkinson's disease. *Neuron*. **2003**, 37, 899-909.
- Khan A, Singh P, Srivastava A. Synthesis, nature and utility of universal iron chelator - Siderophore: A review. *Microbiol Res*. **2018**, 212-213, 103-111.
- Khaorapong N, Kuroda K, and Ogawa M. Intercalation of 8-hydroxyquinoline into Al-smectites by solide-solid reactions. *Clays and Clay Minerals*. **2002**, 50(4), 428 – 434.
- Kim CM, Shin SH. Effect of iron-chelator deferiprone on the in vitro growth of staphylococci. *J Korean Med Sci*. **2009**, 24, 289–295.
- Knez D, Sobic I, Pisljar A, Mitrovic A, Jukic M, Kos J, and Gobec S. Biological evaluation of 8-hydroxyquinolines as multi-target directed ligands for treating Alzheimer's disease. *Curr Alzheimer Res*. **2019**, 16(9), 801-814.
- Kock F, Hauptmann M, Osterloh A, Shaberle TF, Poppert S, Frickmann H, Menzel KD, Peschel G, Pfarr K, Schiefer A, Konig GM, Hoerauf A, Fleischer B, and Keller C. *Orientia tsutsugamushi* is highly susceptible to the RNA polymerase switch region inhibitor corallopyronin a in vitro and in vivo. *Antimicrob Agents Chemother*. **2018**, 62, 1732-1749.
- Kohlhoff SA, and Hammerschlag MR. Treatment of Chlamydial infections: 2014 update. *Expert Opin Pharmacother*, **2015**, 16(2), 205-212.
- Kohlhoff SA, Huband MD, and Hammerschlag MR. *In vitro* activity of AZD0914, a novel DNA gyrase inhibitor, against *Chlamydia trachomatis* and *Chlamydia pneumoniae*. *Antimicrob Agents Chemother*. **2014**, 58(12), 7595-7596.
- Kohn W, Sham LJ. Self-consistent equations including exchange and correlation effects. *Phys Rev*. 1965, 140(4A), A1133–A1138.
- Kong H, Cheng W, Wei H, Yuan Y, Yang Z, and Zhang X. An overview of recent progress in siderophore-antibiotic conjugates. *Eur J Med Chem*. **2019**, 15, 182, 111615.
- Koppenol WH. The Haber-Weiss cycle-70 years later. *Redox Rep*. **2001**, 6(4), 229-234.
- Koroleva EA, Kobets NV, Zayakin ES, Luyksaar SI, Shabalina LA, and Zigangirova NA. Small molecule inhibitor of type three secretion suppresses acute and chronic

- Chlamydia trachomatis* infection in a novel urogenital Chlamydia model. *Biomed Res Int.* **2015**, 2015, 484853.
- Kos J, Zadrazilova I, Nevin E, Soral M, Gonec T, Kollar P, Oravec M, Coffey A, O'Mahony J, Laiptai T, Kralova K, and Jampilek J. Ring-substituted 8-hydroxyquinoline-2-carboxanilides as potential antimycobacterial agents. *Bioorg Med Chem.* **2015**, 23(15), 4188-4196.
- Krysmann MJ, Kelarakis A, Dallas P, Giannelis EP. Formation mechanism of carbogenic nanoparticles with dual photoluminescence emission. *J Am Chem Soc.* **2012**, 134(2), 747-750.
- Kuo CC, Takahashi N, Swanson AF, Ozeki Y, and Hakomori SI. An N-linked high-mannose type oligosaccharide, expressed at the major outer membrane protein of *Chlamydia trachomatis*, mediates attachment and infectivity of the microorganism to HeLa cells. *J Clin Invest.* **1996**, 98, 2813–2818.
- Le Bahers T, Adamo C, and Ciofni I. A qualitative index of spatial extent in charge transfer excitations. *J Chem Theory Comput.* **2011**, 7(8), 2498-2506.
- Le Bahers T, Brémond E, Ciofni I, and Adamo C. The nature of vertical excited states of dyes containing metals for DSSC applications: insights from TD-DFT and density based indexes. *Phys Chem Chem Phys.* **2014**, 16(28), 14435-14444.
- Lebel M and Pharm D. Ciprofloxacin: Chemistry, mechanism of action, resistance, antimicrobial spectrum, pharmacokinetics, clinical trials, and adverse reactions. *Pharmacotherapy.* **1988**, 8(1), 3-33.
- Lei L, Li Z, and Zhong G. Rottlerin-mediated inhibition of *Chlamydia trachomatis* growth and uptake of sphingolipids is independent of p38-regulated/activated protein kinase (PRAK). *PloS One*, **2012**, 7(9), e44733.
- Lescoat G, Léonce S, Pierré A, Goufer L, and Gaboriau F. Antiproliferative and iron chelating efficiency of the new bis-8-hydroxyquinoline benzylamine chelator S1 in hepatocyte cultures. *Chem Biol Int.* 2012, 195, 165-172.
- Li G, Magana D, and Dyer RB. Photoinduced Electron Transfer in Folic Acid Investigated by Ultrafast Infrared Spectroscopy, *J Phys Chem B.* **2012**, 116(10), 3467-3475.
- Li L, and Xu B. Synthesis and characterization of 5-substituted 8-hydroxyquinoline derivatives and their metal complexes. *Tetrahedron.* **2008**, 64, 10986-10995.

- Liang S, Bulir D, Kaushic C, Mahony J. Considerations for the rational design of a Chlamydia vaccine. *Hum Vaccin Immunother.* **2017**, 13(4), 831-835.
- Lin LC, Chattopadhyay S, Lin JC, and Hu CJ. Advances and Opportunities in Nanoparticle- and Nanomaterial-Based Vaccines against Bacterial Infections. *Adv Healthc Mater.* **2018**, 7(13), e1701395.
- Liu G, Men P, Harris PL, Rolston RK, Perry G, Smith MA. Nanoparticle iron chelators: a new therapeutic approach in Alzheimer disease and other neurologic disorders associated with trace metal imbalance. *Neurosci Lett.* **2006**, 406(3), 189-193.
- Liu ZD, and Hider RC. Design of iron chelators with therapeutic application. *Coord Chem Rev.* **2002**, 232, 151-171.
- Loeper N, Graspeuntner S, Ledig S, Kaufhold I, Hoellen F, Schiefer A, Henrichfreise B, Pfarr K, Hoerauf A, Shima K, and Rupp J. Elaborations on Corallopyronin A as a Novel Treatment Strategy Against Genital Chlamydial Infections. *Front Microbiol.* **2019**, 10, 943-952.
- Ma H, Chiu F, and Li R. Mechanistic investigation of the reduction in antimicrobial activity of ciprofloxacin by metal cations. *Pharm Res.* **1997**, 14, 366-370.
- Ma Y, Zhou T, Kong X, and Hider RC. Chelating agents for the treatment of systemic iron overload. *Curr Med Chem.* **2012**, 19(17), 2816–2827.
- Mabey D, and Peeling RW. 39 – Chlamydia: Genital and ocular infections; infertility; atypical pneumonia. Medical Microbiology (Eighteenth edition). *Churchill Livingstone.* **2012**, 381-389.
- Mallavadhani UV, Sahoo L, Kumar KP, Murty US. Synthesis and antimicrobial screening of some novel chalcones and flavones substituted with higher alkyl chains. *Med Chem Res.* **2014**, 23, 2900-2908.
- Marin S, Vlasceanu GM, Tiplea RE, Bucur IR, Lemnaru M, Marin MM, and Grumezescu AM. Applications and toxicity of silver nanoparticles: a recent review. *Curr Top Med Chem.* **2015**, 15(16), 1596-1604.
- Mariotti SP, Pascolini D, Rose-Nussbaumer J. Trachoma: global magnitude of a preventable cause of blindness. *Br J Ophthalmol.* **2009**, 93(5), 563-8.
- Marsh JW, Ong VA, Lott WB, Timms P, Tyndall JD, and Huston WM. CtHtrA: the lynchpin of the chlamydial surface and a promising therapeutic target. *Future Microbiol.* **2017**, 12, 817-829

- Martell AE, and Motekaitis RJ. Determination and Use of Stability Constants. *VCH, New York*. **1992**.
- Marwaha S, Uvell H, Salin O, Lindgren AE, Silver J, Elofsson M, and Gylfe A. N-acylated derivatives of sulfamethoxazole and sulfafurazole inhibit intracellular growth of *Chlamydia trachomatis*. *Antimicrob Agents Chemother*. **2014**, 58(5), 2968-2971.
- Mattioli F, Puntoni M, Marini V, et al. Determination of deferasirox plasma concentrations: do gender, physical and genetic differences affect chelation efficacy? *Eur J Haematol*. **2015**, 94(4), 310-317.
- McShan AC, and De Guzman RN. The bacterial type III secretion system as a target for developing new antibiotics. *Chem Biol Drug Des*. **2015**, 85(1), 30-42.
- Mercado-Blanco J, van der Drift KM, Olsson PE, Thomas-Oates JE, van Loon LC, Bakker PA. *J Bacteriol*. **2001**, 183(6), 1909-1920.
- Merrell BJ, McMurry JP. Folic acid. *StatPearls [Internet]*. *Treasure Island (FL): StatPearls Publishing*. **2020**.
- Merzel RL, Boutom SM, Chen J, Frey C, Shedden K, Marsh EN, Banaszak Holl MM, Folate binding protein: therapeutic natural nanotechnology for folic acid, methotrexate, and leucovorin. *Nanoscale*. **2017 b**, 9(7), 2603-2615.
- Merzel RL, Frey C, Chen J, Garn R, van Dongen M, Dougherty CA, Kandaluru AK, Low PS, Marsh ENG, Banaszak Holl MM. Conjugation Dependent Interaction of Folic Acid with Folate Binding Protein. *Bioconjug Chem*. **2017 a**, 28(9), 2350-2360.
- Mestrovic T, and Ljubin-Sternak S. Molecular mechanisms of *Chlamydia trachomatis* resistance to antimicrobial drugs. *Front Biosci (Landmark Ed)*. **2018**, 23, 656-670.
- Miethke M, and Marahiel MA. Siderphore-based iron acquisition and pathogen control. *Microbiol Mol Biol Rev*. **2007**, 71(3), 413-451.
- Miethke M, and Marahiel MA. Siderphore-based iron acquisition and pathogen control. *Microbiol Mol Biol Rev*. **2007**, 71(3), 413-451.
- Miethke M, Kraushaar T, and Marahiel MA. Uptake of xenosiderophores in *Bacillus subtilis* occurs with high affinity and enhances the folding stabilities of substrate binding proteins. *FEBS Letters*. **2013**, 587(2), 206-213.
- Mishra MK, Kotta K, Hali M, Wykes S, Gerard HC, Hudson AP, Whittum-Hudson JA, and Kannan RM. PAMAM dendrimer-azithromycin conjugate nanodevices for the treatment of *Chlamydia trachomatis* infections. *Nanomedicine*. **2011**, 7(6), 935-944.

- Mitchell HK. Folic Acid. IV. Absorption Spectra. *J Am Chem Soc.* **1944**, 66(2), 274-278.
- Mohammadi G, Valizadeh H, Barzegar-Jalali M, Lotfipour F, Adibkia K, Milani M. et al. Development of azithromycin-PLGA nanoparticles: physicochemical characterization and antibacterial effect against salmonella typhi. *Colloids Surf B Biointerfaces.* **2010**, 80, 34-39.
- Mohammadzadeh F, Dolatian M, Jorjani M, Afrakhteh M, Majd H A, Abdi F, and Pakzad R. Urogenital Chlamydia trachomatis treatment failure with azithromycin: A meta-analysis. *Int J Reprod Bio Med.* **2019**, 17, 603-620.
- Mojica SA, Eriksson AU, Davis RA, Bahnan W, Elofsson M, and Gylfe Å. Red fluorescent *Chlamydia trachomatis* applied to live cell imaging and screening for antibacterial agents. *Front Microbiol.* **2018**, 9, 3151-3163.
- Mojica SA, Salin O, Bastidas RJ, Sunduru N, Hedenström M, Andersson CD, Núñez-Otero C, Engström P, Valdivia RH, Elofsson M, and Gylfe Å. N-Acylated Derivatives of Sulfamethoxazole Block Chlamydia Fatty Acid Synthesis and Interact with FabF. *Antimicrob Agents Chemother.* **2017**, 61(10), pii: e00716-17.
- Mosolygó T, Kincses A, Csonka A, Tönki ÁS, Witek K, Sanmartín C, Maré MA, Handzlik J, Kieć-Kononowicz K, Domínguez-Álvarez E, and Spengler G. Selenocompounds as Novel Antibacterial Agents and Bacterial Efflux Pump Inhibitors. *Molecules.* **2019**, 24(8).
- Naldini G, Grisci C, Chiavarini M, and Fabiani R. Association between human papillomavirus and chlamydia trachomatis infection risk in women: a systematic review and meta-analysis. *Int J Public Health.* **2019**, 64(6), 943-955.
- Nau R, Sorgel F, and Eiffert H. Penetration of drug through the blood-cerebrospinal fluid/blood-brain barrier for treatment of central nervous system infections. *Clin Microbiol Rev.* 2010, 23(4), 858-883.
- Negash KH, Norris JKS, Hodgkinson JT. Siderophore-Antibiotic Conjugate Design: New Drugs for Bad Bugs? *Molecules.* **2019**, 24(18), pii: E3314.
- Nguyen B D, Cunningham D, Liang X, Chen X, Toone E J, Raetz C R, Zhou P, and Valdivia R H. Lipooligosaccharide is required for the generation of infectious elementary bodies in *Chlamydia trachomatis*. *Proc Natl Acad Sci USA.* **2011**, 108(25), 10284-10289.

- Öhrström, M.; Popović-Bijelić, A.; Luo, J.; Stenmark, P.; Högbom, M.; Gräslund, A. Inhibition of chlamydial class Ic ribonucleotide reductase by C-terminal peptides from protein R2. *J Pep Sci.* **2011**, 17, 756-762.
- Oliveri V and Vecchio G. 8-hydroxyquinolin in medical chemistry: A structural spective. *Eur J Med Chem.* **2016**, 120, 252-274.
- Ong VA, Lawrence A, Timms P, Vodstrcil LA, Tabrizi SN, Beagley KW, Allan JA, Hocking JS, and Huston WM. In vitro susceptibility of recent *Chlamydia trachomatis* clinical isolates to the CtHtrA inhibitor JO146. *Microbes Infect.* **2015**, 17, 738-744.
- Ong VA, Marsh JW, Lawrence A, Allan JA, Timms P, and Huston WM. The protease inhibitor JO146 demonstrates a critical role for CtHtrA for *Chlamydia trachomatis* reversion from penicillin persistence. *Front Cell Infect Microbiol.* **2013**, 3, 100-110.
- Pan XS, Fisher LM. *Streptococcus pneumoniae* DNA gyrase and topoisomerase IV: overexpression, purification, and differential inhibition by fluoroquinolones. *Antimicrob Agents Chemother.* **1999**, 43, 1129-1136.
- Panyam J, and Labhasetwar V. Dynamics of endocytosis and exocytosis of poly(D,L-lactide-co-glycolide) nanoparticles in vascular smooth muscle cells. *Pharm Res.* **2003**, 20, 212-220.
- Panyam J, Whittum-Hudson JA, Hudson AP. Nanoparticles for imaging and treating chlamydial infection. *US. Patent* 8,647,673, **2014**.
- Paradkar P N, Domenico I D Durchfort N, Zohn I, Kaplan J, and Ward D M. Iron depletion limits intracellular bacterial growth in macrophages. *Blood.* **2008**, 112(3), 866-874.
- Patel JB, Cockerill FR, Bradford PA, Eliopoulos GM, Hindler JA, Jenkin SG, Lewis JS, Limbago B, Miller LA, Nicolau DP, Powell M, Swenson JM, Traczewski MM, Turnidge JD, Weinstein MP, and Zimmer BL.. Methods for dilution antimicrobial susceptibility tests for bacteria that grow aerobically; approved standard M07-A10. *Clinical and Laboratory Standards Institute (CLSI, USA).* **2015**. 35(2).
- Peach MJG, P. Benfeld, T. Helgaker, D.J. Tozer, Excitation energies in density functional theory: an evaluation and a diagnostic test. *J Chem Phys.* **2008**, 128(4), 044118.
- Pedersen C, Slepkin A, Andersson SB, Fagerberg JH, Bergström CA, and Peterson EM. Formulation of the microbicide INP0341 for *in vivo* protection against a vaginal challenge by *Chlamydia trachomatis*. *Plos One.* **2014**, 9(10), e110918 .

- Perdew JP, Burke K, and Ernzerhof M. Generalized gradient approximation made simple. *Phys Rev Lett.* 77 (18) (1996) 3865-3868.
- Peterman TA, Newman DR, Maddox L, Schmitt K, and Shiver S. Risk for HIV following a diagnosis of syphilis, gonorrhoea or chlamydia: 328,456 women in Florida, 2000-2011. *Int J STD AIDS.* **2015**, 26(2), 113-119.
- Phillips S, Quigley B L, and Timms P. Seventy years of chlamydia vaccine research - Limitations of the past and directions for the future. *Front Microbiol.* **2019**, 10, 70.
- Pierre JL, Baret P, and Serratrice G. Hydroxyquinolines as Iron Chelators. *Curr Med Chem.* **2003**, 10(12), 1077-1084.
- Piña-Vázquez C, and López-Soto LF. The struggle for iron: pathogen vs. host, Chapter 4, Iron storage: a matter of life or death! *Cinvestav.* **2013**.
- Pippi B, Reginatto P, Machado GRM, Bergamo VZ, Lana DFD, Teixeira ML, Franco LL, Alves RJ, Andrade SF, and Fuentefria AM. Evaluation of 8-hydroxyquinoline derivatives as hits for antifungal drug design. *Med Mycol.* **2017**, 55(7), 763-773.
- Porter J, Gyparaki M, Burke L, Huehns E, Sarpong P, Saez V, and Hider R. Iron mobilization from hepatocyte monolayer cultures by chelators: The importance of membrane permeability and the iron-binding constant. *Blood.* **1988**, 72, 1497-1503.
- Potroz MG, and Cho NJ. Natural products for the treatment of trachoma and *Chlamydia trachomatis*. *Molecules*, **2015**, 20, 4180-4203.
- Prachayasittikul V, Prachayasittikul S, Ruchirawat S, and Prachayasittikul V. 8-Hydroxyquinolines: a review of their metal chelating properties and medicinal applications. *Drug Des Dev Ther.* **2013**, 7, 1157-1178.
- Prusty BK, Chowdhury SR, Gulve N, and Rudel T. Peptidase Inhibitor 15 (PI15) Regulates Chlamydial CPAF Activity. *Front Cell Infect Microbiol.* **2018**, 8, 183.
- Q**u T, Qu L, Wang X, Xu T, Xiao X, Ding M, Deng L, and Gou Y. Design, synthesis, and antibacterial activity of novel 8-methoxyquinoline-2-carboxamide compounds containing 1,3,4-thiadiazole moiety. *Z Naturforsch.* **2017**, 73(3-4), 117-122.
- R**akba N, Aouad F, Henry C, Caris C, Morel I, Baret P, Pierre JL, Brissot PW, Lescoat G, and Crichton RR. Iron mobilisation and cellular protection by a new synthetic chelator O-Trensox. *Biochem Pharmacol.* **1995**, 55(11), 1797-1806.

- Rani UA, Ng LY, Ng CY, and Mahmoudi E. A review of carbon quantum dots and their applications in wastewater treatment. *Adv Colloid Interface Sci.* **2020**, 278, 102124.
- Raulston JE. Response of *Chlamydia trachomatis* serovar E to iron restriction in vitro and evidence for iron-regulated chlamydial proteins. *Infect Immun.* **1997**, 65(11), 4539-4547.
- Raymond K, Müller G, and Matzanke B. Complexation of iron by siderophores a review of their solution and structural chemistry and biological function. *Top Curr Chem.* **1984**, 123, 49–102.
- Rbaa M, Jabli S, Lakhrissi Y, Ouhsine M, Almalki F, Hadda T, Moumene SM, Zarrouk A, and Lakhrissi B. Synthesis, antibacterial properties and bioinformatics computation analyses of novel 8-hydroxyquinoline derivatives. *Heliyon.* **2019**, 5(10), 2689-2694.
- Recuero-Checa MA, Sharma M, Lau C, Watkins PA, Gaydos CA, and Dean D. *Chlamydia trachomatis* growth and development requires the activity of host Long-chain Acyl-CoA Synthetases (ACSLs). *Sci Rep.* **2016**, 6, 23148.
- Reimer A, Seufert F, Weiwad M, Ebert J, Bzdyl NM, Kahler CM, Sarkar-Tyson M, Holzgrabe U, Rudel T, and Kozjak-Pavlovic V. Inhibitors of macrophage infectivity potentiator-like PPIases affect neisserial and chlamydial pathogenicity. *Int J Antimicrob Agents.* **2016**, 48, 401-408.
- Reveneau N, Crane DD, Fischer E, Caldwell HD. Bactericidal activity of first-choice antibiotics against gamma interferon-induced persistent infection of human epithelial cells by *Chlamydia trachomatis*. *Antimicrob Agents Chemother.* **2005**; 49(5),1787-1793.
- Ridgway GL, Mumtaz G, Gabriel FG, and Oriel JD. The activity of ciprofloxacin and other 4-quinolones against *Chlamydia trachomatis* and *Mycoplasmas* in vitro. *Eur J Clin Microbiol.* **1984**, 3(4), 344-346.
- Rousseau L, Brémond E, and Lefèvre G. Assessment of the ground spin state of iron(i) complexes: insights from DFT predictive models. *New J Chem.* **2018**, 42(10), 7612-7616.
- Rumpianesi F, Sambri V, Bertini S, Tamba I, and Cevenini R. In vitro activity of ciprofloxacin against *Chlamydia trachomatis* and *Ureaplasma urealyticum*. *Chamioterapia.* **1984**, 3(3), 173-174.

- Rumpianesi F, Sambri V, Bertini S, Tamba I, Cevenini R. *In vitro* activity of ciprofloxacin against *Chlamydia trachomatis* and *Ureaplasma urealyticum*. *Chemioterapia*. **1984**, 3(3), 173-174.
- Runge E, and Gross EKV. Density-functional theory for time-dependent systems. *Phys Rev Lett*. **1984**, 52(12), 997-1000.
- Sadhasivam A, and Vetrivel U. Identification of potential drugs targeting L,L-diaminopimelate aminotransferase of *Chlamydia trachomatis*: An integrative pharmacoinformatics approach. *J Cell Biochem*. **2018**, doi: 10.1002/jcb.27553. [Epub ahead of print].
- Saha M, Sarkar S, Sarkar B, Sharma BK, Bhattacharjee S, Tribedi P. Microbial siderophores and their potential applications: a review. *Environ Sci Pollut Res Int*. **2016**, 23(5), 3984-3999.
- Saha R, Saha N, Donofrio RS, and Bestervelt LL. Microbial siderophores: a mini review. *J Basic Microbiol*. **2012**, 303-317.
- Sahu R, Verma R, Dixit S, Igietseme JU, Black CM, Duncan S, Singh SR, and Dennis VA. Future of human *Chlamydia* vaccine: potential of self-adjuvanting biodegradable nanoparticles as safe vaccine delivery vehicles. *Expert Rev Vaccines*. **2018**, 17(3), 217-227.
- Saleeb M, Mojica S, Eriksson AU, Andersson CD, Gylfe Å, Elofsson M. Natural product inspired library synthesis - Identification of 2,3-diarylbenzofuran and 2,3-dihydrobenzofuran based inhibitors of *Chlamydia trachomatis*. *Eur J Med Chem*. **2018**, 143, 1077-1089.
- Saureu S, and de Graaf C. TD-DFT study of the light-induced spin crossover of Fe(III) complexes. *Phys Chem Chem Phys*. **2016**, 18(2), 1233-1244.
- Savić-Gajić IM and Savić IM. Drug design strategies with metal-hydroxylquinoline complexes. *Expert Opin Drug Discov*. **2020**, 15(3), 383-390.
- Schiefer A, Schmitz A, Schaberle TF, Specht S, Lammer C, Johnston KL, Vassilyev DG, König GM, Hoerauf A and Pfarr K. Corrallopyronin A specifically targets and depletes essential obligate *Wolbachia* endobacteria from filarial nematodes in vivo. *J Infect Dis*. **2012**, 206, 249-257.

- Schuchardt L and Rupp J. *Chlamydia trachomatis* as the cause of infectious infertility: Acute, repetitive or persistent long-term infection? *Curr Top Microbiol Immunol.* **2018**, 412, 159-182.
- Sciortino A, Cannizzo A, and Messina F. Carbon Nanodots: A Review—From the Current Understanding of the Fundamental Photophysics to the Full Control of the Optical Response. *Carbon.* **2018 a**, 4(4), 67.
- Sciortino A, Mauro N, Buscarino G, Sciortino L, Popescu R, Schneider R, Giammona G, Gerthsen D, Cannas M, and Messina F. β -C₃N₄ Nanocrystals: Carbon Dots with Extraordinary Morphological, Structural, and Optical Homogeneity. *Chem Mater.* **2018 b**, 30(5), 1695-1700.
- Serradji N, Vu TH, Kim H, Panyam J and Verbeke P. Inhibition of *Chlamydia trachomatis* growth during the last decade: a mini-review. *Mini Rev Med Chem.* **2018**, 18 (16), 1363-1372.
- Serratrice G, Baret P, Boukhalfa H, Gautier-Luneau I, Luneau D, and Pierre JL. Structural characterization of a tris-salicylate coordination for iron(III) with the tripodal ligand O-TRENSEX, *Inorg. Chem.* 1999, 38(5), 840–841.
- Serratrice G, Boukhalfa H, Béguin C, Baret P, Caris C, Pierre JL. O-TRENSEX, a new tripodal iron chelator based on 8-hydroxyquinoline subunits: thermodynamic and kinetic studies. *Inorg Chem.* **1997**, 36, 3898–3910.
- Sessa R, Di Pietro M, Filardo S, Bressan A, Rosa L, Cutone A, Frioni A, Berlutti F, Paesano R, Valenti P. *Biochem Cell Biol.* **2017**, 95(1), 34-40.
- Shah S, Barton G, and Fischer A. Pharmacokinetic considerations and dosing strategies of antibiotics in the critically ill patient. *J Intensive Care Soc.* **2015**, 16(2), 147-153.
- Sharma VK, McDonald TJ, Sohn M, Anquandah GAK, Pettine M, and Zboril R. Assessment of toxicity of selenium and cadmium selenium quantum dots: A review. *Chemosphere.* **2017**, 188, 403-413.
- Sharpe PC, Richardson DR, Kalinowski DS, and Bernhardt PV. Synthetic and natural products as iron chelators. *Curr Top Med Chem.* **2011**, 11, 591-607.
- Sherrard J, Jensen JS. *Chlamydia* treatment failure after repeat courses of azithromycin and doxycycline. *Int J STD AIDS.* **2019**, 30(10), 1025-1027.
- Shima K, Ledig S, Loeper N, Schiefer A, Pfarr K, Hoerauf A, Graspeuntner S, and Rupp J. Effective inhibition of rifampin-resistant *Chlamydia trachomatis* by the novel DNA-

- dependent RNA-polymerase inhibitor Corallopyronin A. *Int J Antimicrob Agents*. **2018**, 52, 523-524.
- Shivshankar P, Lei L, Wang J, and Zhong G. Rottlerin inhibits chlamydial intracellular growth and blocks chlamydial acquisition of sphingolipids from host cells. *Appl Environ Microbiol*. **2008**, 74(4), 1243-1249.
- Slade JA, Brockett M, Singh R, Liechti GW, Maurelli AT. Fosmidomycin, an inhibitor of isoprenoid synthesis, induces persistence in Chlamydia by inhibiting peptidoglycan assembly. *PLoS Pathog*. **2019**, 15(10), e1008078.
- Slastnikova TA, Rosenkranz AA, Khramtsov YV, Karyagina TS, Ovechko SA, and Sobolev AS. Development and evaluation of a new modular nanotransporter for drug delivery into nuclei of pathological cells expressing folate receptors. *Drug Des Devel Ther*. **2017**, 11, 1315-1334.
- Slepenkin A, Chu H, Elofsson M, Keyser P, Peterson EM. Protection of mice from a Chlamydia trachomatis vaginal infection using a Salicylidene acylhydrazide, a potential microbicide. *J Infect Dis*. **2011**, 204(9), 1313-1320.
- Slepenkin A, Enquist PA, Hägglund U, de la Maza LM, Elofsson M, and Peterson EM. Reversal of the antichlamydial activity of putative type III secretion inhibitors by iron. *Infect Immun*. **2007**, 75(7), 3478-3489.
- Song S, Kim MC, Sim E, Benali A, Heinonen O, and Burke K. Benchmarks and reliable DFT results for spin gaps of small ligand Fe(II) complexes, *J. Chem. Theory Comput*. 14 (5) (2018) 2304–2311.
- Stephens RS. Genomic autobiographies of *Chlamydiae*. In: Stephens RS (ed) Chlamydia. Washington, DC, ASM Press. **1999**, 9-27.
- Stevenson RL, and Freiser H. Tridentate ligands derived from substitution in the methyl group of 8-hydroxyquinoline. *Anal Chem*. **1967**, 39, 1354-1358.
- Su H, Raymond L, Rockey DD, Fischer E, Hackstadt T, and Caldwell HD. A recombinant *Chlamydia trachomatis* major outer membrane protein binds to heparan sulfate receptors on epithelial cells. *Proc Natl Acad Sci USA*. **1996**, 93(20), 11143-11148.
- Sujit Sheth. Iron chelation: an update. *Curr Opin Hematol*. **2014**, 21(3), 179-185.
- Sunduru N, Salin O, Gylfe Å, and Elofsson M. Design, synthesis and evaluation of novel polypharmacological antichlamydial agents. *Eur J Med Chem*. **2015**, 101, 595-603.

- Swart M, and Gruden M. Spinning around in transition-metal chemistry. *Acc Chem Res.* 2016, 49(12), 2690-2697.
- Swart M. Accurate spin-state energies for iron complexes. *J Chem Theory Comput.* **2008**, 4(12), 2057-2066.
- Sylvie Abdelsayed. PhD Thesis. Univ Paris Diderot. **2015**.
- T**ang CW, and VanSlyke SA. Organic electroluminescent diodes. *Appl Phys Lett.* **1987**, 51, 913-915.
- Tang CW, VanSlyke SA, and Chen CH. Electroluminescence of doped organic thin films. *J Appl Phys.* **1989**, 65, 3610-3616.
- Tang FF, Chang HL, Huang YT, and Wang KC. Studies on the etiology of trachoma with special reference to isolation of the virys in chick embryo. *Chin Med J.* **1957a**, 75, 429-447.
- Tang FF, Huang YT, Chang HL, and Wong KC. Isolation of trachoma virus in chick embryo. *J Hyg Epidemiol Microbiol Immunol.* **1957b**, 1, 109-120.
- Tardito S, Barilli A, Bassanetti I, Tegoni M, Bussolati O, Franchi-Gazzola R, Mucchino C, and Marchiò L. Copper-dependent cytotoxicity of 8-hydroxyquinoline derivatives correlates with their hydrophobicity and does not require caspase activation. *J Med Chem.* **2012**, 55(23), 10448-10459.
- Terazzi E, Guénee L, Bocquet B, Lemonnier J, Favera ND, and Piguet C. A simple chemical tuning of the effective concentration : Selection of single-, double-, and triple-stranded binuclear lanthanide helicates. *Chem Eur J.* **2009**, 15, 12719-12732.
- Thompson MG, Corey BW, Si T, Craft DW, and Zurawski DV. Antibacterial Activities of Iron Chelators against Common Nosocomial Pathogens. *Antimicrob Agents Chemother.* **2012**, 56(10), 54195421.
- Tian XT, and Yin XB. Carbon Dots, Unconventional Preparation Strategies, and Applications Beyond Photoluminescence. *Small.* **2019**, 15(48), e1901803.
- Tilbrook GS, and Hider RC. Iron chelators for clinical use. *Met Ions Biol Syst.* **1998**, 35, 691-730.
- Tomasi J, Mennucci B, and Cammi R. Quantum mechanical continuum solvation models. *Chem Rev.* 2005, 105(8), 2999-3094.

- Toti US, Guru BR, Hali M, McPharlin CM, Wykes SM, Panyam J, Whittum-Hudson JA. Targeted delivery of antibiotics to intracellular chlamydial infections using PLGA nanoparticles. *Biomaterials*. **2011**, 32(27), 6606-6613.
- Tremlett WDJ, Tong KKH, Steel TR, Movassghi S, Hanif M, Jamieson SMF, Sohnel T, and Hartinger CG. Hydroxyquinoline-derived anticancer organometallics: Introduction of amphiphilic PTA as an ancillary ligand increases their aqueous solubility. *J Inorg Biochem*. **2019**, 199, 110768-110775.
- Türkel N. Complex formation reactions of Scandium(III), Yttrium(III) and Lanthanum(III) complexes with 8-hydroxyquinoline. *Sci J Chem*. **2013**, 1(2), 21-25.
- Turquist TD, and Sandell EB. Stability constants of iron(III)-8-hydroxyquinoline complexes. *Analytica Chimica Acta*. **1968**, 42, 239-245.
- Uivarosi V. Metal complexes of quinolone antibiotics and their applications: An update. *Molecules*. **2013**, 18, 11153-11197.
- Unemo M, and Shafer W M. Antimicrobial resistance in neisseria gonorrhoeae in the 21st century: past, evolution and future. *Clin Microbiol Rev*. **2014**, 27(3), 587-613.
- Velthuisen EJ, Johns BA, Temelkoff DP, Brown KW, and Danehower SC. The design of 8-hydroxyquinoline tetracyclic lactams as HIV-1 integrase strand transfer inhibitor. *Eur J Med Chem*. **2016**, 117, 99-112.
- Volgyi G, Vizserálek G, TaKács-Novák K, Avdeef A, and Tam KY. Predicting the exposure and antibacterial activity of fluoroquinolones based on physicochemical properties. *Eur J Pharm Sci*. **2012**, 47(1), 21-27.
- Vu TH, Ha-Duong NT, Aubry A, Capton E, Fechter P, Plésiat P, Verbeke P, and Serradji N. In vitro activities of a new fluoroquinolone derivative highly active against *Chlamydia trachomatis*. *Bioorg Chem*. **2018**, 83, 180-185.
- Vu TH, Ha-Duong NT, Aubry A, Capton E, Fechter P, Plésiat P, Verbeke P, and Serradji N. In vitro activities of a new fluoroquinolone derivative highly active against *Chlamydia trachomatis*. *Bioorg Chem*. **2019**, 83, 180-185.
- Vu TH, Serradji N, Seydou M, Bremond E, Ha-Duong NT. Electronic spectroscopic characterization of the formation of iron(III) metal complexes: The 8-hydroxyquinoline as ligand case study. *J Inorg Biochem*. **2020**, 203, 110864-110873.

- Wang SP, and Grayston JT. Three new serovars of *Chlamydia trachomatis*: Da, Ia, and L2a. *J Infect Dis.* **1991**, 163, 403-405.
- WHO guidelines for the treatment of *Chlamydia trachomatis*, **2016**.
<http://www.who.int/reproductivehealth/publications/rtis/chlamydia-treatment-guidelines/en/>
- Wilbraham L, Adamo C, and Ciofni I. Communication: evaluating non-empirical double hybrid functionals for spin-state energetics in transition-metal complexes. *J Chem Phys.* **2018**, 148(4), 041103.
- Wilson BR, Bogdan AR, Miyazawa M, Hashimoto K, Tsuji Y. Siderophores in iron metabolism: From mechanism to therapy potential. *Trends Mol Med.* **2016**, 22(12), 1077-1090.
- Witkin SS, Minis E, Athanasiou A, Leizer J, and Linhares IM. *Chlamydia trachomatis*: the persistent pathogen. *Clin Vaccine Immunol.* **2017**, 24(10), e00203-17.
- Wooldridge KG, and Williams PH. Iron uptake mechanisms of pathogenic bacteria. *FEMS Microbiol Rev.* **1993**, 12(4), 325-348.
- Xia Q, Wang T, Xian J, Song J, Qiao Y, Mu Z, Liu H, Sun Z. Relation of *Chlamydia trachomatis* infections to ectopic pregnancy: A meta-analysis and systematic review. *Medicine (Baltimore).* **2020**, 99(1), e18489.
- Xie F, Cai H, and Peng F. Anti-prostate cancer activity of 8-hydroxyquinoline-2-carboxaldehyde-thiosemicarbazide copper complexes in vivo by bioluminescence imaging. *J Biol Inorg Chem.* **2018**, 23(6), 949-956.
- Xiong MH, Bao Y, Yang XZ, Zhu YH, and Wang J. Delivery of antibiotics with polymeric particles. *Adv Drug Deliv Rev.* **2014**, 78, 63-76.
- Xu X, Ray R, Gu Y, Ploehn HJ, Gearheart L, Raker K and Scrivens WA. Electrophoretic analysis and purification of fluorescent single-walled carbon nanotube fragments. *J Am Chem Soc.* **2004**, 126(40), 12736-12737.
- Yamakawa K, Matsuo J, Okubo T, Nakamura S, Yamaguchi H. Impact of capsaicin, an active component of chili pepper, on pathogenic chlamydial growth (*Chlamydia trachomatis* and *Chlamydia pneumoniae*) in immortal human epithelial HeLa cells. *J Infect Chemother.* **2018**, 24(2),130-137.

- Yanai T, Tew DP, and Handy NC. A new hybrid exchange-correlation functional using the Coulomb-attenuating method (CAM-B3LYP). *Chem Phys Lett.* 2004, 393(1), 51-57.
- Yang J, Cohen Stuart MA, and Kamperman M. Jack of all trades: versatile catechol crosslinking mechanisms. *Chem Soc Rev.* **2014**, 43(24), 8271-8298.
- Yang W, Liu F, Li R, Wang X, Hao W. Multiple stimuli-responsive fluorescent sensor from citric acid and 1-(2-aminoethyl)piperazine. *ACS Appl Mater Interfaces.* **2018**, 10(10), 9123-0128.
- Yang X, Cai P, Liu Q, Wu J, Yin Y, Wang X, and Kong L. Novel 8-hydroxyquinoline derivatives targeting β -amyloid aggregation, metal chelation and oxidative stress against Alzheimer's disease. *Bioorg Med Chem.* **2018**, 26(12), 3191-3201.
- Yilma AN, Singh SR, Dixit S, and Dennis VA. Anti-inflammatory effects of silver-polyvinyl pyrrolidone (Ag-PVP) nanoparticles in mouse macrophages infected with live *Chlamydia trachomatis*. *Int J Nanomedicine.* **2013**, 8, 2421-2432.
- Yuan F, Yuan T, Sui L, Wang Z, Xi Z, Li Y, Li X, Fan L, Tan Z, Chen A, Jin M, and Yang S. Engineering triangular carbon quantum dots with unprecedented narrow bandwidth emission for multicolored LEDs. *Nature Comm.* **2018**, 9, 2249.
- Zayed ME, El-Shishtawy RM, Elroby SA, Obaid AY, Al-Amshany ZM. Experimental and theoretical study of o-substituent effect on the fluorescence of 8-hydroxyquinoline. *Int J Mol Sci.* **2015**, 16(2), 3804-3819.
- Zetterström CE, Hasselgren J, Salin O, Davis RA, Quinn RJ, Sundin C, and Elofsson M. The resveratrol tetramer (-)-hopeaphenol inhibits type III secretion in the gram-negative pathogens *Yersinia pseudotuberculosis* and *Pseudomonas aeruginosa*. *Plos One*, **2013**, 8(12), e81969.
- Zhang H, Kunadia A, Lin Y, Fondell JD, Seidel D, and Fan H. Identification of a strong and specific antichlamydial *N*-acylhydrazone. *PLoS One.* **2017**, 12(10), e0185783.
- Zhang L, Pornpattananangku D, Hu CM, and Huang CM. Development of Nanoparticles for Antimicrobial Drug Delivery. *Curr Med Chem.* **2010**, 17, 585–594.
- Zhang Y, Liu X, Fan Y, Guo X, Zhou L, Lv Y, and Lin J. One-step microwave synthesis of N-doped hydroxyl-functionalized carbon dots with ultra-high fluorescence quantum yields. *Nanoscale.* **2016**, 8, 15281-15287.

- Zhao X, Li H, and Lee RJ. Targeted drug delivery via folate receptors. *Expert Opin Drug Deliv.* **2008**, 5(3), 309-319.
- Zhi B, Yao X, Cui Y, Orr G, and Haynes CL. Synthesis, applications and potential photoluminescence mechanism of spectrally tunable carbon dots. *Nanoscale.* **2019**, 11(43), 20411-20428.
- Zhu BZ, Zhu JG, Fan RM, Mao L. Chapter One - Metal-Independent Pathways of Chlorinated Phenol/Quinone Toxicity. *Adv Mol Tox.* **2011**, 5, 1-43.
- Zhu S, Song Y, Zhao X, Shao J, Zhang J, and Yang B. The photoluminescence mechanism in carbon dots (graphene quantum dots, carbon nanodots, and polymer dots): Current state and future perspective. *Nano Res.* **2015**, 8, 355-381.
- Zigangirova NA, Kost EA, Didenko LV, Kapotina LN, Zayakin ES, Luyksaar SI, Morgunova EY, Fedina ED, Artyukhova OA, Samorodov AV, and Kobets NV. A small-molecule compound belonging to a class of 2,4-disubstituted 1,3,4-thiadiazine-5-ones inhibits intracellular growth and persistence of *Chlamydia trachomatis*. *J Med Microbiol.* **2016**, 65, 91-98.
- Zigangirova NA, Zayakin ES, Kapotina LN, Kost EA, Didenko LV, Davydova DY, Rumyancheva JP, and Gintsburg AL. Development of Chlamydial Type III Secretion System Inhibitors for Suppression of Acute and Chronic Forms of Chlamydial Infection. *Acta Nat.* **2012**, 4(2), 87-97.
- Zuki HM. Spectrofluorometric determination of the stoichiometric and formation constant of 8-hydroxyquinoline complexes with Aluminium, Cadmium, Magnesium and Zinc in aqueous solution. *Ultra Chem.* **2012**, 8(3), 377-385.